Catalytic Conversion of Bio-derived Alcohols to Distillate Range Molecules

By
Emmanuel Canales

A dissertation submitted in partial fulfillment of
the requirements for the degree of

Doctor of Philosophy
(Chemical Engineering)

At the

UNIVERSITY OF WISCONSIN – MADISON

2024

Date of final oral examination: April 22nd, 2024

This dissertation is approved by the following members of the Final Oral Committee:

George W. Huber, Professor, Chemical and Biological Engineering
Victor M. Zavala, Professor, Chemical and Biological Engineering
Thatcher W. Root, Professor, Chemical and Biological Engineering
Ive Hermans, Professor, Chemistry

Abstract

Historically, ethanol has been blended into light-duty fuels in low amounts (up to 15 vol% in gasoline). With technological advancements in batteries, there is a projected decline in the demand for light-duty fuels in the next 20 years. This decline is attributed to the rise of electric vehicles, which is expected to lower the demand for gasoline. As electrification of the light-duty vehicle market increases, there will be a surplus of ethanol since less of it is used for light-duty fuel blending. Concurrently, the demand for transportation fuels such as diesel #2 is projected to increase. While current biofuel technology involves the dehydration of bioethanol to olefins for liquid hydrocarbon production, these processes are mainly limited to producing low molecular weight products tailored for gasoline. Therefore, it is important to focus on how we can shift the use of ethanol from light-duty fuel technology to heavy-duty fuel technology for the development of transportation fuels.

The Guerbet coupling of ethanol followed by etherification is a promising route for upgrading ethanol to distillate-range molecules. The feedstocks obtained from Guerbet coupling are complex oxygenate streams consisting of C_{4+} alcohols, esters, aldehydes, and ketones. There is significant interest in upgrading these complex feedstocks to C_{10+} ethers using acid catalysts. C_{10+} ethers possess similar physicochemical properties relative to diesel #2, suggesting that these molecules have the potential to be used as drop-in fuels for conventional diesel engines.

C_{8+} ethers were synthesized using model feedstocks indicative of ethanol oligomerization products over a $CuMg_xO_y$ catalyst. Initially, a 400+ hour time on stream (TOS) run of gas phase ethanol oligomerization at 75% conversion was conducted to assess the feasibility of producing alcohol feedstocks for a dehydration reactor. The catalyst used in the ethanol oligomerization step was regenerated twice in-situ in an up flow continuous flow reactor, and catalytic activity was fully recovered. The average selectivity to diesel fuel precursors was 86%. Diesel fuel precursors are defined as molecules of interest for drop-in diesel #2 production. The precursor definition includes C_{4+} alcohols, esters, aldehydes, and ketones.

Four different conversion points were studied from 12 – 69% ethanol conversion (referred to as feedstocks MG – 12 to MG – 69). A commercially available Zeolite HY catalyst was used for dehydration reactions in an up flow continuous flow reactor. Based on reaction studies using feedstock MG – 12, it was determined that small concentrations of esters negatively affect both the carbon balance and ether selectivity in the dehydration step. The feedstocks were then assumed to undergo an ester hydrogenolysis step. The hydrogenolysis step breaks down the esters to their parent alcohols, while simultaneously hydrogenating C=O species (i.e aldehydes, ketones) to obtain pure alcohol feedstocks for the dehydration reactor. These feedstocks compositions were then used for reaction studies to understand alcohol structural trends in the dehydration reactor. It was found that alcohol chain length, -OH group positioning and chain branching influence the final ether selectivities obtained. Increasing alcohol chain length favors olefin and coke formation. At the same time, feedstocks with larger C_{6+} alcohol fractions favor C_{10+} ether selectivities. Branched alcohols can undergo cross bi-molecular dehydration, while secondary alcohols mainly favor olefin and coke formation.

Using feedstock MG – 12, it was found that pressure plays a role in favoring bi-molecular dehydration over mono-molecular dehydration. While pure linear alcohol feeds are insensitive to pressure change, the addition of branched and secondary alcohols can increase the selectivity of olefin formation at atmospheric pressure. The coke selectivity was not affected, nor were the

carbon balances for reactions done at both atmospheric pressure and at 100 psig (6.9 bar). The final reaction pressure was maintained at 100 psig for all studies conducted with the continuous flow system to maximize the ether selectivity from this crucial process parameter.

With coworkers, a first technoeconomic analysis was performed to assess the economic and environmental feasibility of the ethanol to diesel process. It was shown that high conversion oligomerization reactors significantly reduced capital and operating costs. These high conversion reactors would produce the largest amount of C_{6+} alcohol content. The largest economic cost factor of the process is the starting feedstock used for bioethanol production, while the second largest cost factor is fuel yield. On an ethanol mass basis, the total fuel yield was 65.6 wt%. The final product was split into three fuel-grades: 26.8 wt% diesel #1, 4.3 wt% gasoline, and 34.5 wt% diesel #2. The diesel range ethers produced were shown to have a positive engine impact. The rich-ether blend led to higher combustion efficiencies and lowered both NO_X emissions and soot compared to fossil diesel #2. The flashpoint was slightly below ASTM standards (50 ºC vs 52 ºC), while having other similar physical properties to fossil diesel. The cetane number of the ether-rich blend was 73, well above the ASTM standard of 40 for diesel #2. The chemical process can be implemented with existing carbon-reduction technology, showing a 132.7% reduction in greenhouse gas emissions if CO_2 capture and renewable utilities were used in tandem.

A feedstock produced from ethanol/butanol oligomerization was studied to determine if the average alcohol carbon size can be shifted from C_{4+} to C_{6+} molecules, by recycling unreacted n-butanol into the oligomerization reactor. The ethanol:butanol ratio was 70:30 mol%, and the reactor was ran at 30% ethanol conversion. The ethanol/butanol oligomerization products had larger fractions of C_{6+} alcohols than the feedstocks previously studied and showed that the yield of C_{10+} ethers can increase with increasing C_{6+} alcohol content. It was also found that the esters negatively affect carbon balances and ether selectivity in the dehydration step. Using an intermediate reaction step with a Cu/ZrO_2 catalyst, esters were minimized by hydrogenolysis reactions to produce their respective alcohols and aldehydes. The Cu/ZrO_2 catalyst can also hydrogenate unsaturated C=O species, allowing C_{4+} aldehydes and ketones to be hydrogenated to their respective alcohols.

A second technoeconomic analysis was implemented with coworkers to assess the economic impact of an ester hydrogenolysis and n-butanol recycling unit. On an ethanol mass basis, the total fuel yield obtained was 63.4 wt%. The fuel-grade cuts were 3 wt% diesel #1, 2.5 wt% gasoline, and 57.9 wt% diesel #2. The fraction to light fuels decreases with the recycling step, showing that we can tailor the process to produce heavy fractions of fuel by tuning the n-butanol recycle ratio. The cetane number of the final diesel blend produced increased from 73 to 90. The technology can be price-competitive with current biodiesel technology that uses vegetables oils for transesterification reactions. In the absence of subsidies, we estimate that the price of vegetable oil feedstock has fluctuated between \$3.3 - 9.6/gal. The price of corn-based ethanol has fluctuated between \$2.3 - 4.6/gal, showing that ethanol feedstocks can offer a favorable economic path towards bio-diesel production.

Lastly, scale-up research studies were conducted in both continuous flow and batch reactors to understand the feasibility of the ethanol to diesel technology at larger dimensions. Using a pellitized version of zeolite Y, it was found that the pellet formulation has a significant impact on the final ether selectivities obtained. Carbon balances and ether selectivities were significantly lower at similar weighted hour space velocities (WHSV) compared to using pure zeolite Y. 75 mL batch reactors were used to screen the optimal conditions to perform dehydration reactions using 450 mL batch reactors. Followed by vacuum filtration, these conditions were used to produced

one liter of sample for engine testing. These findings suggest that it is possible to scale-up the dehydration chemistry to larger reactor volumes for liter production.

Acknowledgments

First off, I need to extend my best regards and wishes to Professor George W. Huber. While in the beginning of my PhD we did not necessarily understand each other, over the years we got to know what drives us to continue working each day. I’m glad that you were able to hear me out and my story as to how I got to this PhD in the first place. For the Huber Group, I am another proud graduate from this historic department and world-renowned research group. For others, you now know that this has been more than just a PhD. Your lab has fundamentally shaped my life forever, and it will be the wisdom, skills and abilities obtained that I will be passing down for generations to come. Being able to say that I have obtained a PhD from one of the best lab groups in the world is rare, and that rarity increases even further when I am now going to be the first in my family and friends to have a PhD. I don’t know if I will ever have the words to express how incredible this feat is, but all I can say is thank you for allowing me to get to this point. This PhD has broken a generational cycle in my family that I have been trying to surpass for as long as I can remember. For that, I will forever be thankful. I have finally paved the way for other generations, whether it be niece, nephews, brothers, sisters. I can now rest.

Another professor I would like to thank for everything is Victor M. Zavala: The man, the myth, the legend. Profe, your words will always have a special place in my heart. Those talks where I needed someone to tell me to keep going, to focus on the end goal and even hear out the traumas that I have dealt with put an ease to my anxiety that I have always experienced throughout my life. You are my second mentor, and I will forever thank you for your wisdom, knowledge and overall empathy that has gotten me to the PhD I will now have. Seeing that Mexicans can do it in the big leagues is amazing and inspiring and was one of the reasons I chose to come here. Sabiendo que si se puede hace una gran diferencia. Por favor, nunca cambias y que sigues siendo una inspiración para las nuevas generaciones. Te agradezco mucho por todo el esfuerzo que haces por nosotros.

I would also like to thank my committee for being there and giving me the advice I needed to further improve as a researcher. I extend my dearest gratitude to Ive Hermans and Thatcher Root, as their expertise and advice has helped me tone my skills to the researcher I am today. Ive, never stop being funny and witty! That energy is needed in the world of academia. Thatcher, your critiques and expertise challenged and helped me see the bigger picture of my work, and how I need to be careful with what I am claiming. I would also like to thank Reid Van Lehn for hearing me out and giving me a space where my voice can be heard as a graduate student and researcher.

In the world of research, nothing can be done without the help of your peers and coworkers. I extend my deepest gratitude to Kevin, Min Soo, Jiayang, Houqian, Hochan, Dr. Aurora Munguía-López, Dr. Brent Handy, Dr. Guadalupe-Cardenas, and others that I may have missed for their expertise, guidance, and support throughout these PhD years. A very big shoutout to Leoncio for being a great mentor/co-worker, as well as a great friend. I would also like to give gratitude to Professor Juan Manuel Restrepo-Florez, as his guidance, friendliness and expertise has fundamentally shaped the way I view process development. I will forever be thankful for working by your side and knowing that we were able to accomplish so much for our process. I also want to thank the mechanical engineering team, and others I may have missed who I have worked with for the past four years on the ethanol to diesel project. Javier Chavarrio – YOU got OUR ideas done! You came and absolutely amazed me! The ester hydrogenolysis work was crucial for our ethanol to diesel process, and it has been an amazing couple of years working by your side. Thank you for not only being a good coworker, but also being a wonderful friend who looks out for me during those tough days. I wish you the best of luck in your PhD, and hopefully one day we make that Colombia trip!

To Dr. Kieshla Rivera-Dones – Thank you for all the support. My expertise in reactor building could not have been developed without your guidance. Our friendship could not have been any better, and having someone I was able to lean on when the days got rough helped me take those baby steps to further better myself.

To Leonardo Gonzalez Chavez – We made it bro. I think we were destined to know each other considering that we saw each other at three separate recruitments at three different locations in the states. Getting through the first year was an experience, and your intelligence will always amaze me and has helped me shape my perspective on life in general. Your advice and even guidance has helped me calm my anxiety too. I loved meeting Annie, and Darby is beautiful. I'm glad Mona is there now. I think Darby needed someone else to bother. Good luck with everything my man. You deserve it.

To Kelly Burton – The powerhouse of GERS. Thank you for making GERS feel like a community. A community where I felt like I belonged. I will always thank you for having your door opened for me and hearing my issues and providing the support that I knew I desperately needed during those rough days. Thank you for being by my side. I would always be grateful for being chosen as a GERS scholar and will carry that title PROUDLY for the rest of my life.

To ALL my friends from BROOKLYN, NEW YORK! Your boy MADE IT! I just showed the world that we aren't just another statistic, that we as people from tough upbringings have the courage, the work ethic and brainpower to obtain what we want in our lives. I have seen a bunch of us grow since middle school, and words cannot express the amount of gratitude I have for you guys.

Oscar, Dave, Chris, Jose, and Joe – y'all made my nights amazing when workdays were rough, and I cannot wait to see what life has in store for us. You guys were there when I needed someone and when I was going through a rough time with my mental health. I love you guys.

Giovanni, Mark, and Johnny – I'll always cherish your remarks and how you guys were always asking how I'm doing. Hopefully we can get back to our soccer days.

Nevada and John – Thank you for being amazing friends. I love you, Nevada! Thank you for being such a supportive friend since middle school. You have been there through thick and thin and have always cared about my well-being. I can't wait to meet Bradley in person! I know I'm behind some gifts!

Ruben and Moe – Can't wait to hang out like we did back in our Buffalo days! I'm ready to watch Ecuador, Mexico and Egypt make us punch the air when the next world cup comes around.

To Kevin, Tamara and Alvin – Y'all know I can't wait to go back home and hang out with y'all. I absolutely feel like it's the good ol' days when we were younger just living life on the streets of Brooklyn. Every time I go back home now, I always want to go see how y'all are doing. I cannot wait to see what life has planned for all of us. Thank you for being honest, funny, and real friends. I promise I won't disappear again. Even after some distant years, you still took me in as family, and that's how I know our bond has never been broken. I love y'all.

Elizabeth Melchor, llegaste en un punto de mi vida muy inesperado. Conociéndote ha sido unas de las mejores experiencias que he tenido en estos últimos años. Desde que te conocí, la vida se ha sentido mucho más divertido, y cada día me encanta conocerte más. Estoy muy feliz de tener a alguien muy inteligente, trabajadora y empática a mi lado. Estoy entusiasmado de a ver que tiene la vida preparada para nosotros.

And finally, this last portion is for my family. The ones who made the sacrifices necessary for me to be successful.

Mama y papa – Yo a veces pensaba que la vida siempre iba ser difícil. Viendo como ustedes trabajaban día al día, me hacía pensar que yo también tenía que hacer lo mismo. De ustedes aprendí que con trabajo duro e inteligencia las cosas en la vida se pueden dar. Tal vez no nacimos con mucho dinero, pero siempre voy a agradecer el esfuerzo que ustedes hicieron para que yo fuera a la universidad. El apoyo que me dieron me ha cambiado la vida. De ustedes salió mi inteligencia, mi ambición de buscar algo mejor; esa ambición que ustedes tenían hace años cuando decidieron venir a este país. Platicando con mucha gente, ellos tienen mucho respeto para ustedes por lo que tuvieron que hacer para llegar a este país. El país que me dio las herramientas para mejorar nuestras vidas. Las herramientas que ahora conozco y que voy a entregar a mi hermanita ¡Mira, hasta ya estoy escribiendo en español! Nunca pensaba que iba poder hacer eso tampoco. Yo nunca pensaba que iba poder hacer todo lo que ha hecho. A veces ni se cómo lo hice. A veces ni se si me lo merezco. Muchas cosas en nuestras vidas han pasado, y de esos obstáculos aprendí como salir adelante. Gracias por todo. No sé qué más que decir. Tengo ganas de llorar y por fin decir – Ya se logró. Si se pudo. Tu hijo pudo lograr algo que nadie en nuestra familia a echo hasta ahora.

To Yarezti Canales – I love you little girl. You are the sunshine to my gloomy day. I hope I can be a good role model to you, and I hope you don’t have to go through the hardships I had to go through growing up. I now know how the education system works, and I will tirelessly help you achieve your goals. I now have the skills, knowledge and abilities that bring people to the next level in life. I promise you I will always be there when you need me. I won't let you down, and I'm going to make sure you keep your head up high. Don't worry, I got your back sis. Sometimes you scare me because at your age, I already feel like you are and will be smarter than I ever will be.

And lastly, to my chubby cat Ebony, for just being a sweet and adorable pet on those days that I couldn't stand doing anything in life. You ask for way too much food man.

Well, I guess that's all folks. I have learned many valuable lessons during my PhD journey. To the little boy who had dealt with so many obstacles in life: You did it. You are enough. And more importantly, you can take a break now. Relax, life is only going to get better.

¡LOS AMO TODOS! ¡MI QUERIDO ABUELITO DOMINGO Y TIO NACHO, EN OTRA VIDA NOS VEREMOS OTRA VEZ! ¡POR AHORA, LOS TRAIGO COMO MIS ANGELES PROTECTORES! ¡AQUÍ ESTOY PARA NUESTRA FAMILIA! ¡SI SE PUDO!

Table of Contents

List of Figures

List of Tables

List of Schemes

Chapter 1. Introduction

1.1 Current bio-ethanol infrastructure

Economic, environmental and energy concerns have motivated research for fuel production from renewable sources. The production of bioethanol from maize in the United States began in 1980 to tackle oversupply in the farming sector. Government action over the years has further established the necessary infrastructure for bio-ethanol production by enacting laws such as the 2005 Energy Policy Act and 2007 Energy Independence and Security Act. These regulations have promoted the production of E85 (85% bio – ethanol, 15% gasoline), though it contributes to only 1% of US bioethanol consumption[1]. Furthermore, a baseline for vehicle fuel economy and standards was added, consisting of 35-mile averages for small and light trucks by 2020, increasing bio-fuel production to 136 billion liters by 2022, and setting requirements that biofuels have at least a 20% carbon emission reduction over their life cycle. These regulations have established an infrastructure in which bioethanol can be taken advantage of to produce commercial fuels from renewable resources.

In 2018, the US alone produced 14.4 billion gallons of ethanol, and promising technology has been developed to produce bioethanol as an additive to fuels. However, these blends typically have a low vol% of ethanol at around 10%, lower energy content per gallon compared to conventional gasoline, and enhanced H_2O solubility which can cause corrosion in engines[2, 3]. Furthermore, increasing the amount of ethanol in the blend requires the development of engines that can comply with federal regulations. These regulations consist of OSHA-approved fuel dispensing equipment, meeting ASTM D4806 standards for ethanol blends, and EPA requirements to reduce the risk of misfuelling. These regulations are required if blends above 10% vol are used, and involve use of specific storage, material and flexible fuel vehicles needed for safe use[4]. It is also projected that the demand for light fuels such as gasoline will decrease, while the demand for transportation fuels such as jet and diesel is projected to increase over the next twenty years[5]. Current technological advancements in light-duty electric vehicles have slowly reduced ethanol blending, increasing supply. Thus, it is important to begin to understand how the current infrastructure can be used to shift the use of bioethanol from light-duty technology to heavy-duty technology.

1.2 Current bioethanol to distillate fuel technology

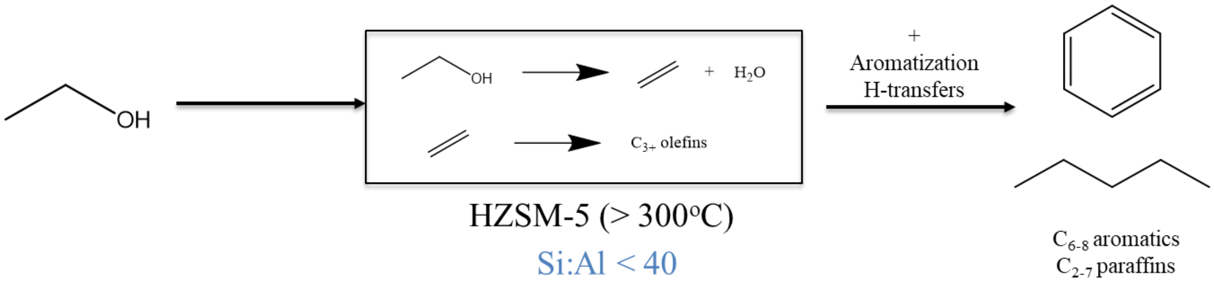

Scheme 1.1. Simultaneous ethanol dehydration and olefin oligomerization to gasoline-range molecules using zeolite catalysts. Using Si:Al ratios < 40 promotes the formation of higher hydrocarbons.

Current bio-fuel technologies involve dehydration of bioethanol to produce liquid hydrocarbons over H-ZSM5, as shown in **Scheme 1.1**. Typically, ethanol undergoes dehydration to ethylene followed by ethylene oligomerization, with both reactions occurring simultaneously above temperatures of 300°C. However, side reactions of C_{5+} species produce C_{6+} aromatics and C_{5+} paraffins, which are molecules mainly suitable for gasoline[3]. Ethanol conversion to olefins is strongly dependent on the silicia to alumina (Si:Al) molar ratios of H-ZSM5. At Si:Al molar ratios greater than 40, activity begins to decrease, and ethylene becomes the major product. At lower Si:Al molar ratios, the conversion of ethylene to higher hydrocarbons increases, though more aromatics are present with increasing Bronsted acid site (BAS) activity[6-8]. Moreover, the concentrations of all aromatics are higher than the concentrations of C_{5+} olefins, suggesting that ethylene oligomerization is limited by undesired side reactions. Other studies of ethanol dehydration to olefins have been conducted over other zeolites such as H-Y and H-BEA, but these have larger pores that contribute to faster coke generation and deactivation of BAS[9]. Additionally, the C_{12+} hydrocarbon products from H-Y and H-BEA are composed of only aromatics and are not suitable additives for diesel and jet fuels.

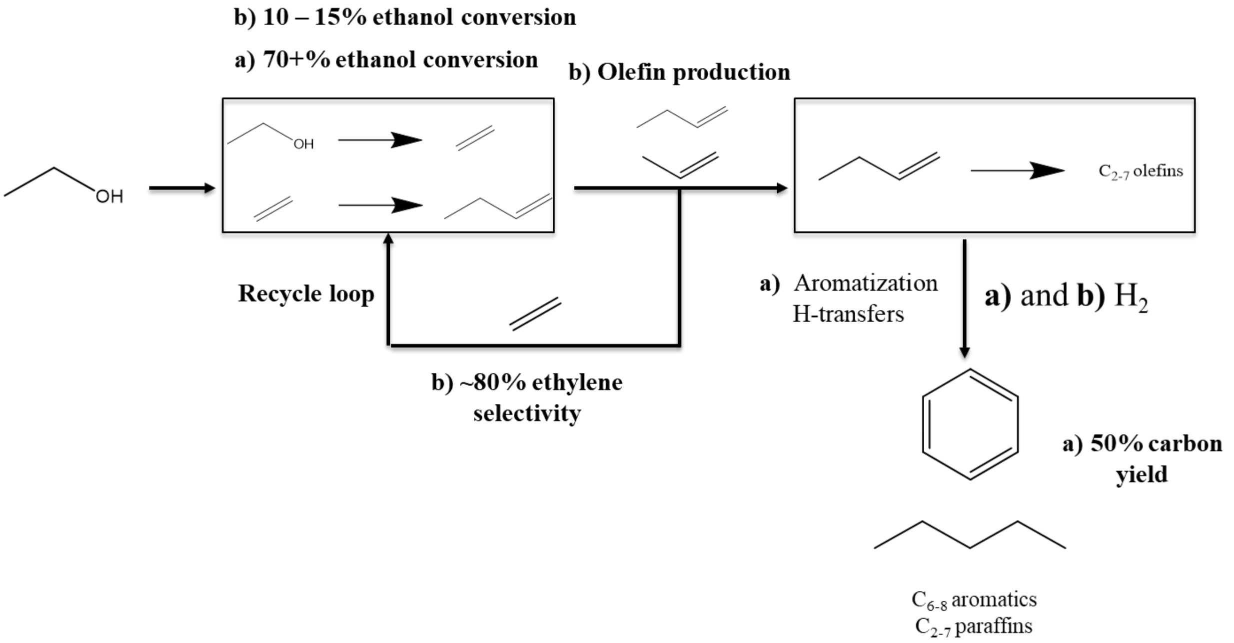

Scheme 1.2. Two step bioethanol upgrading to fuel-range molecules. A) represents pathway for high conversion ethanol reactors and B) represents pathway for low conversion ethanol reactors. This pathway requires a separation unit to remove ethylene from other light olefins.

Scheme 1.2 represents the process for bioethanol upgrading involving ethanol dehydration to C_{3+} olefins at temperatures >450ºC, followed by oligomerization of C_{3+} olefins at 100-250ºC. Side reactions like aromatization, cracking and hydrogen transfer are minimized at lower temperatures, resulting in higher selectivities towards higher n-olefins. It is important to note that in these ethanol-to-olefin routes, olefins cannot directly be used into blendstocks and must undergo an additional hydrogenation step to produce the paraffins necessary for diesel and jet fuel, which increases the costs associated with ethanol upgrading. Furthermore, a two-step ethanol to olefin route is strongly dependent on the ethanol dehydration reactor and can increase capital costs[3]. For example, high ethanol conversions (~75%) results in high yields of light paraffins and aromatics (~50% carbon yield) that cannot be blended into diesel/jet, while low ethanol conversions (10-15%) would have higher selectivities towards ethylene (~80%) but can be costly, as ethylene would need to be recycled and separated from C_{3+} hydrocarbons[3].

1.3 Ethanol growth to larger chain molecules

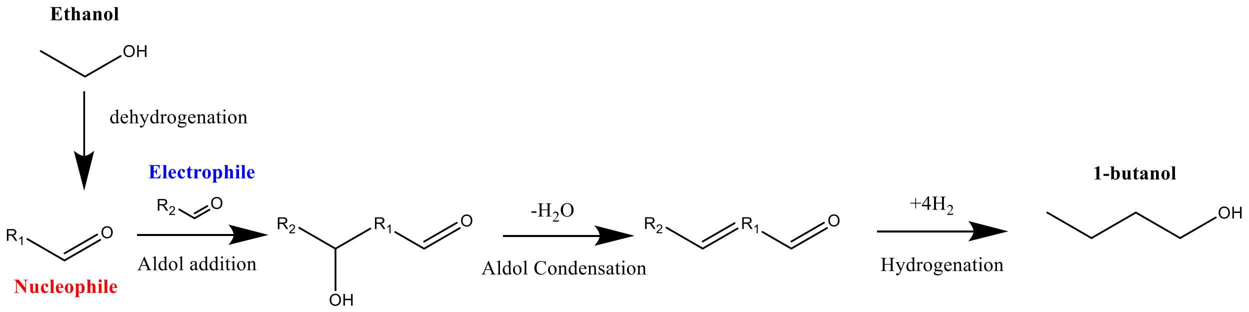

Figure 1.1. Guerbet Coupling Mechanism of ethanol to 1- butanol. Note that R1 is defined as the α-carbon of the nucleophile, which attacks the carbonyl carbon of the electrophile, an aldehyde. Aldol addition and condensation produce an alkenal, which undergoes two hydrogenation steps to produce 1-butanol.

In recent years, Guerbet coupling has gained attention as a pathway to convert ethanol into 1-butanol over base catalysts such as HAP. Alcohol coupling is commonly accepted to occur via the Guerbet mechanism as shown in **Figure 1.1**. It is hypothesized that branching occurs due to higher alcohols forming secondary enolates, which react with an aldehyde derived from any alcohol to produce branched products[10]. The Guerbet mechanism creates a distribution of alcohol products since ethanol and higher alcohols can all undergo coupling to produce their respective nucleophilic enolates. However, to selectively produce linear alcohols, the nucleophile must be derived from ethanol. This may impose limitations for ether production, as branched alcohols are more likely to undergo unimolecular dehydration in the etherification step. Nevertheless, the thermodynamics of Guerbet Coupling suggest that the mechanism is not thermodynamically limited[3], and the main challenge is achieving high ethanol conversion with high selectivity to C_{4+} alcohols. Compared to the two previously mentioned technologies, Guerbet coupling offers a first step to producing higher alcohols necessary for etherification, thereby establishing a direct route to distillate range ethers.

To understand the feasibility of ethanol chain growth to higher alcohols to produce distillate range ethers, A 400+ hr time on stream (TOS) Guerbet coupling run in a continuous packed bed reactor was conducted to assess the product distribution at high ethanol conversion and determine the regeneration capability of a Cu/Mg_xAlO_y catalyst. **Figure 1.2** depicts the diesel precursor selectivity and alcohol conversion as a function of TOS. The catalyst was regenerated twice, showing that catalytic activity can be recovered.

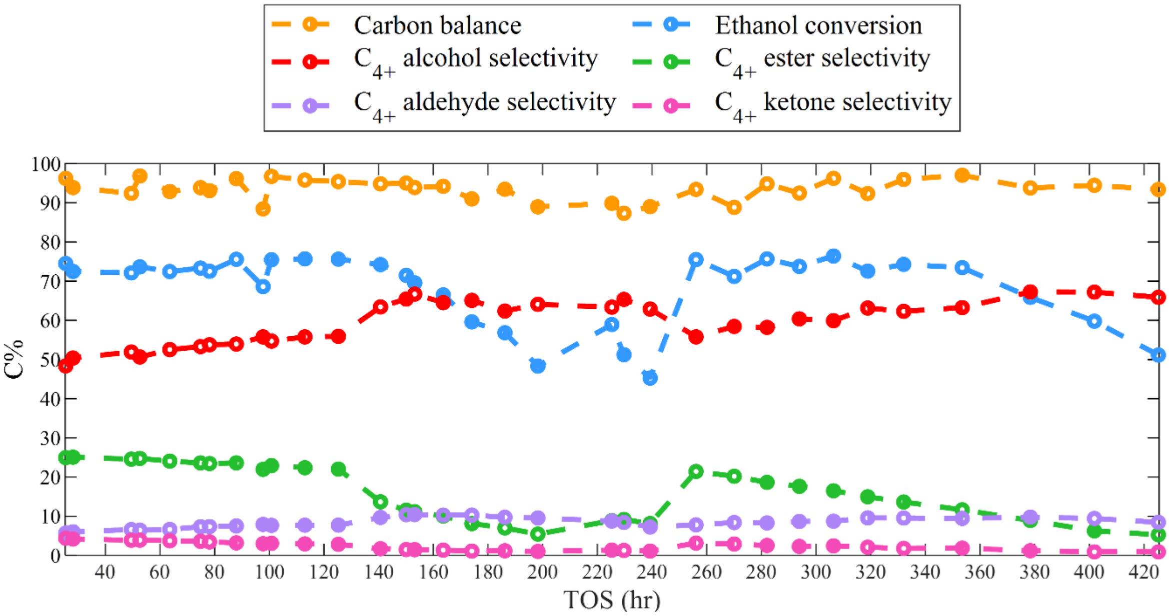

Figure 1.2. Ethanol conversion and selectivity of precursors as a function of time over Cu/Mg_xAlO_y. Reaction Conditions: 325ºC, 300 psig H_2, 2.6 ml/min H_2, ~0.017 ml/min EtOH, WHSV = 0.39 h^{-1}. Regeneration of the catalyst was done at 200 and 240 hr TOS.

Table 1.1. Average-product distribution from guerbet coupling and side reactions over Cu/Mg_xAlO_y catalyst for 425 TOS. Average ethanol conversion: 68.3%. Average diesel precursor selectivity: 86.3%. Each group is categorized based on the four most abundant carbon number molecules.

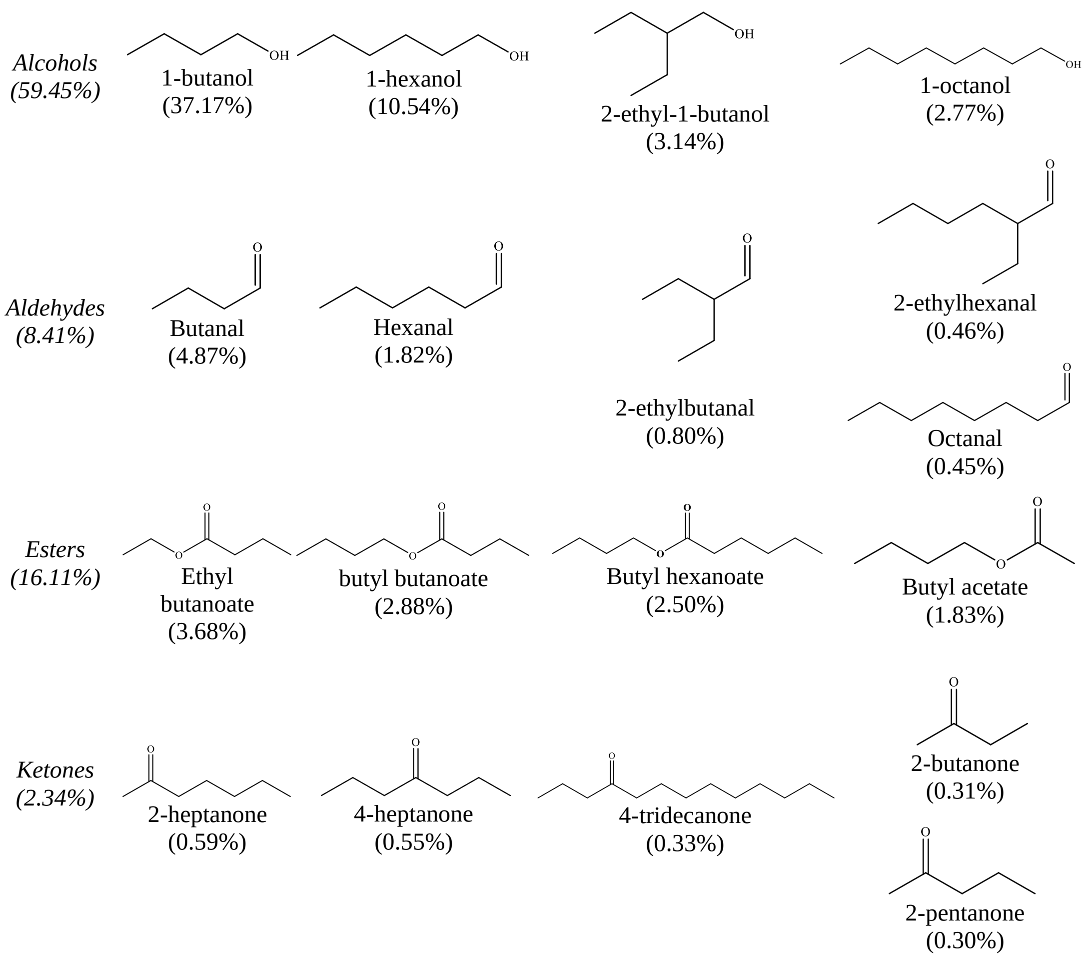

Alcohols (59.45%)	1-butanol (37.17%)	1-hexanol (10.54%)	2-ethyl-1-butanol (3.14%)	1-octanol (2.77%)
Aldehydes (8.41%)	Butanal (4.87%)	Hexanal (1.82%)	2-ethylbutanal (0.80%)	2-ethylhexanal (0.46%) Octanal (0.45%)
Esters (16.11%)	Ethyl butanoate (3.68%)	butyl butanoate (2.88%)	Butyl hexanoate (2.50%)	Butyl acetate (1.83%)
Ketones (2.34%)	2-heptanone (0.59%)	4-heptanone (0.55%)	4-tridecanone (0.33%)	2-butanone (0.31%) 2-pentanone (0.30%)

At high conversions, C_{5+} esters compose 16% of the diesel precursor selectivity. As deactivation becomes more present, the selectivity towards C_{5+} esters and C_{4+} ketones decrease, with an increase in selectivity for C_{4+} alcohols and aldehydes, which will result in change of the chemical composition prior to etherification. It is then important to assess the effect on alcohol dehydration in the presence of by-products from the Guerbet reactor. **Table 1.1** represents the most abundant C_{4+} diesel fuel precursors, consisting of mainly alcohols and esters. The alcohol carbon number distribution can influence the final carbon number distribution of ethers in a dehydration reactor. More information on the product distributions can be found in the work of Cuello-Penaloza and coworkers[11, 12].

1.4 Alcohol dehydration to distillate – range ethers

Bio-ethanol upgrading has been studied in literature and in the Huber group through Guerbet chemistry to produce C_{4+} alcohols over base catalysts such as hydroxyapatite (HAP)[13] and $CuMg_xO_y$ catalysts[11, 12]. These alcohols can then undergo etherification over acid catalysts to produce C_{8+} ethers at high conversion and selectivity. High conversion and selectivity are necessary, as C_{8+} ethers have shown superior physical/engine properties for diesel blends compared to low chain alcohols and diethyl ether, as shown in **Table 1.2**.

Table 1.2. Key fuel properties for current fuels, alcohols and ethers, derived from and reproduced from ref 13 " N. M. Eagan, B. M. Moore, D. J. McClelland, A. M. Wittrig, E. Canales, M. P. Lanci and G. W. Huber, Green Chemistry, 2019, 21, 3300-3318" with permission from the Royal Society of Chemistry. While di-ethyl ether possesses a high cetane number (CN), other physical properties like heating values, boiling and flash point are below the requirements necessary for diesel/jet fuel. It can be shown that heavy ethers (C_{8+}) exhibit similar physical properties to diesel with higher CN's.

Fuel / Pure Compound	Carbon #	Net heating value(MJ kg^{-1})	Freezing Point (°C)	Flash Point (°C)	Cetane
Diesel #2	10 - 22	36.2	-17	> 52	> 40
Ethanol	2	21.2	-114	13	10
1-butanol	4	26.9	-90	29	17
1-hexanol	6	29.4	-45	63	23
2-ethyl-1-butanol	6	29.7	< -15	58	17
1-octanol	8	31.2	-16	81	39
2-ethyl-1-hexanol	8	31.4	-70	73	26
Di-ethyl ether	4	24.1	-116	-45	150
Di-n-butyl ether	8	29.2	-9	25	85
Di-n-hexyl ether	12	31.4	-43	77	117
Di-n-octyl ether	16	32.6	-8	110	118

Single and mixed alcohol feeds were previously analyzed over Amberlyst 70 (A70). While A70 exhibited above 60% conversion and > 90% selectivity for single linear alcohols feeds such as 1-butanol and 1-hexanol, ether selectivity dropped to less than 30% in single branched alcohol feeds such as 2-ethyl-1-butanol[13]. Eagan et. al proposed that the chemistry over the A70 is similar to that of tungsten zirconia, in which unimolecular dehydration activation barriers for branched alcohols are lower than for primary linear alcohols, even though branched and linear alcohols exhibit similar etherification activation barriers[14]. Furthermore, it was found that water inhibits both etherification and A70 activity, suggesting the need for a stable catalyst that can exhibit similar activity to achieve high conversion of alcohols with 80+% selectivity towards distillate range ethers.

1.5 Overview of dissertation

The present dissertation focuses on the development of an alternative, economic route for ethanol to diesel via dehydration of higher alcohols to distillate range ethers. The main contribution was the process chemistry, technoeconomic (TEA) and lifecycle analysis (LCA) of a proposed three step process for the development of C_{10+} ethers for their use as drop-in diesel fuel. The process chemistry was developed to understand the effects of alcohol carbon number distribution and alcohol structure on the final blend distributions obtained from the dehydration reactor. It was found that side products such as esters can negatively affect the ether selectivity in the dehydration step, leading to the implementation of an ester hydrogenolysis unit. This intermediate unit between alcohol coupling and dehydration would break apart esters into their respective alcohols, leading to a pure alcohol feed stream into the dehydration reactor. TEA and LCA were then performed with coworkers to assess the economic and environmental impact of our ethanol to diesel process[15]. We made several improvements, such as implementing an ester hydrogenolysis unit to produce a pure alcohol feed stream for the dehydration reactor, as well as a n-butanol recycling unit to increase the average carbon number of the incoming feedstocks to produce larger chain ethers in the C_{10+} range.

Chapter 2 focuses on the process chemistry for ethanol to diesel route. Here, we show how average alcohol size and structure can shift the ether selectivity from the C_{8+} to C_{10+} range. First, we used our least complex model feedstock mainly containing n-butanol for initial studies. These model feedstocks were taken from a real guerbet coupling reactor[11, 15]. It was found that pressure plays a role in shifting competitive dehydration reactions from mono-molecular dehydration to bi-molecular dehydration, which has been seen in literature[16]. Furthermore, increasing branched and secondary alcohol content lead to higher selectivities towards olefins and coke products. Increasing the alcohol chain size also led to higher selectivities towards olefins and coke products.

A key finding was the negative effects of esters in the reaction stream. Using a guerbet feedstock with esters, it was found that these molecules lower both carbon balances and ether selectivities. This key finding led to the development of an ester hydrogenolysis unit, which breaks apart esters into their respective alcohols to produce pure alcohol streams for the dehydration reactor.

Another key finding was the introduction of n-butanol into the guerbet coupling reactor. This led to an increase in the average alcohol size of the feedstock used for dehydration. It was found that this increase in alcohol size lead shifted ether selectivities from the C_{8+} to C_{10+} range. Furthermore, there was an increase in the final C_{10+} ether yield, as well as a decrease in the production of butyl ether. With the proposed ethanol to diesel route, we showed that we can tailor our process to selectivity produce higher distillate range ethers suitable for drop-in diesel fuel.

Chapter 3 and Chapter 4 focus on the TEA and LCA of the ethanol to diesel process. Chapter 3 consists of the initial analysis in which no ester hydrogenolysis is used for the removal of esters from the dehydration stream. It was shown that high conversion oligomerization reactors significantly reduced capital and operating costs. These high conversion reactors would produce the largest amount of C_{6+} alcohol content. The largest economic cost factor of the process is the starting feedstock used for bioethanol production, while the second largest cost factor is fuel yield. On an ethanol mass basis, the total fuel yield was 65 wt%. The final product was split into three fuel-grades: 26.8 wt% diesel #1, 4.3 wt% gasoline, and 34.5 wt% diesel #2. The diesel range ethers produced were shown to have a positive engine impact. The rich-ether blend led to higher combustion efficiencies and lowered both NO_X emissions and soot compared to fossil diesel #2. The flashpoint was slightly below ASTM standards (50 °C vs 52 °C), while having other similar physical properties to fossil diesel. The cetane number of the ether-rich blend was 73, well above the ASTM standard of 40 for diesel #2. The chemical process can be implemented with existing carbon-reduction technology, showing a 132.7% reduction in greenhouse gas emissions if CO_2 capture and renewable utilities were used in tandem.

Chapter 4 focuses on the improvements of the ethanol to diesel route. In this chapter, an ester hydrogenolysis and n-butanol recycling unit are added to further improve the economics and final diesel fuel yield obtained. On an ethanol mass basis, the total fuel yield obtained was 63.4 wt%. The fuel-grade cuts were 3 wt% diesel #1, 2.5 wt% gasoline, and 57.9 wt% diesel #2. The fraction to light fuels decreases with the recycling step, showing that we can tailor the process to produce heavy fractions of fuel by tuning the n-butanol recycle ratio. The cetane number of the final diesel blend produced increased from 73 to 90 from our previous analysis. The technology can be price-competitive with current biodiesel technology that uses vegetables oils for transesterification reactions. In the absence of subsidies, we estimate that the price of vegetable oil feedstock has fluctuated between \$3.3 - 9.6/gal. The price of corn-based ethanol has fluctuated between $2.3 - 4.6/gal, showing that ethanol feedstocks can offer a favorable economic path towards bio-diesel production.

Chapter 5 focuses on the ongoing difficulties of scaling up the ethanol to diesel process. Initially, continuous flow studies were done over pure powder zeolite Y catalyst. A pellet version of zeolite Y was tested to understand the effects of a binder on the dehydration reactions. It was found that the introduction of the binder lead to a significant decrease in both carbon balances and ether selectivities.

Batch reactors were then used to determine if it is possible to produce diesel-range ethers at the liter scale. 45 mL parr reactors were used for screening of optimal reaction conditions for the dehydration step. Tetrahydrofuran (THF) was used as the solvent for sampling and showed promising results. However, at larger scales, the use of THF would not be feasible and would require more distillation steps. Final products were then analyzed without the presence of THF, showing lower yields of C_{10+} ethers at similar reaction conditions. 450 mL reactors were then used to produce the final liter that would be used for engine testing. Surprisingly, it was found that at larger scales, both the conversion and selectivity towards C_{10+} ethers increased. Multiple reactions were then conducted, with each run undergoing both centrifugation for catalyst removal and vacuum distillation to remove light products from the heavy products. One liter of heavy products was produced and was analyzed in further detail to obtain the final composition of the blend.

References

1. M. Balat and H. Balat, Applied energy, 2009, **86**, 2273-2282.
2. Alternative Fuels Data Center, https://afdc.energy.gov/fuels/ethanol_benefits.html, (accessed January 10 2023).
3. N. M. Eagan, M. D. Kumbhalkar, J. S. Buchanan, J. A. Dumesic and G. W. Huber, Nature Reviews Chemistry, 2019, **3**, 223-249.
4. U. S. D. Energy, Handbook for Handling, Storing, and Dispensing E85 and Other Ethanol-Gasoline Blends, 2016.
5. 2018 Outlook for Energy: A View to 2040, ExxonMobil, Irving, 2018.
6. S. Chaudhuri, C. Halik and J. Lercher, Journal of molecular catalysis, 1990, **62**, 289-295.
7. J. Cejka, A. Corma and S. Zones, Zeolites in Catalysis, Royal Society of Chemistry, 2017.
8. R. E. Morris and P. Nachtigall, Zeolites in catalysis: properties and applications, Royal Society of Chemistry, 2017.
9. F. F. Madeira, N. Gnep, P. Magnoux, S. Maury and N. Cadran, Applied Catalysis A: General, 2009, **367**, 39-46.
10. T. Tsuchida, J. Kubo, T. Yoshioka, S. Sakuma, T. Takeguchi and W. Ueda, Journal of Catalysis, 2008, **259**, 183-189.
11. P. A. Cuello-Penaloza, R. G. Dastidar, S.-C. Wang, Y. Du, M. P. Lanci, B. Wooler, C. E. Kliewer, I. Hermans, J. A. Dumesic and G. W. Huber, Applied Catalysis B: Environmental, 2022, **304**, 120984.
12. P. A. Cuello-Penaloza, J. Chavarrio-Cañas, Y. Du, M. P. Lanci, D. A. Maedke, J. A. Dumesic and G. W. Huber, Applied Catalysis B: Environmental, 2022, **318**, 121821.
13. N. M. Eagan, B. M. Moore, D. J. McClelland, A. M. Wittrig, E. Canales, M. P. Lanci and G. W. Huber, Green Chemistry, 2019, **21**, 3300-3318.
14. J. Rorrer, S. Pindi, F. D. Toste and A. T. Bell, ChemSusChem, 2018, **11**, 3104-3111.
15. J.-M. Restrepo-Flórez, P. Cuello-Penaloza, E. Canales, D. Witkowski, D. A. Rothamer, G. W. Huber and C. T. Maravelias, Sustainable Energy & Fuels, 2023, **7**, 693-707.
16. R. J. Nel and A. de Klerk, Industrial & engineering chemistry research, 2009, **48**, 5230-5238.

Chapter 2. Production of drop-in biodiesel blendstocks via competitive acid-catalyzed dehydration reactions using ethanol oligomerization products

2.1 Introduction

There is a clear societal need to produce low-carbon liquid transportation fuels. In this respect biomass is an inexpensive renewable carbon source that is being used today to produce liquid transportation fuels. The most widely used biofuel is ethanol[2, 3]. Ethanol is used as a gasoline blendstock[2, 3]. In the US, around 10 vol% of ethanol is blended into gasoline[5]. As more electric vehicles are used for light duty transportation vehicles, the demand for gasoline, and the demand for ethanol, is decreasing. However, the demand for heavy transportation fuel is projected to increase[6]. Electrification of transportation for heavy duty vehicles is difficult due to the low energy density, slow charging time, and high cost of batteries[7,8]. New approaches for upgrading ethanol to heavier distillate-range fuels (sustainable aviation fuels and diesel fuels) are needed. A number of approaches have focused on ethanol conversion into jet fuel and these technologies are moving towards commercialization[2]. These approaches primarily focus on jet fuel by producing heavily branched alkanes. However, the branching of alkanes leads to a low cetane number, and only a fraction of these alkanes are in the diesel fuel range[9].

The content of this chapter is largely adapted from the following:

Reproduced from ref. “Emmanuel Canales, Samuel C. Hower, Daniel-Paul Li, Aditya Tambe, David Rothamer and George W. Huber. Production of drop-in biodiesel blendstocks via competitive acid-catalyzed dehydration reactions using ethanol oligomerization products. Sustainable Energy & Fuels, 2024, **8**, 3036-3047” with permission from the Royal Society of Chemistry. **https://doi.org/10.1039/D4SE00362D**

Chapter version: Manuscript – draft.

EC developed and performed experiments, methodology and wrote chapter. SCH performed experiments and methodology. DPL performed experiments. AT performed experiments and methodology.

We have previously proposed a three-step process to convert ethanol into distillate-range ethers as outlined in **Scheme 2.1**[1]. The process first involves ethanol oligomerization to C_{4+} oxygenates which is rich in alcohols over a Cu/Mg_xAl_yO catalyst[10]. This process creates a distribution of oxygenated molecules consisting of C_{4+} alcohols, aldehydes, ketones, and esters. The second step is an ester hydrogenolysis step that hydrogenates esters in this oxygenate stream into alcohols. The products from the hydrogenolysis reactor are a mixture of C_{4+} linear, branched, and secondary alcohols. The last step is dehydration which produces C_{8+} ethers and C_{4+} olefins. Mono-molecular dehydration produces olefins while bimolecular dehydration produces ethers. These ethers possess higher cetane number than diesel fuel. The ethers also have the appropriate boiling point and low volatility suggesting they can be used in diesel blends[11]. C_{10+} ethers also have lower sooting index, water solubility and higher flashpoint temperatures compared to lower chain ethers[12]. Ethers produced from C_{6+} alcohol streams have similar properties relative to diesel #2. While butyl ether may be used as a diesel additive, blending limits can be influenced based on the minimum flashpoint requirement for a diesel #2 blend (> 52 °C), as shown in **Figure 2.1**.

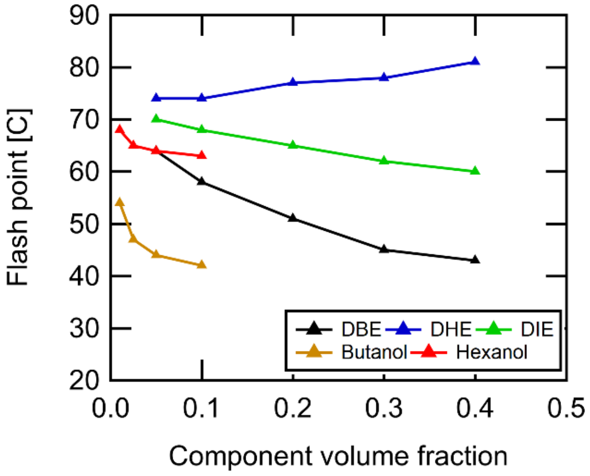

Figure 2.1. Volume lending fractions of alcohols and ethers with fossil diesel as a function of flashpoint temperature. For fossil diesel, the baseline flashpoint temperature was 75 °C.

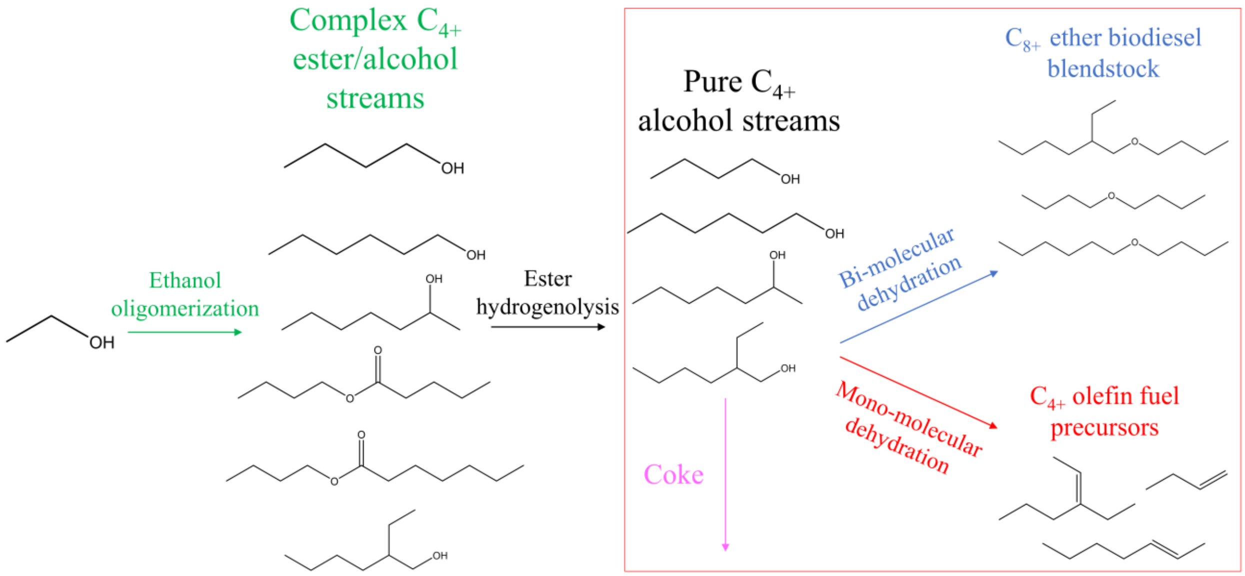

Scheme 2.1. Three step process chemistry for ethanol to diesel-range ethers.

The objective of this paper is to study the catalytic dehydration of mixtures of ethanol oligomerization products over a zeolite Y catalyst in a continuous flow reactor. We try to understand how the reaction conditions and different feed components influence the product selectivity, catalytic activity, and catalytic deactivation for dehydration reactions. Over 100 different products are produced during ethanol oligomerization including linear, branched and secondary C_{4-10} alcohols, aldehydes, ketones, and esters with the primary products being linear alcohols[10]. **Figure 2.2**[1, 4] shows the simulated Guerbet (SG) feedstocks that we will use for etherification in this publication. The SG feed assumes that all the products lighter than C_4 from ethanol oligomerization are distillated and the ketones, aldehydes and acetals are hydrogenated to their respective alcohols. The product selectivity for ethanol oligomerization is a function of conversion[10]. **Figure 2.2** shows the SG product selectivity at four different ethanol conversions from ethanol oligomerization[1]. (e.g. SG-12 represents the simulated Guerbet product from ethanol oligomerization at 12 % ethanol conversion and assuming the ketones, aldehydes and acetals are hydrogenated to their respective alcohols).

The final SG mixtures are a distribution of linear alcohols, branched alcohols, secondary alcohols, and esters. The left-hand side of the graph represents the mol fractions of linear alcohols, while the right-hand axis represents the mol fractions of secondary and branched alcohols, in addition to esters. At an ethanol conversion of 12%, n-butanol is the main product, with low amounts of C_{6+} alcohols and esters. As the ethanol conversion increases, the size of the alcohols produced increases. The secondary and branched alcohol content and the ester content increase with increasing conversion as well. **Table 2.1** shows the detailed composition of the feedstocks shown in **Figure 2.2**.

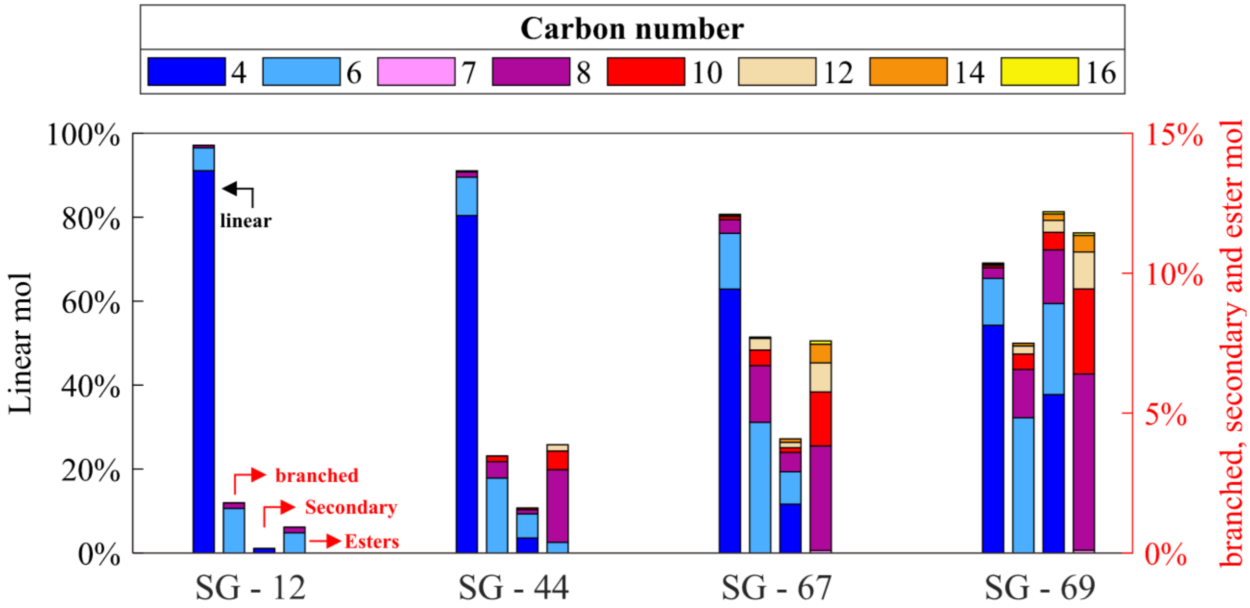

Figure 2.2. Oxygenate distribution of products from ethanol oligomerization as a function of ethanol conversion. These products will be used as feeds for the etherification experiments in this chapter. The conversion was varied by changing the weight hourly space velocity in the reactor. The conversion is shown after the dash. For secondary alcohols, the numbering is defined by 'n+1'. Colors not visibly shown for compounds are present in low amounts (< 1.0%). Data taken from ref 1, 4.

Table 2.1. Simulated guerbet feedstocks from ethanol, post distillation of aldehydes and ketones. Data obtained from simulations from Restrepo-Florez and coworkers from ref 1.

Etherification feed code	**SG – 12**	**SG – 44**	**SG – 67**	**SG - 69**
Ethanol conversion (%)	12.26	44.16	66.51	68.9
Compounds	**Mol%**			
Alcohols				
1-butanol	91.09	80.40	62.88	54.26
2-pentanol	0.16	0.54	1.74	5.66
1-hexanol	5.44	9.15	13.28	11.16
2-ethyl-1-butanol	1.59	2.68	4.67	4.83
2-heptanol	0	0.86	1.16	3.25
1-octanol	0.60	1.26	3.27	2.50
2-ethyl-1-hexanol	0.20	0.59	2.02	1.73
4-nonanol	0	0.15	0.69	1.92
1-decanol	0	0.20	0.75	0.55
2-ethyl-1-octanol	0	0.20	0.56	0.55
4-undecanol	0	0.06	0.17	0.63
1-dodecanol	0	0.06	0.36	0.35
2-ethyl-1-decanol	0	0	0.42	0.29
4-tridecanol	0	0	0.19	0.42
1-tetradecanol	0	0	0.09	0.05
2-ethyl-1-dodecanol	0	0	0.04	0.10
2-pentadecanol	0	0	0.12	0.23
2-heptadecanol	0	0	0	0.08
esters				
Isopropyl acetate	0	0	0	0
Ethyl butanoate	0.14	0.10	0	0
Butyl acetate	0.59	0.28	0	0
Isopropyl butyrate	0	0	0.09	0.10
Butyl butanoate	0	1.09	1.95	3.62
Ethyl hexanoate	0.20	0.92	1.09	1.73
Hexyl acetate	0	0.59	0.70	0.95
Butyl hexanoate	0	0	1.62	2.49
Hexyl butanoate	0	0.60	0.19	0.35
Octyl acetate	0	0.07	0.12	0.21
Octyl butanoate	0	0	0.10	0.17
Butyl octanoate	0	0.17	0.05	0.98
Ethyl decanoate	0	0	0.73	0
Decyl acetate	0	0.05	0.05	0.06
Hexyl hexanoate	0	0	0.10	0.12
Hexyl octanoate	0	0	0.58	0.49
Ethyl dodecanoate	0	0	0.04	0.05
Dodecyl acetate	0	0	0.04	0.05
Octyl octanoate	0	0	0.12	0.09

In this study, we demonstrate how dehydration of ethanol oligomerization products produces distillate range ethers with selectivities ranging from 60% to 80% in a continuous flow reactor with Zeolite HY. We also demonstrate the ability to tune reactant feedstock distributions, which allows for tuning the final average carbon number of the fuel mixtures produced. The oxygenate products are feedstocks that have varying size distributions depending on the ethanol conversion in the first step (10% to 69%), as shown in **Figure 2.1**.

2.2 Experimental methods

2.2.1 Reactor configuration

The etherification of oxygenate species was performed in stainless-steel fixed bed reactors packed with Zeolite HY (Zeolyst International, CBV-720), and the configuration of the system is shown in **Figure 2.3**. The reactor was typically 33 cm long with a catalyst bed length of 17.8 cm, using an outer diameter of 0.95 cm. Prior to loading into the reactor, large batches of zeolite were calcined overnight at 600 ^{o}C in a muffle furnace in static air, with a ramp of 4 ^{o}C/min. The catalyst was then dried at 110 ^{o}C until use. Catalyst beds were diluted with silica chips (Sigma Aldrich) to minimize pressure drop, typically with a 1:2 g_{cat} to g_{beads} ratio. The beads were typically crushed to a size between 30 – 80 mesh (ASTM). Reactant feedstocks were fed with an HPLC pump (Eldex), typically between 0.02 – 0.04 mL/min. Ar was used as the cofeed inert gas, typically with a flowrate of 10 mL/min. The reactor was heated using a furnace (Applied Test Systems, Series 3210) and kept uniform using aluminum blocks. The exact reactor dimensions, bed dilution ratios, gas flowrates, feed flowrates, and analytical techniques used to identify liquid and gas species can be found elsewhere[1].

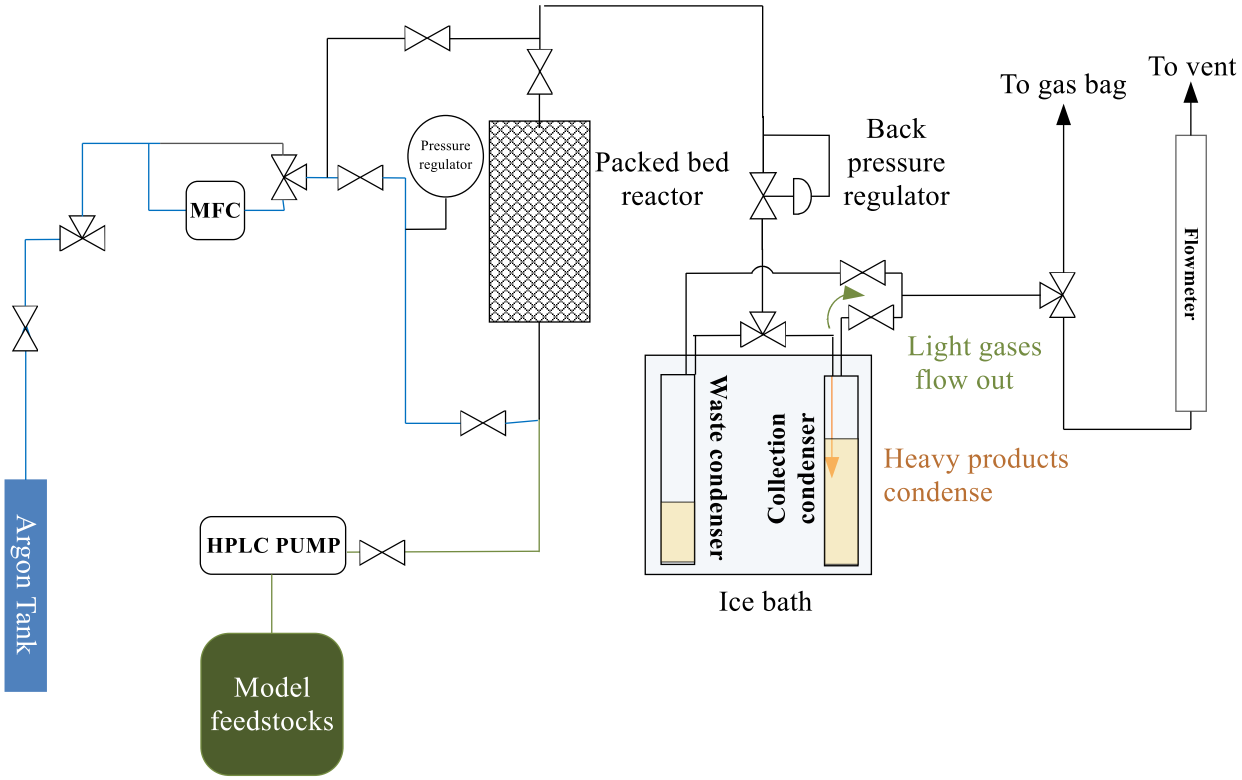

Figure 2.3. Continuous flow set up used for dehydration experiments of C_{4+} alcohol mixtures.

2.2.2 Product analysis of cross etherification species

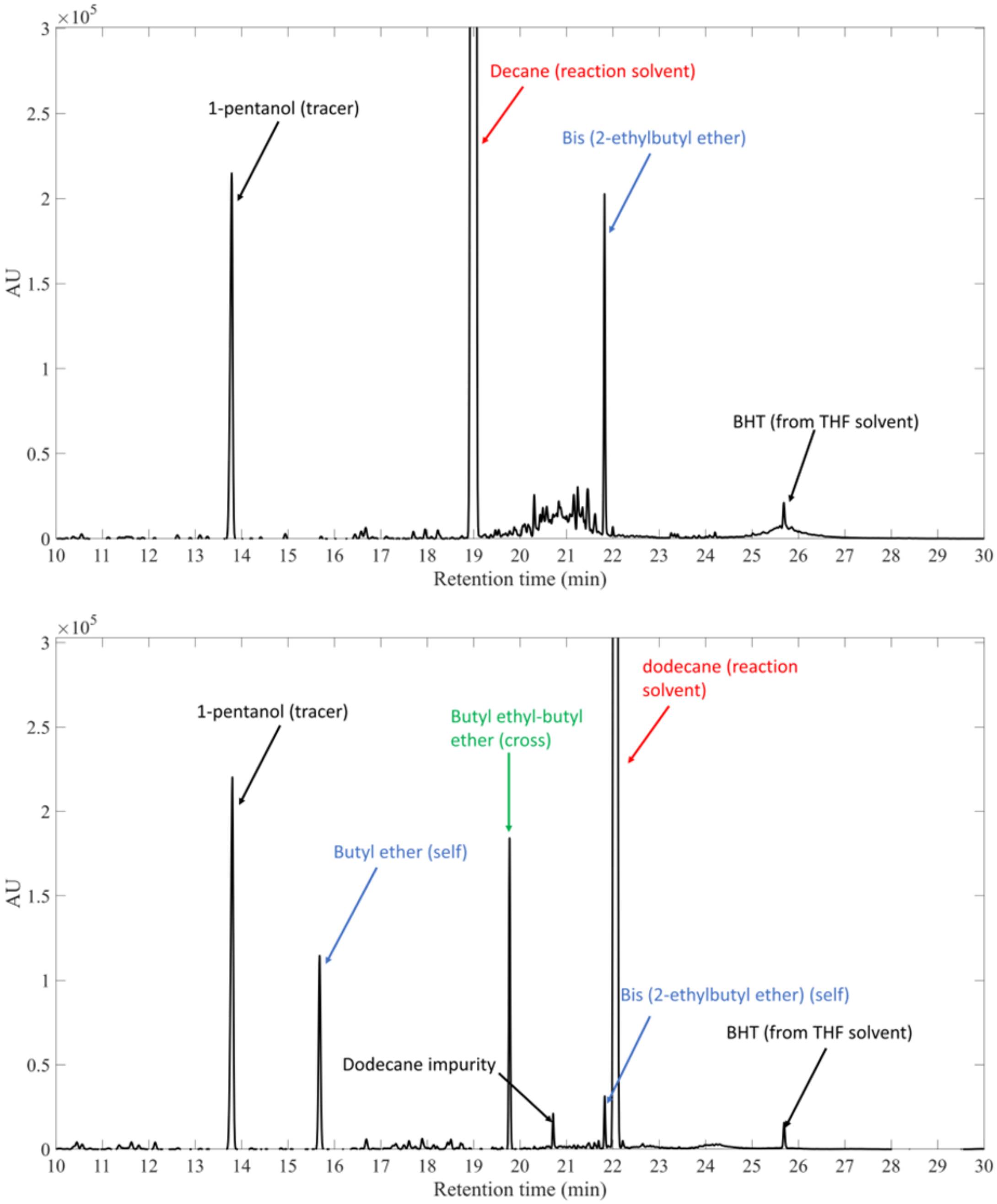

Figure 2.4. Identification of cross etherification products of 2-ethyl-1-butanol and 1-butanol. **Top:** etherification products of 2-ethyl-1-butanol. **Bottom:** Etherification products of equimolar butanol and 2-ethyl-1-butanol. Reaction conditions: 170 ºC, stirrate = 550 rpm in a silicon oil bath.

Due to the complexity of the model/real guerbet feedstocks, standards for cross-ethers are not commercially available. Furthermore, the GC-MS is limited by suggesting wrong oxygenate compounds being formed (i.e oxalic acids) and being unable to further separate ether species of the same carbon number, a phenomenon also observed in the liquid gas-chromatography FID. Therefore, a qualitative analysis of cross-etherification products is needed to assess both the retention time and carbon number of the unidentified cross ethers formed. Response factors for these species were then estimated using effective carbon number theory[13] by linking the response factors to commercially available standards. For cross-etherification, an equimolar reaction mixture of two alcohols was analyzed. Then, single feed alcohol reactions overlapped with the equimolar chromatograms to determine where self-etherification products landed. If one alcohol is removed from the reaction feed, then two peaks must collapse, the first being the self-etherification product of the removed alcohol and the second being the cross-etherification product between the two alcohols in the reaction mixture. Therefore, the major peak that is not observed in both single alcohol chromatograms must be the cross-etherification peak. **Figure 2.4** provides an example of the overall procedure to determine cross-etherification products between linear-linear and linear-branched feeds. 2-ethyl-1-butanol was used to assess the retention time of the self-etherification product. The same procedure was done with 1-butanol. Then, the equimolar mixture chromatograms overlapped with the single-feed alcohols to determine the unknown peak.

2.2.3 Quantification and analysis of coke products

The total organic content (TOC) experiments on the catalyst beds were analyzed using a total organic carbon analyzer (Shimadzu, TOCV) to establish estimated solid coke flowrates, using a carrier gas flowrate of 150 mL/min. Coke flowrates were then used to close carbon balances, with experimental error being less than or equal to 10% for all beds studied. In this paper, we therefore assume that all missing carbon is due to coke products.

The catalyst beds were a mixture of zeolite HY in its powder form, and the addition of inert silica chips between 30 – 80 mesh. The chips were added to minimize pressure drop across the reactor. The bed mixture was made at a 2:1 inert chip to catalyst ratio, using 1.6 – 1.8 g of catalyst. As the catalyst beds cannot be assumed to be uniform, mainly because of the particle size differences between the catalyst and chips used, total organic carbon (TOC) analysis was conducted 12 times for each individual bed using 4 different mass weights. If one were to consider the coke flowrate for each catalyst bed studied, carbon balances improve by 5 – 10%, leading to carbon balances over 90+%. Here, the flowrates were offset by the startup time of reactor, typically between 13 – 20 hours. The reasoning for long start-up times is due to the low flow rates used (0.02 mL/min) and minimal pressure buildup that may occur across the reactor. We assume that the startup time of reaction does not have a significant impact on the amount of carbon found on the catalyst bed and is set to 13 hours for all beds studied. 13-hour start-up times were chosen as this was usually when mass balances would stabilize for the reaction.

Coke flowrates were then calculated for each bed and normalized by the total reaction time. The calculated flowrates were then used to adjust the final carbon balances for all beds studied. For runs that didn’t fully add up to 100% carbon balance after the addition of TOC experiments, it is assumed that the missing carbon is due to the formation of heavy oligomers[14, 15] in the final product that are soluble in the organic liquid phase. This assumption is more evident with runs using esters, as the amount of undetected carbon increases linearly with increasing ester concentration (See **Figure 2.5**). Therefore, it is reasonable to assume that carbon not detected in the liquid or gas phase is in the form of coke products that cannot be detected by conventional gas chromatography methods. **Tables 2.2 – 2.4** summarize the results obtained for all beds studied.

Thermogravimetric analysis (TGA) experiments on catalyst beds were conducted in a TA instruments Q500 Thermogravimetric Analyzer. The ramp was set at 20 °C/min and heated to 800 °C. For both oxygen and nitrogen experiments, a 50 mL/min flowrate was used with a balance inert gas flowrate of 50 mL/min. TGA of MG – 12, MG – 67 and MG – 69 were analyzed to determine the carbon uptake profile. In all cases, the weight changes primarily lied between 25 – 400 °C. The TGA data for these experiments can be found in **Figure 2.6**.

Table 2.2. Average wt% detected by TOC for the linear alcohol feeds. A 95% confidence interval is implemented using a two-tailed test. Reaction temperature = 170 °C.

Etherification feed code	**1-butanol**	**1-butanol**	**1-hexanol**	**1-octanol**
Pressure	0	100	100	100
WHSV (h^{-1})	0.54	0.54	0.54	0.54
Number of samples	12	12	12	12
Average wt% of carbon detected	2.80	4.29	24.88	27.85
Uncertainty interval (+/-)	0.26	0.53	1.94	1.63
Total reaction time (hr)	22.33	46.33	70.65	46.92

Table 2.3. Average wt% detected by TOC for the model feedstocks. A 95% confidence interval is implemented using a two-tailed test. Reaction temperature = 170 °C.

Etherification feed code	**MG – 12**	**MG - 12**	**MG – 44**	**MG - 67**	**MG - 69**
Pressure	0	100	100	100	100
WHSV (h^{-1})	0.54	0.54	0.54	0.61	0.54
Number of samples	12	12	12	12	12
Average wt% of carbon detected	18.97	8.55	25.8	19.87	26.4
Uncertainty interval (+/-)	1.32	0.53	0.97	0.96	1.52
Total reaction time (hr)	45.63	46.67	50.08	66.05	50.25

Table 2.4. Average wt% detected by TOC for the model feedstocks. A 95% confidence interval is implemented using a two-tailed test. * Signifies that the start-up time was set to 26 hrs as the reactor was restarted once. Reaction temperature = 170 °C.

Etherification feed code	SG – 12	SG – 12@15wt%	EtOH/ButOH*	EtOH/ButOH
Pressure	100	100	100	100
WHSV (h^{-1})	0.54	0.54	0.54	1
Number of samples	12	12	12	12
Average wt% of carbon detected	5.65	18.42	24.39	8.36
Uncertainty interval (+/-)	0.86	1.74	2.28	1.40
Total reaction time (hr)	50.50	72.88	92.7	20.97

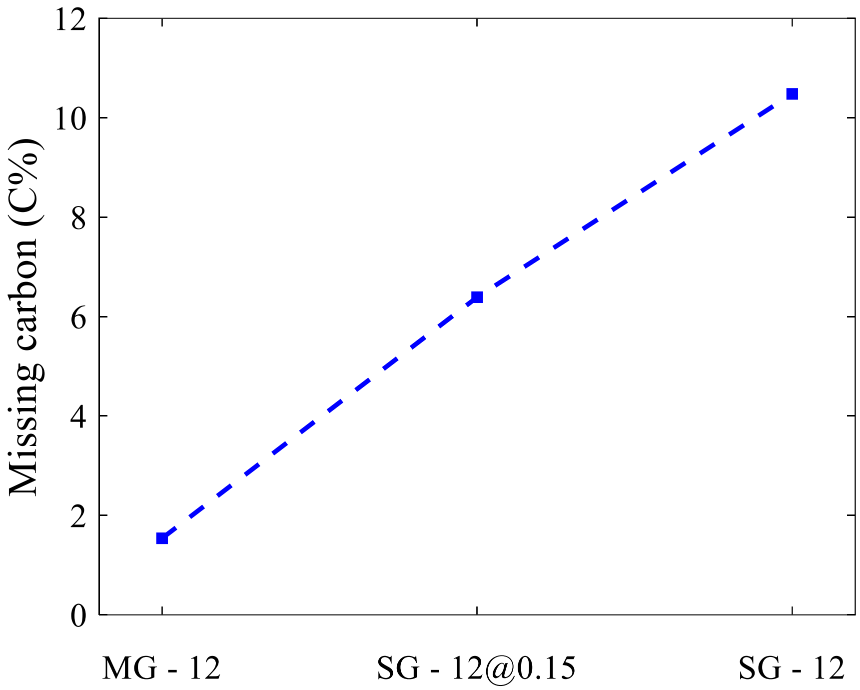

Figure 2.5. Missing carbon as a function of ester concentration. The R^2 value obtained is 0.9969. The missing carbon is defined as carbon that was not detected in the liquid, gas, and solid coke phases. Reaction conditions: T = 170 °C, P = 100 psig, WHSV = 0.54 h^{-1}.

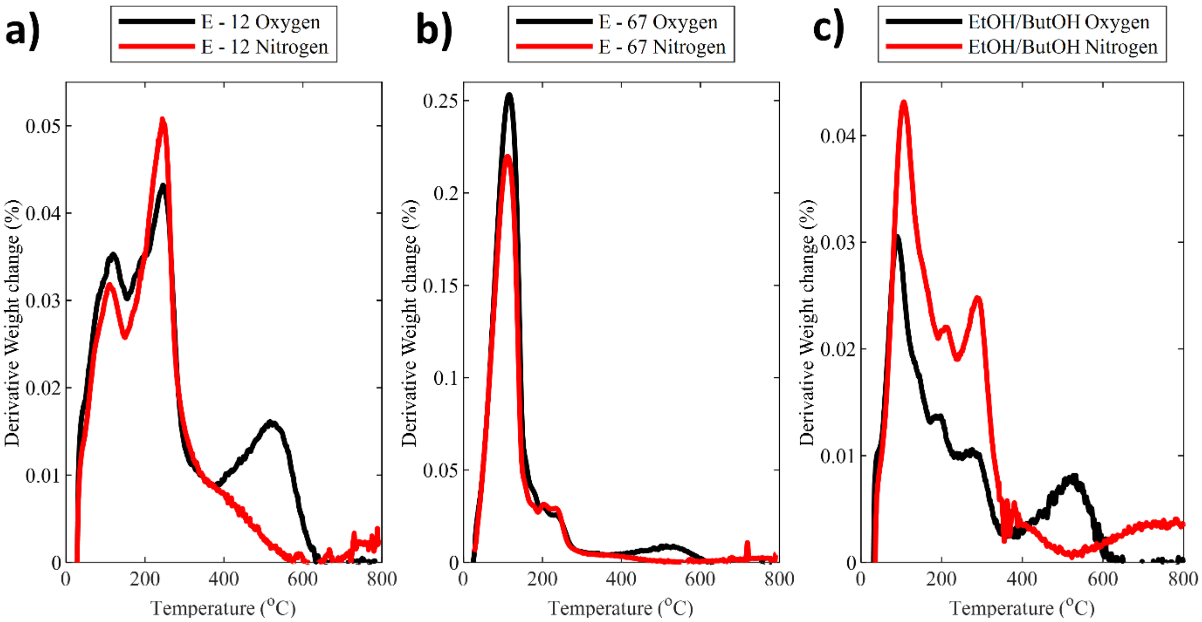

Figure 2.6. A) TGA of spent reaction bed using feedstock MG – 12, B) TGA of spent reaction bed using feedstock MG – 67 and C) TGA of spent reaction bed using EtOH/ButOH oligomerization products at WHSV = 1.0 h^{-1}. Red represents a TGA analysis using nitrogen as the flow gas. Black represents a TGA analysis using oxygen as the flow gas.

2.3 Materials and quantification analysis

2.3.1 Representation of alcohol oligomerization products

The alcohols 1-butanol (Sigma Aldrich, 99.8% anhydrous), 1-hexanol (Sigma Aldrich, >99% anhydrous), 1-octanol (Alfa Aesar, 99%), 1-decanol (Alfa Aesar, 98+%), 1-dodecanol (Thermo Scientific, 98%) and 1-tetradecanol (Acros Organics, 99%) were obtained to represent the linear alcohols obtained from the ethanol oligomerization reactor. The alcohols 2-methyl-1-butanol (Thermo Scientific, 98%), 2-ethyl-1-butanol (Sigma Aldrich, 98%) and 2-ethyl-1-hexanol (Frontier Scientific, 99%) were used to represent branched alcohols. 2-butanol (TCI chemicals, >99%), 2-pentanol (Sigma Aldrich, 98%), 2-heptanol (Acros Organics, 99+%), 2-octanol (TCI chemicals, >98%), 4-nonanol (Santa Cruz Biotechnology, >98%), 2-nonanol (Sigma Aldrich, 99%), and 2-undecanol (Alfa Aesar, 98+%) were obtained to represent secondary alcohols. The esters ethyl butanoate (Sigma Aldrich, 99%), butyl acetate (TCI chemicals, 99+%) and ethyl hexanoate (Sigma Aldrich, 99%) were obtained to represent the esters obtained from the ethanol oligomerization reactor. 1-heptanol (Acros Organics, 98%) and dodecane (Sigma Aldrich, >99% anhydrous) were used for diluting the product mixture to prepare analytical samples. 1-heptanol was used for alcohol feeds, while dodecane was used when esters were present. Dodecane and n-decane (Alfa Aesar, 99+%) were used as the inert solvents for qualitative analysis of cross-etherification products. For bed packing, Quartz wool (Acros Organics, Coarse 9 –30 microns) and silicon dioxide (Sigma Aldrich, fused – granular, 4-20 mesh, 99.9% trace metals basis) was used. For analysis of liquid samples post – reaction using gas chromatography, tetrahydrofuran (99+% Stab. with 250ppm BHT) was used to homogenize the aqueous and organic phase. Calibration standards for liquid products such as ethers and olefins were obtained from the manufacturers mentioned. For the TOC experiments, Potassium hydrogen phthalate (Acros Organics, primary standard) was used to create a four-point calibration curve for quantification of carbon uptake on the catalyst beds.

2.3.2 Quantification of final products obtained from dehydration

Yields were calculated according to **equation 1** on a carbon basis, where $\dot{n}_i$ is the flowrate of the carbon species. Because not all the GC area was assigned to known species, the yield of unknown carbon in the gas and liquid phase were estimated by **equation 2**, and selectivities were also calculated on a carbon basis based on **equation 3**, as shown elsewhere[11]. Since there was overlap between product species in the GC chromatogram, overlapped area was assigned based on GC-MS area overlaps. The ratio of the areas of one product to another, defined as R_{Area}, was assumed to be constant and was then used for the GC-FID area overlaps. The areas were then split into their respective products. **Equation 4** summarizes the GC-area estimation of overlapped products. The overall carbon conversion is represented by **equation 5** and is based on the total carbon converted. The conversion for each reactant is further defined by **equation 6**. For information on the TOS conversion of each reactant for each experiment, refer to **Tables 2.5 – 2.17**. For information on the entire TOS runs of each experiment, refer to **Figures 2.7 – 2.14**.

$$\text{Yield}_i = \frac{\dot{n}_{C,i,out}}{\dot{n}_{C,total,in}} \qquad (1)$$

$$\text{Yield}_{unknown} = \frac{A_{unidentified\ products}}{A_{total,products}} * \sum_i Y_{i,products} \qquad (2)$$

$$\text{Selectivity}_i = \frac{Y_i}{X} \qquad (3)$$

$$R_{Area,MS} = \frac{A_{x,MS}}{A_{y,MS}} = \frac{A_{total,FID} - A_{y,FID}}{A_{y,FID}} = \frac{A_{total,FID}}{A_{y,FID}} - 1 \qquad (4)$$

$$\text{Overall conversion (X)} = \frac{\dot{n}_{C,total,in} - \dot{n}_{C,total,out}}{\dot{n}_{C,total,in}} \qquad (5)$$

$$\text{Conversion}_i = \frac{\dot{n}_{Ci,in} - \dot{n}_{Ci,out}}{\dot{n}_{Ci,in}} \qquad (6)$$

2.3.2a) n-butanol TOS data

Table 2.5. Conversion of 1-butanol at data points (hr) obtained at atmospheric pressure.

Compound	18.4 TOS	21.2 TOS	**Average conversion (C%)**
1-butanol	69.1	69.4	69.2

Table 2.6. Conversion of 1-butanol at data points (hr) obtained at 100 psig.

Compound	25.6 TOS	35.3 TOS	44.9 TOS	**Average conversion (C%)**
1-butanol	73.5	73.7	73.1	73.4

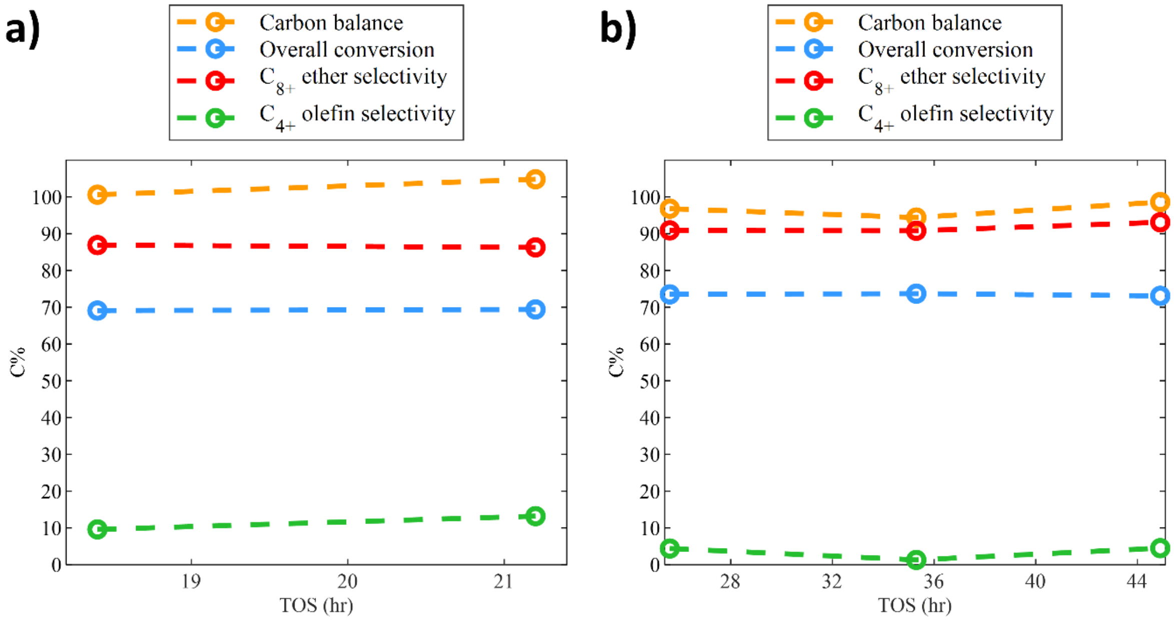

Figure 2.7. TOS data of 1-butanol at a) atmospheric pressure and b) 105 psig. Reaction conditions: T = 170ºC, feedstock flowrate = 0.020 mL/min, Ar flowrate = 10 mL/min, WHSV = 0.539 – 0.540 h^{-1}.

2.3.2b) MG – 12 TOS data

Table 2.7. Conversion of feedstock MG – 12 at data points (hr) obtained at atmospheric pressure.

Compound	21.6 TOS	43.3 TOS	45.6 TOS	**Average conversion (C%)**
1-butanol	74.0	67.6	65.8	69.6
2-pentanol	100.0	100.0	100.0	100.0
1-hexanol	91.7	89.5	89.4	90.4
2-ethyl-1-butanol	100.0	100.0	100.0	100.0
1-octanol	80.5	82.4	80.8	81.5
2-ethyl-1-hexanol	100.0	100.0	100.0	100.0
Overall (C%)	76.3	70.4	68.9	71.9

Table 2.8. Conversion of feedstock MG – 12 at data points (hr) obtained at 100 psig.

Compound	19.2 TOS	21.9 TOS	36.2 TOS	**Average conversion (C%)**
1-butanol	71.9	71.2	70.2	71.1
2-pentanol	100.0	100.0	100.0	100.0
1-hexanol	84.7	85.4	86.7	85.6
2-ethyl-1-butanol	97.0	96.9	96.8	96.9
1-octanol	91.8	88.9	79.2	86.6
2-ethyl-1-hexanol	95.6	95.5	97.2	96.1
Overall (C%)	73.8	73.3	72.4	73.2

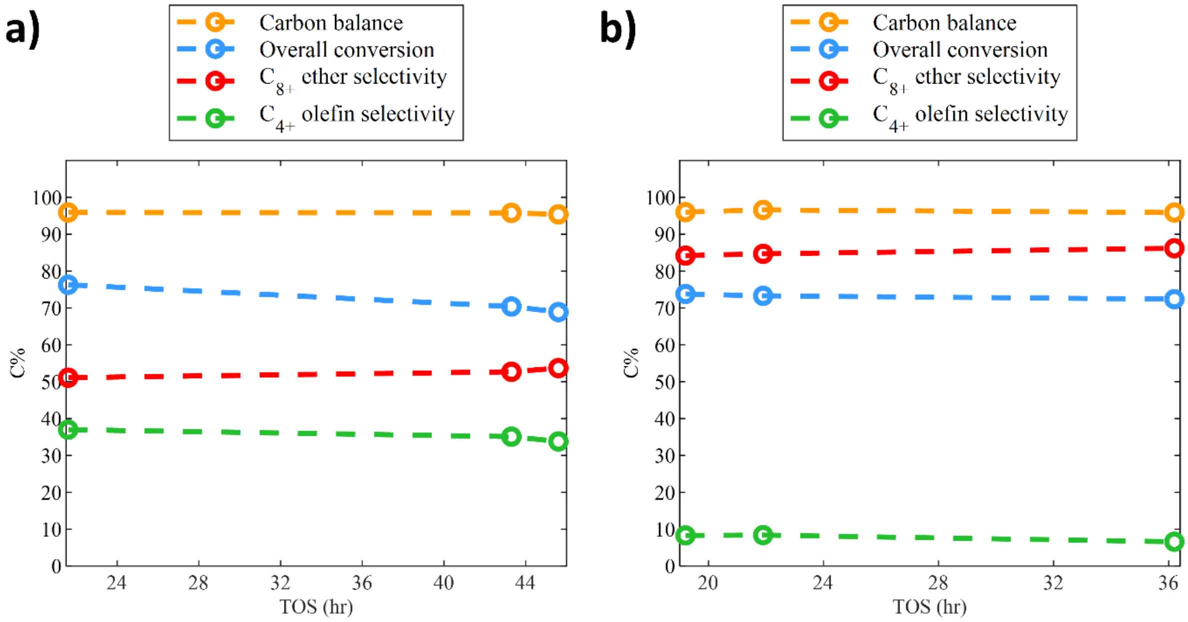

Figure 2.8. TOS data of the 12.3% model feedstock at a) atmospheric pressure and b) 95 psig. Reaction conditions: T = 170 °C, feedstock flowrate = 0.020 mL/min, Ar flowrate = 10 mL/min, WHSV = 0.539 – 0.540 h^{-1}.

2.3.2c) MG – 44, MG – 67 and MG – 69 TOS data

Table 2.9. Conversion of feedstock MG – 44 at data points (hr) obtained at 100 psig.

Compound	25.7 TOS	35.0 TOS	44.4 TOS	48.1 TOS	**Average conversion (C%)**
1-butanol	69.4	68.2	68.2	69.5	68.8
2-pentanol	100.0	100.0	100.0	100.0	100.0
1-hexanol	89.1	88.6	88.3	88.5	88.6
2-ethyl-1-butanol	96.1	95.4	95.3	95.6	95.6
2-heptanol	100.0	100.0	100.0	100.0	100.0
1-octanol	92.7	91.5	91.3	91.4	91.7
2-ethyl-1-hexanol	100.0	100.0	100.0	100.0	100.0
4-nonanol	100.0	100.0	100.0	100.0	100.0
1-decanol	100.0	100.0	100.0	100.0	100.0
2-undecanol	100.0	100.0	100.0	100.0	100.0
1-dodecanol	100.0	100.0	100.0	100.0	100.0
Overall (C%)	75.3	74.3	74.2	75.3	**74.8**

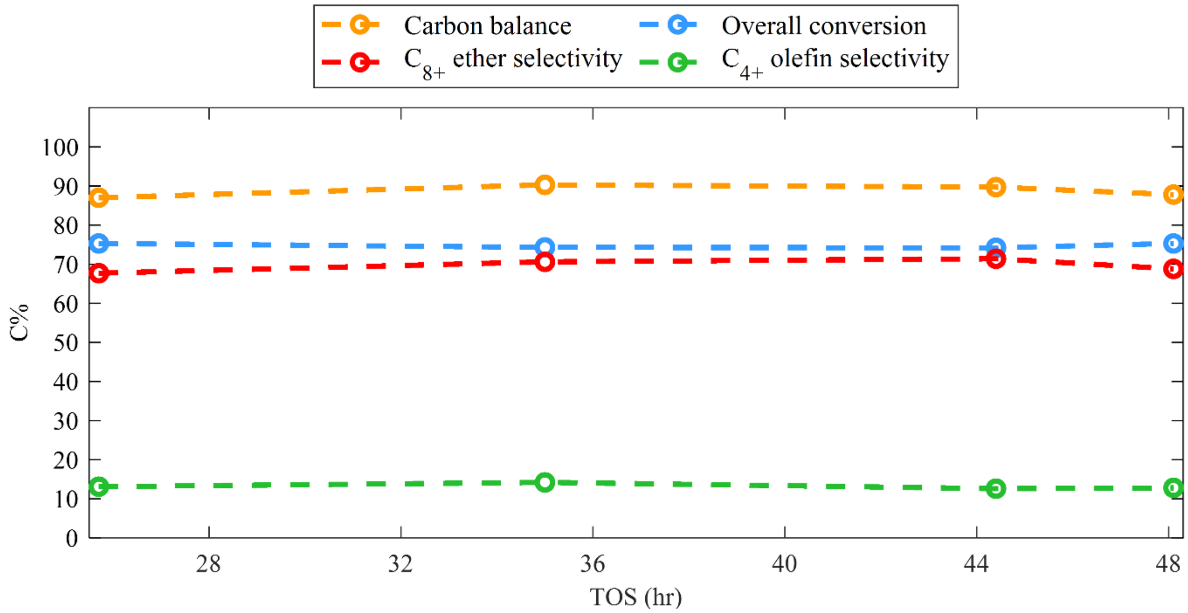

Figure 2.9. TOS of the 44.2% model feedstock. Reaction conditions: T_{avg} = 170.1 °C, P_{avg} = 104 psig, feedstock flowrate =0.020 mL/min, Ar flowrate = 10 mL/min, WHSV = 0.540 h^{-1}.

Table 2.10. Conversion of feedstock MG – 67 at data points (hr) obtained at 100 psig.

Compound	21.4 TOS	31.8 TOS	43.0 TOS	**Average conversion (C%)**
1-butanol	48.6	44.3	46.1	46.4
2-pentanol	100.0	100.0	100.0	100.0
1-hexanol	79.0	79.1	77.0	77.6
2-ethyl-1-butanol	82.0	79.1	79.4	80.2
2-heptanol	100.0	100.0	100.0	100.0
1-octanol	89.1	88.5	88.1	88.6
2-ethyl-1-hexanol	95.5	94.6	94.1	94.7
4-nonanol	100.0	100.0	100.0	100.0
1-decanol	94.4	95.9	94.3	94.8
2-undecanol	100.0	100.0	100.0	100.0
1-dodecanol	94.9	98.6	90.6	94.7
1-tetradecanol	96.3	100.0	92.3	96.2
Overall (C%)	66.4	63.5	64.3	64.7

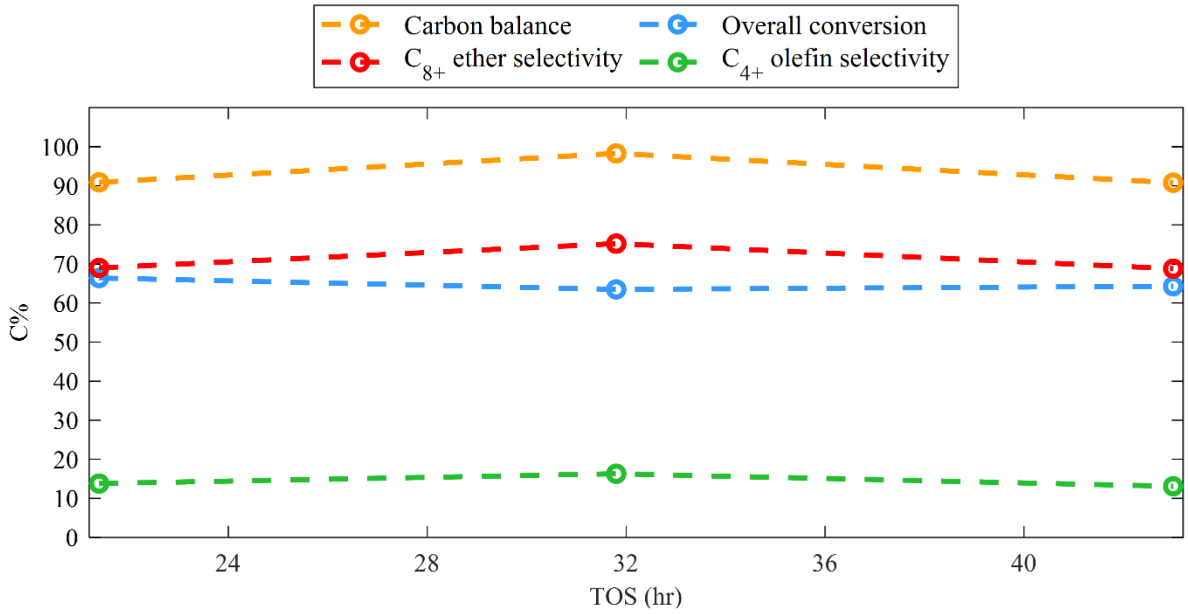

Figure 2.10. TOS of the 66.5% model feedstock. Reaction conditions: T_{avg} = 170.1 ºC, P_{avg} = 106 psig, feedstock flowrate =0.020 mL/min, Ar flowrate = 10 mL/min, WHSV = 0.61 h^{-1}.

Table 2.11. Conversion of feedstock MG – 69 at data points (hr) obtained at 100 psig.

Compound	26.5 TOS	36.7 TOS	**Average conversion (C%)**
1-butanol	63.0	63.4	63.2
2-pentanol	100.0	100.0	100.0
1-hexanol	86.0	86.1	86.0
2-ethyl-1-butanol	93.7	93.9	93.8
2-heptanol	100.0	100.0	100.0
1-octanol	90.4	90.2	90.3
2-ethyl-1-hexanol	98.4	98.5	98.5
4-nonanol	100.0	100.0	100.0
1-decanol	84.9	91.5	88.2
2-undecanol	100.0	100.0	100.0
1-dodecanol	95.5	94.6	95.1
1-tetradecanol	100.0	100.0	100.0
Overall (C%)	78.5	78.7	78.6

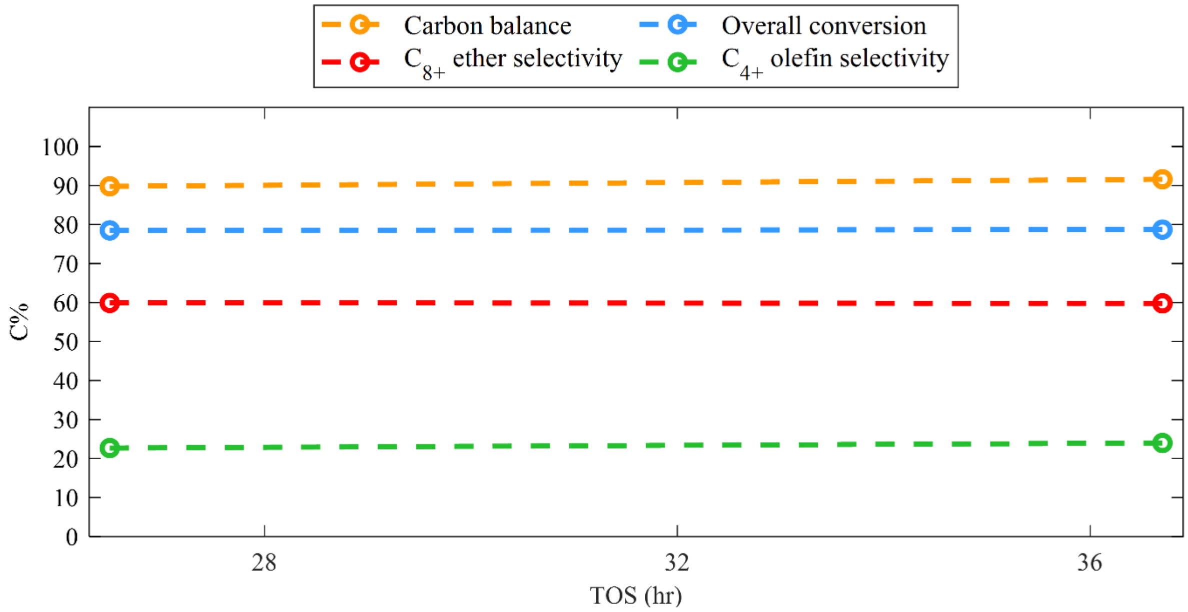

Figure 2.11. TOS of the 68.9% model feedstock. Reaction conditions: T_{avg} = 170.1 °C, P_{avg} = 110 psig, feedstock flowrate =0.020 mL/min, Ar flowrate = 10 mL/min, WHSV = 0.543 h^{-1}.

2.3.2d) Ester feedstocks TOS data

Table 2.12. Conversion of feedstock SG – 12 at data points (hr) obtained at 100 psig.

Compound	25.1 TOS	37.8 TOS	49.5 TOS	**Average conversion (C%)**
1-butanol	77.6	77.3	75.7	76.9
2-pentanol	100.0	100.0	100.0	100.0
1-hexanol	90.9	90.9	90.3	90.7
2-ethyl-1-butanol	98.4	98.4	98.1	98.3
1-octanol	91.1	91.5	90.5	91.0
2-ethyl-1-hexanol	100.0	100.0	100.0	100.0
Ethyl butanoate	100.0	100.0	100.0	100.0
Butyl acetate	22.8	23.3	17.3	21.1
Ethyl hexanoate	100.0	100.0	100.0	100.0
Overall (C%)	79.0	78.8	77.3	78.3

Table 2.13. Conversion of feedstock SG – 12@0.15wt% at data points (hr) obtained at 100 psig.

Compound	23.5 TOS	35.1 TOS	46.7 TOS	48.8 TOS	**Average conversion (C%)**
1-butanol	73.8	74.7	73.8	74.4	74.2
2-pentanol	100.0	100.0	100.0	100.0	100.0
1-hexanol	86.3	87.8	88.3	87.3	87.4
2-ethyl-1-butanol	98.1	97.9	97.7	97.7	97.9
1-octanol	94.4	89.1	87.9	83.5	88.7
2-ethyl-1-hexanol	100.0	100.0	100.0	100.0	100.0
Ethyl butanoate	100.0	100.0	100.0	100.0	100.0
Butyl acetate	17.1	0.7	0.6	0.5	4.72
Ethyl hexanoate	100.0	100.0	100.0	100.0	100.0
Overall (C%)	75.7	76.6	75.8	76.2	76.1

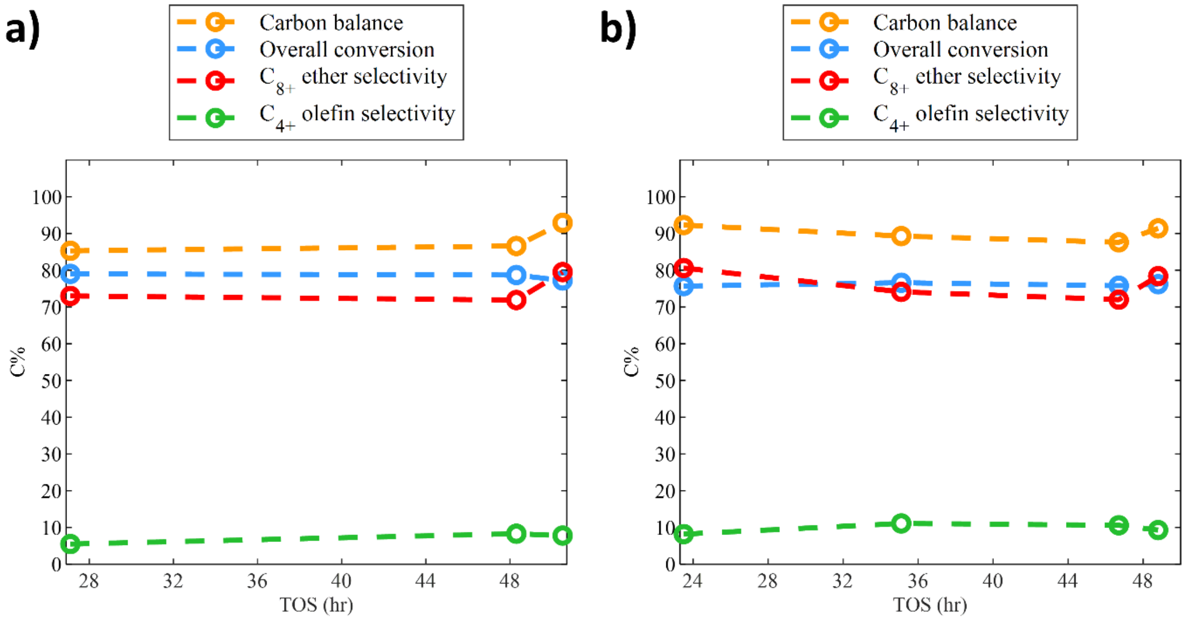

Figure 2.12. TOS of the A) 12.3% simulated feedstock with 1.5 wt% esters and B) 12.3% simulated feedstock with 0.15 wt% esters in the reaction stream. T = 170°C, P = 100 psig, feedstock flowrate =0.020 mL/min, Ar flowrate = 10 mL/min, WHSV = 0.539 - 0.541 h^{-1}.

2.3.2e) 1-hexanol and 1-octanol TOS data

Table 2.14. Conversion of 1-hexanol at data points (hr) obtained at 100 psig.

Compound	20.7 TOS	23.2 TOS	25.8 TOS	37.9 TOS	50.0 TOS	**Average conversion (C%)**
1-hexanol	84.7	84.7	84.5	85.1	84.2	84.7

Table 2.15. Conversion of 1-octanol at data points (hr) obtained at 100 psig.

Compound	19.4 TOS	22.5 TOS	34.4 TOS	46.9 TOS	**Average conversion (C%)**
1-octanol	90.4	91.5	91.6	91.4	91.2

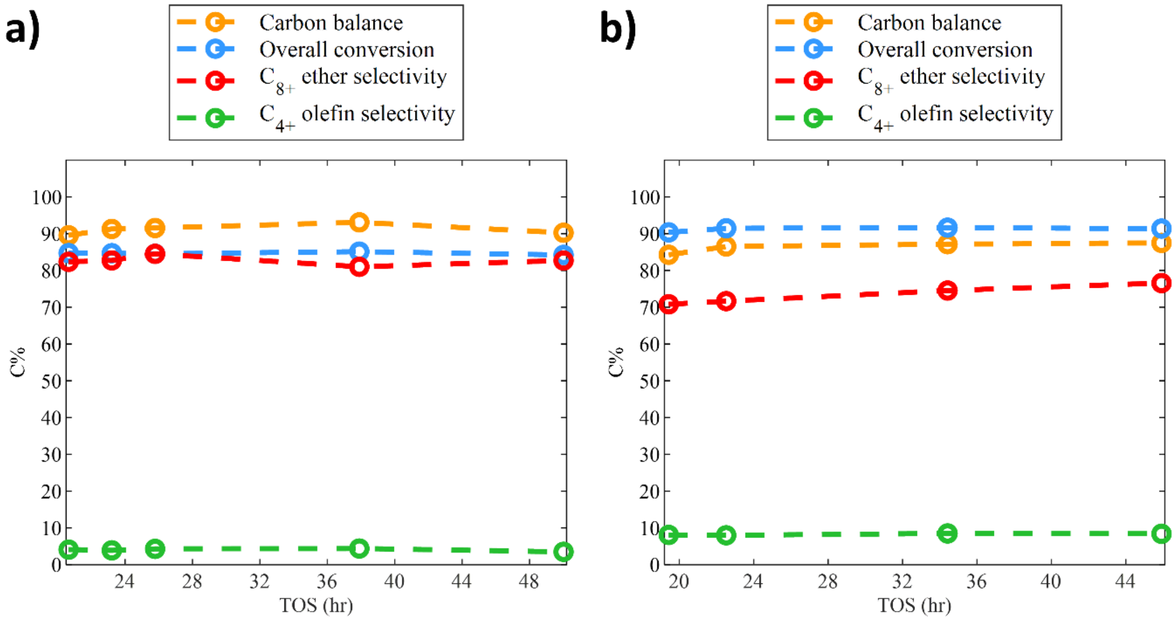

Figure 2.13. TOS of a pure A) 1-hexanol feed and B) 1-octanol feed. T = 171 °C, P = 115 psig, feedstock flowrate =0.020 mL/min, Ar flowrate = 10 mL/min, WHSV = 0.543 h^{-1}.

2.3.2f) EtOH/ButOH oligomerization products TOS data

Table 2.16. Conversion of EtOH/ButOH oligomerization products at data points (hr) obtained at 100 psig and WHSV= 0.54 h^{-1}.

Compound	20.9 TOS	23.1 TOS	25.2 TOS	Average conversion (C%)
1-butanol	61.2	63.9	62.2	62.4
2-butanol	100.0	100.0	100.0	100.0
2-methyl-1-butanol	72.1	74.6	74.2	73.6
1-hexanol	84.1	85.1	84.7	84.6
2-ethyl-1-butanol	92.4	93.5	93.6	93.2
2-heptanol	100.0	100.0	100.0	100.0
2-ethyl-1-hexanol	97.3	97.7	97.5	97.5
1-octanol	91.9	89.4	88.1	89.8
2-octanol	100.0	100.0	100.0	100.0
2-nonanol	100.0	100.0	100.0	100.0
Overall (C%)	80.7	81.9	81.2	81.2

Table 2.17. Conversion of EtOH/ButOH oligomerization products at data points (hr) obtained at 100 psig and WHSV = 1.0 h^{-1}.

Compound	15.9 TOS	17.9 TOS	20.0 TOS	**Average conversion (C%)**
1-butanol	55.9	58.2	48.3	54.1
2-butanol	100.0	100.0	100.0	100.0
2-methyl-1-butanol	57.3	59.3	49.1	55.2
1-hexanol	76.4	77.8	70.6	74.9
2-ethyl-1-butanol	79.7	81.4	73.1	78.1
2-heptanol	100.0	100.0	100.0	100.0
2-ethyl-1-hexanol	91.1	91.7	85.8	89.5
1-octanol	81.7	83.2	75.0	80.0
2-octanol	100.0	100.0	100.0	100.0
2-nonanol	100.0	100.0	100.0	100.0
Overall (C%)	72.7	74.3	66.5	71.1

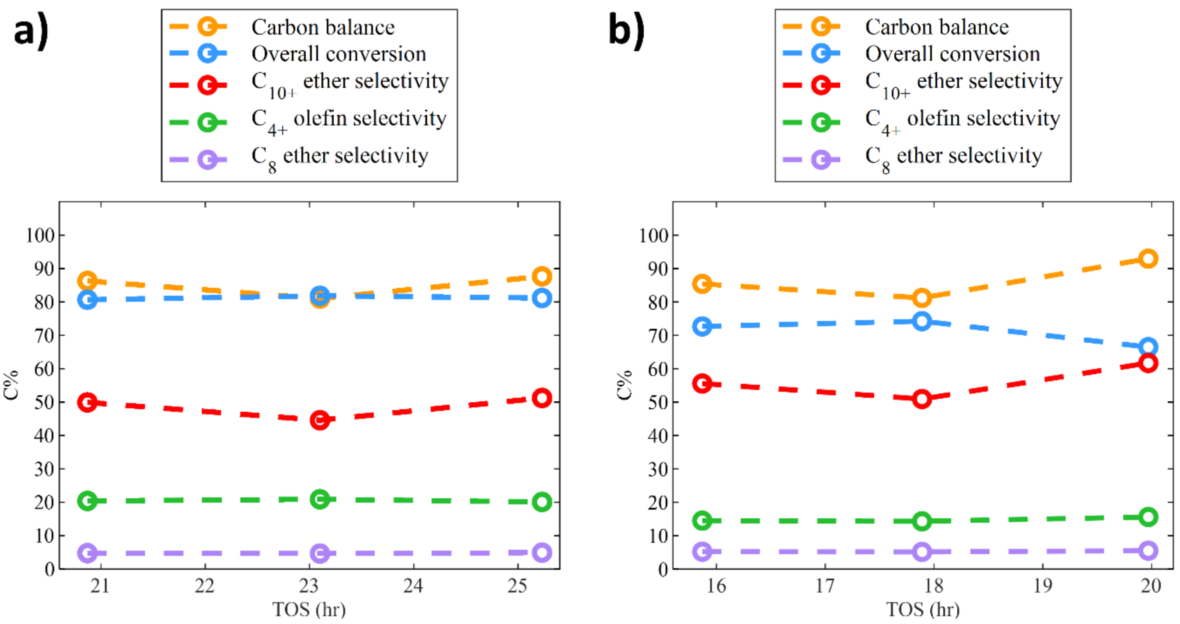

Figure 2.14. TOS data of EtOH/oligomerization dehydration products at A) WHSV = 0.54 h^{-1} and B) WHSV = 1.0 h^{-1}. T = 170 °C, P = 100 psig, feedstock flowrate = 0.02 – 0.04 mL/min, Ar flowrate =10 mL/min. For run A, an in-situ regeneration procedure was attempted at 500 °C using 100 mL/min of Air; however, there were no signs of reaction improvement after > 25 hr TOS.

2.4 Results and discussion

2.4.1 Thermodynamics of bi-molecular and mono-molecular dehydration

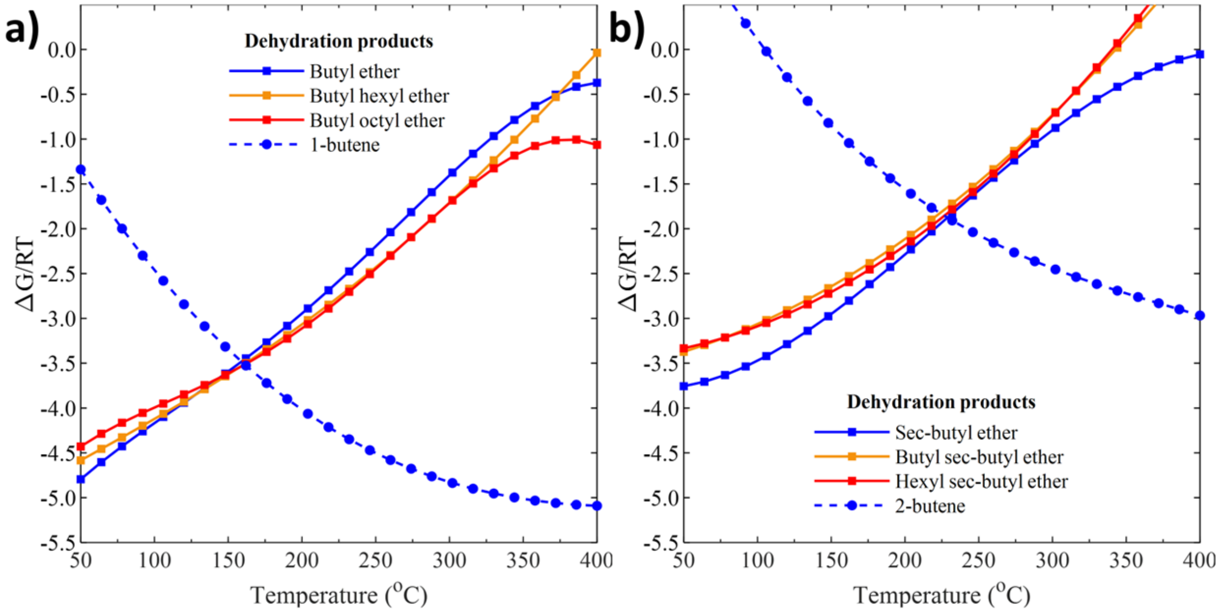

Figure 2.15. Gibbs free energy of dehydration reactions as a function of temperature. **A)** 1-butanol dehydration reactions and **B)** 2-butanol dehydration reactions. Blue signifies competitive dehydration reactions of the parent alcohol. Conditions: 100 psig.

Figure 2.15 shows the Gibbs free energy as a function of temperature for liquid phase dehydration of 2-butanol and 1-butanol. Thermodynamic data was taken from the NIST database, and the model was implemented using UNIFAC parameters in ASPEN. The reactor pressure was 100 psig, and a temperature range from 50 – 400 °C was modeled. The gibbs free energy trends were then fit to a polynomial to highlight the trends on the graph.

Figure 2.15A shows the etherification products for 1-butanol. The free energy formation of ethers of varying linear alcohol feed chain sizes are similar across a wide temperature range, suggesting that bimolecular dehydration is independent of the size of the alcohols in the reaction streams. As the temperature increases, mono-dehydration becomes more favorable. Both monomolecular and bimolecular dehydration are thermodynamically favorable at temperatures from 50 to 300 °C, showing similar results to 2-butanol. A difference between alcohol structure also plays a role in the gibbs free energy formation of ethers. Linear ethers are lower in Gibbs free energy compared to ethers formed from a secondary alcohol.

Figure 2.15B represents the etherification products of 2-butanol, a secondary alcohol. Monomolecular dehydration of 2-butanol produces 2-butene. Bimolecular dehydration of 2-butanol- produces sec-butyl ether. Bimolecular dehydration of 2-butanol with hexanol further produces hexyl-sec butyl ether. At temperatures below 200 °C, the ethers are the thermodynamically favored product. At higher temperatures olefins are the thermodynamically favored product. However, both monomolecular and bimolecular dehydration are thermodynamically favorable at temperatures from 50 to 300°C. The free energy of formation of hexyl-sec butyl ether and sec butyl ether is similar.

2.4.2 Dehydration of pure alcohols

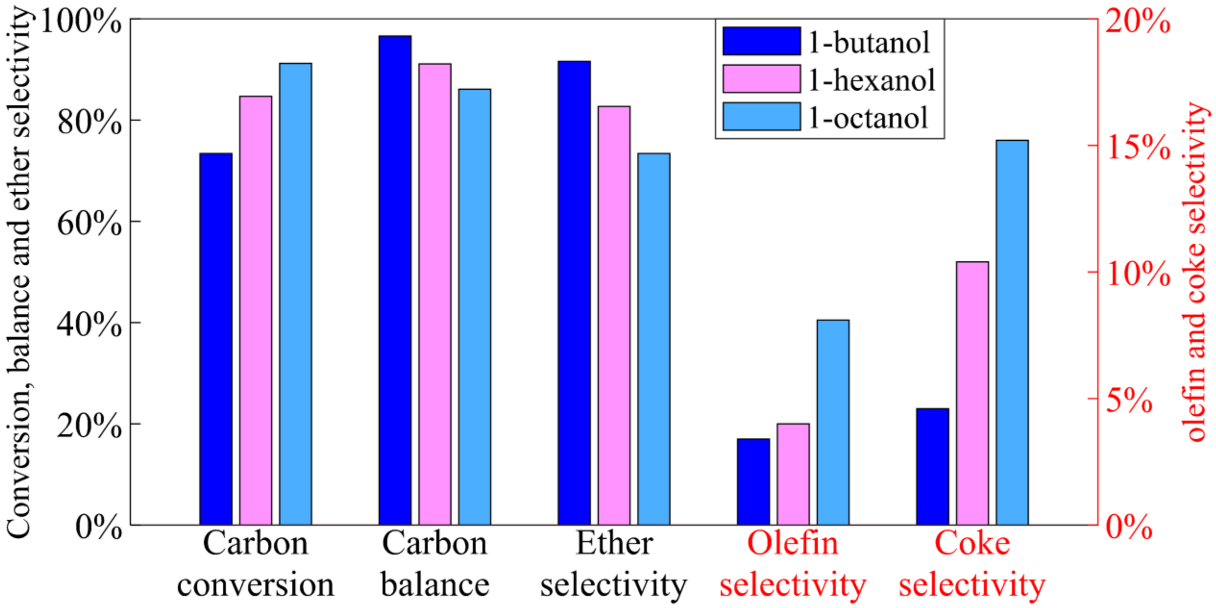

Figure 2.16. Dehydration of pure alcohol over Zeolite HY. T = 170 °C, P = 100 psig, 0.02 mL/min flowrate, WHSV = 0.54 h^{-1}, TOS > 20 hr.

Figure 2.16 shows the dehydration reactions of pure alcohol feeds in a continuous flow reactor. All experiments for the individual alcohols were done at a constant WHSV. The carbon conversion increases with increasing chain length of the alcohol. The carbon balance decreases with increasing alcohol size as the larger alcohols produce more coke (Refer to **Table 2.2**). **Table 2.18** represents the TOS run without any adjustments from TOC, while **Table 2.19** represents the TOS run adjusted based on the TOC experiments. The ether selectivity decreases, and the olefin selectivity increases with increasing carbon length of the alcohol. Based on these findings, a C_{10} alcohol such as 1-decanol would have a coke selectivity around 20%. These results suggest that it would be desirable to remove the C_{10+} alcohols from the feed prior to the etherification step. In all pure alcohol feed runs, the catalyst was shown to be stable for over 40 hr TOS, as shown in **figures 2.7** and **2.13**.

Table 2.18. Linear alcohol results at 100 psig**.** WHSV = 0.54 h^{-1} over HY, flowrate = 0.02 mL/min. The coke selectivity is defined as carbon not detected in the liquid or gas phase.

Alcohol feed	**1-butanol**	**1-hexanol**	**1-octanol**
Liquid and gas carbon balance (%)	96.60	91.15	86.1
Carbon conversion (%)	73.41	84.66	91.21
Ether selectivity (%)	91.60	82.66	73.41
Olefin selectivity (%)	3.40	4.03	8.26
Unknown selectivity (%)	0.37	2.85	3.38
Total coke selectivity	4.63	10.46	14.96

Table 2.19. Linear alcohol results at 100 psig. Adjusted to 100% carbon balance by considering carbon obtained from solid phase TOC analysis. WHSV = 0.54 h^{-1} over HY, flowrate = 0.02 mL/min.

Alcohol feed	**1-butanol**	**1-hexanol**	**1-octanol**
Liquid and gas carbon balance (%)	100	100	100
Carbon conversion (%)	73.41	84.66	91.21
Ether selectivity (%)	91.60	82.66	73.41
Olefin selectivity (%)	3.40	4.03	8.26
Unknown selectivity (%)	0.37	2.85	3.38
Coke on catalyst surface (%)	1.53	5.45	8.95
Coke in liquid phase (%)	3.11	5.01	6.01

2.4.3 The effect of esters in the reaction stream

Feedstocks with the code ‘MG’ represent model guerbet alcohol mixtures that assume all esters from the ethanol oligomerization reactor are broken down to their parent alcohols via ester hydrogenolysis. **Figure 2.17** shows the effects of esters on the dehydration step using MG-12 with different levels of esters. The difference between MG-12 and SG-12 is the presence of esters. SG-12 has an ester content of 1.46 wt%. Another feedstock with 0.15 wt% esters is shown in **Figure 2.17** and represents a feedstock with a significant reduction of esters in the reaction stream, as shown in **Table 2.20**. The presence of esters in the reaction stream increases coke selectivity. It has been shown in the literature that esters of varying structure can play a significant role in coking selectivities over acid catalysts[16]. As the ester concentration decreases, the ether selectivity and carbon balances increase. Small amounts of esters significantly decrease the carbon balance.

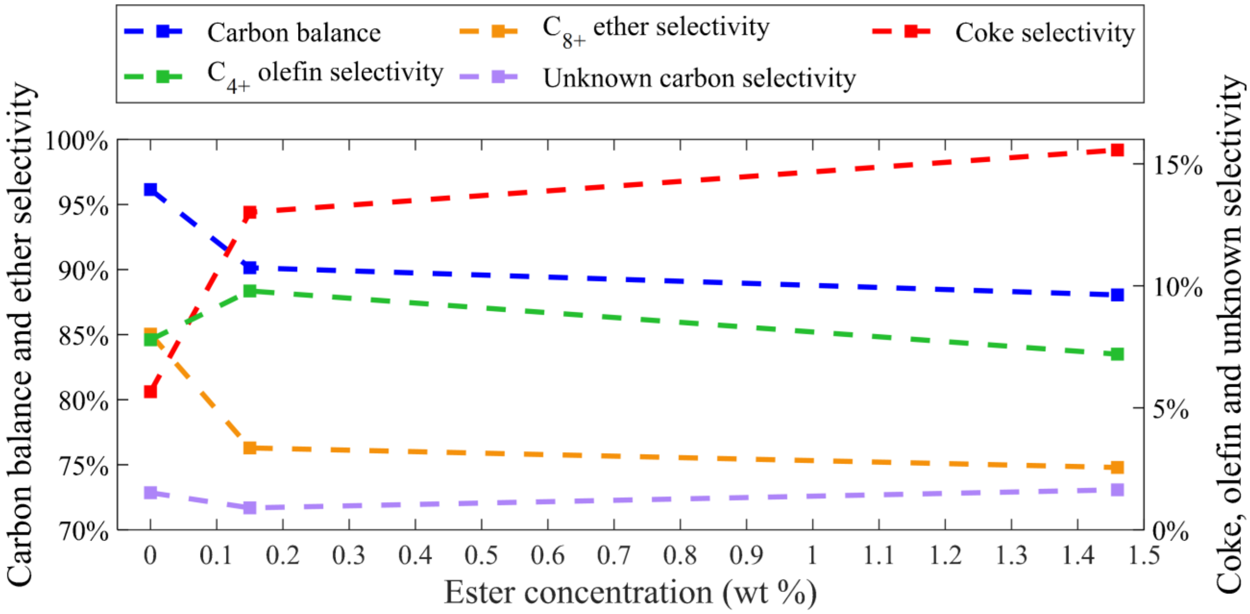

Figure 2.17. Effect of esters on product selectivity. Feedstock MG – 12 with different levels of esters over zeolite HY. T = 170 °C, P = 100 psig, 0.02 mL/min flowrate, 1.8 g HY, WHSV = 0.54 h^{-1}. Feedstock MG – 12 represents an ideal feedstock with 0 wt% of esters.

Table 2.20. Feedstock of SG – 12, where the esters are cut to a total mass of 0.15 wt%. All esters are assumed to be removed equally on a mass basis.

Etherification feed code	**SG – 12@0.15wt%**
Compounds	
Alcohols	
1-butanol	91.85
2-pentanol	0.16
1-hexanol	5.49
2-ethyl-1-butanol	1.61
2-heptanol	0.00
1-octanol	0.60
2-ethyl-1-hexanol	0.20
Esters	
Ethyl butanoate	0.01
Butyl acetate	0.06
Ethyl hexanoate	0.02

As the ester content in the feed increases the heavy oligomer concentration in the product increases. These heavy oligomers are soluble in the alcohol feed. These heavy oligomers have been studied and detected in similar systems, particularly for acid-catalyzed dehydration reactions of sugars from biomass[14, 15]. **Figure 2.5** further supports this theory, as the amount of undetected carbon linearly increases with increasing ester concentration.

Therefore, as much of the esters as possible must be removed from the dehydration reactor stream. Ideally, the total alcohol purity of the reactant stream should be above 99.90 wt% to ensure that esters will not significantly change the reaction. **Tables 2.21 - 2.24** show the detailed distribution of the ester runs obtained with and without TOC adjustments. We conclude that an ester hydrogenolysis step is necessary to produce alcohol rich feedstocks for dehydration. Over zeolites, esters can create side reactions with the reactants and products produced in the dehydration step. Water produced from etherification, which in the presence of an ester over acid catalysts, creates the ester hydrolysis reaction. Over zeolites, as the ester is broken down to its respective alcohol and carboxylic acid, both molecules will compete for dehydration sites as shown by Corma and coworkers[17]. The adsorption of carboxylic acids is stronger than for alcohols. Thus, the carboxylic acids likely cause a decrease in the number of acid sites that are available for dehydration reactions. Other labs have reportedly seen other adsorption effects over large-pore zeolite catalysts, in which upgrading incoming low-chain esters may be difficult. In the case of benzyl alcohol reacting with acetic acid over H-beta, increasing alcohol concentration led to a decrease in ester selectivity and an increase in ether selectivity[18]. This is attributed to alcohols saturating the catalyst surface, blocking acid sites for carboxylic acids to react with other alcohol chains to produce esters.

Table 2.21. Product feedstock composition of the ester cut using SG -12. Leftover carbon not detected in the liquid or gas phase was assumed to go to coke products.

Etherification feed code		**SG – 12@0.15wt%**
Pressure (psig)		100
Overall carbon conversion (%)		76.05
Liquid and gas carbon balance (%)		90.14
Compound	**Carbon #**	
Ethers		
Butyl ether	8	64.39
Butyl ethyl-butane ether	10	0.66
C_{10} linear ethers	10	11.17
Butyl ethyl-hexane ether	12	0.06
Olefins		
C_4 olefins	4	5.40
C_5 olefins	5	0.32
C_6 olefins	6	2.94
C_8 olefins	8	1.13
Unknown gas and liquid products	-	0.90
Coke	-	12.97
Esters		
C_{10} ester	10	0.05

Table 2.22. Product feedstock composition of the ester cut using SG -12. Adjusted to 100% carbon balance by considering carbon obtained from solid phase TOC analysis.

Etherification feed code		**SG – 12@0.15wt%**
Pressure (psig)		100
Overall carbon conversion (%)		76.05
Total carbon balance (%)		100
Compound	**Carbon #**	
Ethers		
Butyl ether	8	64.39
Butyl ethyl-butane ether	10	0.66
C_{10} linear ethers	10	11.17
Butyl ethyl-hexane ether	12	0.06
Olefins		
C_4 olefins	4	5.40
C_5 olefins	5	0.32
C_6 olefins	6	2.94
C_8 olefins	8	1.13
Unknown gas and liquid products	-	0.90
Coke on catalyst surface	-	4.34
Coke in liquid phase	-	8.63
Esters		
C_{10} ester	10	0.05

Table 2.23. Comparison between esters in stream and effects of pressure on etherification. Leftover carbon not detected in the liquid or gas phase was assumed to go to coke products.

Etherification feed code		1-butanol	1-butanol	SG-12	MG-12	MG-12
Pressure (psig)		0	100	100	0	100
Overall carbon conversion (%)		69.24	73.41	78.33	72.24	73.17
Liquid and gas carbon balance (%)		102.72	96.6	88.26	93.78	96.15
Compound	**Carbon #**					
Alcohols						
Ethanol	2	-	-	0.09	-	-
Ethers						
Ethyl butyl ether	6	-	-	0.30	-	-
Butyl ether	8	86.60	91.60	63.50	46.48	70.40
Butyl ethyl-butane ether	10	-	-	0.81	0.11	0.77
C_{10} linear ethers	10	-	-	9.08	5.25	13.51
Butyl ethyl-hexane ether	12	-	-	-	-	0.12
C_{12} linear ethers	12	-	-	1.37	0.44	0.23
Olefins						
C_4 olefins	4	11.39	3.40	3.53	24.70	3.l4
C_5 olefins	5	-	-	0.18	0.41	0.26
C_6 olefins	6	-	-	2.99	6.75	3.19
C_8 olefins	8	-	-	0.48	1.63	1.21
Other products						
Unknown gas and liquid products	-	5.94	0.37	1.86	5.63	1.91
Coke	-	-	4.63	14.99	8.61	5.26
Esters						
Butyl butanoate	8	-	-	0.25	-	-
C_{10} ester	10	-	-	0.56	-	-

Table 2.24. Comparison between esters in stream and effects of pressure on etherification. Adjusted to 100% carbon balance by considering carbon obtained from solid phase TOC analysis.

Etherification feed code		1-butanol	1-butanol	SG-12	MG-12	MG-12
Pressure (psig)		0	100	100	0	100
Overall carbon conversion (%)		70.78	73.41	78.33	72.26	73.17
Total carbon balance (%)		100.00	100.00	100.00	100.00	100.00
Compound	**Carbon #**					
Alcohols						
Ethanol	2	-	-	0.09	-	-
Ethers						
Ethyl butyl ether	6	-	-	0.30	-	-
Butyl ether	8	80.45	91.60	63.50	46.44	70.40
Butyl ethyl-butane ether	10	-	-	0.81	0.11	0.77
C_{10} linear ethers	10	-	-	9.08	5.25	13.51
Butyl ethyl-hexane ether	12	-	-	-	-	0.12
C_{12} linear ethers	12	-	-	1.37	0.44	0.23
Olefins						
C_4 olefins	4	10.58	3.40	3.53	24.68	3.14
C_5 olefins	5	-	-	0.18	0.41	0.26
C_6 olefins	6	-	-	2.99	6.74	3.19
C_8 olefins	8	-	-	0.48	1.63	1.21
Other products						
Unknown gas and liquid products	-	5.52	0.37	1.86	5.62	1.91
Coke on catalyst surface	-	3.45	1.53	1.62	8.68	3.15
Coke in liquid phase	-	-	3.11	13.38	-	2.11
Esters						
Butyl butanoate	8	-	-	0.25	-	-
C_{10} ester	10	-	-	0.56	-	-

2.4.4 Pressure effects on Dehydration

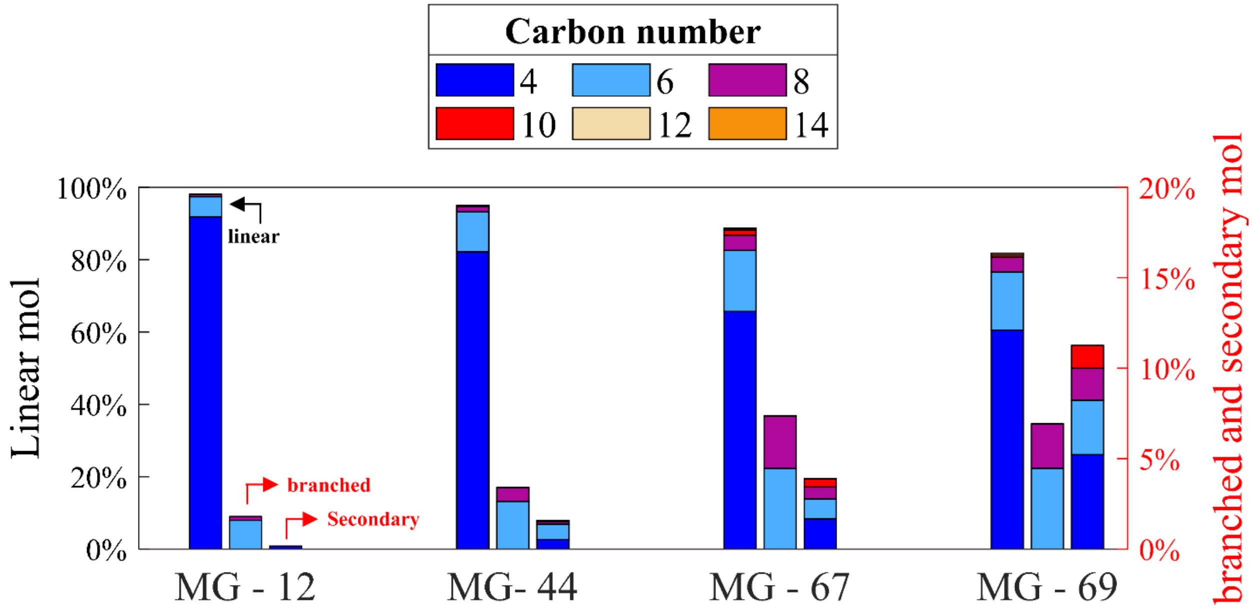

Figure 2.18. Alcohol distribution of products from ethanol oligomerization as a function of ethanol conversion, assuming 100% ester hydrogenolysis. These products will be used as model feedstocks for the etherification experiments in this paper. The conversion was varied by changing the weight hourly space velocity in the ethanol oligomerization reactor. The conversion is shown after the dash. For secondary alcohols, the numbering is defined by 'n+1'. Colors not visibly shown for compounds are present in low amounts (< 1.0%).

The alcohol distribution of MG – 12 is shown in **Figure 2.18**, and a detailed breakdown of the feedstock studied can be found in **Table 2.25**. The effect of pressure on dehydration was studied with n-butanol and MG – 12 feeds as shown in **Figure 2.18**. **Figure 2.18A** depicts the carbon number distributions for the ethers and olefins. The left-hand side depicts the selectivities of the ethers based on carbon number, while the right-hand side depicts the selectivities of the olefins based on carbon number. In all cases, the olefin selectivity was lower than the ether selectivity. **Figure 2.18B** depicts that increasing the pressure does not affect the conversion or carbon balances with the butanol and MG – 12 feeds. In all cases, the unknown products were below 10%

selectivity. For pure n-butanol, pressure had minimal impact on the product distributions. The ether selectivity slightly increases, and the olefin selectivity slightly decreases with pressure for n-butanol, (**Figure 2.18A**). For 1-butanol at 0 psig, the true coke selectivity based on TOC experiments is 3.5% (see Table **2.24**). In **Figure 2.18B**, the coke selectivity is zero as the carbon balances were over 100% when only the gas and liquid phase were analyzed. A noticeable pressure effect is observed with MG – 12 (See **Tables 2.23** and **2.24**). One plausible explanation is that pressurizing the system above the reactant vapor pressures shifts the reaction phase from gas to liquid (See **Table 2.26**). Due to the significant change in selectivities, all further reactions were conducted at 100 psig.

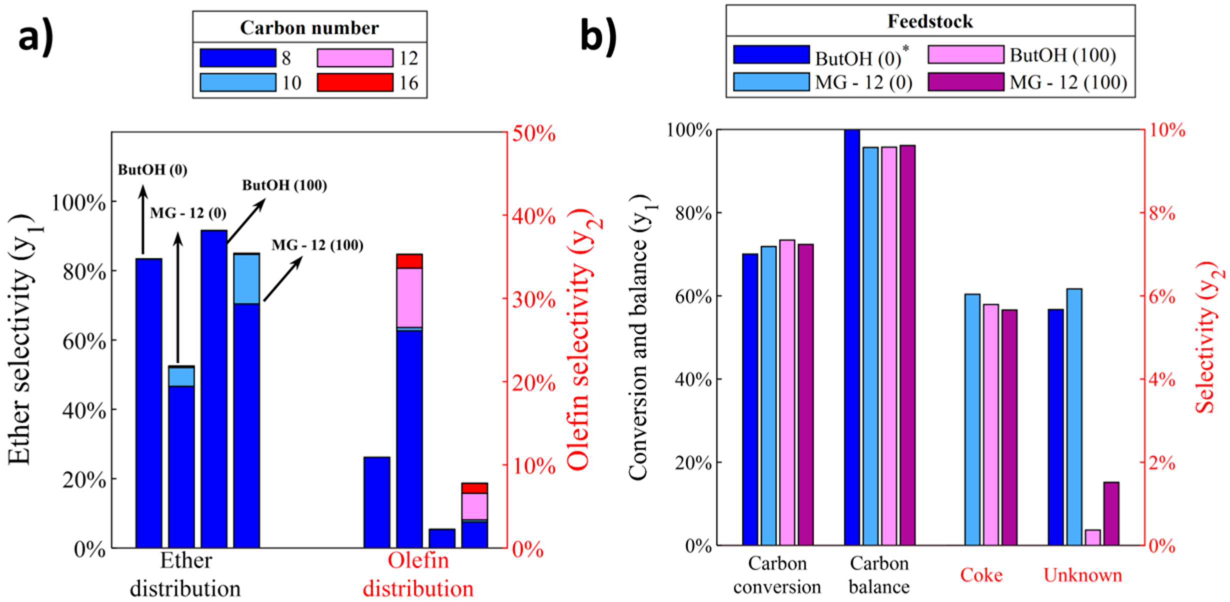

Figure 2.19. Dehydration distributions of pure 1-butanol and MG-12 feedstock streams. **A)** Final product distributions as a function of carbon number; **B)** Reaction parameters as a function of pressure. T = 170 °C, P = 0 - 100 psig, 0.02 mL/min flowrate, WHSV = 0.54 h^{-1}, TOS > 20 hr. For olefins, the numbering is ‘n/2’. Values next to feedstock represent operating pressure. Asterisk signifies carbon balances were normalized to 100% due to overestimation of carbon in the liquid phase.

Table 2.25. Model feedstock composition, assuming 100% ester hydrogenolysis and removal of light compounds < C_4. For alcohols that could not be purchased, the mol lumping method was used to maintain the alcohol structure composition of feedstocks. 'L/B' represents the linear to branched alcohol ratio. 'L/S' represents the linear to secondary alcohol ratio.

Etherification feed code	**MG – 12**	**MG – 44**	**MG – 67**	**MG - 69**
Ethanol conversion (%)	12.26	44.16	66.51	68.9
Compounds		**Mol%**		
Alcohols				
1-butanol	91.81	82.20	67.88	60.53
2-pentanol	0.16	0.53	1.78	5.22
1-hexanol	5.64	11.06	15.16	16.05
2-ethyl-1-butanol	1.59	2.63	4.77	4.46
2-heptanol	0	0.85	1.18	3.00
1-octanol	0.60	1.46	3.69	4.18
2-ethyl-1-hexanol	0.20	0.77	3.11	2.46
4-nonanol	0	0.15	0.71	1.77
1-decanol	0	0.25	0.82	0.61
2-undecanol	0	0.06	0.37	1.26
1-dodecanol	0	0.05	0.42	0.41
1-tetradecanol	0	0	0	0.05
Alcohol structure				
Linear **(L)**	98.05	95.02	88.74	81.82
Branched **(B)**	1.79	3.40	7.36	6.92
Secondary **(S)**	0.16	1.58	3.89	11.26
Alcohol ratios				
L/B	55	28	12	12
L/S	617	60	23	7

Table 2.26. Vapor pressure of alcohols at 170 °C. Parameters were taken from NIST[19], where values were then extrapolated using Antoine's equation.

Compound	**Vapor pressure (psi)**
linear	
1-butanol	69.0
1-hexanol	14.5
1-octanol	7.00
branched	
2-methyl-1-butanol	47.9
2-ethyl-1-hexanol	9.7
secondary	
2-butanol	114.6
2-octanol	18.1

2.4.5 Dehydration of Model feedstocks

Rorrer and Eagan reported that alcohol structure is important in etherification, in which high linear alcohol streams increase the rate of etherification.[11, 20] However, the feeds they used were single alcohol feeds, linear alcohol-only mixtures, or binary reaction mixtures of linear and branched alcohols. While branched alcohols can still undergo etherification to some extent, secondary alcohols will mainly produce olefins. It is therefore unclear how complex C_{4+} alcohol distributions affect the final size and selectivities for ether and olefin distributions obtained from competitive dehydration reactions. Other groups have studied etherification of alcohols over polymeric acidic resin catalysts (i.e Amberlyst 70), though these catalysts typically suffer from swelling due to water being formed during dehydration reactions, and thus catalyst stability further becomes an issue at temperatures above 150 °C [11, 21-24]. H-exchanged zeolites are robust catalysts that are not affected by swelling, though dealumination may be important in high water content streams and/or at reaction temperatures above 170 °C[25, 26]. The recent advancements in understanding the effects of water on zeolite structure suggest that these materials will be of interest for future processes that require water-tolerant catalysts for dehydration reactions[27].

Figure 2.2 depicts the molecular distribution of four different feedstocks obtained from an ethanol oligomerization reactor[4]. As the ethanol conversion increases, larger fractions of branched and secondary molecules are present in the reaction stream. The ester composition further increases with increasing ethanol conversion. As shown in **Scheme 2.1**, all the esters are assumed to undergo 100% hydrogenolysis conversion to produce alcohol-rich streams. The alcohol-rich feedstocks are then used for the dehydration step to produce diesel-range ethers and olefin fuel precursors. These alcohol-rich streams are depicted in **Figure 2.18**, and a detailed breakdown can be found in **Table 2.25**. Some alcohols were substituted for commercially available alcohol because those alcohols could not be purchased commercially. For example, 2-ethyl-1-hexanol (C_8) was used in place of C_{10+} branched alcohols (2-ethyl-1-octanol, 2-ethyl-1-decanol, and 2-ethyl-1-dodecanol). For secondary alcohols, C_{15+} secondary alcohols (were 4-undecanol, 4-tridecanol, 2-pentadecanol, and 2-heptadecanol) were replaced with 2-undecanol (C_{11}). The lumping method was used to maintain the structural composition of linear, branched, and secondary alcohols.

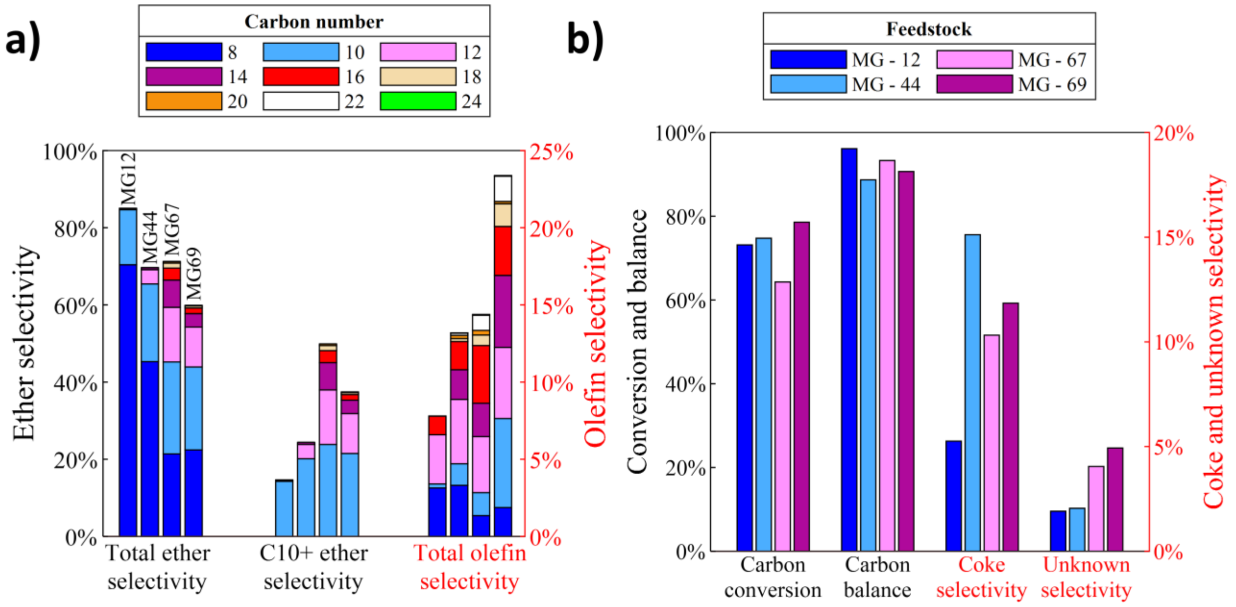

Figure 2.20. Dehydration distributions of model feedstocks. **A)** Final product distributions as a function of carbon number and structure; **B)** Reaction parameter distributions as a function of ethanol conversion. T = 170 °C, P = 100 psig, 0.02 mL/min flowrate, WHSV = 0.54 – 0.61 h^{-1}, TOS > 30 hr. For olefins, the numbering is 'n/2'. Colors not visibly shown for compounds are present in low amounts (< 1.0%). 'MG' followed by the value represents the model feedstock obtained at the respective ethanol conversion in the ethanol oligomerization step.

Figure 2.20 is the product selectivity, conversion and carbon balance obtained from the four model feedstocks studied with **Table 2.27 and 2.28** showing both the unadjusted and adjusted distributions of the products for each model feedstock studied. **Figure 2.20A** shows that as the linear alcohol content of the feed decreases the C_{8+} ether selectivity decreases. As the branched and secondary alcohol content of the feed increases the olefin selectivity increases. Feedstocks with larger fractions of C_{6+} alcohols shift the ether selectivity from C_{8+} to C_{10+} ethers. The increase in C_{6+} alcohol content also shifts the olefin selectivity from C_{4+} to C_{6+} olefins. The unknown carbon detected increases with increasing complexity of the feedstock. **Figure 2.20B** shows that the carbon balance decreases with increasing the ethanol conversion. This effect is likely due to an increase in the C_{6+} alcohol content, branched alcohols, and secondary alcohols of the feed.

Both MG–67 and MG–69 have similar branched alcohol content (7.4 mol% vs. 6.9 mol%, respectively, see **Table 2.25**). However, the secondary alcohol content is 7 mol% higher for MG – 69. The increase in secondary alcohol content led to an increase in coke selectivity on the catalyst surface by about 4% (See **Table 2.28**). While larger chain alcohols are present in MG – 69, the linear alcohol distribution is similar (see **Table 2.25**, L/B and L/S ratios). Thus, secondary alcohols can lead to higher surface coke selectivities. While branched alcohols can still undergo bi-molecular dehydration to some extent, secondary alcohols are less likely to produce ethers and mainly undergo mono-dehydration. Secondary alcohols may either be adsorbing strongly over HY, or the olefins produced are possibly undergoing side reactions (i.e acid-catalyzed oligomerization), leading to a decrease in the carbon balance via coking mechanisms[28, 29]. The olefins produced from branched alcohols can also undergo the same side reactions that secondary alcohol derived olefins encounter, though reactivity differences to coke products are still unclear. We conclude that secondary alcohols will likely not undergo etherification at our current conditions, with olefins the main by-products from secondary alcohols. The increase in secondary alcohol content led to an increase in the overall coke selectivity by about 1.5%. Further increasing the secondary alcohol content will lead to higher coke selectivities (See **Table 2.27**). The increase in secondary alcohol content can lower the final blend stock yields, as well as increase the CO_2 emissions produced from coke removal through catalyst regeneration. Measuring the amount of carbon on the catalyst after reaction was done using total organic carbon content (TOC) analysis (see **Table 2.3**). The catalyst bed of MG – 67 had a higher coke content than MG – 69.

Table 2.27. Product feedstock composition post-etherification. Leftover carbon not detected in the liquid or gas phase was assumed to go to coke products.

Etherification feed code		MG-12	MG-44	MG-67	MG-69
Ethanol conversion (%)		12.26	44.16	66.51	68.90
Overall C_{4+} alcohol conversion (%)		73.17	74.76	64.72	78.58
Liquid and gas carbon balance (%)		96.15	88.70	93.32	90.69
Compound	**Carbon #**	**Selectivity %**			
Ethers					
Butyl ether	8	70.40	45.29	21.38	22.42
Butyl ethyl-butane ether	10	0.77	1.16	2.07	1.36
C_{10} linear ethers	10	13.51	18.97	21.76	20.14
Butyl ethyl-hexane ether	12	0.12	0.18	1.43	0.53
Hexyl ethyl-butane ether	12	-	0.16	1.11	0.56
C_{12} linear ethers	12	0.23	3.35	11.62	9.26
Hexyl ethyl-hexane ether	14	-	0.03	0.81	0.25
Octyl ethyl-butane ether	14	-	0.00	0.40	0.24
C_{14} linear ethers	14	-	0.44	5.84	2.99
Decyl ethyl-butane ether	16	-	-	0.23	-
C_{16} linear ethers	16	-	0.06	2.88	1.45
Decyl ethyl-hexane ether	18	-	-	0.14	-
Dodecyl ethyl-butane ether	18	-	-	0.06	-
C_{18} linear ethers	18	-	-	1.11	0.51
Dodecyl ethyl-hexane ether	18	-	-	0.04	-
C_{20} linear ethers	20	-	-	0.36	0.16
Olefins					
C_4 olefins	4	3.14	3.31	1.35	1.87
C_5 olefins	5	0.26	1.40	1.49	5.77
C_6 olefins	6	3.19	4.17	3.63	4.61
C_7 olefins	7	1.21	1.92	2.16	4.66
C_8 olefins	8	-	1.83	3.74	3.17
C_9 olefins	9	-	0.19	0.68	1.47
C_{10} olefins	10	-	0.21	0.30	0.15
C_{11} olefins	11	-	0.14	0.98	1.64
C_{12} olefins	12	-	0.02	0.05	0.04
Other products					
Unknown gas and liquid products	-	1.91	2.05	4.05	4.93
Coke	-	5.26	15.12	10.32	11.85

Table 2.28. Product feedstock composition post-etherification. Leftover carbon not detected in the liquid or gas phase was assumed to go to coke products. Adjusted to 100% carbon balance by considering carbon obtained from solid phase TOC analysis.

Etherification feed code		MG-12	MG-44	MG-67	MG-69
Ethanol conversion (%)		12.26	44.16	66.51	68.90
Overall C_{4+} alcohol conversion (%)		73.17	74.76	64.72	78.58
Total carbon balance (%)		100	100	100	100
Compound	**Carbon #**	**Selectivity %**			
Ethers					
Butyl ether		70.40	45.29	21.38	22.42
Butyl ethyl-butane ether		0.77	1.16	2.07	1.36
C_{10} linear ethers		13.51	18.97	21.76	20.14
Butyl ethyl-hexane ether		0.12	0.18	1.43	0.53
Hexyl ethyl-butane ether		-	0.16	1.11	0.56
C_{12} linear ethers	12	0.23	3.35	11.62	9.26
Hexyl ethyl-hexane ether	14	-	0.03	0.81	0.25
Octyl ethyl-butane ether	14	-	-	0.40	0.24
C_{14} linear ethers	14	-	0.44	5.84	2.99
Decyl ethyl-butane ether	16	-	-	0.23	-
C_{16} linear ethers	16	-	0.06	2.88	1.45
Decyl ethyl-hexane ether	18	-	-	0.14	-
Dodecyl ethyl-butane ether	18	-	-	0.06	-
C_{18} linear ethers	18	-	-	1.11	0.51
Dodecyl ethyl-hexane ether	18	-	-	0.04	-
C_{20} linear ethers	20	-	-	0.36	0.16
Olefins					
C_4 olefins	4	3.14	3.31	1.35	1.87
C_5 olefins	5	0.26	1.40	1.49	5.77
C_6 olefins	6	3.19	4.17	3.63	4.61
C_7 olefins	7	-	1.92	2.16	4.66
C_8 olefins	8	1.21	1.83	3.74	3.17
C_9 olefins	9	-	0.19	0.68	1.47
C_{10} olefins	10	-	0.21	0.30	0.15
C_{11} olefins	11	-	0.14	0.98	1.64
C_{12} olefins	12	-	0.02	0.05	0.04
Other products					
Unknown gas and liquid products	-	1.91	2.05	4.05	4.93
Coke on catalyst surface	-	3.15	10.47	5.65	9.57
Coke in liquid phase	-	2.11	4.65	4.67	2.28
Final ether yields					
C_8 ether yield	-	51.51	33.86	13.84	17.62
C_{10+} ether yield	-	0.71	18.20	32.27	29.41

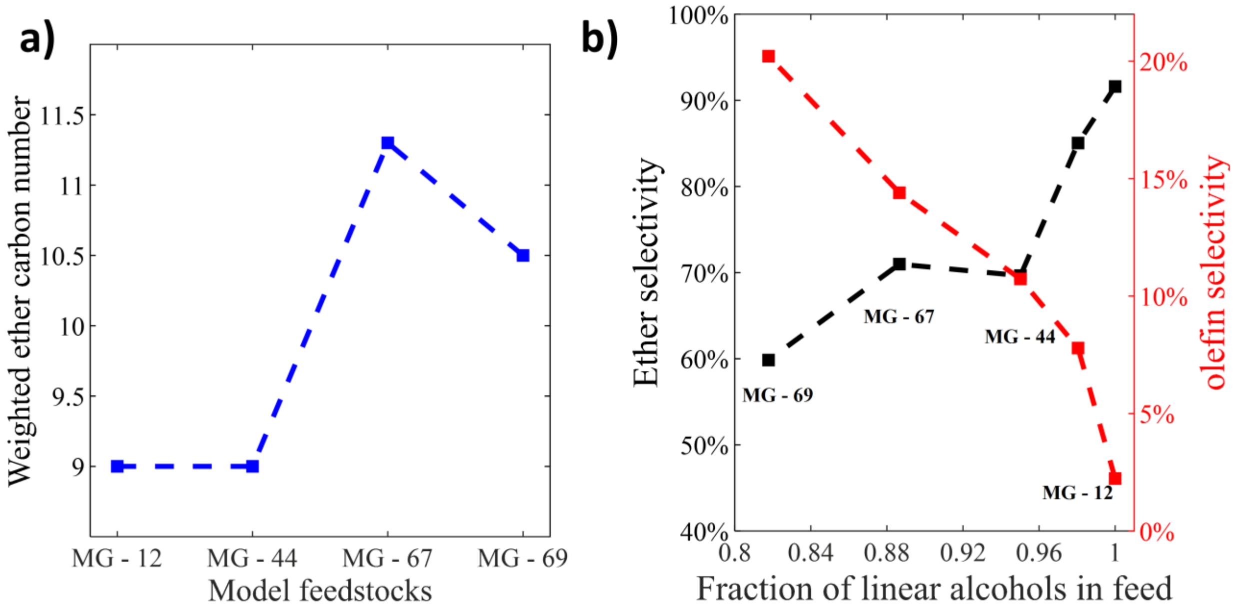

Figure 2.21. **A)** Average carbon number of ethers produced as a function of ethanol conversion. Product carbon numbers were calculated based on total ether product analyzed in the liquid phase and **B)** Product selectivities of model feedstocks as a function of linear alcohol content. F = 1 represents a pure 1-butanol stream as a reference reaction.

As shown in **Figure 2.21A** the size of the ethers does not increase from feedstock MG – 12 to MG – 44 likely because the n-butanol content in both feedstocks was similar (91.8 vs. 82.20 mol %, respectively). However, the ether size increases from 9.0 to 11.3 with feedstock MG – 67. MG – 67 has lower n-butanol content (67.88 mol %), while also having higher fractions C_{6+} linear and branched alcohols. The ether size decreased to 10.5 with feedstock MG – 69 likely due to the higher fractions of secondary alcohols. **Figure 2.21B** shows the ether and olefin selectivities as a function of the alcohol linearity of the feedstock. The ether selectivity decreases with decreasing linear alcohol fraction in the feed. This trend is consistent with other studies[11, 20]. As the fraction of linear alcohols continues to decrease, coking and mono-dehydration reactions become more prominent. We conclude that high linear alcohol streams above 80 mol% are needed to maintain the C_{8+} ether selectivity above 60%.

2.4.6 Dehydration of oligomerization feeds from ethanol and n-butanol mixtures

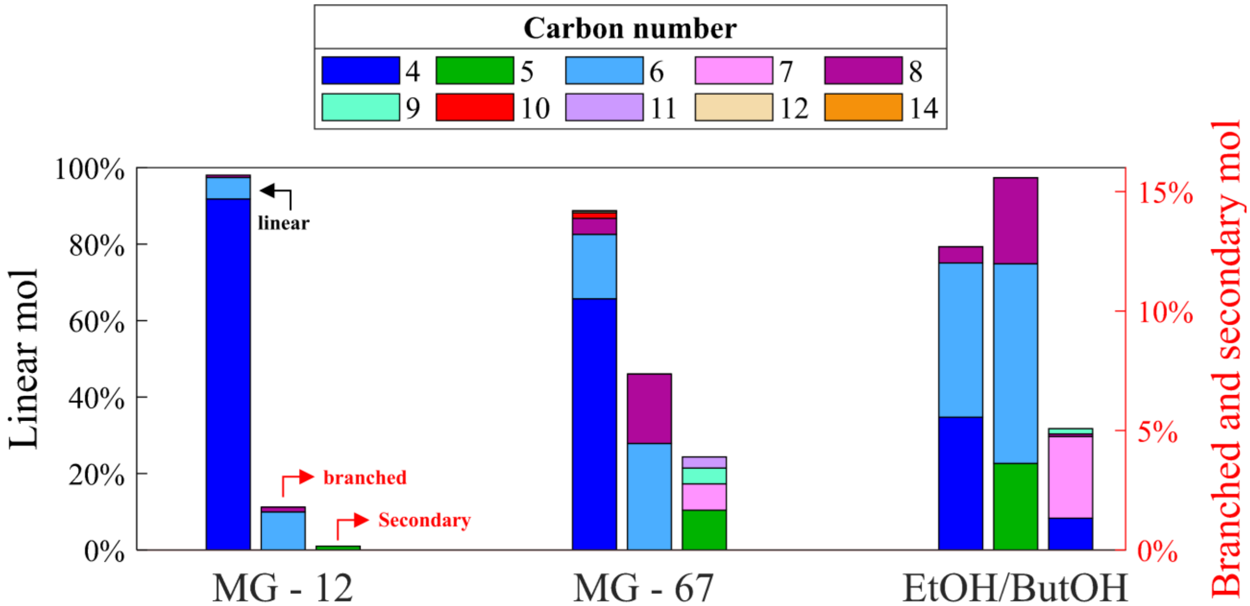

Figure 2.22. Alcohol distribution from Guerbet conversion of ethanol with EtOH/ButOH. Secondary alcohol numbering is defined by ‘n’. Colors not visibly shown for compounds are present in low amounts (< 1.0%).

Our research team has shown that the C_{10+} ethers can be maximized by feeding in a mixture of ethanol and butanol into the Guerbet reactor[30]. **Figure 2.22** shows the products from the Guerbet reaction for MG-12, MG-67 and ethanol/butanol (EtOH/ButOH) oligomerization. These feeds were then used for the dehydration reaction. A detailed breakdown of the EtOH/ButOH oligomerization feedstock can be found in **Table 2.29**.

Table 2.29. Feedstock of EtOH/ButOH oligomerization products used for the n-butanol recycling unit analysis. 'L/B' represents the linear to branched alcohol ratio. 'L/S' represents the linear to secondary alcohol ratio.

Alcohol	Mol%
1-butanol	34.73
2-butanol	1.33
2-methyl-1-butanol	3.62
1-hexanol	40.35
2-ethyl-1-butanol	8.36
2-heptanol	3.42
2-ethyl-1-hexanol	3.60
1-octanol	4.26
2-octanol	0.11
2-nonanol	0.22
Alcohol ratios	
L/B	5
L/S	16

MG – 12 was chosen as it has the lowest selectivity to C_{10+} ethers, while MG – 67 was chosen as it has the highest selectivity to C_{10+} ethers. The EtOH/ButOH oligomerization step assumes that un-reacted n-butanol from the process can be separated and recycled back into the ethanol oligomerization step. Recycling of n-butanol increases the overall C_{6+} alcohol content from the Guerbet feed. However, the linear alcohol content decreases when the butanol is recycled. The increase in branched alcohol content is expected due to the addition of n-butanol to the oligomerization step, as nucleophilic alcohols that are larger than ethanol react to form larger branched products[11, 31]. The secondary alcohol content slightly increases with butanol addition compared to MG – 67. The alcohols from the feeds in **Figure 2.22** were then used for dehydration. **Tables 2.28** and **2.30** show the detailed dehydration products from MG – 12, MG – 67 and the EtOH/ButOH oligomerization products. The carbon balances are lower for the EtOH/ButOH products at WHSV = 0.54 h^{-1}, as well as the overall ether selectivity. The WHSV was doubled to assess the effects on carbon balance. **Table 2.30** shows that doubling the space velocity has a negligible effect on the carbon balances and slightly increasing the C_{10+} ether selectivity. While higher WHSVs lead to higher selectivities, the conversion further decreases. Here, determining the quality of the raw blends produced from an economic point of view should be assessed by engine testing. The supported engine testing can then help provide a sensitivity analysis on whether the slight increases in carbon balances produce better raw blends, while minimizing the amount of recycled reactant materials. This kind of analysis has been shown by Restrepo-Florez and coworkers[1], where surrogate blends were tested, and the information was feed into a techno-economic analysis to understand the economic factors of the ethanol to diesel route.

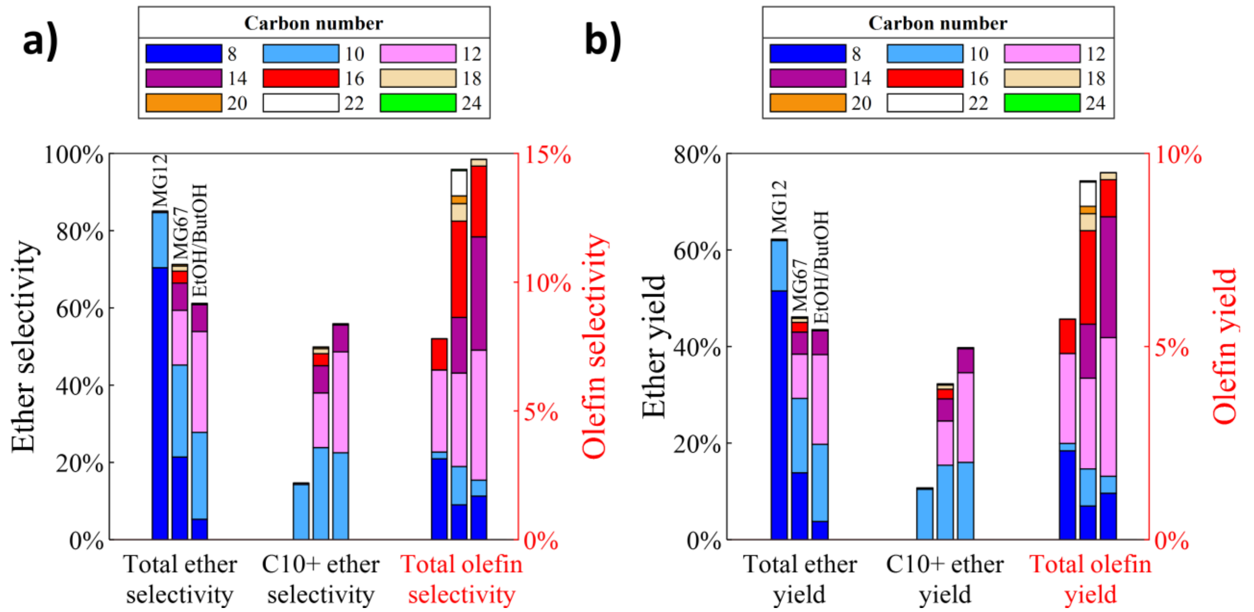

Figure 2.23. A) Selectivity distributions of ethers and olefins and **B)** Yield distributions of ethers and olefins. For MG – 12 and MG 67, the WHSV = 0.54 h^{-1} (Flowrate = 0.02 mL/min) with TOS > 30 hr. For the EtOH/ButOH oligomerization products, the WHSV = 1.0 h^{-1} (Flowrate = 0.04 mL/min) with TOS ~ 21 hr. T = 170 ºC, P = 100 psig. For olefins, the numbering is defined as ‘n/2’.

Table 2.30. Final dehydration product distribution of EtOH/ButOH oligomerization products at varying WHSV. Leftover carbon not detected in the liquid or gas phase was assumed to go to coke products (non-adjusted). The final coke distribution was adjusted to 100% carbon balance by considering carbon obtained from solid phase TOC analysis.

Etherification feed code		EtOH/ButOH	EtOH/ButOH
WHSV (h^{-1})		0.54	1.00
Overall C_{4+} alcohol conversion (%)		81.23	71.13
Liquid and gas carbon balance (%)		85.00	86.53
Compound	**Carbon #**	**Selectivity %**	
Ethers			
Butyl ether	8	4.77	5.27
Butyl ethyl-butane ether	10	0.94	1.56
C_{10} linear ethers	10	19.29	20.94
Butyl ethyl-hexane ether	12	0.38	0.85
Hexyl ethyl-butane ether	12	1.91	3.17
C_{12} linear ethers	12	20.03	22.10
Hexyl ethyl-hexane ether	14	0.78	1.71
Octyl ethyl-butane ether	14	0.31	0.47
C_{14} linear ethers	14	4.45	4.78
C_{16} linear ethers	16	0.48	0.30
Olefins			
C_4 olefins	4	2.56	1.69
C_5 olefins	5	1.12	0.62
C_6 olefins	6	8.37	5.05
C_7 olefins	7	4.47	4.40
C_8 olefins	8	3.64	2.75
C_9 olefins	9	0.29	0.26
Other products			
Unknown liquid and gas products	-	7.75	5.14
Coke selectivity (non-adjusted)	-	18.47	18.94
Coke on catalyst surface	-	4.63	9.44
Coke in liquid phase	-	13.84	9.50
Final Ether yields			
C_8 ether yield	-	3.88	3.75
C_{10+} ether yield	-	39.06	39.74

As shown in **Figure 2.23**, the C_{10+} ether selectivity obtained from MG-67 is 50%, while the C_{10+} ether selectivity is 56% using the EtOH/ButOH product stream. As shown with the linear alcohol feeds, larger alcohols can lead to lower carbon balances and lower overall ether selectivity. This may explain why the selectivity only increased by less than 10% across the two feedstocks.

Figure 9b shows the ether and olefin yields. The C_{10+} ether yield increases because of the presence of larger fractions of C_{6+} alcohols for MG – 12 and MG – 67 (11% vs 32%). The EtOH/ButOH oligomerization products further support that while stronger alcohol adsorption effects may be present, larger fractions of C_{6+} alcohols increase the C_{10+} ether yield. The C_{10+} ether yield for MG – 67 was 32%, while for the dehydration of EtOH/ButOH oligomerization products the C_{10+} ether yield was 40%. Furthermore, the butyl ether yield was lower for the dehydration of EtOH/ButOH oligomerization products compared to MG – 67 (4% vs. 14%). The implementation of an n-butanol recycling unit can therefore be used to significantly reduce the production of C_8 ethers and shift the final product carbon number to the C_{10+} range. Because EtOH/ButOH oligomerization products were used to represent a recycle feed stream of n-butanol, it is therefore possible to further increase the C_{10+} ether yields while re-using unconverted alcohol in the dehydration steps.

The coke content on the catalyst was measured after using the MG – 12, MG – 67 and EtOH/ButOH feeds. The graphs for these experiments can be found in **Figure 2.6**. In all cases, the presence of both soft coke and hard coke is observed on all beds. Volatile compounds are within the temperature region of 50 – 200 ºC. The soft coke region is in the temperature range of 200 – 400 ^{O}C, while the hard coke region is in the temperature range of 400 – 600 ^{O}C[32]. In all cases when oxygen is present, the largest change in weight occurs within the volatile and soft coke region. In the nitrogen experiments, there is minimal change in weight between the region of 400 – 600 ºC. In all cases, the lowest mass change is in the hard coke region. This trend is also observed when analyzing the EtOH/ButOH oligomerization beds, in which most of the weight loss is in the volatile compound region.

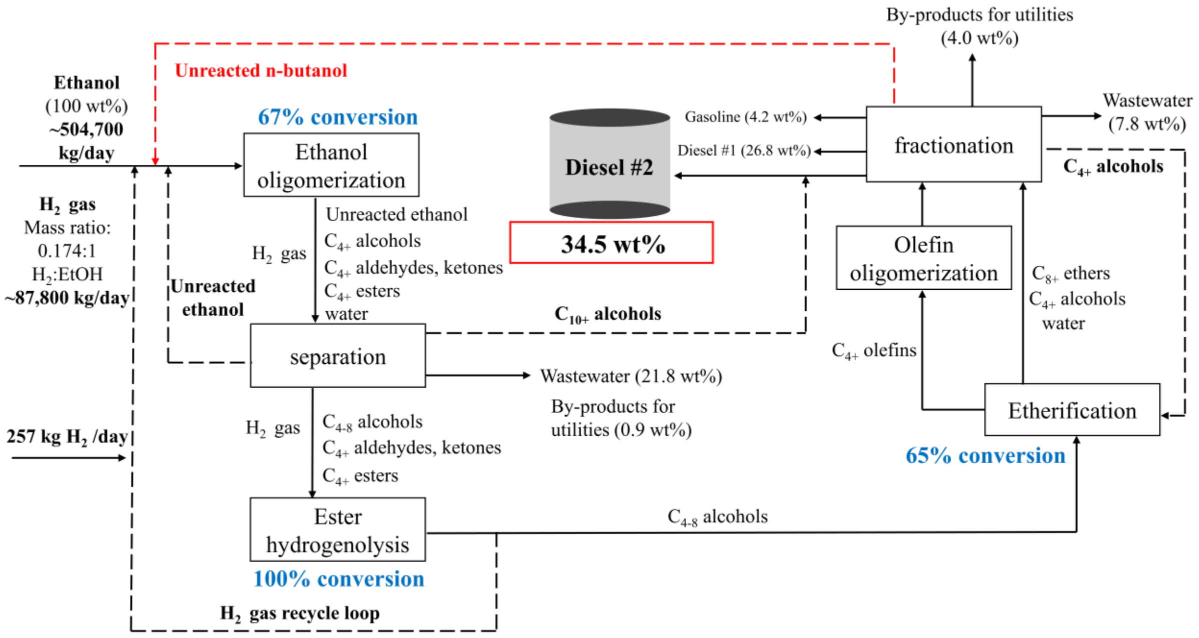

Scheme 2.2. Proposed process diagram of ethanol to diesel fuel range ethers. Important design parameters are represented by dashed lines. Red line signifies the proposed n-butanol recycling unit and is not considered in the final mass balance. Fuel yields and mass outputs are shown on a dry ethanol basis. The hydrogen balance is based on an ethanol oligomerization reactor operating at 325 °C and 300 psig, with a partial pressure ratio of 4:1 for H_2: Ethanol. Most of the hydrogen is recycled, therefore low amounts of hydrogen is further added into the system. The daily bio-ethanol production is based on the production of approximately 60 MMgal/year of anhydrous ethanol. Data and overall process diagram is derived from ref 1.

Scheme 2.2 represents a block-flow diagram of the proposed ethanol to diesel technology. In the first step, ethanol is oligomerized at around 67% single pass-conversion to produce the reactant oxygenate distribution. Water removal will be needed throughout the process, as it is known to inhibit etherification reactions[11, 33, 34]. In the second step ester hydrogenolysis, the esters undergo hydrogenolysis to their parent alcohols and ketones. Aldehydes and acetals are hydrogenated to their respective alcohols in this same step. C_{10+} alcohols are then removed and blended directly into diesel. These C_{10+} alcohols have properties suitable for diesel #2. Water is also removed prior to dehydration. The alcohol rich feedstocks are then used as a feed for the dehydration reactor at 65% single pass carbon conversion. The final product is then further separated, and the raw blend is cut into three specific fuel grades. Lighter alcohols are distillated and sent back to the etherification reactor. The final diesel #2 yield obtained with this approach is 34.5 wt% or 49.5 carbon % on a dry ethanol basis[1]. The composition of the final diesel #2 blend can be found in **Table 2.31**. The byproducts of this process include hydrogen and light gases (i.e olefins and paraffins) used for utilities (i.e steam generation), as well as wastewater produced from ethanol oligomerization and dehydration. Diesel #1 is mainly composed of di-butyl ether, while the gasoline fraction mainly consists of light molecules such as $C_1 – C_2$ alcohols, esters and olefins. The addition of a n-butanol recycling unit would further increase the alcohol size of the incoming dehydration feedstock. The increase in feedstock size allows us to further increase the chain sizes of the final ethers produced in the blend. A rigorous process analysis of this process is reported by Restrepo – Florez and coworkers[30].

Table 2.31. Final diesel #2 composition obtained from the overall process. C% represents the product carbon fraction with respect to the initial ethanol flowrate. Data was taken from Restrepo and coworkers[1].

Compounds	Carbon #	Flowrate (kmol/hr)	C%
Olefins			
1-nonene	9	0.266	0.26
8-methyl-4-nonene	10	0.383	0.42
2- methyl-2-undecene	12	0.960	1.26
2-methyl-2-tridecene	14	0.570	0.87
2-methyl-1-tetradecene	15	0.029	0.05
2-methyl-1-pentadecene	16	0.304	0.53
9-methyl-8-heptadecene	18	0.68	0.13
2-methyl-1-nonadecene	20	0.013	0.03
7-hexyl-7-pentadecene	21	0.042	0.10
1-tetracosene	24	0.013	0.03
Alcohols			
1-hexanol	6	0.537	0.35

2-ethyl-1-butanol	6	0.246		0.16
2-heptanol	7	0.206		0.16
1-octanol	8	0.713		0.62
2-ethyl-1-hexanol	8	1.918		1.68
4-nonanol	9	0.188		0.19
1-decanol	10	1.970		2.16
4-undecanol	11	0.256		0.31
1-dodecanol	12	0.547		0.72
2-butyl-1-octanol	12	0.626		0.82
4-tridecanol	13	0.289		0.41
1-tetradecanol	14	0.134		0.21
4,10-dimethyl-1-dodecanol	14	0.067		0.10
1-pentadecanol	15	0.188		0.31
Esters				
Butyl butyrate	8	2.873		2.52
Ethyl caproate	8	1.635		1.43
Hexyl acetate	8	1.053		0.92
Butyl caproate	10	2.440		2.67
Hexyl butyrate	10	0.282		0.31
Octyl acetate	10	0.188		0.21
Octyl butyrate	12	0.156		0.21
Butyl capyrlate	12	0.078		0.10
Ethyl caprate	12	1.095		1.44
Decyl acetate	12	0.078		0.10
Hexyl hexanoate	12	0.156		0.21
Hexyl caprylate	14	0.871		1.34
Ethyl laurate	14	0.067		0.10
Dodecyl acetate	14	0.067		0.10
Octyl octanoate	16	0.176		0.31
Ethers				
Butyl ether	8	3.675		3.22
C_{10} ethers	10	12.475		13.66
C_{12} ethers	12	5.105		6.71
C_{14} ethers	14	1.050		1.61
Di-octyl ether	16	0.242		0.40
Feedstock				
Ethanol	2	456.480	**Total C%**	**49.46**

2.5 Conclusions

Alcohols can be dehydrated into ethers using zeolite-based catalysts in a continuous flow reactor. Olefins and coke are the undesired reactions. Mono- and Bi-molecular dehydration reactions for linear alcohols are thermodynamically favorable at the temperature (170 ^{O}C) used in this study. Secondary alcohols prefer mono-molecular dehydration at the reaction conditions used in this study. Bi-molecular dehydration is thermodynamically more favorable than mono-molecular dehydration at temperatures less than 190°C for linear alcohols. Esters can cause undesired coke formation in the dehydration step. Dehydration experiments concluded that increasing the pressure from gas to liquid increases ether selectivity. Experiments showed that the pressurized reactions are stable for up to 50 hr TOS, and evidence of deactivation is present with esters at 1.5 wt% before 50 hours. Branched alcohol and secondary alcohols are more selective to olefins, while linear alcohols promote cross-etherification of branched alcohols. Feedstocks with high linear alcohol content led to higher ether selectivities. Feedstocks with higher branched and secondary alcohol content are more likely to produce a distribution of C_{4+} olefins. Increasing the secondary alcohol content was shown to increase coke selectivities. It was shown that for pure linear alcohol feeds, the ether selectivity decreases as a function of carbon chain length. However, feedstocks with larger fractions of C_{6+} alcohols were shown to be more selective towards C_{10+} ethers. Small chain olefins can be oligomerized and hydrogenated to distillate range paraffins, while the ethers produced can be directly blended into diesel. As C_{10+} ethers are better candidates for diesel #2, understanding the trade-off between alcohol chain length and C_{10+} ether yields will be crucial to produce biodiesel blends capable of being used in freight fuels. Without n-butanol recycling a 34.5 wt% (49.5 carbon %) yield of diesel #2 can be achieved from ethanol. The diesel #2 yield can further increase by recycling of n-butanol.

2.6 Acknowledgements

We would like to thank Dustin Witkowski for providing the flashpoint temperature data for alcohols and ethers in this article. We would also like to thank Juan-Manuel Restrepo-Florez for providing the detailed composition of the Diesel #2 blend.

This material is based upon work supported by the U.S. Department of Energy's Office of Energy Efficiency and Renewable Energy (EERE) under the Co-Optima program award number DE-EE0008480. The views expressed herein do not necessarily represent the views of the U.S. Department of Energy or the United States Government.

References

1. J.-M. Restrepo-Flórez, P. Cuello-Penaloza, E. Canales, D. Witkowski, D. A. Rothamer, G. W. Huber and C. T. Maravelias, Sustainable Energy & Fuels, 2023, **7**, 693-707.
2. N. M. Eagan, M. D. Kumbhalkar, J. S. Buchanan, J. A. Dumesic and G. W. Huber, Nature Reviews Chemistry, 2019, **3**, 223-249.
3. R. A. Dagle, A. D. Winkelman, K. K. Ramasamy, V. Lebarbier Dagle and R. S. Weber, Industrial & Engineering Chemistry Research, 2020, **59**, 4843-4853.
4. P. A. Cuello-Penaloza, R. G. Dastidar, S.-C. Wang, Y. Du, M. P. Lanci, B. Wooler, C. E. Kliewer, I. Hermans, J. A. Dumesic and G. W. Huber, Applied Catalysis B: Environmental, 2022, **304**, 120984.
5. Alternative Fuels Data Center, https://afdc.energy.gov/fuels/ethanol_benefits.html, (accessed January 10 2023).
6. 2018 Outlook for Energy: A View to 2040, ExxonMobil, Irving, 2018.
7. J. C. González Palencia, V. T. Nguyen, M. Araki and S. Shiga, Energies, 2020, **13**, 2459.
8. D. Smith, R. Graves, B. Ozpineci, P. Jones, J. Lustbader, K. Kelly, K. Walkowicz, A. Birky, G. Payne and C. Sigler, An Assessment of Technology and Knowledge Gaps (US DOE report ORNL/SPR-2020/7), 2019.
9. J. Heveling, A. van der Beek and M. de Pender, Applied catalysis, 1988, **42**, 325-336.
10. P. A. Cuello-Penaloza, J. Chavarrio-Cañas, Y. Du, M. P. Lanci, D. A. Maedke, J. A. Dumesic and G. W. Huber, Applied Catalysis B: Environmental, 2022, **318**, 121821.
11. N. M. Eagan, B. M. Moore, D. J. McClelland, A. M. Wittrig, E. Canales, M. P. Lanci and G. W. Huber, Green Chemistry, 2019, **21**, 3300-3318.
12. N. A. Huq, X. Huo, G. R. Hafenstine, S. M. Tifft, J. Stunkel, E. D. Christensen, G. M. Fioroni, L. Fouts, R. L. McCormick and P. A. Cherry, Proceedings of the National Academy of Sciences, 2019, **116**, 26421-26430.
13. J. T. Scanlon and D. E. Willis, Journal of Chromatographic Science, 1985, **23**, 333-340.
14. I. Van Zandvoort, Y. Wang, C. B. Rasrendra, E. R. van Eck, P. C. Bruijnincx, H. J. Heeres and B. M. Weckhuysen, ChemSusChem, 2013, **6**, 1745-1758.
15. I. Van Zandvoort, E. J. Koers, M. Weingarth, P. C. Bruijnincx, M. Baldus and B. M. Weckhuysen, Green Chemistry, 2015, **17**, 4383-4392.
16. M. Bertero, G. de la Puente and U. Sedran, Renewable Energy, 2013, **60**, 349-354.
17. A. Corma, H. Garcia, S. Iborra and J. Primo, Journal of Catalysis, 1989, **120**, 78-87.
18. S. R. Kirumakki, N. Nagaraju and S. Narayanan, Applied Catalysis A: General, 2004, **273**, 1-9.
19. N. I. S. Technology, NIST chemistry WebBook.
20. J. Rorrer, S. Pindi, F. D. Toste and A. T. Bell, ChemSusChem, 2018, **11**, 3104-3111.
21. J. H. Badia, C. Fité, R. Bringué, E. Ramírez and M. Iborra, Journal of industrial and engineering chemistry, 2016, **42**, 36-45.
22. J. Guilera, E. Ramírez, C. Fité, M. Iborra and J. Tejero, Applied Catalysis A: General, 2013, **467**, 301-309.
23. J. Tejero, F. Cunill, M. Iborra, J. Izquierdo and C. Fité, Journal of molecular catalysis A: chemical, 2002, **182**, 541-554.

24. R. Bringué, M. Iborra, J. Tejero, J. F. Izquierdo, F. Cunill, C. Fité and V. J. Cruz, Journal of Catalysis, 2006, **244**, 33-42.
25. W. Lutz, H. Toufar, R. Kurzhals and M. Suckow, Adsorption, 2005, **11**, 405-413.
26. R. Dimitrijevic, W. Lutz and A. Ritzmann, Journal of Physics and Chemistry of Solids, 2006, **67**, 1741-1748.
27. R. Simancas, A. Chokkalingam, S. P. Elangovan, Z. Liu, T. Sano, K. Iyoki, T. Wakihara and T. Okubo, Chemical Science, 2021, **12**, 7677-7695.
28. M. Guisnet and P. Magnoux, Applied Catalysis A: General, 2001, **212**, 83-96.
29. C. H. Bartholomew, Applied Catalysis A: General, 2001, **212**, 17-60.
30. J.-M. Restrepo-Flórez, J. E. Chavarrio, E. Canales, P. Cuello-Peñaloza, D. Witkowski, S. Subramanian, D. A. Rothamer, C. T. Maravelias, and G. W. Huber, In preparation.
31. N. M. Eagan, M. P. Lanci and G. W. Huber, ACS Catalysis, 2020, **10**, 2978-2989.
32. R. Ahmed, C. Sinnathamb and D. Subbarao, Journal of Applied Sciences, 2011, **11**, 1225-1230.
33. I. Hoek, T. Nijhuis, A. Stankiewicz and J. Moulijn, Applied Catalysis A: General, 2004, **266**, 109-116.
34. M. Kang, J. F. DeWilde and A. Bhan, ACS catalysis, 2015, **5**, 602-612.

Chapter 3. Ethanol to diesel: a sustainable alternative for the heavy-duty transportation sector

3.1 Introduction

The projected increase in the market share of electric vehicles[1] added to the expected rise in fuel efficiency[2] will lead to a reduction in the gasoline demand. In contrast, the consumption of middle distillates is surging, a trend that is expected to continue for the next thirty plus years[3] because air, terrestrial, and maritime freight, where most middle distillates are consumed, are difficult to electrify and their use is increasing.[4, 5] Consequently, middle distillates will continue to play a prominent role in the 21st-century energy landscape. Paradoxically, the biofuel industry in the U.S. has focused on the production of ethanol, which is blended exclusively with gasoline.[3, 6] In 2021, the United States produced 17 billion gallons of ethanol, almost an order of magnitude larger than biodiesel.[6, 7] Other countries have followed a similar trend. For example, Brazil, the second largest biofuels producer, manufactured ∼8 billion gallons of ethanol in 2021, with only approximately 1.8 billion gallons of biodiesel.[8, 9] Ethanol capacity will increase even more if lignocellulosic ethanol production plants are established.[10] This landscape can become challenging for two reasons.

The content of this chapter is largely adapted from the following:

Reproduced from ref. “Juan-Manuel Restrepo-Flórez, Paolo Cuello-Penaloza, Emmanuel Canales, Dustin Witkowski, David A. Rothamer, George W. Huber, Christos T. Maravelias. Ethanol to diesel: a sustainable alternative for the heavy-duty transportation sector. Sustainable Energy Fuels. **2023**. 7, 693-707" with permission from the Royal Society of Chemistry. **https://doi.org/10.1039/D2SE01377K**

*JM-Restrepo-Florez performed technoeconomic and lifecycle analysis, as well as written portions. PCP performed guerbet coupling experiments, product analysis and written portion. EC performed etherification experiments, product analysis and written portion. DW performed fuel property analysis, and written portion. JM-Restrepo Florez and PCP contributed equally to this paper. *

First, the sustainable alternatives for middle distillates, critically needed to mitigate climate change, are scarce and their production capacity is low. Second, a reduction in gasoline demand may lead to a surplus of ethanol in the market if gasoline supply is stable. Furthermore, the most common renewable diesel fuels, biodiesel and green diesel, are produced from vegetable oils and animal fats.[11] These feedstocks have limited availability and are expensive on an energy basis (~0.042$ per MJ).[12] In contrast corn grain (0.01–0.023$ per MJ),[13] and lignocellulosic biomass (0.003–0.005$ per MJ)[14] are between 1.8-4 and 8–14 times lower in cost, respectively, and are widely available.

One option to simultaneously tackle the aforementioned challenges is to catalytically upgrade ethanol into middle distillates.[3, 15] This approach takes advantage of existing and developing ethanol production infrastructure while producing the biofuels for which there is a more urgent need. Furthermore, this technology may be pivotal in repurposing existing ethanol production infrastructure as we transition toward an electrified light vehicle fleet. Additionally, from an energy security perspective, the production of biomass derived fuels is advantageous as it reduces the vulnerability of the energy system to abrupt changes in oil prices. A diesel production approach based on the catalytic upgrading of ethanol can exploit the diverse chemistries and catalysts available to transform ethanol into a wide range of molecules with varied properties, from olefins to ethers.[3, 6, 15, 16] From a business stand point, in the US the production of biofuels may take advantage of the renewable fuel standard program.[17] For example, benefits for the production of biomass-based diesel with more than 50% reduction in GHG have oscillated between 0.075–5.25$ per Gal.[17] Additionally, a temporary tax credit of 1$ per Gal is also available.[18] Motivated by these advantages researchers have developed ethanol upgrading processes to produce drop-in jet fuel.[3, 19-25] Although bioethanol-derived jet fuel only represents a small share of the fuel market, its use shows the potential of ethanol upgrading as a practical, scalable, and potentially profitable technology. Chemically, ethanol-to-jet fuel upgrading has relied on two approaches: (1) a single pot process in which dehydration and oligomerization occur simultaneously.[19] (2) A process in which dehydration, oligomerization, and hydrogenation occur sequentially.[20] While the upgrading of ethanol to jet fuel has been reported and a significant body of experimental work,[3, 6, 21] techno-economic analysis (TEA),[19, 20, 22, 23, 26, 27] and lifecycle (LCA) studies[19, 26, 28, 29] exist, there is a significant lag in studies where the upgrading of ethanol to diesel is studied.[15, 24, 30-32]

In principle, upgrading ethanol into diesel can be accomplished by ethanol dehydration to ethylene, followed by a sequence of oligomerization reactions.[24] However, this approach has significant challenges. First, the distillate yield may be low, a consequence of the molecular size distribution characteristic of oligomerization catalysts.[3] Second, the formation of highly branched products in oligomerization reactions leads to fuels with low cetane number.[33] An alternative approach, based on Guerbet chemistry and etherification, has been suggested for the upgrading of ethanol into diesel. In this approach, ethanol is first transformed into higher alcohols using Guerbet chemistry, and then these alcohols are transformed into ethers.[34, 35] This approach has significant advantages in comparison with other cases in which the final product consists mainly of paraffins, namely, the distillate yield is higher;[34] and more importantly, the chemical and physical properties of ethers of higher alcohols are advantageous in diesel production. Ethers with more than ten carbons have viscosity, density, flash point, and boiling range similar to fossil diesel.[34, 36] Additionally, they have a very high cetane number (>100), making them ideal candidates for the production of high-quality diesel (for reference, in the U.S. the minimum cetane number for diesel is 40).[37] A high cetane number may enable the design of engine operation strategies with lower NO_x emissions.[38] This characteristic allows us to postulate the possibility of producing diesel by catalytically upgrading ethanol into a diesel fuel blend with advantages over its fossil counterpart. This is in contrast with biofuel production strategies in which molecules or blends with similar, rather than superior, properties to fossil fuels are pursued.

In this work, we study the catalytic upgrading of ethanol to diesel based on Guerbet coupling and etherification. In this process, ethanol is transformed into higher alcohols which are then converted into a high cetane number ether blend. Minor olefin by-products are oligomerized. Bench-scale laboratory results, techno-economic analysis (TEA), and lifecycle analysis (LCA) are used to demonstrate the feasibility of transforming ethanol into a high cetane number diesel in a cost-effective and environmentally sustainable process. The results presented are the outcome of an iterative and collaborative effort between experimentalists, fuel property modelers, and process systems engineers. This synergistic collaboration has allowed us to tailor the experiments performed based on process modeling needs while ensuring that the fuels produced display desirable properties. Specifically, we provide accurate estimations of the macroscopic properties of the fuels produced (viscosity, density, low heating value, distillation curve, flash point, cloud point, and cetane number) and we show how the diesel produced can be used as a fossil diesel substitute.

3.2 Technology overview

The ethanol upgrading approach envisioned in this work relies on three technologies: ethanol Guerbet coupling, higher alcohol etherification, and olefin oligomerization. In **Figure 3.1**, a schematic representation of the proposed refinery is presented, as well as the connections among the technologies employed and the main chemical components present in the connecting streams. At a high level, anhydrous ethanol is fed to the system and transformed into higher alcohols (C4+) using Guerbet coupling. These alcohols are subsequently transformed into ethers in an etherification reaction. Both of these reactions produce a small fraction of low molecular weight olefins as byproducts. Because of their size, these olefins are unsuitable to be used in diesel. To alleviate this limitation, the olefins are oligomerized to increase their average molecular weight. The biorefinery produces primarily diesel. The other by-products include: gasoline, which is produced with suitable low molecular weight species that cannot be blended with diesel; and steam, which is generated by burning low molecular weight paraffins (C2–C4), olefins (C2), and hydrogen. Steam produced in this way is used to partially offset the process energy needs.

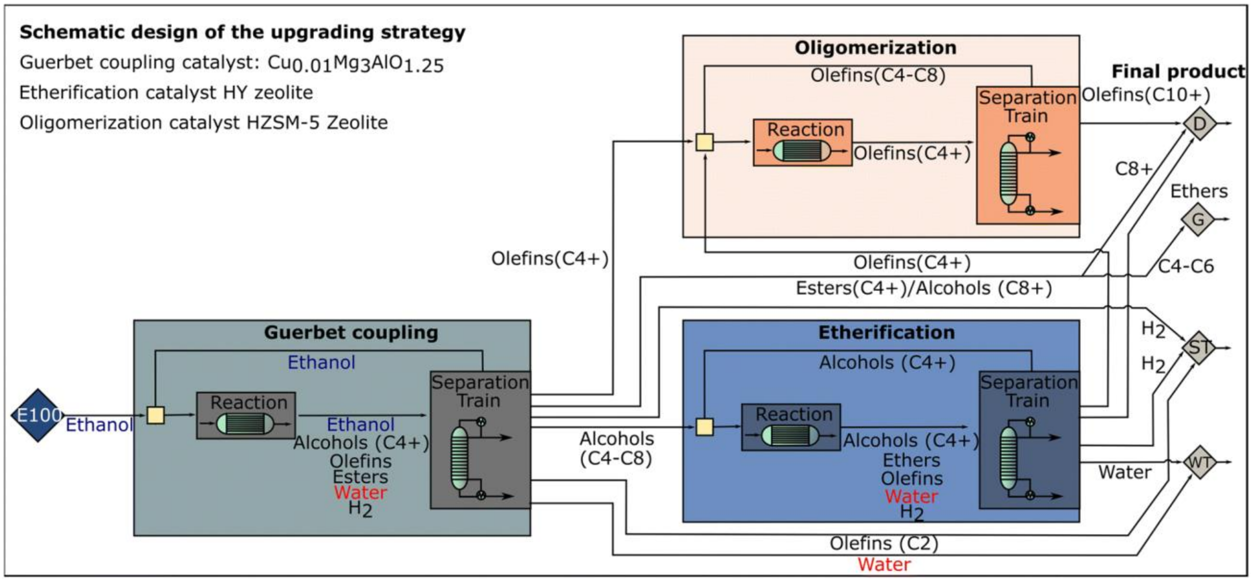

Figure 3.1. Schematic representation of an ethanol upgrading biorefinery based on Guerbet coupling, etherification, and olefin oligomerization. D: diesel, G: gasoline, ST: steam, WT: waste water.

3.2.1 Guerbet coupling

This reaction involves three mechanistic steps that all occur in one single reactor: (1) dehydrogenation of two alcohols to aldehydes, (2) aldol condensation, and (3) hydrogenation to form a higher alcohol.[34, 39] Continued condensation of reaction products is possible, although in practice products with more than 12 carbons are rare with C4–C8 alcohols as the most abundant species. As noted by Eagan and coworkers,[34] Guerbet chemistry is an oligomerization pathway that introduces branching in a more predictable way than olefin oligomerization. The main products of this reaction are higher alcohols. Byproducts include esters, olefins, aldehydes, ketones, and aromatics.[34, 39-43] Additionally, a mole of water is produced per each mole of condensation reaction.

Several heterogeneous catalysts can be used for the Guerbet coupling of ethanol.[3, 34, 39, 43-45] These catalysts include hydroxyapatites,[34, 46] metal oxides,[47, 48] and decomposed layered double hydroxides.[49] The selection of the catalyst influences both conversion and selectivity. In this work, we use a Cu-based hydrotalcite-derived catalyst ($Cu_{0.01}Mg_3AlO_{1.25}$). This catalyst is stable for more than 100 hours.[43] Additionally, it has been shown that this class of Cu-based catalysts has a higher selectivity toward C6+ alcohols[43, 50] in comparison with other catalysts commonly used in Guerbet reactions.[42, 51, 52]

3.2.2 Etherification

The etherification of higher alcohols can be accomplished using acid catalysts.[15, 34] In general, the product consists of a blend of ethers, olefins, and water.[34, 36] The formation of olefins increases with temperature and with the fraction of branched to linear alcohols in the feedstock.[34] Available catalysts for this reaction include acid resins,[34, 53] alumina,[54-56] and zeolites.[53, 57] In this work, we use HY zeolite. This catalyst is both stable and commercially available at a low cost making it advantageous in future industrial applications. The selectivity of the catalyst was determined for different feed compositions as detailed in the methods section.

3.2.3 Oligomerization

Oligomerization of low molecular weight olefins is commonly used in the petrochemical industry.[3, 58, 59] Oligomerization reactions increase the average size of the molecules used as feedstock. The molecular weight distribution of the products is a function of the feedstock composition and the catalyst used. Typically, it follows a Schultz–Flory distribution.[3, 60] The reaction conditions are a function of the composition, with C3+ olefins requiring milder conditions than ethylene.[3, 21, 61] Both homogeneous and heterogeneous catalysts have been used for these processes. In line with the principles of green engineering, we have selected a heterogeneous zeolite catalyst (HZSM-5) for this process.[62] The selected catalyst is known for producing a larger fraction of high molecular weight products, albeit their branching is usually high and their cetane number low.[62, 63] We use this catalyst for the oligomerization of C3+ olefins. We have modeled the oligomerization reaction based on the data reported by Bond and coworkers.[62]

3.3 Methods

3.3.1 General approach

To synergistically couple experimental studies and modeling, we follow the approach described in **Figure 3.2:**

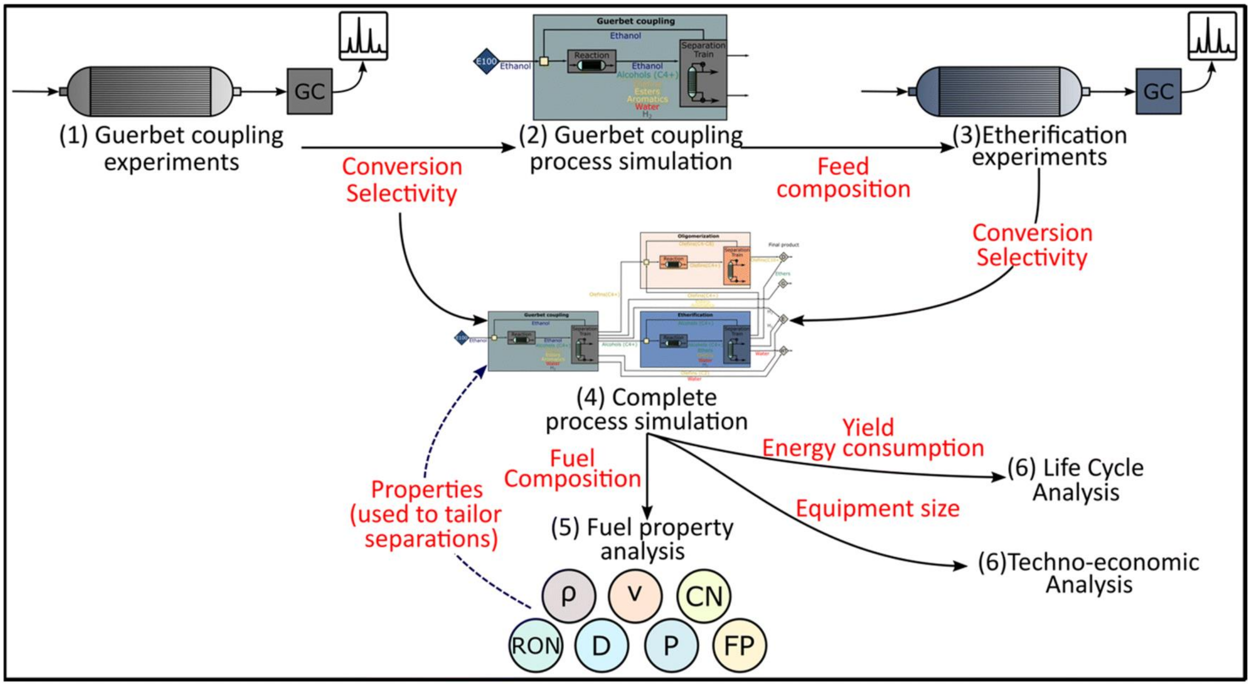

Figure 3.2. Approach followed in this work to couple experimental and simulation results. The flow of information at the different stages is shown in red fonts.

(1) We use a set of Guerbet coupling experiments previously performed by some of the authors and partially reported with minor variations in Cuello-Penaloza et al. 2022.[43] These experiments were aimed at establishing the impact of ethanol conversion on selectivity.

(2) We use the results from the Guerbet experiments to inform process simulations of the Guerbet coupling area of the biorefinery. The main goal of these simulations is to determine the composition of the etherification reactor feed.

(3) We perform etherification experiments using the feed compositions determined. These experiments have as a main objective to determine the conversion and selectivity obtained for the feeds of interests.

(4) Using the results both from etherification and Guerbet coupling experiments we perform a full plant simulation (Guerbet coupling, etherification, and oligomerization). This simulation allows us to calculate the final product composition (diesel) as well as the size of the equipment used in the biorefinery.

(5) With the composition resulting from the full plant simulation we analyze the properties of the fuels produced. If necessary, the separations within the plant are adjusted in an iterative manner to tailor the final products such that they meet ASTM standards.[64, 65]

(6) Finally, once the properties of the fuel products have been established, we perform TEA and LCA to determine the minimum fuel selling price (MFSP) and greenhouse gas (GHG) emissions.

Simulations are based on experimental results. Specifically, both the stoichiometry and the operational conditions in the process simulations are the same as those in the experiments.

3.3.2 Etherification experiments

The etherification of alcohol streams is carried out in an upward configuration flow reactor (33 cm long, 17.8 cm catalyst bed, 0.95 cm outer diameter) made of stainless-steel. The reactors are packed with 1.6–1.8 g (WSHV = 0.54–0.61 h^{-1}) of powder HY catalyst (Si/Al = 30) obtained from Zeolyst International and mixed with 30–80 mesh silica chips (Sigma Aldrich) in a 2 : 1 inert to catalyst mass ratio to minimize pressure drop. Model feedstocks are made in house and fed with a syringe pump (Eldex) at 0.02 mL min^{-1}, with Ar gas cofeed at 10 mL min^{-1}. Products flowing out of the reactor are crashed through a removable 140 mL glass condenser (ace glass) in a cold ice bath. Gases which do not condense are sent to a three-way valve positioned to flow through a bubble meter, gas bag or vent. Gas and liquid samples are collected simultaneously every 3–5 hours, with overnight samples being collected every 16–22 hours. The outlet flow of the reactor is redirected from the produce collection to a waste condenser when collection is conducted and switched back when a new condenser is placed. To reduce sampling error due to low product volumes, 1.46 mL of 1-heptanol is generally added to the condenser prior to collection. After collection, the sample mass is weighed, and the liquid is diluted with tetrahydrofuran (THF) with twice the predicted collected volume to ensure both the organic and aqueous phase are analyzed. The liquid is then diluted with THF including a known amount of 1-pentanol as an internal standard.

3.3.3 Analytical techniques

The reaction products for etherification are analyzed and quantified via GC-FID (Shimadzu 2014) equipped with a RTX-VMS column (Restek). Products are quantified with GC-FID via external standards when reference compounds can be obtained. When they cannot, response factors are estimated via the effective carbon number method. Products are identified via external standards when available, or via GC-MS suggestions. Gas bags are used to collect the gases and these are analyzed in the aforementioned gas GC equipment configuration. In cases in which no standards are obtainable, e.g. for cross-etherification products, equimolar batch reactions are conducted to identify the retention times for said products. The batch reactor data is overlapped with continuous flow data to identify cross-etherification products, in which then effective carbon number theory is either used, or a standard of the same carbon number is obtained.

3.3.4 Techno-economic analysis

Capital costs and direct operating costs are estimated based on processes simulations performed in Aspen Plus V.10®. These simulations are set based on the experimental results. For the full plant integrating Guerbet chemistry, etherification, and oligomerization, Aspen Energy Analyzer is used to perform heat integration based on pinch analysis[66] and to design a heat exchanger network. The MFSP of diesel is determined by applying a discounted cash flow analysis. A facility able to process 176.4 MTon per year (~60 MMGal per year) of anhydrous ethanol is designed. We assume 30 years of operation, as well as 40% equity and a 10 year loan at an 8% interest rate for financing. A discount rate of 10% and a 21% income tax rate are used. The economic parameters, biorefinery size, and installation factors used correspond to those reported in the most recent NREL report for lignocellulosic ethanol production.[67] All values are calculated in 2021 USD (see **Table 3.1** for more details). The cost of the catalysts is determined based on commercial data for zeolites (etherification and olefin oligomerization), and it is calculated using the recently develop tool CatCost® for the Guerbet catalyst[68] (See **Figure 3.3** and **Table 3.2**).

3.3.5 life cycle analysis

LCA is performed to understand the GHG emissions associated with the designed process. We are interested in the global warming potential (g CO_2-eq). The TRACI 2.1 (ref. 69) methodology is used to determine the impact factors and GaBi® is used to model the process. The results are presented using MJ of fuel as a functional unit. A cradle to grave analysis is performed where the end use phase is modelled assuming that all carbon contained in the fuel is transformed into CO_2. The system boundary includes the following processes: lignocellulosic feedstock production and transportation, ethanol production from lignocellulosic residues, ethanol upgrading, fuel transport, distribution, and fuel combustion. The main product of the upgrading process is diesel (#1 and #2), to account for the co-production of gasoline we use the displaced burden method.[70] Some of the byproducts are used to offset the energy needs of the refinery (i.e., the energy obtained from the combustion of energy rich by-products in ethanol upgrading). Life Cycle Inventories (LCI) for ethanol upgrading are established based on the process simulations in this work. For the emissions associated with lignocellulosic ethanol production, we use a range of values representative of current literature.[29, 71, 72] For other processes the LCI is established based on the energy database from GaBi®.

3.3.6 Fuel property analysis

Models from the literature were used to calculate relevant physical properties of the fuel blends produced in this work. Density was calculated using a linear by volume mixing rule.[73, 74] Liquid kinematic viscosity was calculated using the UNIFAC-VISCO method.[75] The flash point was modeled using the mixing rule of Liaw and coworkers.[76] Flash point data for each component was used where available and supplemented with predicted flash points for individual components using the group contribution model of Carroll and coworkers.[77] The cloud point of the fuel blend is treated as the thermodynamic equilibrium boundary temperature between the one-phase (liquid) and two-phase (solid/liquid) region for the fuel mixture.[78] Similar to the cloud point, the distillation curve for each blend was calculated as a thermodynamic equilibrium between the liquid and gas phase.[79] Finally, the derived cetane number (DCN) was estimated using an autoignition model that incorporates group contribution methods to calculate global initiation and chain branching rate constants for each component in the blend.[80] The model was recently developed to provide accurate DCN estimates for oxygenated components and blends with wide ranges of individual cetane numbers, where linear by volume mixing rules are no longer sufficient. Further details on the calculations can be seen in section 3.3.10.

3.3.7 Financial parameters used in this study

Table 3.1 Financial and cost assumptions used in this study.

General parameters		**Source**
Reference capacity	504 Ton/day	**67**
Financial variables		**67**
Equity	40%	
Loan interest	8%	
Loan term (years)	10	
Operation period (years)	30	
Depreciation period (years)	7	
Construction period (years)	3	
% year -2	8%	
% year -1	60%	
% year 0	32%	
Startup time (years)	0.25	
Feedstock use during start up (% of Normal)	50%	
Variable cost during start up (% of Normal)	75%	
Fixed cost during start up (% of Normal)	100%	
Discount rate	10%	
Income tax	21%	
Working capital (% of FCI)	5%	
Base year for analysis	2007	
Direct costs		**67**
OSBL (% of ISBL)	40%	
Warehouse (% of ISBL)	4%	
Site development (% of ISBL)	9%	
Additional piping (% of ISBL)	4.5%	
Indirect costs		**67**

Proratable expenses (% TDC)	10%	
Field development (% TDC)	10%	
Home Office & construction fee (% TDC)	20%	
Contingency (% TDC)	40%	
Other cost (Start-Up, permits, etc.)	10%	
Materials		
Ethanol ($/kg)	0.999	**67**
H_2 ($/Kg)	1.43	**23**
Utilities		
Water ($/KJ)	2.24×10^{-7}	**67,81**
Low pressure steam ($/KJ)	2.00×10^{-6}	
Medium pressure steam ($/KJ)	2.32×10^{-6}	
Fired heat ($/KJ)	$4.48 \text{ x} 10^{-6}$	
Electricity ($/KJ)	1.68×10^{-5}	
Waste management		
Waste treatment ($/Kg)	0.0364	**82**

For the estimation of the catalyst cost, we have used the recently developed tool CatCost[83]. This tool allows to calculate the cost of a new catalyst considering a candidate process and using a reference quantity of catalyst to be produced. In this case, the process was conceived based on the wet impregnation procedure developed by Cuello-Penaloza and coworkers[43]. A schematic of this process is shown in **Figure 3.3**. The costs of the catalyst for different ethanol conversions are shown in **Table 3.2**. Note that the cost of the catalyst changes with conversion because the size of the lot changes, both as a function of conversion and WHSV.

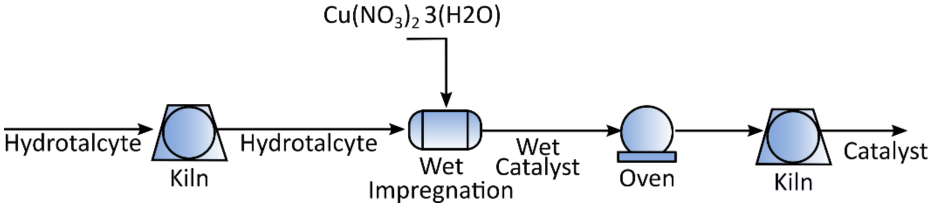

Figure 3.3. Proposed process for the preparation of the Cu-based catalyst used in this work using wet impregnation.

Table 3.2. Catalyst cost as a function of ethanol conversion

Ethanol conversion (%)	Catalyst cost ($/Kg)
12	16.26
15	14.24
20	12.75
40	13.27
66	10.95

3.3.8 Catalyst selectivities

The selectivity of the Guerbet coupling reaction as a function of conversion is shown in **Table 3.3**. This data is based on the results reported by Cuello-Penaloza and coworkers[50] with minor variations. Some simplification assumptions were applied in this work. These simplifications reduce the set of species that are treated in the process design and are listed below:

- Components with carbon selectivity less than 0.1% are ignored
- All butenes are treated as 1-butene
- All pentenes are treated as 1-pentene
- Linear alcohols with 4 carbons are treated as 1-butanol
- Linear alcohols with 6 carbons are treated as 1-hexanol
- Linear alcohols with 7 carbons are treated as 2-heptanol
- Linear alcohols of 8 carbons are treated as 1-octanol
- Branched alcohols of 8 carbons are treated as 2-ethylhexan-1-ol
- Aromatic alcohols are excluded from calculations for simplicity
- Linear alcohols of 9 carbons are treated as 4-nonanol
- Branched alcohols of 10 carbons are treated as 2-ethyloctan-1-ol
- Branched alcohols of 12 carbons are treated as 2-ethyl-1-decanol
- Aldehydes and ketones are hydrogenated to alcohols
- Acetic acid, 1-methylpropyl ester is treated as butyl acetate
- Acetic acid, 2-ethylbutyl ester is treated as hexyl acetate

- Butanoic acid, 2-ethyl, butyl ester is treated as hexyl butanoate
- Acetic acid, 2-ethylhexyl ester is treated as octyl acetate
- Butyric acid, 2-ethylhexyl ester is treated as octyl butanoate
- 2-ethylbutyl hexanoate is treated as hexyl hexanoate
- Unidentified C14 esters are assumed to be hexyl octanoate
- Unidentified C16 esters are assumed to be octyl octanoate
- We do not consider acetals or hemiacetals in calculations and are treated as their parent alcohols
- Unknown components are distributed proportionally among identified species

Table 3.3. Carbon selectivity as a function of single-pass ethanol conversion in the Guerbet coupling reaction.

Component	**Conversion (%)**						
	68.9	**66.5**	**44.2**	**19.1**	**14.5**	**12.3**	**3.1**
Paraffins							
methane	0.10	0.00	0.00	0.00	0.00	0.00	0.00
n-propane	0.10	0.10	0.00	0.00	0.00	0.00	0.00
n-butane	0.00	0.00	0.00	0.00	0.00	0.30	0.00
n-pentane	0.21	0.21	0.00	0.00	0.00	0.00	0.00
Olefins							
ethylene	0.00	0.00	0.00	0.00	0.00	0.00	0.15
1-butene	0.10	0.00	0.22	0.27	0.14	0.15	0.00
1-pentene	0.00	0.42	0.11	0.00	0.00	0.45	0.15
hexenes/dienes/trienes	0.00	0.10	0.00	0.00	0.00	0.00	0.00
Alcohols							
methanol	0.31	0.21	3.11	0.54	0.14	5.89	2.94
isopropanol	2.28	1.14	2.44	1.88	1.66	2.11	13.14
1-butanol	32.82	42.22	53.41	61.51	70.73	69.11	67.70
2-pentanol	4.24	1.46	0.44	0.27	0.14	0.15	0.00
1-hexanol	10.04	13.30	9.11	8.87	7.75	6.19	5.87
2-ethylbutan-1-ol	4.35	4.68	2.67	2.69	2.35	1.81	0.93
2-heptanol	3.42	1.35	1.00	0.67	0.14	0.00	0.00
1-octanol	3.00	4.37	1.67	2.15	1.52	0.91	0.46
2-ethylhexan-1-ol	2.07	2.70	0.78	0.81	0.55	0.30	0.00
4-nonanol	2.59	1.04	0.22	0.40	0.00	0.00	0.00
1-decanol	0.83	1.25	0.33	0.40	0.28	0.00	0.00
2-ethyloctan-1-ol	0.83	0.94	0.33	0.54	0.00	0.00	0.00
4-undecanol	1.04	0.31	0.11	0.00	0.00	0.00	0.00
1-dodecanol	0.62	0.73	0.11	0.13	0.00	0.00	0.00
2-ethyl-1-decanol	0.52	0.83	0.00	0.00	0.00	0.00	0.00

4-tridecanol	0.83	0.42	0.00	0.13	0.00	0.00	0.00
1-tetradecanol	0.10	0.21	0.00	0.00	0.00	0.00	0.00
2-ethyl-1-dodecanol	0.21	0.10	0.00	0.00	0.00	0.00	0.00
1-Pentadecanol	0.52	0.31	0.00	0.00	0.00	0.00	0.00
1-Heptadecanol	0.21	0.00	0.00	0.00	0.00	0.00	0.00
Esters							
methyl acetate	0.21	0.10	0.00	0.54	0.00	0.00	0.00
ethyl acetate	3.42	2.70	10.33	8.19	8.72	8.61	4.64
isopropyl acetate	0.00	0.10	0.00	0.13	0.00	0.00	0.00
ethyl butanoate	5.49	3.43	4.72	3.02	2.42	2.04	0.62
butyl acetate	3.21	2.29	3.78	1.48	1.66	0.91	1.55
butanoic acid, isopropyl ester	0.10	0.10	0.00	0.00	0.00	0.00	0.00
butyl butanoate	4.35	2.60	1.44	0.54	0.28	0.00	0.00
ethyl hexanoate	2.07	1.46	1.22	0.67	0.42	0.30	0.00
hexyl acetate	1.14	0.94	0.78	0.27	0.00	0.00	0.00
butyl hexanonate	3.73	2.70	0.00	0.27	0.00	0.00	0.00
hexyl butanoate	0.52	0.31	1.00	0.13	0.00	0.00	0.00
ethyl octanoate	0.00	0.00	0.00	0.13	0.00	0.00	0.00
octyl acetate	0.31	0.21	0.11	0.94	0.00	0.00	0.00
octyl butanoate	0.31	0.21	0.00	0.27	0.00	0.00	0.00
butyl octanoate	1.76	0.10	0.33	0.13	0.00	0.00	0.00
ethyl decanoate	0.00	1.46	0.00	0.00	0.00	0.00	0.00
decyl acetate	0.10	0.10	0.00	0.54	0.00	0.00	0.00
hexyl hexanoate	0.21	0.21	0.00	0.00	0.00	0.00	0.00
hexyl octanoate	1.04	1.35	0.11	0.40	0.00	0.00	0.00
ethyl dodecanoate	0.10	0.10	0.00	0.00	0.00	0.00	0.00
dodecyl acetate	0.10	0.10	0.00	0.00	0.00	0.00	0.00
Component	**Conversion (%)**						
	68.9	**66.5**	**44.2**	**19.1**	**14.5**	**12.3**	**3.1**
octyl octanoate	0.21	0.31	0.00	0.00	0.00	0.00	0.00
Ethers							
diethyl ether	0.31	0.73	0.11	0.54	0.55	0.00	1.85
3-ethoxy-1-butene	0.00	0.00	0.00	0.54	0.55	0.76	0.00

In **Tables 3.4** and **3.5,** we show the selectivity of each alcohol toward ethers and olefins in the etherification reactor. Note that the feed contains multiple reactants and that the numbers in the table represent the fraction of the carbon originally contained in the feedstock that is redirected toward each of the possible products.

Table 3.4. Carbon selectivity of different alcohols in the etherification reaction when a feedstock similar to the one produced by the Guerbet area with 12% conversion is used. A4: Butanol, A5: 2-pentanol, A6: 1-hexanol, A6-2: 2-ethylbutan-1-ol, A8: 1-octanol, A8-2: 2-ethylhexan-1-ol, E8: dibutyl ether, E10: butyl hexyl ether, E10-2: butyl ethyl butane ether, E12: hexyl ether, E12-4: butyl octyl ether, E14: hexyl octyl ether, O4: butenes, O5: pentenes, O6: hexenes, O8: octenes, UI: unidentified

Reactants	E8	E10	E10_2	E12_4	E12	E14
A4	80.68	5.73	0.42	0.04	0.00	0.00
A5	0.00	0.00	0.00	0.00	0.00	0.00
A6	0.00	76.09	0.00	0.00	1.15	8.64
A6-2	0.00	0.00	17.61	0.00	0.00	0.00
A8	0.00	0.00	0.00	5.46	0.00	82.15
A8-2	0.00	0.00	0.00	0.00	0.00	0.00
	O5	**O4**	**O6**	**O8_2**	**O8**	**UI**
A4	0.00	5.62	0.00	0.00	0.00	7.50
A5	100.00	0.00	0.00	0.00	0.00	0.00
A6	0.00	0.00	10.77	0.00	0.00	3.35
A6-2	0.00	0.00	83.39	0.00	0.00	0.00
A8	0.00	0.00	0.00	0.00	12.39	0.00
A8-2	0.00	0.00	0.00	100.00	100	0.00

Table 3.5. Carbon selectivity of different alcohols in the etherification reaction when a feedstock similar to the one produced by the Guerbet area with 66% conversion is used. A4: Butanol, A5: 2-pentanol, A6: 1-hexanol, A6-2: 2-ethylbutan-1-ol, A8: 1-octanol, A8-2: 2-ethylhexan-1-ol, E8: dibutyl ether, E10: butyl hexyl ether, E10-2: butyl ethyl butane ether, E12: hexyl ether, E12-2: butyl ethyl hexane ether, E12-3: hexyl ethyl butane ether, E12_4: butyl octyl ether, E14: hexyl octyl ether, E14_2: hexyl ethyl hexane ether, E14_3: octyl ethyl butane ether, E16: octyl ether, O4: Butenes, O5: pentenes, O6: hexenes, O7: heptenes, O8: octenes, UI: unidentified

Reactants	E8	E10	E10_2	E12	E12_2	E12_3	E12_4	E14	E14_2
A4	62.62	25.79	2.46	0.00	1.42	0.00	5.74	0.00	0.00
A5	0.00	0.00	0.00	0.00	0.00	0.00	0.00	0.00	0.00
A6	0.00	56.59	0.00	25.20	0.00	2.40	0.00	5.67	1.54
A6-2	0.00	0.00	19.99	0.00	0.00	8.88	0.00	0.00	0.00
A7	0.00	0.00	0.00	0.00	0.00	0.00	0.00	0.00	0.00
A8	0.00	0.00	0.00	0.00	0.00	0.00	44.89	20.19	0.00
A8-2	0.00	0.00	0.00	0.00	14.69	0.00	0.00	0.00	7.29

	E14_3	E16	O4	O5	O6	O7	O8	UI	
A4	0.00	0.00	0.49	0.00	0.00	0.00	0.00	1.48	
A5	0.00	0.00	0.00	33.85	0.00	0.00	0.00	66.15	
A6	0.00	0.00	0.00	0.00	8.61	0.00	0.00	0.00	
A6-2	2.86	0.00	0.00	0.00	14.91	0.00	0.00	53.36	
A7	0.00	0.00	0.00	0.00	0.00	90.12	0.00	9.88	
A8	2.76	11.46	0.00	0.00	0.00	0.00	20.70	0.00	
A8-2	0.00	0.00	0.00	0.00	0.00	0.00	29.32	48.71	

Modeling the olefin oligomerization reactions was challenging due to a lack of a kinetic model and/or experimental results for the oligomerization process. To alleviate these limitations, we have relied on an approximation that uses literature data for the oligomerization reactions. In this approach, we assume that each olefin only reacts with itself to form dimers, trimers, and tetramers. Selectivities are estimated considering data available for a HZSM-5 zeolite[84, 85] . This approximate treatment is justified because the stream that is oligomerized is small and represents only ~5% by mass of the total components that are used to produce fuels.

Table 3.6. Carbon selectivities for the oligomerization catalyst.

	Conversion	dimer	trimer	tetramer	pentamer	hexamer	References
1-Butene	95	30.0	22.0	20.0	13.0	15.0	Based on [84]
pentenes	50	90.0	10.0	0.0	0.0	0.0	Based on [85]
hexenes	50	90.0	10.0	0.0	0.0	0.0	Based on [85]
heptenes	50	90.0	10.0	0.0	0.0	0.0	Based on [85]
octenes	50	100.0	0.0	0.0	0.0	0.0	Based on [85]

3.3.9 Capital costs

Table 3.7. Installed costs of the different unit operations used in the Guerbet coupling area for different single-pass ethanol conversions. Costs are $MM.

	12%	15%	20%	44%	66%
Reactor	27.82	24.95	21.05	12.38	10.08
Compressor 1	1.99	1.99	1.96	1.84	1.78
Compressor 2	0.47	1.45	1.45	1.40	N/A
Pumps	0.57	0.53	0.48	0.41	0.39
Flash tank 1	0.49	0.48	0.41	0.25	0.21

Flash tank 2	0.10	0.09	0.09	0.09	N/A
Molecular sieves	2.01	2.28	2.35	2.12	1.27
Decanter	N/A	N/A	N/A	N/A	0.10
Column 1	7.65	6.60	5.69	7.05	5.48
Column 2	N/A	N/A	N/A	N/A	1.20
Column 3	1.63	1.77	2.17	2.12	0.97
Column 4	11.91	7.22	4.02	9.51	4.44
Column 5	33.26	26.77	17.57	10.72	8.62
Column 6	N/A	N/A	N/A	N/A	0.53
Column 7	N/A	N/A	N/A	N/A	0.73

Table 3.8. Capital costs of the different unit operations used in the etherification area.

	Cost (MM$)
Reactor	8.29
Pumps	0.19
Flash vessel	0.08
Column 1	5.23
Column 2	6.78
Column 3	5.14
Column 4	2.61
Column 5	1.27
Column 6	4.36
Column 7	1.98
Column 8	0.93
Column 9	1.97
Column 10	2.84
Column 11	6.71
Column 12	1.01
Column 13	11.07

Table 3.9. Capital costs of the different unit operations used in the oligomerization area.

	Cost (MM$)
Reactor	2.53
Pumps	0.46
Molecular sieves	0.11
Column 1	1.94

Table 3.10. Capital costs of the different unit operations used in the fractionation area.

	Cost (MM$)
Column 1	1.01
Column 2	0.70

3.3.10 Fuel property calculations

Models from the literature were used to calculate relevant physical properties of the fuel blends produced in this work. Density was calculated for each blend using a linear by volume mixing rule:

$$\rho_{blend}=\sum_{i=1}^{N} f_{V,i}\rho_i \qquad (1)$$

where $f_{V,i}$ is the volume fraction and ρ_i is the density of component i in the mixture. Experimental data for the density of each component was used where available. Where data was not available, density was calculated using the GCVOL group contribution method[86]. Liquid viscosity for each blend (v) was calculated using the UNIFAC-VISCO method[75].

$$\ln(MW\eta)=\sum x_i \ln(MW_i v_i)+\frac{\Delta^* G^E}{RT} \qquad (2)$$

In **equation 2**, MW is the molecular weight of the blend, x_i, MW_i and v_i are the mole fraction, molecular weight, and kinematic viscosity of component i in the mixture, and R and T are the universal gas constant and temperature, respectively. The excess molar free energy of activation for flow ($\Delta^* G^E$) is calculated using the UNIFAC-VISCO group contribution method. Details on the theory and required equations to calculate $\Delta^* G^E$ are provided elsewhere[86]. The interaction parameters used to calculate the excess Gibbs activation energy are taken from[75, 86]. Where experimental data on component viscosity was not available, it was supplemented using the Joback and Reid method[87]. The flash point of the mixtures was modeled using the mixing rule (**equation 3**) of Liaw et al.[88]

$$\sum \frac{x_i \gamma_i P_{S,i}(T_{FP})}{P_S(T_{FP,i})} = 1 \qquad (3)$$

where x_i is the mole fraction of component i, γ_i is its' activity coefficient, $P_{S,i}(T_{FP})$ is the saturation pressure of component i at the mixture flash point, and $P_S(T_{FP,i})$ is the saturation pressure of component i at its own flash point temperature. To solve this summation, activity coefficients are calculated using the UNIFAC group contribution method[89]. Flash point data for each component was used where available and supplemented with predicted flash points for individual components using the group contribution model of Carroll et al.[77]. Calculation of the component flash point requires knowledge of its' boiling point. Where data was not available, the method of Joback and Reid[88] was again used. Finally, saturation pressures for each component are calculated using the model of Nanoolal et al.[90].

The cloud point of the fuel blend is treated as the thermodynamic equilibrium boundary temperature between the one-phase (liquid) and two-phase (solid/liquid) region for the fuel mixture[78]. Assuming a single component is responsible for the cloud point of the blend and that the heat capacity difference between solid and liquid phases is small relative to the enthalpy of fusion for each component, an expression for the freeze point of component i ($T_{f,i}$) in a mixture can be derived:

$$\frac{1}{T_{f,i}} = \frac{1}{T_{m,i}} - \frac{R \ln\left(x_i^L \gamma_i^L\right)}{\Delta H_{fus,i}\left(T_{m,i}\right)} \qquad (4)$$

where $T_{m,i}$ is the melting point, R is the universal gas constant, x_i^L is the mole fraction, γ_i^L is the activity coefficient, and $\Delta H_{fus,i}(T_{m,i})$ is the enthalpy of fusion for the liquid component in the mixture. **Equation 4** is solved to determine the freeze point of each component in the bioblendstock. The cloud point temperature of the bioblendstock is then considered to be the highest predicted freeze point[91, 92]. The enthalpy of fusion is estimated for each component using the Joback and Reid method[88]. Experimental data is used for the melting point of each component where available, with the Joback and Reid method again used to supplement for cases where data is not available. Activity coefficients are calculated using the UNIFAC method[89].

Similarly to the cloud point, the distillation curve for each blend was calculated as a thermodynamic equilibrium between the liquid and gas phase[79]. The gas phase is treated as ideal, whereas the liquid is again treated non-ideally and characterized by an activity coefficient determined from UNIFAC. Component vapor pressures are calculated using the groups contribution model of Nannoolal et al[90]. A set of N differential equations (N is the number of components in the blend) are integrated to determine the liquid mole fractions of each component during the distillation using the Rayleigh equation[93]. The determined mole fractions are then used to solve for mixture temperature. Liquid mole fractions are translated into distillate volume assuming ideal mixing behavior.

Finally, the derived cetane number (DCN) was estimated using a simple autoignition model that incorporates group contribution methods to calculate global initiation and chain branching rate constants for each component in the blend[80]. The model was recently developed to provide accurate DCN estimates for oxygenated components and blends with wide ranges of individual cetane numbers, where typical linear by volume mixing rules are no longer sufficient.

The cetane number correlation used in this work is based on data acquired in an ignition quality tester (IQT). The IQT injects fuel into a constant volume chamber and measures the ignition delay in a relatively constant temperature and pressure environment. The measured ignition delay is related to cetane number through an empirical correlation given in the ASTM D6890 standard and is referred to as the derived cetane number (DCN). In this work, a correlation was used to predict the ignition delay of blends based on a four-step autoignition model.

$$\tau_{\mathrm{mix}}=\frac{1}{\sum x_{f,i}k_{\alpha_{p},i}}\ln\left(1+\frac{\sum x_{f,i}k_{\alpha_{p},i}}{\sum x_{f,i}\frac{k_{1p,i}}{x_{c,crit}}}\right)+\tau_{\mathrm{inj}} \qquad (5)$$

In **equation 5**, $x_{f,i}$ is the mole fraction of component i in the fuel mixture only (i.e., $\sum_{i\neq air} x_{f,i} = 1$). The total initiation rate and net branching coefficient of each component was parameterized assuming they could be written as a sum of contributions from their functional groups (**Equations 6** and **7**).

$$\frac{k_{1p,i}}{x_{c,crit}} = k_{1_0} + \sum k_{1_{f,j}} N_{f,j} \qquad (6)$$

$$k_{\alpha_{p},i}=k_{\alpha_0}+\sum k_{\alpha_{f,j}} N_{f,j} \qquad (7)$$

$N_{f,j}$ is the number of functional groups of type j in the compound, and $k_{1_{f,j}}$ and $k_{\alpha_{f,j}}$ are the contributions of function group j to the initiation and chain branching process, respectively. Table 1 specifies all functional groups considered in the model and their respective coefficient values. $k_{\alpha_{p},i}$ was constrained such that if it made the argument inside the natural log of the ignition delay expression negative after being calculated, it was set to 1E-10 [ms^{-1}] to prevent imaginary numbers from appearing in the results.

The standard ASTM D6890 correlation given by **equation 8** was used to transform all ignition delay data in this work.

$$\mathrm{DCN}=4.46+\frac{186.6}{\tau_{\mathrm{mix}}} \qquad (8)$$

Table 3.11. Group contributions for initiation and chain branching determined from optimization procedure.

Nomenclature	**Description**	$k_{1_{f,j}}$ [1/ms]	$k_{\alpha_{f,j}}$ [1/ms]
$N_{f,\,CH}$	No. CH groups	-2.244E-4	0.2487
$N_{f,\,CH2}$	No. CH_2 groups	-4.221E-4	0.3099
$N_{f,\,CH3}$	No. CH_3 groups	-1.453E-4	-0.0404
$N_{f,\,QC}$	No. quaternary carbons	0.0243	-0.2737
$N_{f,\,OH}$	No. alcohol groups	0.0131	-1.3357
$N_{f,\,O=CH}$	No. aldehyde groups	0.0628	-0.0698
$N_{f,\,-O-}$	No. ether groups	0.0339	0.2854
$N_{f,\,CH2ring}$	No. CH_2 ring groups	2.917E-4	0.0526
$N_{f,\,CHring}$	No. CH ring groups	-0.0022	0.2991
$N_{f,\,C=C}$	No. carbon-carbon double bonds	-0.0012	-0.2285
$N_{f,\,C=O}$	No. ketone groups	-0.003	-0.0928
$N_{f,\,COO}$	No. ester groups	0.0012	-0.8434
$N_{f\,,AR}$	No. aromatic rings	0.0107	-0.7666
k_{1_0}, k_{α_0}	Constant values	0.0073	-0.0557
τ_{inj}	Constant physical injector delay (0.3206 ms)	-	-

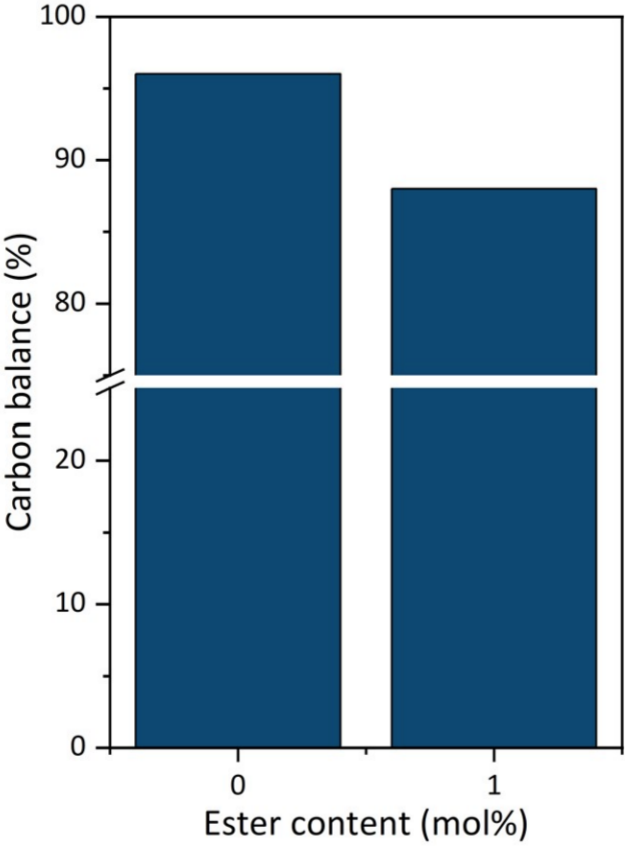

Figure 3.4. Carbon balance in the presence and absence of esters for the G – 12 feedstock.

Table 3.12. Detailed composition of the feed stream for the etherification area.

	G-12	**G-66**
Ethanol	0.19	0.00
N-Butanol	91.01	62.88
2-Pentanol	0.16	1.74
1-Hexanol	5.49	13.29
2-ethyl-butanol	1.61	4.67
2-heptanol	0.00	1.16
octanol	0.60	3.27
2-ethyl-hexanol	0.20	2.02
2-heptanol	0.00	0.69
1-octanol	0.00	1.31
2-ethyl-hexanol	0.00	0.17
4-nonanol	0.00	0.36
1-decanol	0.00	0.42
4-tridecanol	0.00	0.19
1-tetradecanol	0.00	0.09
4,10-dimethyl-1 dodecanol	0.00	0.04
1-pentadecanol	0.00	0.12
Ethyl-butyrate	0.37	0.00
N-butyl acetate	0.14	0.00
Isopropyl-butyrate	0.00	0.09
N-butyl-N-butyrate	0.00	1.95
Ethyl-caproate	0.20	1.09
N-hexyl-acetate	0.00	0.70
Butyl-caproate	0.00	1.62
Hexyl-butyrate	0.00	0.19
N-octyl-acetate	0.00	0.12
N-octyl-butyrate	0.00	0.10
Butyl-caprylate	0.00	0.05
Ethyl-caprate	0.00	0.73
Decyl-acetate	0.00	0.05
Hexyl-hexanoate	0.00	0.10
Hexyl-caprylate	0.00	0.58
Ethyl-laurate	0.00	0.04
Dodecyl-acetate	0.00	0.04
1-octanol-octanoate	0.00	0.12
Ethyl-butyl-ether	0.02	0.00

3.4 Results

3.4.1 Guerbet Coupling - Experimental Results

The product selectivity in the Guerbet coupling reaction as a function of ethanol conversion is shown in **Figure 3.5**. This data is partly based on experiments reported by Cuello-Penaloza et al.[50] At low conversion (e.g., 3% and 12%) low molecular weight alcohols (C1–C4) are the most abundant products. As the conversion increases so does the fraction of higher alcohols (C6+) and esters (see section 3.3.8 for a detailed product composition). The increase in higher alcohols (C6+) is important in the context of diesel production by etherification. We note that the production of esters, secondary alcohols, and branched alcohols can be regarded as undesirable. Esters cause undesired reactions during etherification (see etherification section), while branched and secondary alcohols are more prone to form olefins instead of ethers.[34] Since the production of esters and secondary alcohols increases with conversion, and the ratio of linear to branched alcohols diminishes (**Figure 3.5**), then a trade-off appears. Higher conversions are desired because they lead to the production of larger alcohols, require equipment with lower size, and usually consume less energy in pumping and separations because the streams associated are smaller. However, at these higher conversions more undesirable products are obtained.

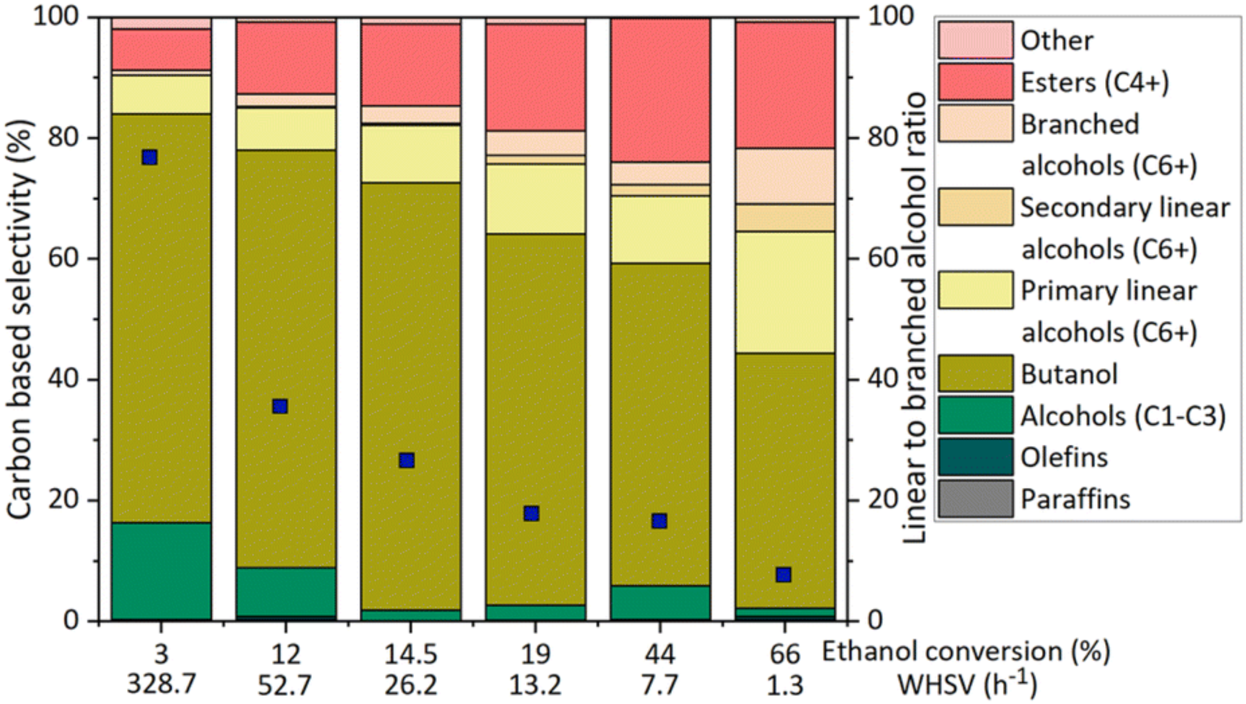

Figure 3.5. Product distribution as a function of ethanol conversion in a Guerbet coupling reaction performed using Cu/Mg_xALO_y as catalyst. The linear to branched alcohol ratio is indicated by a blue square (defined as the ratio of the carbon selectivities of linear to branched alcohols). In the reaction, aldehydes and ketones are also produced, these species are accounted for by lumping them with their respective alcohols since they can be easily hydrogenated to form their parent alcohols, for example using a dual bed catalyst. The data is based on the report by Cuello-Penaloza et al.[50]

3.4.2 Guerbet Coupling – Process Modelling

Using the experimental results obtained for Guerbet coupling, we synthesize process layouts for conversions between 12–66% (**Figure 3.6**). The 3% conversion is too low to be economically relevant so was not used in this analysis. We study how conversion affects: (1) the process configuration; (2) the composition of the stream fed to the etherification reactor (note that this is different from the results discussed in Figure **3.5** because the effect of separation operations in now considered); and (3) the capital and operating costs of the Guerbet coupling area.

The process configuration is shown in **Figure 3.6**. The Guerbet reactor is followed by a flash tank that allows recycling of the carrier gas. Once the carrier gas is removed, a distillation column (column 1) is used to recover unconverted ethanol as the top product, while keeping an anhydrous blend of higher alcohols (C4+) as the bottom product. For low to moderate conversion (12–44%), all the butanol produced remains in the bottom product of distillation column 1. At high conversion, a fraction of the butanol is obtained in the top product, thus for high conversion (66%), 1-butanol heteroazeotropic distillation is required to separate ethanol, butanol and water before recycling. These results are consistent with the results of Nezam and coworkers.[41] A molecular sieving unit is used to remove the remaining water from the recycle stream. Finally, two distillation columns (columns 4 and 5) are used to remove esters and olefin byproducts. At low conversion, column 4 operates under vacuum and a compressor is required, this compressor is followed by a flash tank to remove low molecular weight olefins and paraffins.

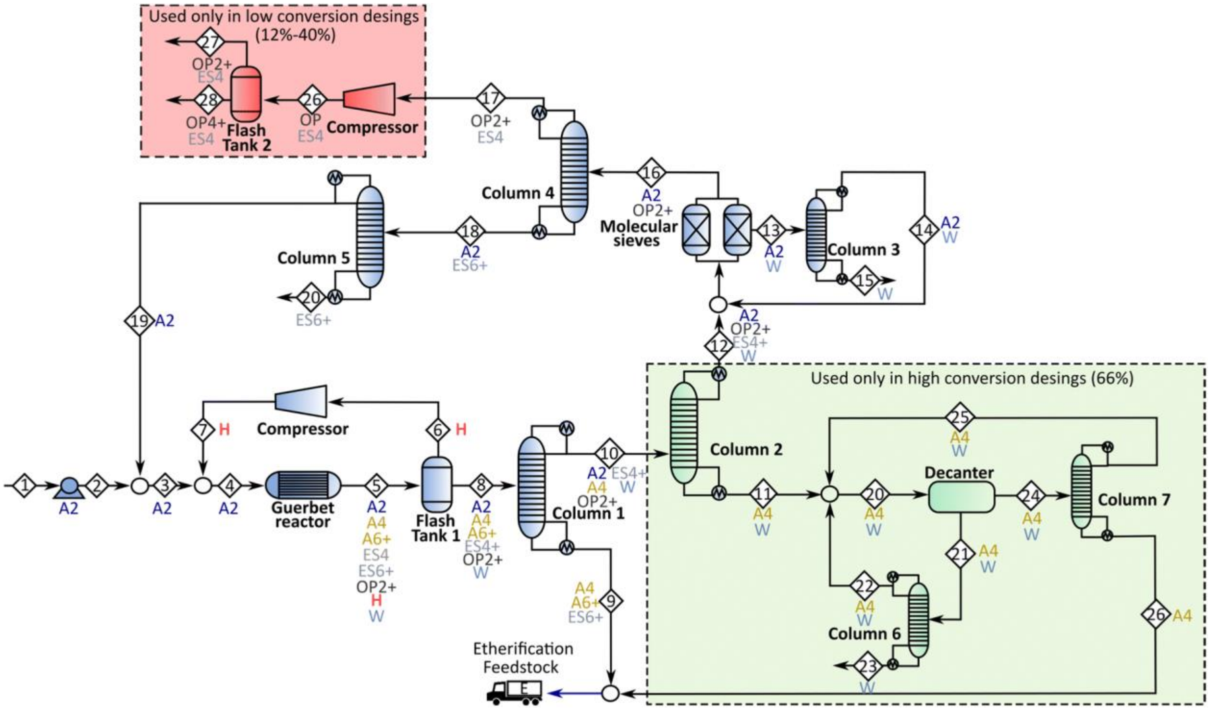

Figure 3.6. Layout for the Guerbet coupling area. Operations inside the green square (heteroazeotropic distillation of 1-butanol) are used only at high conversion (66%), while those in red are only used at low conversions (12–40%). Chemical species are labeled such that A: alcohols, ES: esters, OP: olefins/paraffins, H: hydrogen, and W: water, the numerical characters indicate the carbon length. The blue stream is the one containing all the higher alcohols which serve as the feed to the etherification area.

In **Figure 3.7**, we show the annual operating costs (**Figure 3.7a)** capital costs (**Figure 3.7b**), and composition of the stream used for etherification (**Figure 3.7c**) as a function of conversion. As expected, both capital and operating costs are significantly reduced when the conversion increases; e.g., when conversion increases from 12% to 66% capital costs are reduced by ~50%, and operating costs by ~10%. For capital costs, separations play the most prominent role. For operating costs, feedstock is the most important factor; although utilities are also significant. When conversion increases from 12% to 66% the cost of utilities is reduced ~7 times (from ~20MM$ per year to ~3MM$ per year). This result is important for sustainability because lower utility consumption leads to lower environmental impact. The composition of the stream fed to the etherification area is also significantly affected by conversion (**Figure 3.7c** and **Table 3.12**). At low conversion, this stream contains mainly 1-butanol with a small fraction of C6+ alcohols and an almost negligible amount of esters. While at high conversion, a larger fraction of C6+ alcohols and esters are present. For reference, 1-butanol composition drops from ~90% to ~60% when the conversion increases from 12% to 66%. In parallel, higher alcohol content in the etherification feed stream increases from ~8% to ~30%, with a concurrent increase in esters from 0.7% to 7.5%. We note that low molecular weight olefins, C1–C3 alcohols, water, and a significant fraction of C4–C6 esters have been removed from the reactor outlet stream by means of separation operations in the Guerbet area.

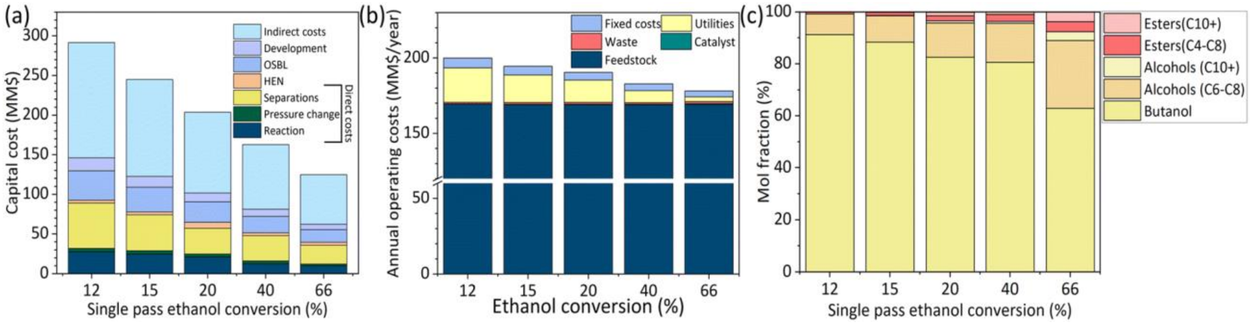

Figure 3.7. (a) Capital costs (b) annualized operating costs (c) and composition of the etherification feed stream as a function of conversion for the Guerbet coupling area. Details on the capital costs and operating conditions can be found in section 3.3.9.

4.3.3 Etherification - Experimental results

Since the alcohols used in etherification are those produced in the Guerbet area, we prepare two representative feed streams resembling the composition obtained at low (12%) and high (66%) single-pass ethanol conversion in the Guerbet area (see **Figure 3.7c**), we refer to these feeds as G-12% and G-66%, respectively. First, we are interested in establishing if the presence of esters in the reaction feed affects product selectivity. To address this question, we use the G-12% feedstock which is simpler. We perform etherification of this feedstock under two conditions: (1) we assume that the G-12 stream contains a mol fraction of esters of ~1% (ethyl butanoate 15%, butyl acetate 63%, and ethyl hexanoate 22%) and (2) we assume that no esters are present in the reaction. We observe that the carbon balance of the reaction drops from 96% to less than 90% when esters are present in the reaction feed stream (see **Figure 3.4**), indicating that esters may lead to the formation of undesirable products. This result points toward the need to remove as much of the esters as is economically possible from the etherification reactor feed.

Second, we are interested in understanding how the composition of the etherification reactor feed affects the product distribution. Considering that esters may affect the carbon balance, we perform these experiments in their absence. Both the feed and product composition of the etherification reaction are shown in **Figure 3.8a**. For the G-12% feed, which is richer in 1-butanol, the main product is di-n-butyl ether, with minor quantities of larger ethers (C10+), and low molecular weight olefins. On the other hand, for the G-66% feed, a larger fraction of ethers with more than 10 carbons is formed; however, more olefin by-products are obtained as well. In the etherification reaction, multiple alcohols are present in the feed. Each of these alcohols participates in different reactions. Consequently, the original carbon contained in each alcohol is distributed among the products that result from the reactions in which the alcohol is involved. In **Figure 3.8b**, we show how the carbon contained in each alcohol is distributed among four types of products: di-n-butyl ether, ethers with more than 10 carbons, olefins, and what is labelled as unassigned carbon (UA), where we group products that were detected by the analytical techniques used but whose identity is unknown. In general, β-branched and secondary alcohols lead mainly to the formation of olefins. In contrast, linear primary alcohols lead predominantly to the production of ethers. We note that the fraction of carbon used for the production of unidentified species is large for some alcohols (e.g., A5), however the alcohols for which this is the case are present in the feed at low concentration, such that the overall fraction of unidentified species is only ∼5%.

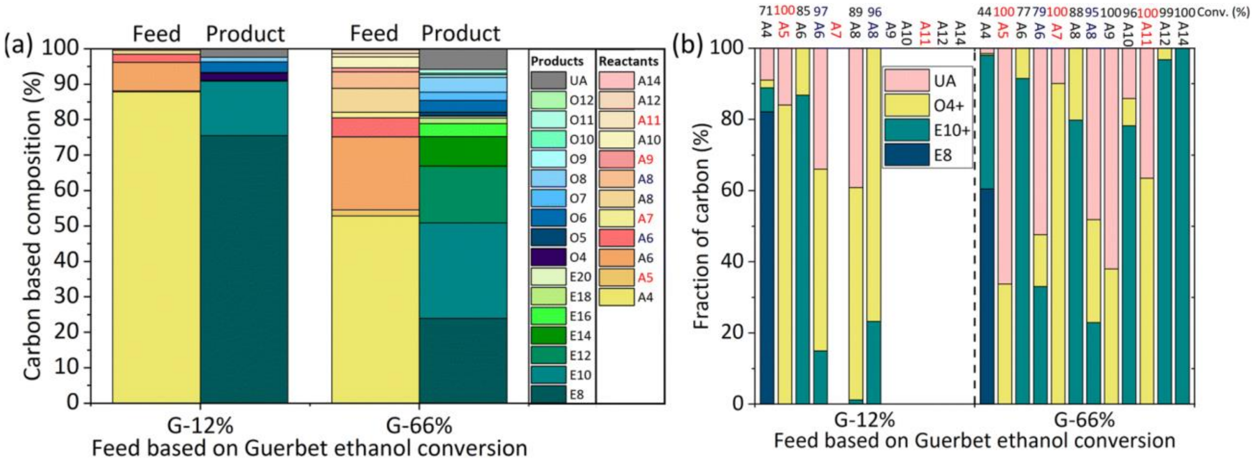

Figure 3.8. Experimental results obtained for different etherification reaction conditions (a) feed and product composition in the etherification reaction when G-12% and G-66% feeds are used (b) carbon selectivity for each alcohol in the feed for the G-12% and G-66% reactor feeds. The conversion as a % of carbon is shown above for each alcohol. Chemical species in the figure are labelled using the following convention: a letter indicates the functional group (A: alcohols, O: olefins, E: ethers, UA: unidentified components), and a numerical character the carbon length. Additionally, for alcohols we use a color code, such that linear alcohols are shown in black, secondary alcohols in red, and branched alcohols in blue.

3.4.4 Etherification - process modelling

Di-n-butyl ether is the primary product obtained when a G-12% feedstock is used in etherification (**Figure 3.8b**). In contrast, when a G-66% feedstock is used, a smaller fraction of di-n-butyl ether is produced with a concomitant increase of ethers with more than 10 carbons. Considering that di-n-butyl ether has a flash point significantly lower than diesel #2 (~25 °C vs. 52 °C), we use the G-66% feedstock for the rest of this work. Consequently, we synthesize an etherification area to process this feedstock (**Figure 3.9**). At a high level, the unit operations in this area can be divided into a preconditioning sub-area and a reaction/separation sub-area. In the preconditioning sub-area, the ester content of the feed stream to the etherification reactor is reduced to less than 0.3% (mol mol^{-1}). The reaction/separation area consists of a reactor, and a sequence of unit operations that enable recycling unconverted alcohols while simultaneously obtaining relatively pure ether streams that will be used in the final diesel blend. We have made the design decision to not feed alcohols with ten or more carbons to the etherification reactor (see distillation column 3). These alcohols are large enough to have physiochemical properties compatible with diesel so that they can be blended directly into diesel fuel. They are also in small enough quantities to not cause concerns with the melting point of the fuel blend. Removing them in the preconditioning sub-area before etherification allows us to reduce the ester content of the etherification reactor feed to less than 0.3% (mol mol^{-1}).

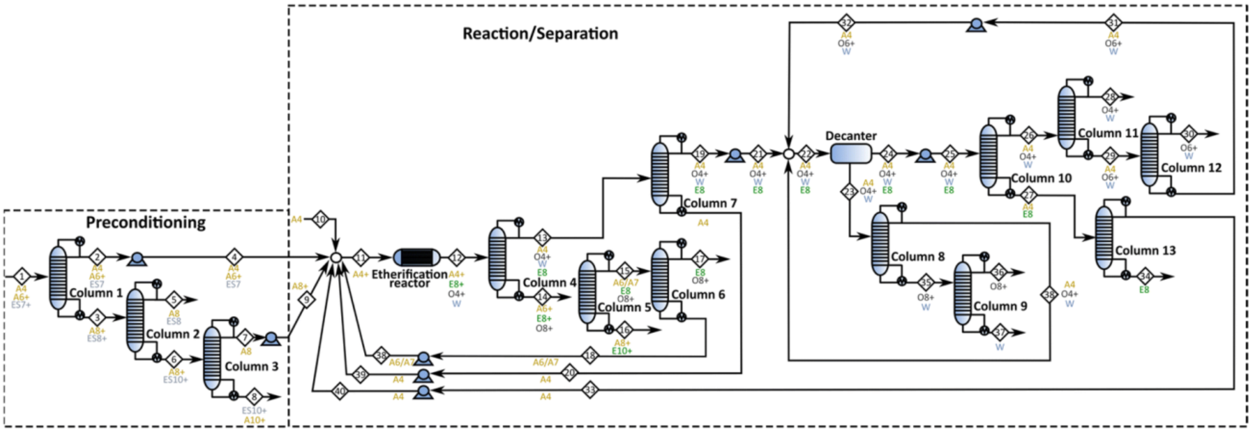

Figure 3.9. Layout for the etherification area. Chemical species in the figure are labelled using the following convention: a letter indicates the functional group (A: alcohols, O: olefins, E: ethers, UA: unidentified components), and a numerical character the carbon length.

3.4.5 Process modelling and fuel characterization

Using the results obtained from both Guerbet coupling and etherification, we synthesize a biorefinery for the upgrading of ethanol into diesel following the approach shown in **Figure 3.2**. For this design we use the experimental data (**Figure 3.5** and **3.8**) for G-66% from the Guerbet step and etherification steps. A Sankey diagram showing the mass flows within the biorefinery is presented in **Figure 3.10a**. A total fuel yield of ~65 wt% is obtained. This fuel is fractionated into three main products: diesel #2 (52.6%), diesel #1 (41.0%), and gasoline (6.4%). The composition of these fuel fractions is shown in **Figure 3.10b**. In the case of diesel, the product is dominated by ethers, but the presence of other molecules (esters, alcohols, and olefins) produced by the catalytic reactions used is also significant. We note that the diesel #2 blend is richer in ethers with more than 10 carbons, while the diesel #1 blend is constituted mainly of di-n-butyl ether (~75%). The gasoline fraction on the other hand, consists of low molecular weight components obtained in the Guerbet and etherification areas (methanol, ethanol, esters, and olefins). We estimate the properties of these fuels and compare them with respect to the ASTM standard[64, 65] (**Figure 3.11**). For diesel #2, all properties are close to those of a typical fossil diesel, with a cetane number significantly higher than the minimum required (73 vs. 40).[64]

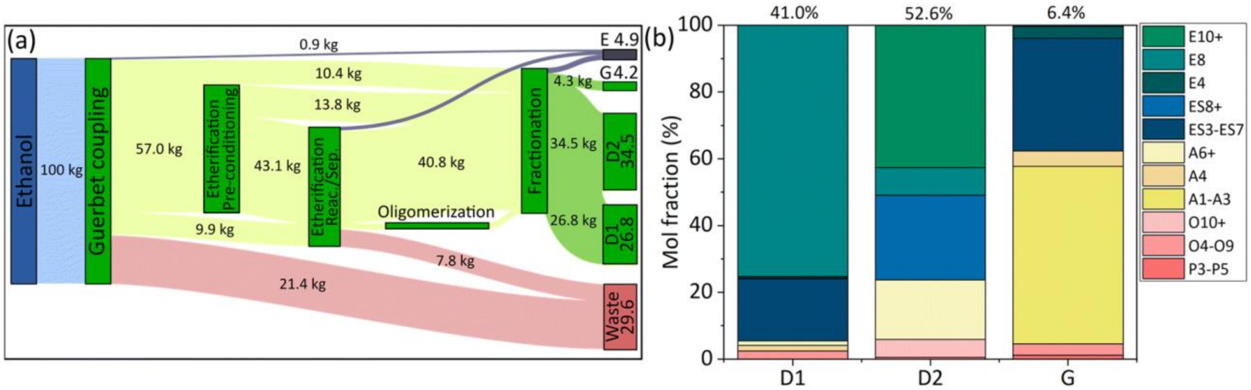

Figure 3.10. (a) Sankey diagram with the mass flows within the biorefinery. Yellow arrows represent material flows of fuel precursor elements, red arrows waste streams, blue arrows by-products used in electricity production, and green arrows fuel streams (D1: diesel #1, D2: diesel #2, and G: gasoline). (b) Composition of the fuels produced. Chemical species in the figure are labelled using the following convention: a letter indicates the functional group (A: alcohols, E: ethers, ES: esters, O: olefins, and P: paraffins), and a numerical character the carbon length.

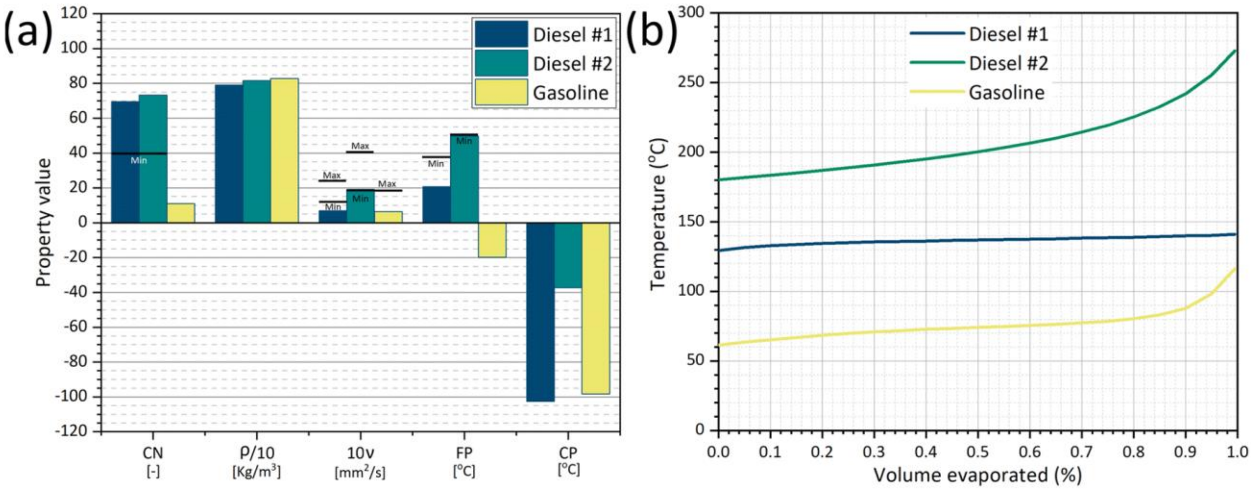

Figure 3.11. (a) Properties of the different fuels produced. CN: cetane number, D: density, V: viscosity, FP: flash point, CP: cloud point. The ASTM requirements for the properties that are constrained are indicated by horizontal black lines (b) distillation curve of the fuels produced.

This result is promising and suggests that the proposed catalytic approach can lead to the production of biofuels with superior properties. Both the density and viscosity of diesel #2 fall within the expected range, and the flash point is only slightly under the standard (50 °C vs. 52 °C). This result is not limiting considering that the initial boiling point of the produced diesel #2 (closely related to the flash point) can be increased, if needed. For example, the distillation conditions can be modified to increase the initial boiling point with only a minor impact on fuel yield. The cold flow properties of diesel #2 are outstanding, with a cloud point of ∼−37 °C, such that it could be used as a winter fuel. The diesel #1 obtained presents a lower flash point (∼21 °C vs. 38 °C) and viscosity (∼0.7 $mm^2\ s^{-1}$vs. 1.3 $mm^2\ s^{-1}$) than the ones required in the ASTM standard.[64] This implies that the produced diesel #1 can only be used in blends and not as a drop-in biofuel. Finally, the gasoline fraction satisfies the viscosity requirement,[65] and has an estimated RON value (based on the cetane number) of ∼99. The distillation curve of the produced fuels is shown in **Figure 3.11b**. In all cases, the fuels boil in the expected range. However, for diesel #2, we have a T90 that is lower than the ASTM requirement (241 °C vs. 288 °C for diesel #2). The fact that our diesel #2 has a lower T90 may impact the fraction that can be blended with a fossil diesel. However, from an operational standpoint there is good evidence that having a lower T90 does not impact engine operation and may actually be beneficial considering that the diesel #2 produced satisfied the flash point requirements.[94] We note that for diesel #1, the curve is very flat which is explained by the fact that this fraction is mainly constituted of di-n-butyl ether. The properties of the fuels produced are similar to those of fossil diesel; therefore, they are suitable to be used in heavy duty transportation applications such as trucks and ships.

3.4.6 Economics

The installed capital costs associated with the different biorefinery areas are shown in **Figure 3.12a**. The Guerbet and etherification areas have the higher capital costs, and within them, the capital cost of separation units is dominant. It is noteworthy that the HEN also has a significantly high capital cost. The total capital investment is estimated at ~353$MM. The annualized capital and operating costs are shown in In **Figure 3.12a**. Operating costs are dominant, with the cost of feedstock been the most important component. We assume that the ethanol upgrading plant is installed as an extension of a lignocellulosic ethanol production plant that operates as described in the most recent NREL report.[67] Under this assumption, the energy by-products obtained in the ethanol production plant can be used to satisfy the energy needs of ethanol upgrading. The economic analysis reflects this assumption.

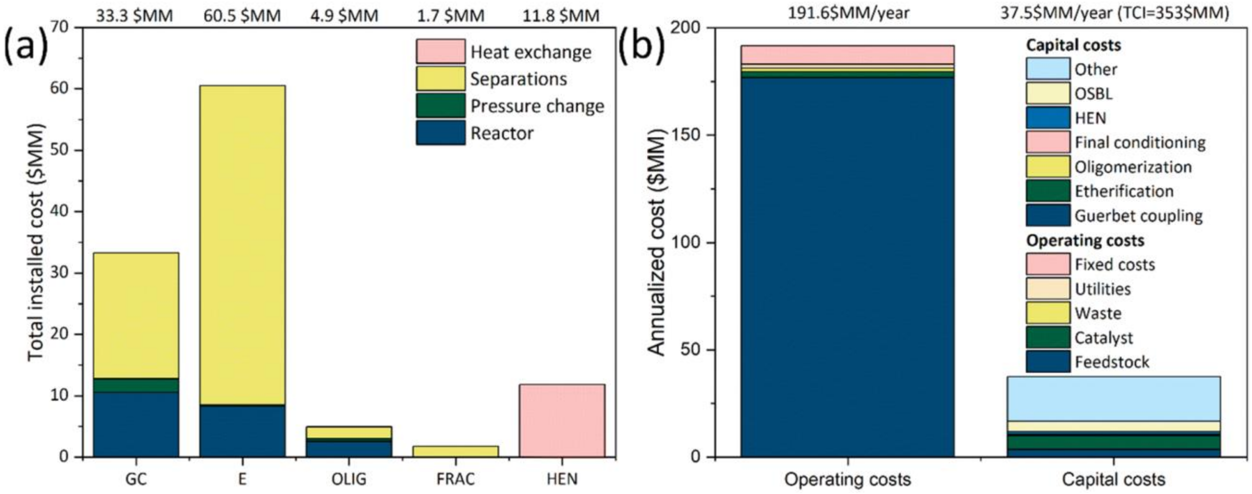

Figure 3.12. (a) Installed capital costs of the different areas in the biorefinery (b) annualized capital and operating costs. GC: Guerbet coupling, E: etherification, OLIG: oligomerization, FRAC: fractionation, HEN: heat exchanger network, OSBL: outside battery limits.

Figure 3.13a shows the breakdown of the minimum selling price which was calculated to be equal to 5.89$US per Gal (7.68$ per GDE). We used an ethanol price of 2.98$ per Gal, which is the MFSP estimated for ethanol from corn stover when all by-products in ethanol production are used within the process and no credits for electricity sales are obtained.[67] Alternatively, if we use an ethanol price of 1.75$ per Gal (the average corn grain ethanol price in the last 10 years)[95] we obtain a MFSP of 4.06$US per Gal (5.29$ per GDE). The sensitivity of the MFSP to different parameters is shown in **Figure 3.13b**, where the parameters are grouped into three categories: parameters related to capital costs, parameters related to operating costs, and financial parameters. The plot shows the percentual change in the MFSP (x-axis) when the parameters in the y-axis change between the limits shown at the left and right side of each bar (e.g., when the price of ethanol is 1$US per Gal, the MFSP is reduced by ~40%). The range selected for each parameter reflects plausible possible improvements in the design, or the possibility of having overoptimistic assumptions in our analysis. For comparison, the estimated production cost of traditional biodiesel obtained by the transesterification of fatty acids has ranged between 3.92–6.00$ per

GDE.[96] Additionally, since traditional biodiesel is mostly produced from vegetable oils it has the disadvantage of directly competing with food. Other technologies to produce biodiesel, like fast pyrolysis, show the potential to have lower production costs (~3.03–4.54$ per GDE) while eliminating the competition with food. However, in these cases the properties of the fuels produced cannot be precisely tailored like in the ethanol to diesel approach described here.

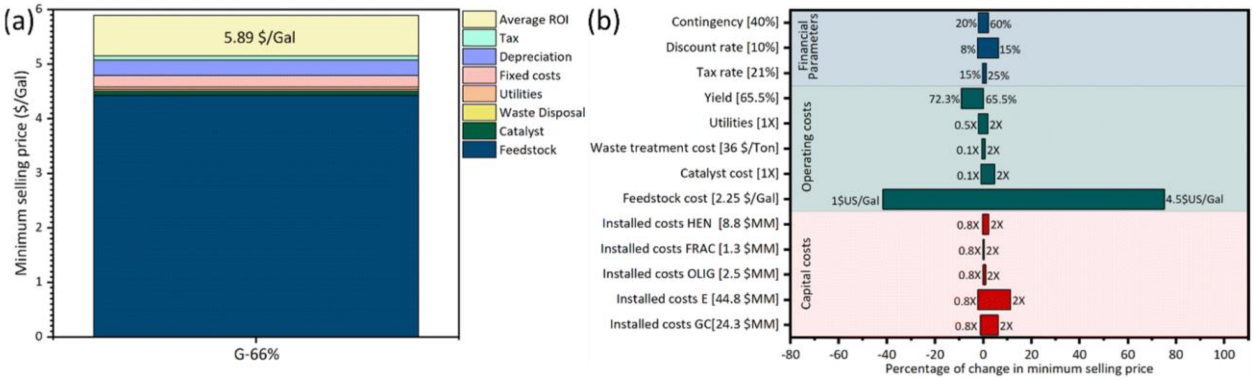

Figure 3.13. a) Breakdown of the MFSP (b) tornado plot showing the sensitivity of the MFSP to changes in different parameters of interests (y-axis). The value within the bracket on the y-axis represents the value of the parameter in the reference case. GC: Guerbet coupling, E: etherification, OLIG: oligomerization, FRAC: fractionation, HEN: heat exchanger network.

The sensitivity analysis reveals that the capital costs of the Guerbet and etherification areas are the most important parameters related to capital costs. The cost of feedstock and the fuel yield are the most important parameters related to operating costs. Finally, the most important financial parameter is the discount rate. These results point toward two research directions. First, designing more less capital-intensive separation trains may be important especially in the Guerbet and etherification areas. Second, designing more selective catalysts leading to the formation of smaller amounts of by-products may improve the fuel yield. Finally, since the MFSP is heavily dependent on the ethanol cost, finding strategies to produce cheaper ethanol (e.g. by using high value low volume co-products[97]), will have a direct impact on the MFSP of diesel.

3.4.7 Energy analysis

A Sankey diagram with the energy flows within the biorefinery is shown in **Figure 3.14a**. These energy flows have been normalized to those required to process 100 MJ of ethanol. Efficiency factors have been used to ensure that these flows represent energy of the same "quality". Boiler efficiency is assumed to be 80%. Additionally, an overall energy balance in the ethanol production plant is used to determine the LHV of the biomass used to produce excess electricity.[67] The figure reflects the utilization of excess energy generated in ethanol manufacture and upgrading to satisfy the refinery energy needs. The biorefinery area that consumes the largest amount of energy is Guerbet coupling (25.1 MJ), followed by etherification (21.8 MJ). The energy consumption in these areas could be reduced if a simpler separation train is developed. Considering that the main group of by-products consists of esters, which need to be removed before etherification, it would be important to develop either catalysts or processes leading to a reduction of these components. For example, if no significant amounts of esters are produced, then the whole pre-conditioning sub-area could be avoided, saving approximately 5.8 MJ of energy.

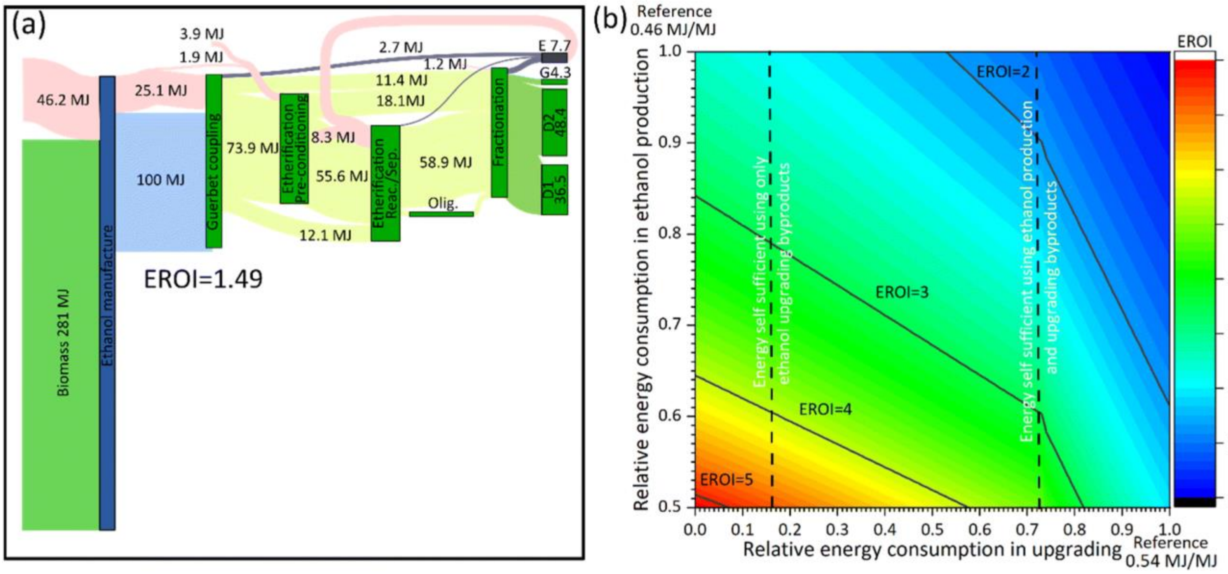

Figure 3.14. Energy analysis of the ethanol upgrading biorefinery (a) Sankey diagram showing energy flows (LHV) within the biorefinery (b) sensitivity analysis showing the EROI value as a function of the energy consumed in ethanol production (y-axis), and ethanol upgrading (x-axis), values are presented as relative values with respect to the reference. The vertical dashed line represents the reduction in energy consumption in ethanol upgrading that is required to obtain a self-sufficient refinery (i.e., a biorefinery in which the energy contained in the byproducts is sufficient to satisfy all energy needs). The energy flows in the figure correspond to those observed when 100 MJ of ethanol are processed.

We emphasize that improvements in the upgrading energy consumption are contingent on the development of better catalyst, and simpler separation trains. On the other hand, reducing energy in ethanol production is possible if improvements in biomass productivity, and biomass preprocessing (drying, chopping, etc.) are achieved,[98] or if the sustainable manufacturing of fertilizers is developed.[99] For example, increasing biomass yield by a factor of three in comparison with current practices may lead to reductions in energy consumption of ~15%. Likewise, reducing the energy in preprocessing depot facilities (from 750 MJ Mg^{-1} to 500 MJ Mg^{-1}) while increasing the densification factor (above 6) may lead also to ~15% less energy consumption.[98] Another avenue consists in reducing the energy expended in separations.

The estimated energy return on investment (EROI) of the biorefinery is ∼1.49. The EROI is defined as the ratio between the energy produced by a process and the energy required to produce/extract that energy.[100] Since the EROI > 1, we have a net energy gain. However, the EROI value is low, considering that typical fossil fuels have an EROI ∼20, and that a value close to 3 has been suggested as a minimum for a fuel in a sustainable society.[100, 101] To understand the effect that technological improvements may have on the EROI we perform a sensitivity analysis (**Figure 3.14b**). We analyze two factors: the cumulative energy consumed during the upgrading process (x-axis), and the cumulative energy used in the production of the ethanol feedstock used (y-axis). Improving either of them will have a significant impact on the biorefinery's EROI. For reference, if no improvement in ethanol manufacture is achieved but the energy consumed during ethanol upgrading is reduced by ∼50%, the EROI increases to ∼2. The same improvement can be obtained if no improvement in ethanol upgrading is achieved but the energy used in ethanol production is reduced by ∼40%. A reduction in energy consumption in upgrading by 50% accompanied by a 30% reduction in the energy consumed in ethanol production lead to an EROI of ∼3. We emphasize that improvements in the upgrading energy consumption are contingent on the development of better catalyst, and simpler separation trains. On the other hand, reducing energy in ethanol production is possible if improvements in biomass productivity, and biomass preprocessing (drying, chopping, etc.) are achieved,[98] or if the sustainable manufacturing of fertilizers is developed.[99] For example, increasing biomass yield by a factor of three in comparison with current practices may lead to reductions in energy consumption of ∼15%. Likewise, reducing the energy in pre-processing depot facilities (from 750 MJ Mg^{-1} to 500 MJ Mg^{-1}) while increasing the densification factor (above 6) may lead also to ∼15% less energy consumption.[98] Another avenue consists in reducing the energy expended in separations.

3.4.8 Environmental analysis

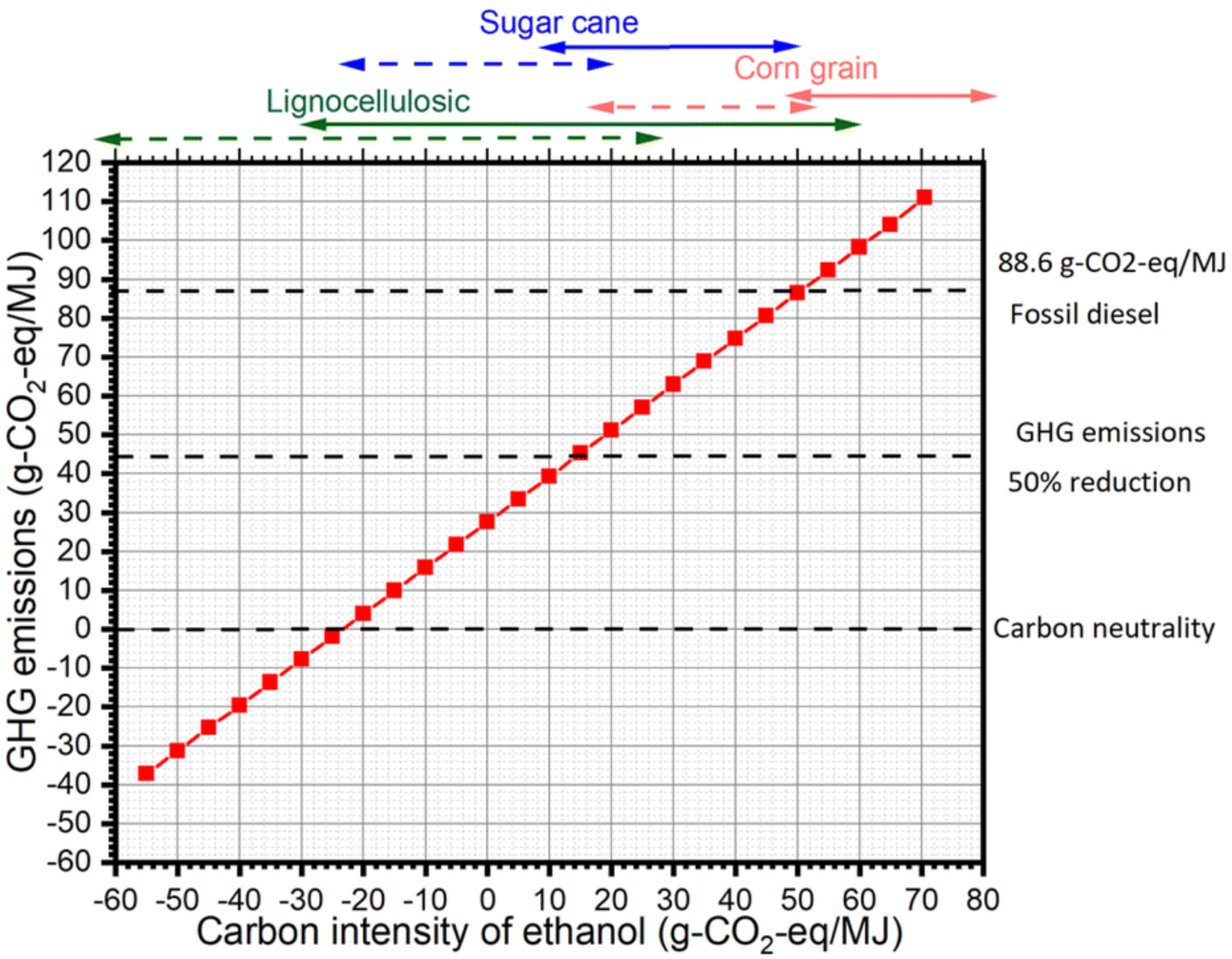

Figure 3.15. Greenhouse gas emissions as a function of ethanol carbon intensity (g CO_2-eq per MJ ethanol). Typical ranges for ethanol produced from lignocellulosic residues, sugar cane, and corn grain are shown on top of the figure. Dashed lines correspond to the range of carbon intensities that could be obtained if CO_2 capture at the fermentation outlet is implemented.

In **Figure 3.15**, we analyze the GHG emissions per MJ of energy contained in the fuel as a function of the carbon intensity of the ethanol used as feedstock. We assume that energy by-products obtained in the upgrading process are used to satisfy the refinery energy needs. We note that a 50% reduction in GHG emissions in comparison with fossil diesel is attainable when the carbon intensity of the ethanol feedstock is below 14 g CO_2-eq per MJ ethanol; this value falls within the range commonly reported for lignocellulosic ethanol and sugar cane ethanol.[102] To obtain a carbon-neutral diesel fuel, ethanol with carbon intensity lower than −23.4 g CO_2-eq per MJ ethanol is required. This low carbon intensity falls into the range predicted in some studies for lignocellulosic ethanol. Alternatively, it could be obtained by implementing a carbon capture technology in the ethanol production process. In particular, capturing at the fermentation outlet is not energy intensive (~0.015 MJ per MJ of ethanol[103]) provided that the composition of this stream is mostly CO_2. A reduction of ~33.6 g CO_2-eq per MJ ethanol could be attained by implementing CO_2 capture at this outlet.[103, 104]

Additional improvements in the upgrading process as the technology develops may lead to a reduction in the energy consumed, thus improving current estimates. For example, if the upgrading process can be done in an energy self-sufficient design (such that the energy in the upgrading coproducts is enough to satisfy all the upgrading energy needs), then it would be possible to reduce the energy consumption by more than 0.39 MJ per MJ of ethanol processed. For reference, common carbon intensities for lignocellulosic ethanol range between −29 to 70 g CO_2-eq per MJ ethanol depending on the assumptions made, geographic location, and impact factors for chemicals used in the process (e.g., corn steep liquor, ammonia, and glucose).[72, 102, 105, 106] Corn ethanol without CO_2 capture has carbon intensities from ~50 to 117 g CO_2-eq per MJ ethanol.[102] Finally, ethanol produced from sugar cane has carbon intensities reported from 9 to 55 g CO_2-eq per MJ ethanol.[102]

3.4 Conclusions

This works presents an integrated approach between experimental heterogeneous catalysis and process systems engineering towards the design of an ethanol upgrading biorefinery for the production of diesel. The fuels produced exhibit advantageous properties in comparison with their fossil counterparts, especially with respect to the cetane number (>70 for both diesel #1 and diesel

#2) and cold flow properties (cloud point lower than −35 °C). The experimental results demonstrate the selective transformation of ethanol into higher alcohols, and the subsequent conversion of these alcohols to ethers of high molecular weight. Coproducts include olefins and esters. Systems engineering was used to first synthesize a process based on the experimental results, and then perform TEA and LCA. The produced diesel has an MFSP of 5.89$ per Gal (6.86$ per GGE), and, importantly, the process has a net energy gain (EROI = 1.41 > 1). The analysis of the GHG emissions showed that if corn stover is used as feedstock, then a 50% GHG reduction is possible. Additionally, if the ethanol carbon intensity is sufficiently low, we demonstrate the possibility of obtaining carbon neutral diesel fuel. Future research in this area should focus on finding strategies that can lead to the simplification of the necessary separations and the development of more selective catalysts, as such improvements will have an impact on both the EROI of the fuels produced and GHG emissions.

3.5 Acknowledgments

This material is based upon work supported by the U.S. Department of Energy's Office of Energy Efficiency and Renewable Energy (EERE) under the Co-Optima program award number E-EE0008480. The views expressed herein do not necessarily represent the views of the U.S. Department of Energy or the United States Government.

References

1. IEA, Global EV Outlook 2021, 2021.
2. IEA, Annual Energy Outlook 2021, Washington DC, 2021.
3. N. M. Eagan, M. D. Kumbhalkar, J. S. Buchanan, J. A. Dumesic and G. W. Huber, Nature Reviews Chemistry, 2019, **3**, 223-249.
4. V. Smil, IEEE Spectr., 2019, **56**, 22.
5. V. Smil, IEEE Spectr., 2016, 2016.
6. R. A. Dagle, A. D. Winkelman, K. K. Ramasamy, V. Lebarbier Dagle and R. S. Weber, Industrial & Engineering Chemistry Research, 2020, **59**, 4843-4853.
7. EIA, Monthly Energy Review - June 2021, Washington DC, 2021, vol. 159.
8. DOE, Global Ethanol Production by Country or Region, http://www.agri-outlook.org/%0A
9. Statista, Biodiesel Production in Brazil from 2009 to 2021, https://www.statista.com/statistics/877042/brazil-biodiesel-production/.
10. M. Slupska and D. Bushong, Biofuels, Bioprod. and Biorefin., 2019, **13**, 857-859.
11. S. Singh and D. Singh, Renewable and sustainable energy reviews, 2010, **14**, 200-216.
12. EPA, Overview for Renewable Fuel Standard Program, https://www.macrotrends.net/2538/soybean-oil-prices-historical-chart-data
13. corn grain price, https://markets.businessinsider.com/commodities/corn-price.
14. M. Langholtz, B. Stokes and L. Eaton, 2016 Billion - Ton Report: Advancing Domestic Resources for a Thriving Bioeconomy, Oak Ridge, Tennesse, 2016.
15. J. M. Restrepo-Flórez and C. T. Maravelias, Energy & Environmental Science, 2021, **14**, 493-506.
16. J. Sun and Y. Wang, ACS catalysis, 2014, **4**, 1078-1090.
17. EPA, Overview for Renewable Fuel Standard, https://www.epa.gov/renewable-fuel-standard-program/overview-renewable-fuel-standard
18. DOE, Biodiesel Income Tax Credit, https://afdc.energy.gov/laws/396, 2022.
19. J. R. Hannon, L. R. Lynd, O. Andrade, P. T. Benavides, G. T. Beckham, M. J. Biddy, N. Brown, M. F. Chagas, B. H. Davison and T. Foust, Proceedings of the National Academy of Sciences, 2020, **117**, 12576-12583.
20. S. Geleynse, K. Brandt, M. Garcia-Perez, M. Wolcott and X. Zhang, ChemSusChem, 2018, **11**, 3728-3741.
21. J. S. Lopez, R. A. Dagle, V. L. Dagle, C. Smith and K. O. Albrecht, Catalysis Science & Technology, 2019, **9**, 1117-1131.
22. K. Atsonios, M.-A. Kougioumtzis, K. D. Panopoulos and E. Kakaras, Applied Energy, 2015, **138**, 346-366.
23. L. Tao, J. N. Markham, Z. Haq and M. J. Biddy, Green Chemistry, 2017, **19**, 1082-1101.
24. E. C. Tan, L. J. Snowden-Sawn, M. T. Abhijit-Dutta, S. Jones, K. K. R. M. G. R. Dagle, A. Padmaperuama, M. Gerber, A. H. Sahir, L. Tao and Y. Zhang, Biofuels, Bioprod. and Biorefin., 2016, **19**, 1082-1101.
25. W.-C. Wang, L. Tao, J. Markham, Y. Zhang, E. Tan, L. Batan, M. Biddy, W.-C. Wang, L. Tao, Y. Zhang, E. Tan, E. Warner and M. Biddy, Review of Biojet Fuel Conversion Technologies-Nrel/tp-5100-66291, 2016.
26. B. C. Klein, M. F. Chagas, T. L. Junqueira, M. C. A. F. Rezende, T. de Fátima Cardoso, O. Cavalett and A. Bonomi, Applied Energy, 2018, **209**, 290-305.
27. J. T. Crawford, C. W. Shan, E. Budsberg, H. Morgan, R. Bura and R. Gustafson, Biotechnology for Biofuels, 2016, **9**, 1-16.

28. M. D. Staples, R. Malina, H. Olcay, M. N. Pearlson, J. I. Hileman, A. Boies and S. R. Barrett, Energy & Environmental Science, 2014, **7**, 1545-1554.
29. J. Han, L. Tao and M. Wang, Biotechnology for Biofuels, 2017, **10**, 1-15.
30. N. A. Huq, X. Huo, G. R. Hafenstine, S. M. Tifft, J. Stunkel, E. D. Christensen, G. M. Fioroni, L. Fouts, R. L. McCormick and P. A. Cherry, Proceedings of the National Academy of Sciences, 2019, **116**, 26421-26430.
31. J.-M. Restrepo-Flórez, J. Ryu, D. Witkowski, D. A. Rothamer and C. T. Maravelias, Energy & Environmental Science, 2022, **15**, 4376-4388.
32. J.-M. Restrepo-Flórez and C. T. Maravelias, in Computer Aided Chemical Engineering, Elsevier, 2022, vol. 49, pp. 103-108.
33. J. Heveling, A. van der Beek and M. de Pender, Applied catalysis, 1988, **42**, 325-336.
34. N. M. Eagan, B. M. Moore, D. J. McClelland, A. M. Wittrig, E. Canales, M. P. Lanci and G. W. Huber, Green Chemistry, 2019, **21**, 3300-3318.
35. USA Patent Office, 2021, US Pat.2021/0363085A0363081.
36. J. E. Rorrer, A. T. Bell and F. D. Toste, ChemSusChem, 2019, **12**, 2835-2858.
37. J. Yanowitz, M. A. Ratcliff, R. L. McCormick, J. D. Taylor and M. J. Murphy, Compendium of Experimental Cetane Number Data, Report number NREL/SR-540-36805, 2017, p. 78.
38. L. Ou, H. Cai, H. J. Seong, D. E. Longman, J. B. Dunn, J. M. Storey, T. J. Toops, J. A. Pihl, M. Biddy and M. Thornton, Environmental science & technology, 2019, **53**, 12904-12913.
39. J. T. Kozlowski and R. J. Davis, Acs Catalysis, 2013, **3**, 1588-1600.
40. I. Nezam, J. Zak and D. J. Miller, Industrial & Engineering Chemistry Research, 2020, **59**, 13906-13915.
41. I. Nezam, L. Peereboom and D. J. Miller, Journal of cleaner production, 2019, **209**, 1365-1375.
42. United States of America, 2019, US Pat.2019/0031585A0031581.
43. P. A. Cuello-Penaloza, R. G. Dastidar, S.-C. Wang, Y. Du, M. P. Lanci, B. Wooler, C. E. Kliewer, I. Hermans, J. A. Dumesic and G. W. Huber, Applied Catalysis B: Environmental, 2022, **304**, 120984.
44. A. Galadima and O. Muraza, Industrial & Engineering Chemistry Research, 2015, **54**, 7181-7194.
45. Q. Zhang, J. Dong, Y. Liu, Y. Wang and Y. Cao, Journal of Energy Chemistry, 2016, **25**, 907-910.
46. T. Tsuchida, J. Kubo, T. Yoshioka, S. Sakuma, T. Takeguchi and W. Ueda, Journal of Catalysis, 2008, **259**, 183-189.
47. H. S. Ghaziaskar and C. C. Xu, RSC advances, 2013, **3**, 4271-4280.
48. J. Pang, M. Zheng, L. He, L. Li, X. Pan, A. Wang, X. Wang and T. Zhang, Journal of Catalysis, 2016, **344**, 184-193.
49. United States of AMerica, 2020, US Pat.10669221B10669222.
50. P. A. Cuello-Penaloza, J. Chavarrio-Cañas, Y. Du, M. P. Lanci, D. A. Maedke, J. A. Dumesic and G. W. Huber, Applied Catalysis B: Environmental, 2022, **318**, 121821.
51. D. D. Petrolini, N. Eagan, M. R. Ball, S. P. Burt, I. Hermans, G. W. Huber, J. A. Dumesic and L. Martins, Catalysis Science & Technology, 2019, **9**, 2032-2042.
52. J. J. Bravo-Suárez, B. Subramaniam and R. V. Chaudhari, Applied Catalysis A: General, 2013, **455**, 234-246.
53. E. Medina, R. Bringué, J. Tejero, M. Iborra and C. Fité, Applied Catalysis A: General, 2010, **374**, 41-47.

54. O. V. Larina, K. V. Valihura, P. I. Kyriienko, N. V. Vlasenko, D. Y. Balakin, I. Khalakhan, T. Čendak, S. O. Soloviev and S. M. Orlyk, Applied Catalysis A: General, 2019, **588**, 117265.
55. R. J. Nel and A. de Klerk, Industrial & engineering chemistry research, 2009, **48**, 5230-5238.
56. N. Makgoba, T. Sakuneka, J. Koortzen, C. Van Schalkwyk, J. Botha and C. Nicolaides, Applied Catalysis A: General, 2006, **297**, 145-150.
57. V. O. Samoilov, D. N. Ramazanov, A. I. Nekhaev, S. V. Egazar'yants and A. L. Maximov, Fuel Processing Technology, 2015, **140**, 312-323.
58. A. Forestière, H. Olivier-Bourbigou and L. Saussine, Oil & Gas Science and Technology-Revue de l'IFP, 2009, **64**, 649-667.
59. J. Skupinska, Chemical reviews, 1991, **91**, 613-648.
60. G. J. Britovsek, R. Malinowski, D. S. McGuinness, J. D. Nobbs, A. K. Tomov, A. W. Wadsley and C. T. Young, ACS Catalysis, 2015, **5**, 6922-6925.
61. C. P. Nicholas, Applied Catalysis A: General, 2017, **543**, 82-97.
62. J. Q. Bond, D. M. Alonso, D. Wang, R. M. West and J. A. Dumesic, Science, 2010, **327**, 1110-1114.
63. C. Flego, M. Marchionna and C. Perego, in Studies in Surface Science and Catalysis, Elsevier, 2005, vol. 158, pp. 1271-1278.
64. ASTM D975-20c, Standard Specification for Diesel Fuel, 2014.
65. ASTM D4814-14b, Standard Specification for Automotive Spark-Ignition Engine Fuel, 2014.
66. B. Linnhoff and E. Hindmarsh, chemical engineering science, 1983, **38**, 745-763.
67. D. Humbird, R. Davis, L. Tao, C. Kinchin, D. Hsu, A. Aden, P. Schoen, J. Lukas, B. Olthof and M. Worley, Process design and economics for biochemical conversion of lignocellulosic biomass to ethanol: dilute-acid pretreatment and enzymatic hydrolysis of corn stover, National Renewable Energy Lab.(NREL), Golden, CO (United States), 2011.
68. F. G. Baddour, L. Snowden-Swan, K. M. V. Allsburg, J. Super, E. Tan, J. Frye, J. White, J. Schaidle, M. Talmadge, J. Hensley and S. Habas, CatCost An estimation tool to aid commercialization and R&D decisions for catalytic materials, 2018, pp. 1–54
69. M. Ryberg, M. D. Vieira, M. Zgola, J. Bare and R. K. Rosenbaum, Clean Technologies and Environmental Policy, 2014, **16**, 329-339.
70. N. Von Der Assen, P. Voll, M. Peters and A. Bardow, Chemical Society Reviews, 2014, **43**, 7982-7994.
71. K. Gerbrandt, P. L. Chu, A. Simmonds, K. A. Mullins, H. L. MacLean, W. M. Griffin and B. A. Saville, Current opinion in biotechnology, 2016, **38**, 63-70.
72. J. A. Obnamia, G. M. Dias, H. L. MacLean and B. A. Saville, Applied Energy, 2019, **235**, 591-601.
73. A. König, L. Neidhardt, J. Viell, A. Mitsos and M. Dahmen, Computers & Chemical Engineering, 2020, **134**, 106712.
74. A. König, M. Siska, A. M. Schweidtmann, J. G. Rittig, J. Viell, A. Mitsos and M. Dahmen, Chemical Engineering Science, 2021, **237**, 116562.
75. Y. Gaston-Bonhomme, P. Petrino and J. Chevalier, Chemical engineering science, 1994, **49**, 1799-1806.
76. H.-J. Liaw and Y.-Y. Chiu, Journal of hazardous materials, 2006, **137**, 38-46.

77. F. A. Carroll, C.-Y. Lin and F. H. Quina, Industrial & Engineering Chemistry Research, 2011, **50**, 4796-4800.
78. F. I. Mirante and J. A. Coutinho, Fluid Phase Equilibria, 2001, **180**, 247-255.
79. A. M. Ferris and D. A. Rothamer, Fuel, 2016, **182**, 467-479.
80. D. Witkowski and D. A. Rothamer, Simple autoignition model for the derived cetane number of oxygenated compounds and fuel blends., in Spring Technical Meeting of The Central States Section of the Combustion Institute, Detroit, 2022.
81. A. Technology, Aspen Plus, (2017).
82. S. M. Sen, D. M. Alonso, S. G. Wettstein, E. I. Gürbüz, C. A. Henao, J. A. Dumesic and C. T. Maravelias, Energy & Environmental Science, 2012, **5**, 9690-9697.
83. Guide, U. CatCost 1-62, (2021).
84. J. Q. Bond, A. A. Upadhye, H. Olcay, G. A. Tompsett, J. Jae, R. Xing, D. M. Alonso, D. Wang, T. Zhang and R. Kumar, Energy & Environmental Science, 2014, **7**, 1500-1523.
85. M. A. Maselosne, University of Cape Town, 2011.
86. E. C. Ihmels and J. Gmehling, Industrial & engineering chemistry research, 2003, **42**, 408-412.
87. I. Bandrés, C. Lahuerta, A. Villares, S. Martín and C. Lafuente, International Journal of Thermophysics, 2008, **29**, 457-467.
88. K. G. Joback and R. C. Reid, Chemical Engineering Communications, 1987, **57**, 233-243.
89. A. Fredenslund, J. Gmehling and P. Rasmussen, (Elsevier, 1986), DOI: 10.1520/mnl10861m.
90. Y. Nannoolal, K. Rarey and D. Ramjugernath, Fluid Phase Equilibria, 2008, **269**, 117-133.
91. H. Imahara, E. Minami and S. Saka, Fuel, 2006, **85**, 1666-1670.
92. L. Seniorita, E. Minami and H. Kawamoto, Journal of Advanced Research in Fluid Mechanics and Thermal Sciences, 2020, **76**, 117-125.
93. J. G. Stichlmair, H. Klein and S. Rehfeldt, Distillation: principles and practice, John Wiley & Sons, 2021.
94. M. Groendyk and D. Rothamer, Fuel, 2017, **194**, 195-210.
95. NDEE, Average Corn Grain Price, https://neo.ne.gov/programs/stats/inf/66.html.
96. I. R. E. Agency, Road Transport: the Cost of Renewable Solutions, 2013.
97. K. Huang, W. Won, K. J. Barnett, Z. J. Brentzel, D. M. Alonso, G. W. Huber, J. A. Dumesic and C. T. Maravelias, Applied energy, 2018, **213**, 585-594.
98. R. T. Ng and C. T. Maravelias, Applied Energy, 2017, **205**, 1571-1582.
99. L. Wang, M. Xia, H. Wang, K. Huang, C. Qian, C. T. Maravelias and G. A. Ozin, Joule, 2018, **2**, 1055-1074.
100. C. A. Hall, J. G. Lambert and S. B. Balogh, Energy policy, 2014, **64**, 141-152.
101. C. A. Hall, S. Balogh and D. J. Murphy, Energies, 2009, **2**, 25-47.
102. EPA, Lifecycle Greenhouse Gas Results, https://www.epa.gov/fuels-registration-reporting-and-compliance-help/lifecycle-greenhouse-gas-results, accessed 17 September 2022.
103. C. H. Geissler and C. T. Maravelias, Applied Energy, 2021, **302**, 117539.
104. Z. Huang, G. Grim, J. Schaidle and L. Tao, Applied energy, 2020, **280**, 115964.
105. S. Kim, X. Zhang, A. D. Reddy, B. E. Dale, K. D. Thelen, C. D. Jones, R. C. Izaurralde, T. Runge and C. Maravelias, Environmental Science & Technology, 2020, **54**, 10797-10807.
106. M. Wang, J. Han, J. B. Dunn, H. Cai and A. Elgowainy, Environmental research letters, 2012, **7**, 045905.

Chapter 4. Advanced diesel from ethanol, a pathway to produce sustainable and high-quality drop-in biofuels

4.1 Introduction

The consumption of diesel fuel is projected to remain constant in the U.S. at ~4 million barrels per day for the next 30 years[1]. With CO_2 emissions of 10.18 kg/gal[2], this consumption would represent the release of ~1.7 million tons of CO_2 into the environment every day (~10% of the total US emissions). Diesel fuel primarily powers ships, trucks, and heavy-duty vehicles, which pose challenges for electrification, unlike lighter vehicles. This makes it a complex sector to decarbonize[3]. Biofuels will play a significant role in these applications in the energy transition and are part of the long-term vision of the U.S. DOE[4]. A significant amount of research has been devoted to analyzing different renewable diesel production pathways[5-9](Table 1). These efforts have been focused on identifying biofuel alternatives satisfying three requirements: 1) economic feasibility, 2) low greenhouse gas emissions (<60% of fossil diesel), and 3) operability, which has been assessed based on the fuel properties. Ideal production pathways should lead to the production of sustainable diesel with equal or superior properties than those of fossil diesel.

The content of this chapter is largely adapted from the following reference:

Juan-Manuel Restrepo-Flórez**, Javier E. Chavarrio**, Emmanuel Canales**, Paolo Cuello-Peñaloza, Dustin Witkowski, Srinath Subramanian, David A. Rothamer, Christos T. Maravelias, and George W. Huber. Advanced diesel from ethanol, a pathway to produce sustainable and high-quality drop-in biofuels. In preparation.

JM Restrepo Florez conducted TEA and LCA analysis. JE Chavarrio conducted Guerbet Coupling experiments. EC conducted etherification experiments. These authors contributed equally to the manuscript. *DW conducted fuel characterization modeling. SS conducted engine testing experiments.*

For reference, at a commercial scale in the U.S., the most widely produced renewable alternatives to diesel are hydroprocessed esters and fatty acids (HEFA) and biodiesel, both derived from vegetable oils, a feedstock with limited availability and high price[10].

Table 4.1. Main pathways to produce renewable diesel fuel from biomass (adapted from Gaspar et al 2021[5] except for ethanol Guerbet coupling and etherification which is based on Restrepo-Flórez et al, 2023[11]). MFSP: Minimum Fuel Selling Price (prices are shown before any tax benefit is applied), ΔGHG: reduction in greenhouse gas emissions relative to fossil diesel.

	CN [-]	Flash point [°C]	Cloud point [°C]	Energy Density [MJ/L]	Viscosity [mm^2/s]	Density [kg/m^3]	MFSP [$/GDE]*	ΔGHG [%]
Diesel	>40	>52		~35	1.9-4.1	>820	1.8-3.5**	[-]
Biodiesel	>47	>93	-5 to 15	33	1.9-6	880	5.3	39-90
Renewable diesel HEFA	>70	>61	-39	34.4	2-4	770-790	4.7-7.8	60-80
Fischer Tropsch Diesel	>70	>61	-34 to 10	34	2-4	770-790	5.5	89
HTL fuel	30-68	>55	-60 to 20	34.5-36.9	2.3-2.7	800-879	4.3-6.7	62-73
Farnesane	58.6	110	-73	33.5	14	773	7.8-9.4	61
Isoalkanes from VFA	48	74	-80	34.6	1.49	780	12.5	<60%
Ethanol-to-distillate	55-68	>54	-60.1	35	2.0-4.8	786	4.7-7.2	>90%
Fatty acid fusel esters	50-60	>130	-10	>30	2.9-3.7	817-861	3.8-5.3	53%
Short chain esters from oilseed crops	52	111	-18	29.6	1.7	871	25.1	20-53
Polyoxymethylene ethers	73-75	62-63	-27-19	20-32	1.9	1.0662	6.4-7	81
4-butoxyheptane	80	64	-80	30.8	0.795	791	11.0	27
Alkoxyalkanoates from lactate esters	44-62	65-117	<-50	23-33	1.2-2.3	900-930	7.8	65
Fatty alkyl ethers	74-104	>150	-5 to -16	34-36		830-850	6.3	57-75
Ethanol Guerbet coupling and etherification	73.2	>50	-37	27.5	1.92	815	4-7.7	>50
This work	94	~52	-28.9	29.36	1.7	794.7	4.6-8.4	0-144

*MFSP is in 2021 dollars **Diesel spot price

Among the pathways in **Table 4.1**, we are interested in ethanol upgrading by Guerbet coupling and etherification[11]. This pathway has several advantages in terms of fuel properties, GHG emission reduction, and feedstock availability, while simultaneously showing technoeconomic feasibility[11]. From a fuel property perspective, it has been demonstrated that it is possible to produce a renewable diesel #2 that satisfies most ASTM requirements with a high cetane number (>70) and good cold flow properties (cloud point <-37°C)[11]. These outstanding fuel properties are the result of using an ether rich blend as diesel fuel. Ethers are known for their high cetane number and have been identified as a potential diesel replacement in several studies[12-14]. In terms of GHG mitigation potential, the possibility of obtaining more than 60% reduction in comparison with fossil diesel has been shown[11]. Furthermore, depending on the carbon intensity of the ethanol used, it is possible to produce carbon neutral or carbon negative diesel fuel. We note that a pathway based on ethanol upgrading is particularly well positioned in terms of feedstock availability. Not only is there already ethanol infrastructure in the U.S., with a production capacity close to 17 billion gallons per year[15, 16], but also, there are emerging technologies (e.g., fermentation of lignocellulosic residues[17-19] and syngas[20]) that may disrupt the ethanol market by increasing the supply while reducing the environmental impacts and costs of ethanol production.

Despite the advantages of ethanol upgrading via Guerbet coupling and etherification, we have identified three limitations hindering the deployment of this technology. First, the Guerbet coupling reaction of ethanol has as a main product 1-butanol[21-24]. The overabundance of 1-butanol in the etherification reaction leads to the production of a significant fraction of dibutyl ether, with a flash point (25°C) well below the diesel #2 requirement (>52°C)[25]. Consequently, the yield of diesel #2 gets is reduced; for reference, in our previous work, we found a maximum diesel #2 yield of ~50%[11]. Second, the most effective Guerbet coupling catalysts for diesel production (i.e., those that produce the highest amount of C6+ alcohols) also produce significant amounts of esters, aldehydes, and ketones[21, 26]. Esters significantly affect the ether selectivity in etherification reactions, while the aldehydes and ketones produced are not suitable to be used in diesel due to their physicochemical properties (low molecular weight aldehydes and ketones have a low flash point). Third, while it is expected that the diesel #2 produced by Guerbet coupling and etherification would improve the emission profile in comparison with diesel fuel based on results obtained with di-butyl-ether[27], the blends developed in this work have not been characterization in terms of engine performance.

In this work, we address the previous limitations and present a new strategy for the catalytic upgrading of ethanol into diesel #2. We present laboratory experimental results that are incorporated into process design, technoeconomic analysis (TEA), lifecycle assessment (LCA), as well as characterization of the fuels produced in terms of their physicochemical properties and their experimental evaluation in a diesel engine. The developed process uses four catalytic steps: Guerbet coupling, hydrogenolysis, etherification, and oligomerization. Importantly, we implement a butanol recycling strategy that significantly improves the production of C6+ alcohols. While this strategy has been suggested in the literature[23], this is the first time that experimental evidence supporting the effect of butanol recycling on alcohol distribution is presented. Furthermore, the hydrogenolysis step used, also employed for the first time in this type of application, allows us to efficiently remove esters, aldehydes, and ketones, transforming them into alcohols. This work is the result of a collaborative effort among catalyst experts, fuel property modelers, process and systems engineers, and engine researchers. This broad and convergent synergy has enabled us to couple all the biofuel production stages presenting a comprehensive view of this novel and promising diesel production strategy.

4.2 Experimental methods

4.2.1 Guerbet Coupling catalyst

A 0.3% wt. $Cu/Mg_{2.9}AlO$ catalyst was prepared through co-precipitation of $Cu(NO_3)_2\cdot 3H_2O$ (Sigma-Aldrich 61194), $Al(NO_3)_3\cdot 9H_2O$ (Sigma-Aldrich 237973) and $Mg(NO_3)_3\cdot 6H_2O$ (Sigma-Aldrich 237175) precursors at pH 10. The resulting cake was filtered, washed with deionized water, dried overnight at 110 °C (Lab-line, 3511) and calcined for 2h at 600 °C under heating ramp of 4 °C min^{-1}. A thorough description of the synthesis procedure accompanied with reagent proportions and catalyst characterization can be found in our previous publications[21, 26].

4.2.2 Hydrogenolysis catalyst

Zirconia (ZrO_2) support was prepared through oxidative treatment of zirconium (IV) hydroxide ($Zr(OH)_4$, Aldrich 46417-1, 97%) as described elsewhere[28]. Briefly, $Zr(OH)_4$ was calcined at 500 °C for 5 h on a 4 °C min^{-1} heating ramp and static air atmosphere in a muffle furnace (ThermoFisher Scientific, Thermlyne) to obtain a white powder assumed to be Zirconia (ZrO_2). Textural characterization by nitrogen physisorption was carried out in an ASAP 2020 (Micromeritics), yielding BET surface area of 146 m^2 g^{-1} and BJH pore volume of 0.14 cm^3 g^{-1}. Cu/ZrO2 catalyst with a theoretical metal load of 10% wt. was synthesized through incipient wetness impregnation by dissolving $Cu(NO_3)_2 \cdot 3H_2O$ (Sigma-Aldrich 61194, 99%) Milli-Q water, heated up to 60 °C for a complete dissolution of the salt[29] and added dropwise to the zirconia. After impregnation of the support, it was dried overnight (at least 12h) in an oven (Lab-line, 3511) at 110 °C and subsequently crushed and calcined (4 °C min^{-1}) at 500 °C for 5 h on a static air atmosphere.

4.2.3 Reaction conditions for Guerbet Coupling and Hydrogenolysis

Guerbet coupling and hydrogenolysis reactions were performed independently in the same reaction setup, thereby description of the reaction procedure varies only in reaction condition. For simplicity, reaction conditions for hydrogenolysis will be described in the main text, while those for Guerbet coupling will be given inside brackets. The calcined catalyst was sieved to 177-354 μm (mesh 80-45) and packed into a stainless-steel fix bed reactor (16 in long, 3/8 in outer diameter) by using 100-500 mg of the catalyst. Such powder was fixed at the center of the reactor by placing layers of glass wool (Acros organics, 393611000) and silica chips (Sigma-Aldrich, 342831) at each end, and then reduced in situ at 300 °C (1 °C min^{-1}) for 2 hours under 20mL min^{-1} of pure hydrogen flow (101 kPa)[28] [325 °C (4 °C min^{-1}) for 12 hours under 50 mL min^{-1} of pure hydrogen flow (101 kPa)[21] for Guerbet coupling]. Isothermal profile along the catalytic bed was attained by using aluminum blocks between the reactor and the electric tube furnace (Thermo Fisher, Lindberg blue M Mini-Mite); the temperature was measured with a K-type thermocouple, which was embedded in the aluminum heating block. After reduction, the reactor was cooled down to 200°C and pressurized to 420 psig [325 °C and 300 psig] with a back-pressure regulator (Equilibar, ZF0SVN8). A blend of butanol – hexyl acetate of composition 95% – 5% mol [ethanol-butanol 70%-30% mol], respectively, was fed with a syringe pump (Teledyne ISCO) at 6-18 µL min^{-1} [23-93 µL min^{-1}], with pure H_2 cofeed at 36-109 mL min^{-1} [2.5–10.3 mL min^{-1}] to a preheated section maintained at ~190 °C [>200 °C] to ensure feed was in gaseous phase when contacting the catalyst. The molar ratio of esters to hydrogen of the gaseous phase entering the reactor was kept constant at 1:480 for hydrogenolysis experiments, while for Guerbet coupling reactions the molar ratio of alcohols to hydrogen was maintained at 4:1. After reaction, products were collected in a removable 110 mL glass condenser (Ace glass) immersed in a dry ice bath. With the aim of reducing sampling error due to low product mass collection, 15 mL of 1-propanol (Sigma-Aldrich, 96566) were loaded to the condenser before collection of products with sample collection time of typically for 1-2 h. Gases that did not condense were sent to a three-valve, which led the gaseous flow to vent or towards an online gas GC (Shimadzu 2010) equipped with a flame ionization detector (FID) and thermal conductivity detector (TCD) for gas phase sampling. Liquid samples were prepared to be analyzed through gas chromatography by diluting them with 1-propanol and adding a known amount of 1-pentanol as internal standard. Such liquid products were analyzed via GC-FID (Shimadzu 2014), and quantification was performed by using external standards. Product's identity was further supported by gas chromatography – mass spectrometry (Shimadzu GCMS-QP2010). For further description of analysis methods for liquid and gas phases please refer to our previous publications[21, 23].

4.2.4 Etherification

The etherification of the ethanol/butanol Guerbet coupling products is carried out in an upward configuration continuous flow reactor made of stainless steel. The bed was packed with 1.8 g of powder HY catalyst (Si/Al = 30). The composition of the catalyst bed, reactor dimensions, and collection procedure can be found elsewhere[11]. Ar gas was flown at 10 mL/min, and the liquid flowrate varied to obtain WHSV = 1 h^{-1}. For determining cross-etherification species, the analytical techniques for product identification were also taken from elsewhere[11].

4.2.5 Engine Testing

The experiments were performed in a single-cylinder research version of the General Motors 1.9L (Z19DTH). The test cell has a customized fuel system to deliver high-pressure fuel to the engine and a HORIBA 5-gas emissions bench and a hydrocarbon analyzer to measure common engine-out pollutants. The test cell has precise control over intake (air temperature and pressure) and boundary conditions (oil and coolant temperature). More details about the test cell setup and engine geometry can be found in[27]. The fuels used in the study were obtained from manufacturers with high purity levels.

4.3 Catalytic pathway and technology overview

A schematic of the technology developed is shown in **Figure 4.1**. Anhydrous ethanol is used as the feedstock of a Guerbet reaction, in which higher alcohols (C4+) are obtained as a main product along with esters, aldehydes, and ketones as byproducts. Wastewater is a byproduct of this process. The outlet from the Guerbet coupling reaction is used as the feedstock for hydrogenolysis in which esters, aldehydes, and ketones are transformed into their parent alcohols. The hydrogenolysis reaction product consists mainly of higher alcohols, and unconverted ethanol. In this work, we implement a recycle strategy in which unconverted ethanol and a significant fraction of the butanol produced are recycled to the Guerbet reactor. This recycle leads to an operation in which ethanol and butanol are cofed to the Guerbet reactor. The partial recycling of butanol reduces the butanol content in the etherification reaction. The fraction of unrecycled butanol, along with the C6+ alcohols produced are split into two fractions: 1) the C4-C8 alcohols, which are fed to an etherification reaction in which ethers with 8-16 carbons are produced and 2) the larger alcohols (C10+), which are used directly in the diesel blend. Olefins (C4-C8) are produced in the etherification process and are oligomerized to increase their average molecular weight such that they can be blended into diesel.

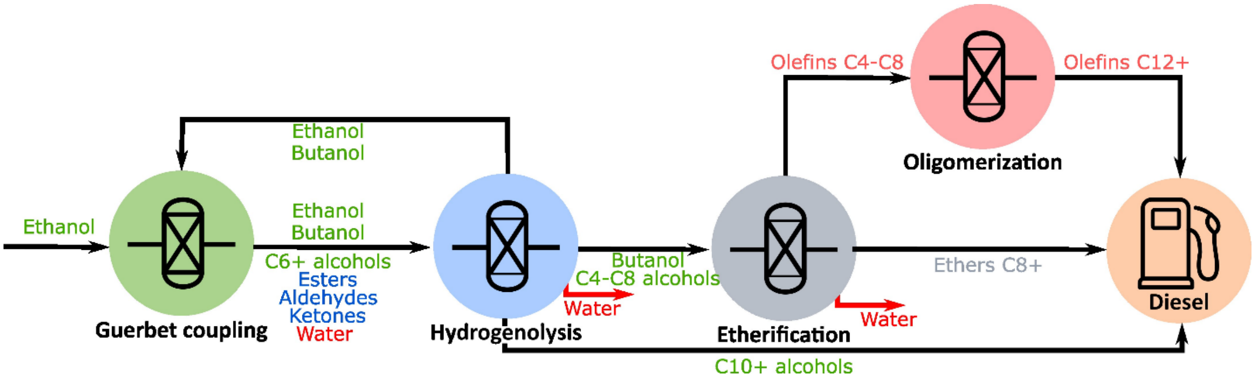

Figure 4.1. Schematic of the technology developed in this work.

4.3.1 Guerbet Coupling

For the Guerbet coupling reaction, we used a Cu/Mg_3AlO catalyst that we have previously studied[21,26]. This catalyst has important advantages in comparison with other Guerbet coupling catalysts: it is low cost, it produces a larger fraction of C6+ alcohols, and it is stable (it has been evaluated for more than 100 hours on stream)[21]. Guerbet coupling reactions with a cofeed of ethanol-butanol 70-30 % mol were performed to study the feasibility of recycling ethanol and butanol into the Guerbet coupling reactor. We evaluated the catalyst under three different space velocities WHSV=1.33, 6.5 and 26.2 $g_{ethanol}\ g_{cat}^{-1}h^{-1}$ (~70%, 50% and 30% ethanol conversion, respectively). Control experiments with a pure ethanol feed were also performed at the same WHSV and reaction conditions. Our experimental results for C_6 and C_8 alcohols are displayed in **Figure 4.2**, and complete data for all the experiments is presented in **Table 4.2**.

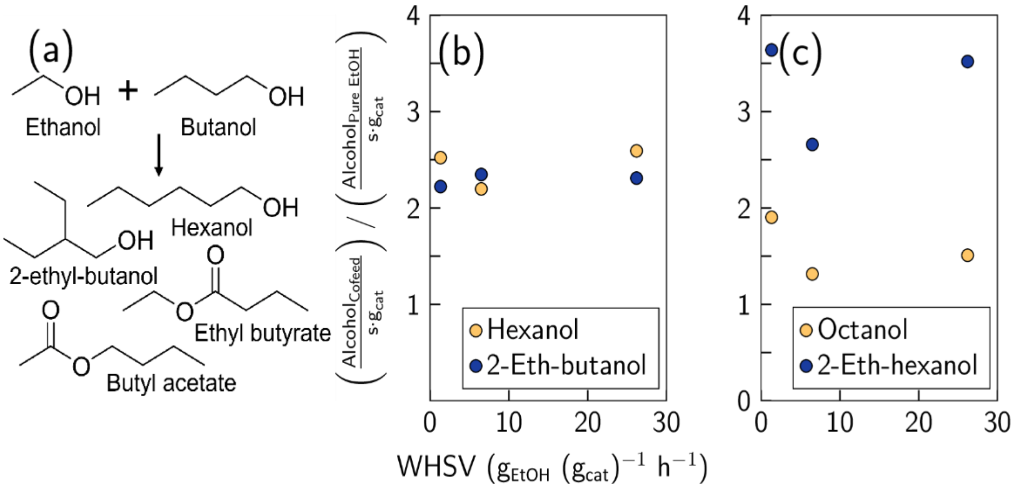

Figure 4.2. a) Conversion of ethanol and butanol into C_6 alcohols and esters. Ratio of molar flow of alcohols in cofeed strategy / alcohols in control experiments, normalized by unit of time and mass of catalyst: (b) Hexanol and 2-ethyl-butanol, and (c) Octanol and 2-ethyl-hexanol. T=325 °C, P_{tot}=300 psig, (Ethanol+Butanol):H_2= 4:1, 100-300 mg 0.1%Cu/Mg_3AlO.

Table 4.2. Detailed mole flow in inlet and outlet of Guerbet coupling reactor for cofeed (Ethanol (70% mol) / Butanol (30%)) and control experiments (pure ethanol feed). WHSV values reported are in units of $g_{ethanol}$ h^{-1} g_{cat}^{-1}.

	Cofeed 1		Control 1		Cofeed 2	
WHSV (h^{-1})	26.27		26.27		6.53	
Mass catalyst (g)	0.1005		0.1003		0.1002	
	C flow (μmol C/min)					
Compound	**inlet**	**outlet**	**inlet**	**outlet**	**inlet**	**outlet**
Methane				5.82		2.67
ethylene				0.16		0.07
ethane				0.12		0.07
propane		3.83		0.19		0.19
propene				0.26		0.55
methanol						
1-butene		3.27		0.81		0.10
n-butane						0.24
acetone						
acetaldehyde		150.38		129.06		30.51
n-pentane		1.04				0.77
diethyl ether		0.18		0.81		0.03
pentenes				1.21		
n-hexane		0.68		1.85		0.01
ethanol	1910.51	1402.82	1918.15	1282.04	473.28	275.68
2-propanol				1.09		0.31
butyraldehyde		228.03		59.29		56.71
ethyl acetate		31.31		33.59		9.07
2-butanol				1.06		0.25
2-butanone		2.02		3.71		0.87
1-butanol	1626.66	1427.11		268.31	401.28	329.95
cis-crotyl alcohol		0.73		1.26		
1,1-diethoxyethane		1.11		11.52		0.71
2-pentanone		9.86		4.48		3.50
2-pentanol				0.72		
2-methyl-1-butanol		1.07				0.19
2-ethylbutanal		7.66		3.78		0.20
ethyl butanoate		25.76		11.57		9.27
butyl acetate		22.98		4.90		7.52
hexanal		18.88		8.72		7.32
2-ethylbutan-1-ol		23.49		10.15		10.02
1,1-diethoxybutane		1.25		2.74		0.62
1-butoxy-1-ethoxyethane				4.50		1.49
1-hexanol		98.20		37.82		35.88
4-heptanone		0.51		2.39		3.43
2-heptanol						0.29
2-heptanone		1.87		0.85		1.15
2-ethylhexanal		2.98		1.10		1.62
2-ethylbutyl acetate						
butyl butanoate		18.35		1.49		7.24
ethyl hexanoate		4.56		2.59		2.61
3-octanone						0.18
hexyl acetate		1.81		0.82		0.93
octanal		2.18		1.76		1.40
2-ethylhexan-1-ol		8.11		2.30		4.25

1,1-dibutoxyethane		1.61		1.15		1.06
1-octanol		10.62		7.02		5.61
4-nonanone		2.24		1.01		1.98
2-nonanone						0.39
2-Ethylbutyl butyrate						0.12
butyl hexanoate		5.56		0.51		3.69
hexyl butanoate				0.70		
octyl acetate		0.40				
2-ethyloctan-1-ol						0.47
decanal				0.60		0.49
2-hexyl-1-octanol		0.98		0.70		1.10
1-decanol		1.47		1.11		0.68
4-undecanone						1.23
hexyl hexanoate		1.26				0.39
butyl decanoate						0.32
decyl acetate						
butyl decanoate						
2-ethylhexyl ester butanoate						
2-undecanone						
2-butyl-1-octanol						
2-ethyl-1-decanol						
1-dodecanol						
2-tridecanone						
Missing Carbon		10.96		0.53		47.88

	Control 2		Cofeed 3		Control 3	
WHSV (h^{-1})	6.53		1.33		1.33	
Mass catalyst (g)	0.1		0.7429		0.4047	
	C flow (μmol C/min)					
Compound	**inlet**	**outlet**	**inlet**	**outlet**	**inlet**	**outlet**
Methane		0.14		0.76		0.60
ethylene		0.04		0.44		0.26
ethane		0.03		0.28		0.08
propane		0.06		0.43		
propene		0.33		1.17		0.04
methanol		0.06		1.90		0.72
1-butene		0.33		0.80		
n-butane		0.01		0.10		
acetone		0.00		9.74		0.77
acetaldehyde		27.57		92.12		34.83
n-pentane						
diethyl ether		0.22				1.49
pentenes		0.86		0.14		
n-hexane		1.31				
ethanol	479.54	275.39	718.60	244.07	411.03	111.14
2-propanol		0.23		2.26		0.82
butyraldehyde		17.23		127.99		33.42
ethyl acetate		7.65		33.80		16.50
2-butanol		0.03				
2-butanone		0.49		11.40		1.24
1-butanol		72.88	612.70	368.37		73.33

cis-crotyl alcohol		0.48				
1,1-diethoxyethane		5.64				2.94
2-pentanone		1.34		34.88		7.15
2-pentanol		0.09		3.91		0.59
2-methyl-1-butanol				1.23		
2-ethylbutanal		0.45		11.48		3.65
ethyl butanoate		4.08		41.35		14.59
butyl acetate		1.41		34.09		13.18
hexanal		3.59		20.95		4.85
2-ethylbutan-1-ol		3.88		22.32		5.47
1,1-diethoxybutane		1.67				0.72
1-butoxy-1-ethoxyethane		2.52				
1-hexanol		15.39		51.09		11.04
4-heptanone		0.71		19.86		5.52
2-heptanol				0.94		
2-heptanone		0.32		9.92		2.30
2-ethylhexanal		0.67		5.79		1.35
2-ethylbutyl acetate				1.25		
butyl butanoate		0.72		35.40		4.12
ethyl hexanoate		1.17		9.72		3.54
3-octanone				1.00		
hexyl acetate		0.34		5.13		1.50
octanal		0.91		3.91		1.65
2-ethylhexan-1-ol		1.44		9.70		1.45
1,1-dibutoxyethane		0.62		1.06		0.68
1-octanol		3.99		8.56		2.45
4-nonanone		0.45		8.23		1.35
2-nonanone		0.08		2.38		1.19
2-Ethylbutyl butyrate				1.29		
butyl hexanoate		0.40		17.01		4.97
hexyl butanoate		0.38				
octyl acetate		0.13		1.09		
2-ethyloctan-1-ol		0.25		0.82		
decanal		0.42				
2-hexyl-1-octanol		0.68		2.08		0.16
1-decanol		1.26		1.41		0.18
4-undecanone		0.21		2.83		0.36
hexyl hexanoate		0.44		5.01		0.97
butyl decanoate						
decyl acetate		0.02				
butyl decanoate		0.03				
2-ethylhexyl ester butanoate				0.83		
2-undecanone				0.82		
2-butyl-1-octanol		0.03				
2-ethyl-1-decanol		0.35				
1-dodecanol		0.40		1.11		
2-tridecanone						1.13
Missing Carbon		16.90		55.72		36.74

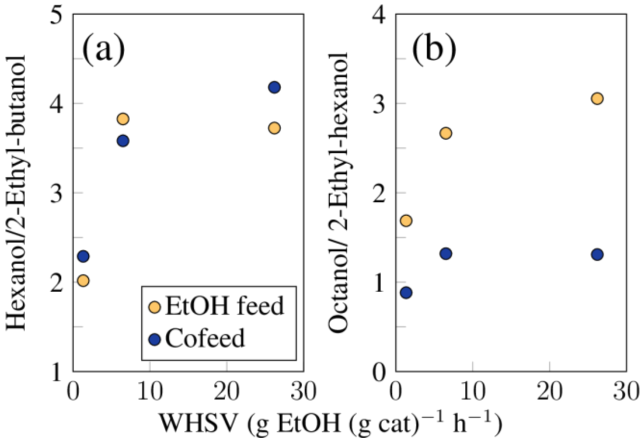

Figure 4.3. Mol ratio of (a) Hexanol to 2-Ethyl-butanol and (b) Octanol to 2-Ethyl-hexanol when cofeeding Ethanol (70% mol) / Butanol (30%) (blue circles) accompanied with control experiments with pure ethanol feed (yellow circles). T=325°C, P_{tot}=300 psig, Ethanol+Butanol:H_2= 4:1, 100-300 mg 0.1%Cu/Mg_3AlO.

The motivation for recycling butanol into the Guerbet coupling reactor is to increase the production of hexanol by facilitating the overall reaction ethanol + butanol → hexanol + H_2O. However, there are many side reactions, for example, 2-ethyl-butanol is also synthesized from these two reactants when ethanol acts as the electrophile. Esterification reactions produce butyl acetate and ethyl butyrate as shown in **Figure 4.2A**. The products pool becomes even more complex since alcohols can react with themselves. For example, two ethanol molecules can produce butanol or ethyl acetate and two butanol molecules can produce 2-ethyl-hexanol or butyl butyrate.

Previous etherification studies over acid catalysts have demonstrated that linear alcohols undergo preferentially bimolecular dehydrations to produce ethers, whereas branched alcohols form olefins through monomolecular dehydration[11]. Therefore, tracking the ratio of linear to branched alcohols is important. **Figures 4.3A** and **4.3B** show this ratio for C_6 and C_8 alcohols, respectively. Our results indicate the catalyst is selective to form linear alcohols (values >1). For C_6 alcohols, the ratio of hexanol to 2-ethyl-butanol is slightly higher in the cofeed experiments than in the control, indicating that cofeeding butanol facilitates the production of hexanol more than its branched counterpart. On average, the outlet hexanol molar flowrate is 3.4 and 3.2 higher than the molar flow of 2-ethyl-butanol for the cofeed and pure ethanol feed experiments, respectively (see **Table 4.2** for carbon flowrates in each run). For C_8 alcohols, a more noticeable difference is observed. **Figure 4.3B** shows that cofeeding ethanol and butanol produces more 2-ethyl-hexanol in comparison with the control experiment. For reference, in the co-feed case the Octanol/2-ethyl-hexanol ratio is close to one; in contrast, in the control experiments, it ranges between ~1.5-3 depending on the WHSV. This increase in relative concentration of 2-ethyl-hexanol in the cofeed experiments can be explained by considering that octanol is formed only from the coupling of ethanol and hexanol, with the former acting as nucleophile and the latter as electrophile. In contrast, 2-ethyl-hexanol is produced either when hexanol is the nucleophile and ethanol the electrophile or by coupling of two butanol molecules. Thus, cofeeding butanol enhances butanol self-condensation to form 2-ethyl-hexanol.

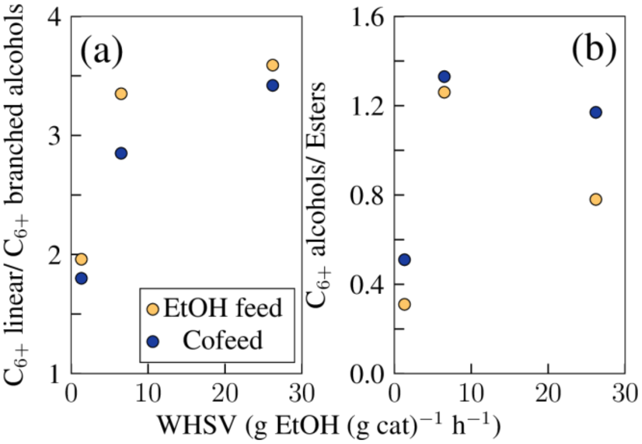

Figure 4.4. (a) C6+ Linear to branched alcohols ratio and (b) C6+ alcohols to ester ratio when cofeeding Ethanol (70% mol) / Butanol (30%) (blue circles) accompanied with control experiments with pure ethanol feed (yellow circles). T=325°C, Ptot=300 psig, Ethanol+Butanol:H2= 4:1, 100-300 mg 0.1%Cu/Mg3AlO.

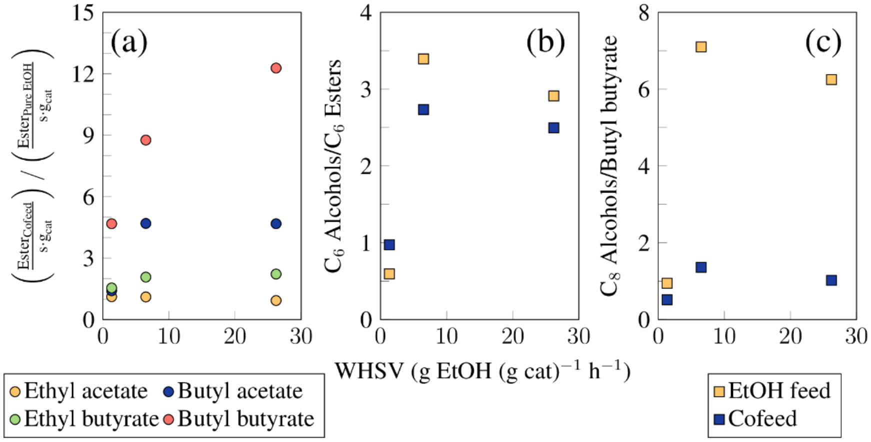

Figure 4.5. (a) Mol flow of esters in cofeed strategy / esters in control experiments, (b) mol ratio of C6 alcohols to C6 esters, and (c) mol ratio of C8 alcohols to butyl butyrate as a function of WHSV for cofeed strategy and control experiments.

Figure 4.4A shows that overall linear alcohols are formed preferentially, demonstrating that a cofeed strategy is selective to produce the most relevant diesel fuel precursors. A comparison of molar production of linear and branched alcohols between cofeed and control experiments is presented in Figures **4.3B-C**. The data indicates that cofeeding alcohols boosts the formation of hexanol and 2-ethyl-butanol by a factor of 2.2 (**Figure 4.3B**). This suggests that butanol presence in the feed does not change the nucleophilic/electrophilic role of ethanol in the reaction. Similarly, **Figure 4.3C** shows that the production of C8 alcohols is enhanced by the cofeed of butanol to the reactor, with the caveat that the formation of the branched alcohol is more accelerated than the formation of octanol.

Figure 4.5A shows the production of esters from ethanol/butanol coupling. Production of ethyl acetate remained unchanged in cofeed and control experiments. In contrast, production of other esters like ethyl butyrate, butyl acetate, and butyl butyrate is enhanced. The data shows that butyl acetate is produced preferentially over ethyl butyrate, which is due to the large excess of ethanol (70% mol in feed) that induces formation of acetaldehyde and subsequently dehydrogenative coupling between acetaldehyde and butanol. The presence of butanol in cofeed experiments leads to a higher production of butyl butyrate compared to the control experiments. The overall selectivity of C6+ alcohols with respect to esters is presented in **Figure 4.4B**. This figure suggests that the Guerbet coupling stage will benefit from a cofeed strategy since the ratio C_{6+} alcohols to esters improves. We note that the production of long chain alcohols competes strongly with ester formation, given that the values in **Figure 4.4B** are around 1.

The carbon yield to diesel fuel precursors (alcohols, aldehydes, ester, ethers, and ketones) is presented in **Table 4.3**. The values reported have been calculated by using the information contained in **Table 4.2** and equation **Error! Reference source not found.**). For simplicity, the i nformation has been condensed into categories based on functional groups. In **equation** Error! Reference source not found., $n_{C,in}$ refers to the total carbon flow rate entering the Guerbet reactor, while $n_{C,i,out}$ refers to the carbon flowrate at the outlet of the reactor specifically for the compound i.

$$Y_i = \frac{n_{C,i,out}}{n_{C,in}} \quad (1)$$

Table 4.3. Carbon yields of main compound categories for cofeed and control experiments at ethanol contact times. Conditions: 325 °C, 300 psig, P(EtOH+ButOH):PH2=4.

Experiment	**Cofeed 1**	**Control 1**	**Cofeed 2**	**Control 2**	**Cofeed 3**	**Control 3**
WHSV (h^{-1})	26.27	26.27	6.53	6.53	1.33	1.33
C balance (%)	99.7	100.0	94.5	96.5	95.8	91.1
EtOH conversion (%)	26.57	33.16	41.75	41.87	66.04	73.88
Diesel fuel precursor yield (%)	7.76	6.18	13.41	10.68	28.90	23.54
C6+ alcohol (%)	4.04	3.08	6.67	5.77	7.36	5.05
C6+ aldehyde (%)	0.90	0.83	1.26	1.26	3.17	2.80
C6+ ester (%)	2.28	1.18	3.67	1.90	11.43	10.43
C4+ ketones (%)	0.47	0.65	1.46	0.75	6.86	4.92

As presented in **Table 4.3**, the yield to diesel fuel precursors increases in our cofeed strategy in comparison to the control experiments. Percentage increments were between 1.58 to 5.36. The main contributors for such indicator are alcohols and esters, which show an average increment of ~1 percentage point each one.

4.3.2 Hydrogenolysis

Table 4.4. Composition used to evaluate the hydrogenolysis catalyst. Real G-66 data from a previous work[11]. Renormalized G-66 refers to the mol fractions produced when molecules with alkyl chains with more than eight carbons are neglected. Experimental G-66 represents the mol fraction of the simulated Guerbet stream produced in-house. In all the columns the overall alcohol and ester mol fraction was targeted to remain constant.

Compound	Real G-66 (%)	Renormalized G-66 (%)	Experimental G-66 (%)
1-Butanol	62.88	64.54	63.86
2-pentanol	1.74	1.79	2.08
1-hexanol	13.28	13.63	13.63
2-ethyl-1-butanol	4.67	4.79	4.99
2-heptanol	1.16	1.19	1.19
1-octanol	3.27	3.36	3.32
2-ethyl-1-hexanol	3.04	3.12	3.27
4-nonanol	0.69		
1-decanol	0.75		
2-undecanol	0.36		
1-dodecanol	0.36		
1-tetradecanol	0.09		
2-Pentadecanol	0.12		
2-Heptadecanol	0.00		
Isopropyl acetate	0.00		
ethyl butanoate	0.00		
Butyl acetate	0.00		
Isopropyl butyrate	0.09		
Butyl butanoate	1.95	2.23	2.20
Ethyl hexanoate	1.09	1.25	1.22
Hexyl acetate	0.70	0.80	0.86
Butyl hexanoate	1.62	1.85	1.83
Hexyl butanoate	0.19	0.21	0.22
Ethyl octanoate	0.00	0.00	0.00
Octyl acetate	0.12	0.14	0.16
Octyl butanoate	0.10	0.12	0.15
Butyl octanoate	0.05	0.06	0.07
Ethyl decanoate	0.73		
Decyl acetate	0.05		
Hexyl hexanoate	0.10	0.12	0.12
Hexyl octanoate	0.58	0.66	0.64
Ethyl dodecanoate	0.04		

Dodecyl acetate	0.04		
Octyl octanoate	0.12	0.13	0.19
Alcohol mol frac.	92.42	92.42	92.35
Ester mol frac.	7.58	7.58	7.65

The molar composition of the stream fed to the etherification area is a complex mixture of alcohols and esters, whose ester mole fraction, if left untreated, can be as high as 7.5%[11] (see **Table 4.4** for full description of the molar composition). Ideally, the ester concentration in the etherification reactor should be kept low since esters have a detrimental effect, decreasing the yield and selectivity of bimolecular dehydration products[11]. Here, we aim to decrease the ester content in the etherification feed through hydrogenolysis using a Cu/ZrO_2 catalyst[30, 31]. Copper has been reported as a transition metal for selective hydrogenation of C=O bonds, with ability to perform C-O scissions and negligible activity for C-C bond cleavage[32]. We initially conducted catalytic studies with a model feed of 5% hexyl-acetate and 95% butanol at WHSV=0.05, 0.16, 0.40, and 0.81 $g_{ester}\ g_{cat}^{-1}\ h^{-1}$. Experimental results for the catalytic reduction of esters through hydrogenolysis are shown in **Figure 4.6** for the hexyl acetate – butanol model feed. Concentrations presented in the panels (a) and (b) refer to the liquid phase after condensation of the effluents leaving the hydrogenolysis reactor.

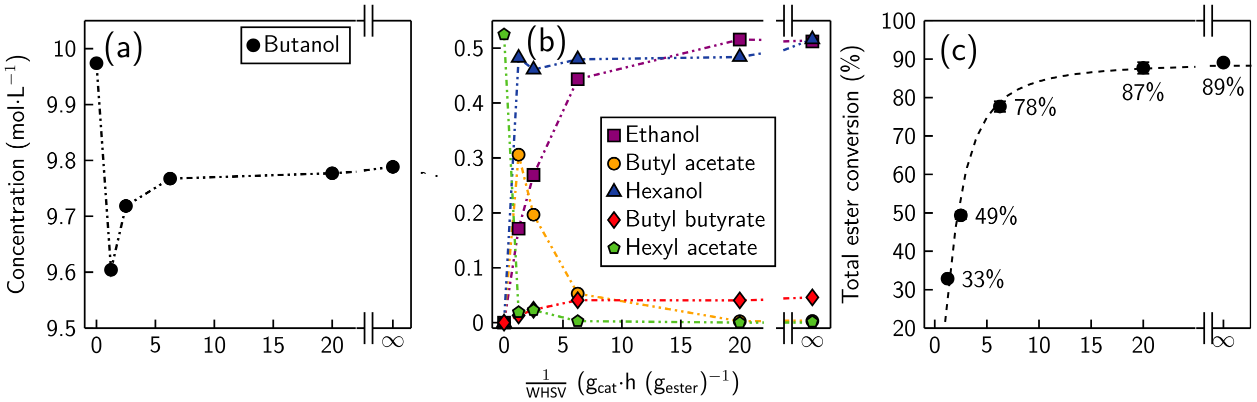

Figure 4.6. (a) and (b) mole concentration (M) in the liquid product at the outlet of the hydrogenolysis reactor for the reactants and most abundant products and (c) total ester conversion as a function of the inverse of the WHSV for a blend of 5% hexyl acetate and 95% butanol (mol/mol), T=200 °C, P_{tot}=420 psig, hexyl acetate:H_2= 1:480, 100-300 mg of 10% wt. Cu/ZrO_2. Data at 1/WHSV = ∞ corresponds to the equilibrium concentrations from Aspen Plus.

Table 4.5. Mole concentration in the outlet of hydrogenolysis reactor for the model mixture Hexyl acetate – Butanol 95-5% mol, accompanied by the percentage of ethyl, butyl, and hexyl chains identified at the outlet of the reactor with respect to those that were fed. Data reported at WHSV=0 was obtained from Aspen Plus, while data at WHSV=∞ represents the mole concentration of all the species in the feed.

WHSV (h^{-1})	∞ (Feed)	0.81	0.40	0.16	0.05	0 (ASPEN)
Compound	**(mM)**	**Mole concentration outlet reactor (mM)**				
acetaldehyde		9.17	0.01	0.01	10.89	1.59
ethanol		171.27	269.11	443.35	515.67	512.26
butyraldehyde		30.24	20.40	32.59	39.27	6.27
ethyl acetate		6.90	6.96	13.47	19.84	0.10
1-butanol	9973.90	9604.26	9718.54	9767.44	9777.09	9788.50
ethyl butanoate		5.04	2.54	5.44	3.37	3.10
butyl acetate		305.99	196.61	52.88	2.55	3.48
1-hexanol		482.34	460.94	479.58	483.80	516.31
butyl butanoate		13.14	23.50	40.85	40.50	45.98
hexyl acetate	524.94	19.08	22.85	2.77	0.08	0.16
butyl hexanoate		1.91	2.81	4.51	4.52	1.83
hexyl hexanoate		0.00	0.51	0.26	0.00	0.09
	Balance of Alkyl chains (%)					
Ethyl chain	-	101.9	100.8	103.1	101.3	-
Butyl chain	-	100.8	101.5	100	95.4	-
Hexyl chain	-	97.8	98.2	96.1	92.2	-

As observed in **Figure 4.6A**, butanol concentration presents a rapid decrease from 9.97 M to 9.6M (1/WHSV=1.23). Interestingly, butyl acetate exhibits the opposite trend (see Figure 3(b)) by going from 0 to 0.3M in the same contact time frame. In addition, hexanol concentration is observed to grow rapidly reaching values close to those of hexyl acetate at contact time zero, while ethanol rises more modestly as contact time increases, reaching similar concentrations to hexanol at high contact times (~20 h). The observed trend is an indication for a two-stage process, where initially hexyl acetate undergoes a transesterification reaction ruled by hexyl acetate + butanol → butyl acetate + hexanol, and then butyl acetate undergoes the hydrogenolysis, releasing the ethanol and butanol moiety, explaining the concentration rise of butanol and ethanol at 1/WHSV>1.23 h. We believe that butyl acetate is the main species that undergoes the hydrogenolysis reaction, however, we do not preclude that a fraction of the hexyl acetate fed to the system can also undergo catalytic reduction. Interestingly, butyl acetate arises as the predominant ester between 1/WHSV= 1.33 and 6.25 h, while butyl butyrate concentration becomes more important at contact times higher than 6.25 h. A complete description of the molar concentrations of all the species identified in the outlet of the hydrogenolysis reactor is presented in **Table 4.5**.

Based on the species identified experimentally and considering the poor ability of copper to cleave C-C bonds, we postulate that the system can be accurately described by **reactions R1** and **R2**. (R1) is hydrogenolysis of the ester. (R2) involves hydrogenation of the aldehyde.

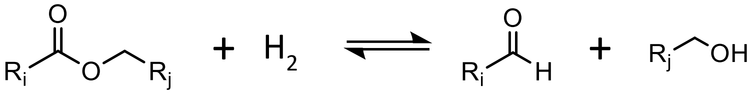

(R1)

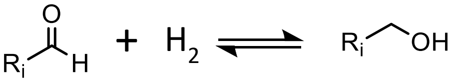

(R2)

We have performed thermodynamic equilibrium calculations at the reaction conditions in Aspen Plus V12.1 by implementing a linearly independent set of equilibrium reactions derived from the systematic combination of ethyl, butyl, and hexyl chains in reactions (R1) and (R2) (See table S4). Thermodynamic equilibrium calculations represent the limit case at which WHSV=0 h^{-1}. For comparison purposes, the results of the thermodynamic calculations are depicted in **Figure 4.6A** and **B** at 1/WHSV=∞, and complete data for all the products is presented in **Table 4.5**. **Figures 4.6A** and **B** show that extrapolation of the experimental molar concentration of all the species identified in the outlet of the hydrogenation reactor agree with the thermodynamic equilibrium calculations performed in Aspen.

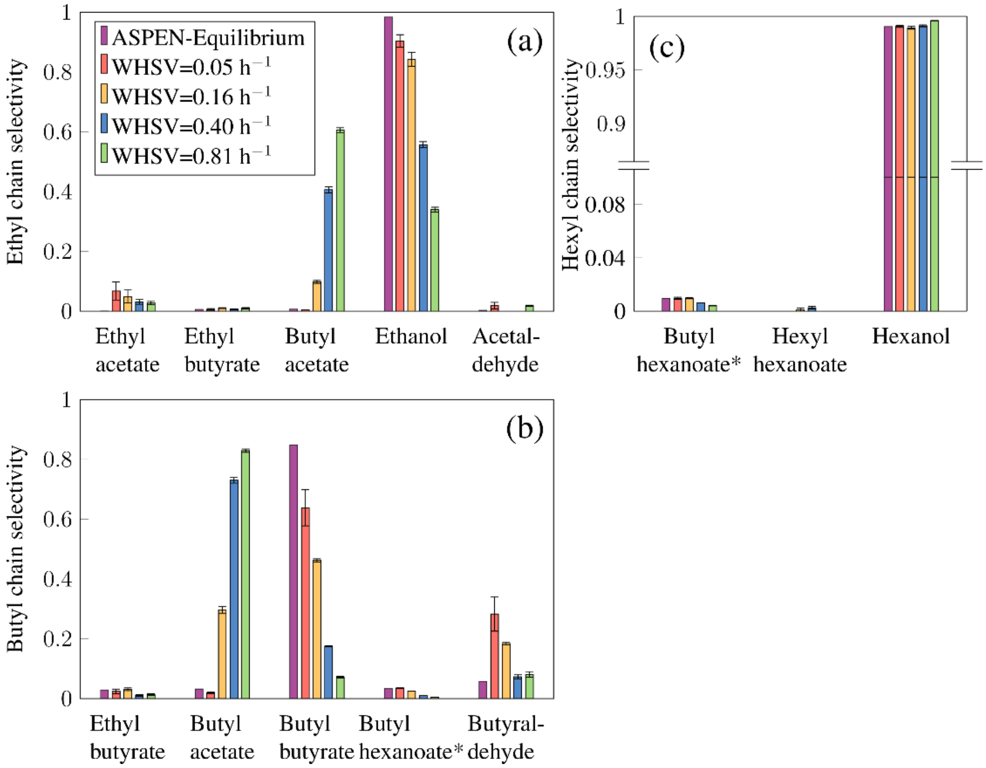

Figure 4.7. Alkyl chains selectivity at various WHSV for a blend of 5% hexyl acetate and 95% butanol, T=200°C, P_{tot}=420 psig, hexyl acetate:H_2= 1:480, 100-300 mg 10%wt. Cu/ZrO_2. The butyl hexanoate marked with *in figure (b) and (c) represents the sum of butyl hexanoate and hexyl butanoate given that both esters had similar retention times in our analytics and peak deconvolution was not possible to differentiate both species.

In reactions (R1) and (R2) it is observed that bond transformations come from C-O cleavage and hydrogenation of C=O, which implies no change of identity in alkyl chains R_i and R_j. In other words, the moles of each alkyl chain are conserved (alkyl chain balance is usually >95% for all our experiments (see **Table 4.5**)). This fact allows us to easily identify the fate of each alkyl chain and represent our results in terms of alkyl chain selectivity as defined by the **equation 2**.

$$S_{j,k} = \frac{\mathrm{mol}\ \left(ac_j\right)_k^{\mathrm{outlet}}}{\sum_i \mathrm{mol}\ \left(ac_j\right)_k^{\mathrm{outet}}} \qquad (2)$$

Where $S_{j,k}$ represents the selectivity of alkyl chain j to product k and $\left(ac_j\right)_k$ is the alkyl chain j in product k in the outlet of the reactor, with j= ethyl, butyl, hexyl. In our case, k adopts the name of those compounds identified in the reactor product and shown on the x-axis of **Figure 4.7A-C**. As depicted in **Figure 4.7A**, ethyl chains from hexyl acetate formed initially butyl acetate (due to hexyl acetate and butanol transesterification), and subsequently underwent hydrogenolysis, which released the ethyl moieties to form ethanol.

Other species containing ethyl chains like ethyl acetate, ethyl butyrate and acetaldehyde were detected as products with low preference for ethyl chains. **Figure 4.7B** shows the selectivity for butyl chains. The results point out that reacted butanol molecules formed preferentially butyl acetate, butyl butyrate and butyraldehyde. Finally, **Figure 4.7C** presents the selectivity for the hexyl chains. The data indicates that hexyl chains were hydrogenated to form hexanol, while butyl hexanoate was identified with a hexyl selectivity lower than 2%. Once again, our experimental data was compared with thermodynamic equilibrium calculations, demonstrating that at low WHSV values the alkyl chains tend to follow the equilibrium distribution.

Overall, the data presented in **Figure 4.6** shows that at high contact time (1/WHSV) the system converts most of the hexyl and acetate moieties into hexanol and ethanol, respectively. **Figure 4.8** shows that butanol conversion remains low (<4%), which indicates that the goal of performing the catalytic reduction of esters, while maintaining the butanol unreacted was satisfactorily achieved. **Figure 4.8** also depicts the stability of the Cu/ZrO_2 catalysts by tracking conversion of the reactants as a function of time on stream (TOS). Both for hexyl acetate and butanol the conversion remains unchanged up to 60 h. Deactivation of the catalyst in such a timeframe and conversion regime is then assumed as negligible, since carbon and mass balances were typically between 93-100%.

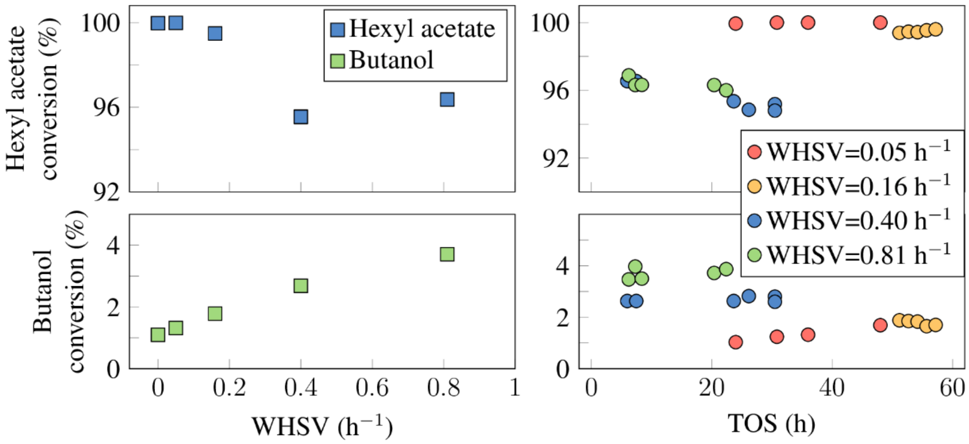

Figure 4.8. Hexyl acetate and Butanol conversion as a function of WHSV (left) and TOS (h) (right).

While it is known that esters have a negative impact on the etherification reaction,[11] the effect of each ester is still unclear. Thus, to track the effectiveness of the hydrogenolysis reaction, we define a total esters conversion (**Equation 3**). This function tracks the fraction of ester functionality removed without tracking particular esters. Experimental results are shown in Figure 3(c) along with the equilibrium value obtained through simulations (1/WHSV=∞). The fraction of esters removed increases monotonically as the contact time increases, approaching the thermodynamic limit (89.1%) when 1/WHSV is 20 h (ester removal ~87.7%).

$$\text{Total ester conversion}=1-\frac{\sum_i \text{ester}_i^{\text{outlet}}}{\sum_i \text{ester}_i^{\text{inlet}}} \quad (3)$$

After the initial characterization, we tested the catalyst with a realistic Guerbet coupling stream, consisting of a complex mixture of alcohols and esters with varied alkyl chain lengths. The composition of this stream is based on previous work at 66% ethanol single-pass conversion [11]. Herein, the complexity of the stream is reduced by neglecting compounds containing alkyl chains higher than eight carbons (See **Table 4.4** for composition). Equilibrium calculations were also carried out for this system using Aspen plus®. Given the presence of secondary alcohols in the Guerbet coupling stream, new chemical reactions to define the equilibrium between secondary alcohols and their respective ketones were added (**Reaction R3** and **Table 4.6**).

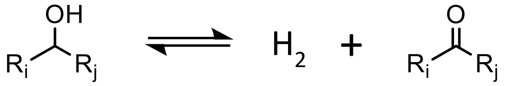

(R3)

Table 4.6. Linearly independent reactions for the hydrogenolysis equilibrium reactor using a simulated Guerbet stream. Item starts from 13 because these reactions are a complement for **Table 4.2**.

item	Reaction
13	2-Pentanone+H_2 ⇋ 2-Pentanol
14	2-Heptanone+H_2 ⇋ 2-Heptanol
15	2-Ethyl-butanal+H_2 ⇋ 2-Ethyl-butanol
16	2-Ethyl-hexanal+H_2 ⇋ 2-Ethyl-hexanol
17	Octanal + H_2 ⇋ Octanol
18	Ethyl octanoate + H_2 ⇋ Ethanol + Octanal
19	Butyl octanoate + H_2 ⇋ Butanol + Octanal
20	Hexyl octanoate + H_2 ⇋ Hexanol + Octanal
21	Octyl octanoate + H_2 ⇋ Octanol + Octanal
22	Octyl Acetate + H_2 ⇋ Octanol + Acetaldehyde
23	Octyl butyrate + H_2 ⇋ Octanol + Butyraldehyde
24	Octyl hexanoate + H_2 ⇋ Octanol + hexanal

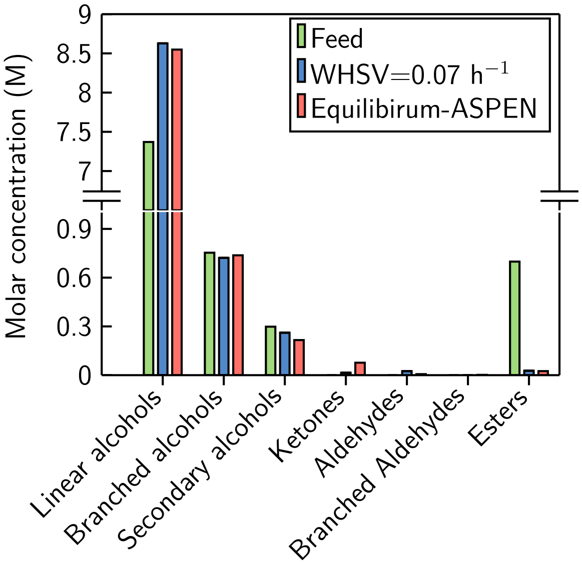

Figure 4.9. Molar concentration in liquid phase for hydrogenation of a simulated Guerbet coupling stream. Experiment conducted at WHSV=0.07 h^{-1}, T=200 °C, P_{tot}=420 psig, Ester:H_2= 1:480, 500 mg 10 % wt. Cu/ZrO_2.

Figure 4.9 presents the results of a catalytic esters reduction test using the simulated Guerbet coupling stream. The molar concentration distribution of the feed used in the experiment, the experimental liquid phase molar concentrations obtained in this study, and the equilibrium concentrations achieved in our simulations are shown in the figure. The results were calculated for the liquid phase after condensation of the products. The molar concentration of linear alcohols increased due to the hydrogenolysis of esters. Negligible dehydrogenation of branched alcohols was observed as predicted by thermodynamics. On the contrary, secondary alcohols dehydrogenation to their respective ketones was observed. Overall, branched and secondary alcohols remained almost unchanged, while the main catalytic activity was due to hydrogenolysis of esters and hydrogenation of aldehydes. Our results suggest that butyl butyrate, hexyl butyrate, and butyl hexanoate became the predominant esters in the outlet stream of the reactor, owing to butanol and hexanol being the most abundant species in the feed. Overall, the ester mol fraction was reduced from 7.6% to 0.3%, the linear alcohols mol fraction increased from 80.81 to 89.1%, and the total alcohols mol composition increased from 92.3 to 99.3%. The total ester conversion calculated by Equation (3) is 96.0±0.2%, while the thermodynamic limit predicted in Aspen is 96.35%. This result is shown in **Figure 4.9**, where the molar concentration of esters from our experiment and the thermodynamic equilibrium concentration is virtually the same. A complete description of the molar concentration of each species identified in the outlet of the reactor can be found in **Table 4.7**. These results highlight the feasibility of using hydrogenolysis to remove the esters produced in the Guerbet coupling reactor.

Table 4.7. Molar concentration distribution of all the species identified in our experiment for the Guerbet coupling stream Renormalized G-66 presented in **Table 4.4** run at WHSV=0.07 h^{-1}. Molar concentrations in the liquid phase for the feed, the experimental results after reaction and equilibrium concentrations predicted by Aspen are presented in mmol/L.

	Mole concentration (mM)		
Compound	**Feed**	**Experiment (WHSV=0.07 h^{-1})**	**Equilibrium (ASPEN)**
Ethanol	0.00	239.16	198.07
Butanol	5824.53	6376.23	6271.45
Hexanol	1243.16	1625.34	1658.94
Octanol	302.81	386.49	420.13
2-ethyl-butanol	455.13	439.07	445.11
2-ethyl-hexanol	298.25	282.55	292.33
2-pentanol	189.71	170.42	181.31
2-heptanol	108.54	91.10	34.65
Acetaldehyde	0.00	7.41	0.62
Butyraldehyde	0.00	17.19	4.02
Hexanal	0.00	0.37	1.56
Octanal	0.00	0.00	0.13
2-ethyl-butanal	0.00	0.00	1.56
2-Ethyl-hexanal	0.00	0.00	0.37
2-pentanone	0.00	9.83	4.87
2-heptanone	0.00	5.09	71.87
Butyl butyrate	200.66	13.97	14.64
Butyl acetate	0.00	0.00	0.66
Ethyl acetate	0.00	0.00	0.01
Ethyl butyrate	0.00	1.79	0.59
Hexyl acetate	78.44	0.00	0.15
Ethyl hexanoate	111.27	0.00	0.09
Hexyl butyrate	20.07	7.58	2.95
Butyl hexanoate	166.91	0.00	2.95
Hexyl hexanoate	10.94	0.00	0.76
Ethyl octanoate	0.00	0.00	0.25
Butyl octanoate	6.38	2.75	0.73
Hexyl octanoate	58.37	0.89	0.19
Octyl octanoate	17.33	0.54	0.05
Octyl acetate	14.59	0.00	0.05
Octyl butyrate	13.68	0.00	0.73
Octyl hexanoate	0.00	0.00	0.19

4.3.3 Process design

Table 4.8. Results for Guerbet coupling with 30% conversion using a cofeed strategy. The table shows the carbon stoichiometry of the reaction, i.e., it shows that at 30% conversion 73.73 mols of ethanol and 26.27 mols of butanol, yield a blend consisting of parafins (P), olefins (O), alcohols (A), aldehydes (AL), ketones (K), esters (ES) and some other minor components.

Component	Symbol	Carbon stoichiometry
Ethanol	A2	-73.73
Butanol	A4	-26.27
ethane	P2	0.03
n-propane	P3	0.09
n-butane	P4	0.01
n-pentane	P5	0.15
n-hexane	P6	0.00
ethylene	O2	0.03
propene	O3	0.25
1-butene	O4	0.14
1-pentene	O5	0.15
2-propanol	A3	0.52
2-butanol	A4-2	0.11
2-methyl-1-butanol	A5-2N	0.09
2-ethylbutan-1-ol	A6-2	4.50
1-hexanol	A6	16.13
2-heptanol	A7-2N	0.13
2-ethylhexan-1-ol	A8-2	1.91
1-octanol	A8	2.52
2-ethyloctan-1-ol	A10-2	0.21
1-decanol	A10	0.31
2-hexyl-1-octanol	A12-2	0.50
acetaldehyde	AL2	13.72
butyraldehyde	AL4	25.50
2-ethyl-2-butenal	AL6-2	0.09
hexanal	AL6	3.29
2-ethylhexanal	AL8-2	0.73
octanal	AL8	0.63
decanal	AL10	0.22
2-butanone	K4	0.39
2-pentanone	K5	1.57
2-heptanone	K7	2.06
3-octanone	K8	0.08
2-nonanone	K9	1.07
4-undecanone	K11	0.55
ethyl acetate	ES4	4.08
ethyl butanoate	ES6	4.17
butyl acetate	ES6-2	3.38
butyl butanoate	ES8	3.26
ethyl hexanoate	ES8-2	1.18
acetic acid, hexyl ester	ES8-3	0.42
butyl hexanonate	ES10	1.66

butanoic acid, 2-ethyl, butyl ester	ES10-2	0.14
hexyl hexanoate	ES12	0.62
butyl decanoate	ES14	0.14
diethyl ether	E4	0.01
1-propoxy-1-ethanol	B5	0.64
1,1-diethoxybutane	B8	0.28
1-butoxy-1-ethoxyethane	B8-2	0.67
1,1-dibutoxyethane	B10	0.48
COx	CO2	1.20

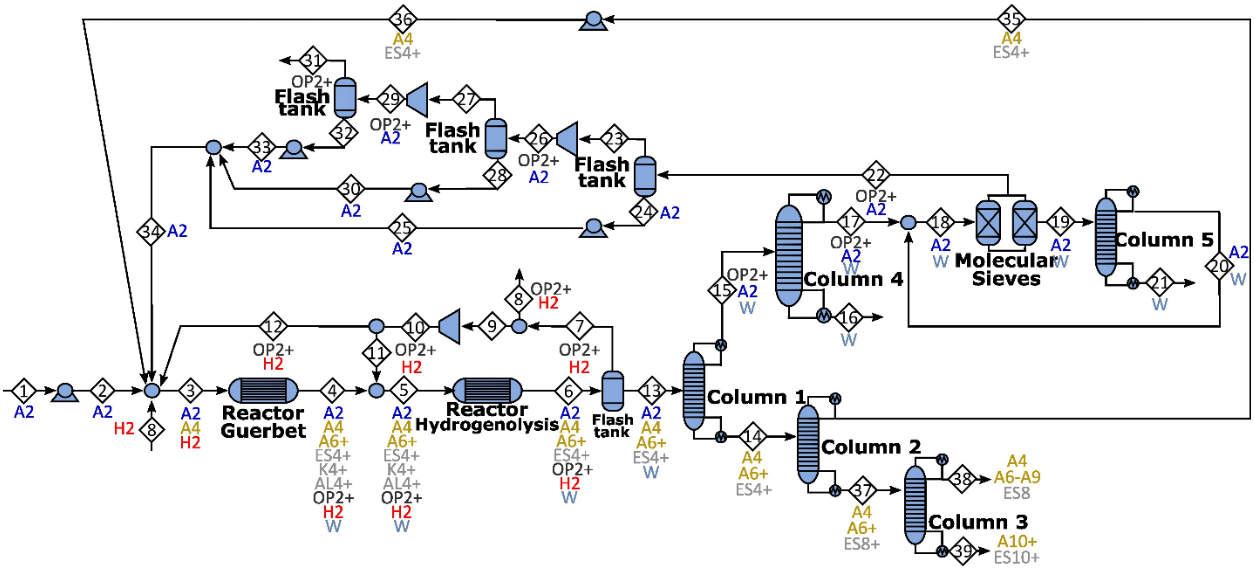

Figure 4.10. Layout of the Guerbet and hydrogenolysis area. Chemical species labeling: A: alcohols, ES: esters, K: ketones, AL: aldehydes, OP: olefins/paraffins, H: hydrogen, and W: water. The numerical characters indicate the carbon length.

Based on the results of Guerbet coupling with butanol recycling and hydrogenation results (**Figures 4.2, 4.6** and **Table 4.8**), we synthesize a process for the conversion of ethanol into higher alcohols (**Figure 4.10**). Specifically, we implement a butanol recycle strategy ensuring an ethanol to butanol ratio in the reactor feed close to 70:3, using the results for a 30% single-pass ethanol conversion in the Guerbet step (See **Table 4.8**). Additionally, we implement a hydrogenolysis step to remove the esters. We select operational conditions (temperature, pressure, and hydrogen to alcohols ratio) to ensure full conversion of ketones and aldehydes and 95% conversion of esters.

The Guerbet coupling reactor operates at 325 °C and 25 bar with hydrogen as a carrier gas in a 1:4 molar ratio of hydrogen:(ethanol + butanol). The hydrogenolysis reactor operates at 200 °C and 25 bar, with a hydrogen:ester ratio of 400:1. Both reactors operate at a slightly higher pressure than the one reported experimentally to facilitate subsequent separations. The products of the hydrogenolysis reactor are partially condensed in a flash tank, enabling hydrogen recycling. A sequence of distillation columns and a molecular sieving unit are used to recover and recycle the reactants (ethanol and butanol) (streams 34 and 36), a higher alcohol rich stream (stream 37), and wastewater (streams 16 and 21). We note that column 3 splits stream 37, rich in higher alcohols, into a heavy product at the bottom containing alcohols with more than 10 carbons, and a light product, at the top, rich in C4-C9 alcohols which is the feedstock for the etherification area. The heavy stream is blended directly into the diesel product. The composition of the etherification feedstock stream is shown in **Table 4.9**. The most abundant alcohol is hexanol, in contrast with the results of Retrepo-Florez et al, where butanol was the main alcohol[11]. The esters fraction is 0.32 % mol, thus, the etherification feed consists almost entirely of alcohols.

Table 4.9. Composition of the stream fed to the etherification area. L/B represents the linear to branched alcohol ratio. L/S represents the linear to secondary alcohol ratio.

Chemical species	Symbol	Mol percentage
N-Butanol	A4	34.622
2-Butanol	A4-2N	1.324
2-Methyl-1-butanol	A5-2	3.612
1-Hexanol	A6	40.221
2-Ethyl-1-butanol	A6-2	8.329
2-Heptanol	A7-2N	3.406
2-Ethyl-1-hexanol	A8-2	3.592
1-Octanol	A8	4.245
2-Octanol	A8-2N	0.109
2-Nonanol	A9-2N	0.219
N-Butyl-N-Butyrate	ES8	0.210
Ethyl-Caproate	ES8-2	0.080
N-Hexyl-acetate	ES8-3	0.032
L/B	5	
L/S	16	

4.4 Producing ethers and olefins from higher alcohols

4.4.1 Etherification

The alcohol rich stream produced in the Guerbet coupling area (stream 38) is used as a feedstock in an etherification reaction that uses HY zeolite as catalyst (see **Table 4.9** for feedstock composition). For simplicity, in the etherification catalyst characterization experiments we have assumed complete removal of esters prior to entering the reactor (i.e., we did not include the small fraction of ES8, ES8-2 and ES8-3 shown in **Table 4.9**). The addition of n-butanol in the ethanol oligomerization reactor leads to increased C6+ alcohol content, compared to when only ethanol is used. Here, the C6+ alcohol mol fraction is at ~60%, compared to our previous reported work, where we used a dehydration feed stream containing 30 mol% of C6+ alcohols[11]. We also note that the addition of n-butanol in the oligomerization reactors leads to an increase in branched alcohols. This is expected, as alcohols larger than ethanol react as nucleophiles to produce larger branched products over alcohol coupling catalysts[23]. Furthermore, the size of the secondary alcohols increases with the introduction of the n-butanol recycling stream, leading to an increase in the average size of the final olefin fuel precursors obtained from the dehydration reactor.

Table 4.10. Carbon selectivity for etherification reaction using EtOH/recycled-ButOH oligomerization products (the feed stream is shown consist of the alcohols shown in table 3). Carbon not detected in the liquid or gas phase was assumed to go to coke products.

Compound	Carbon #	Selectivity
Ethers		
Butyl ether	8	5.28
Butyl ethyl-butane ether	10	1.56
C_{10} linear ethers	10	20.98
Butyl ethyl-hexane ether	12	0.85
Hexyl ethyl-butane ether	12	3.18
C_{12} linear ethers	12	22.20
Hexyl ethyl-hexane ether	14	1.72
Octyl ethyl-butane ether	14	0.47
C_{14} linear ethers	14	4.81
C_{16} linear ethers	16	0.30
Olefins		
Butenes	4	1.70
C_5 olefins	5	0.62
C_6 olefins	6	5.05
Heptenes	7	4.41
C_8 olefins	8	2.76
Nonenes	9	0.26
Unknown products	-	5.19
Coke	-	18.66

A detailed breakdown of the selectivity obtained in the etherification reaction (defined as the percentage of total mols of carbon contained in a product to the total mols of carbon converted) is shown in **Table 4.10**. Compared to our previous results[11], we observe a reduction in the selectivity toward light ethers (e.g., n-butyl ether), showing a shift toward the production of larger distillate-range molecules. We note that while the C_{10+} ether selectivity slightly changes between previous results (~50% vs. ~56% in this paper), there is also a noticeable change in the yield of C_{10+} ethers. We previously reported that a relevant economic factor for our ethanol to diesel technology is fuel yield[11]. In the current work, we increase the yield of distillate range molecules by reducing the butyl ether yield from 14% to 4%. This can be attributed to an increase in the fraction of C_{6+} alcohols in the feed stream. These results are an indication that the butanol recycling strategy implemented succeeded in reducing the amount of low molecular weight ethers formed.

This demonstrates the possibility of using the butanol recycle fraction as a control variable to tune the molecular weight distribution of the products. In addition to the ethers obtained, we also observed a fraction of olefins (4 to 9 carbons). These olefins result from the dehydration of β −branched alcohols and secondary alcohols in the reaction blend[11]. Finally, we note that a large fraction of coke is produced (~18%). This indicates that further research is needed to develop tailored catalysts to reduce the coke yield. The catalyst used was tested by running a flow reactor for 21 h continuously. The results are shown in **Figure 4.11**, where we show conversion, carbon balance, and product selectivity as a function of time on stream. These values remain relatively stable throughout the test.

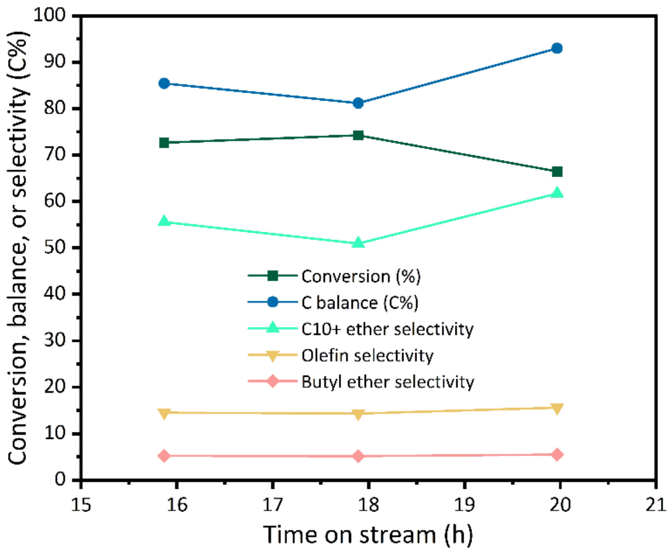

Figure 4.11. TOS data for EtOH/oligomerization dehydration products. Reaction conditions: T= 170 °o., P= 110 psig, feedstock flowrate = 0.040 mL/min, Ar flowrate = 10 mL/min, WHSV = 1.085 h^{-1}.

Table 4.11. Set of reactions used in the etherification reactor model. Conversion for each reaction was determined based on the experimental results obtained. Chemical species labeling: letter indicates species type, and number carbon length. A: alcohol, O: olefins, E:Ethers, and W: water. If more than one ether of length "X" is produced it is indicated with a second number (e.g., E12-1, and E12-2). Secondary alcohols are shown by adding the particle 2N to the name (e.g., A9-2N).

Item	Reaction	Conversion
1	2A4->E8+W	0.159
2	A4 + A6-2 --> E10 + W	0.115
3	A4 + A6 --> E10-1+ W	0.258
4	A4 + A8-2 --> E12 + W	0.153
5	A4 + A8 --> E12-3 + W	0.195
6	A4--> O4 + W	0.013
7	A4-2N --> O4 + W	1
8	A5-2 -->O5 + W	0.491
9	A6 + A6-2 --> E12-1 + W	0.03
10	2 A6 --> E12-2+ W	0.372
11	A6 + A8 --> E14 + W	0.373
12	A6 + A8-2 --> E14-1+ W	0.272
13	2 A6 --> E12-2 + W	0.028
14	A6-2 + A8 --> E14-2 + W	0.035
15	A6-2 --> O6+ W	0.385
16	A7-2N --> O7 + W	1
17	A8-2 --> O8 + W	0.432
18	2 A8 --> E16-3 + W	0.04
19	A8 --> O8 + W	0.107
20	A8-2N --> O8 + W	0.432
21	A8-2N --> O8 + W	0.432
22	A9-2N --> O9 + W	1

Table 4.11 shows the conversion for each of the reactions that are happening in the dehydration step. Each alcohol in the feedstock can undergo different reactions leading to the formation of ethers or olefins. The observed ether and olefin carbon selectivity is shown in **Figure 4.12**. The carbon selectivity ($S_{i,j}=n_{i,j}^{\mathrm{out}}/n_{i}^{\mathrm{Conv}}$) is defined as the ratio between the mols of carbon in product j coming from alcohol i ($n_{i,j}^{\mathrm{out}}$), and the mols of alcohol i converted (n_{i}^{Conv}). It is important to note that this selectivity is a function of the feed composition, since the presence of other alcohols determines the type of products that can be formed. We highlight that in the case of 1-butanol, around 50% of the carbon is converted into E10+ ethers (linear and branched).

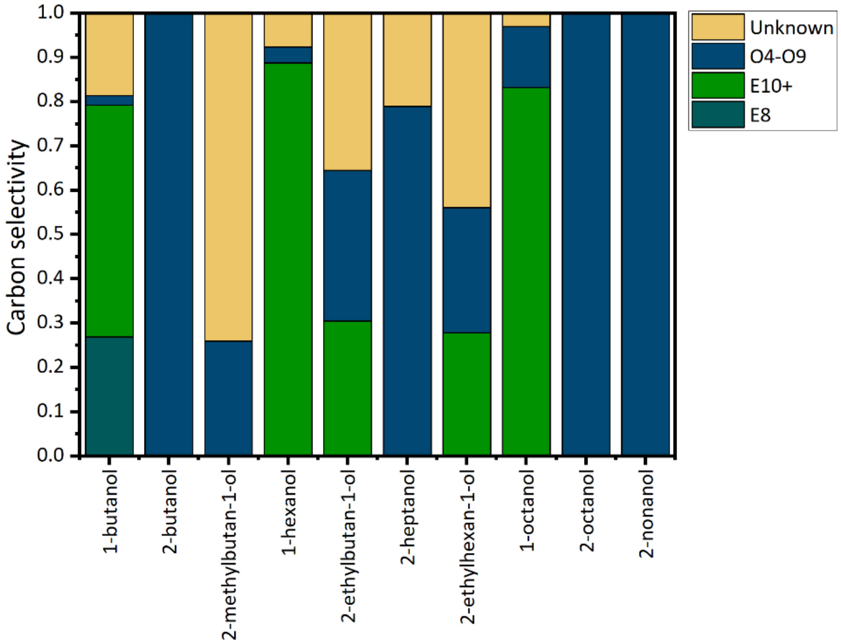

Figure 4.12. Carbon selectivity for the etherification reaction when HY zeolite is used as catalyst. Reaction conditions: T= 170.1 ºC, P = 110 psig, feedstock flowrate = 0.040 mL/min, Ar flowrate = 10 mL/min, WHSV = 1.085 h^{-1}. Chemical species labeling in the legend: letter indicates species type, and number carbon length. O: olefins, E: Ethers.

4.4.2 Process Design

Using the results in **section 4.4.1**, we synthesize a process for the conversion of higher alcohols into diesel fuel (see layout in **Figure 4.13**). We have made two assumptions about the etherification reaction: 1) we assume that the reaction does not require a carrier gas to be performed, and 2) we assume that the coke formation can be neglected. These assumptions are reasonable given that this is a low TRL process and are in line with the expected performance for a catalyst used at an industrial scale. At a high level, a blend of alcohols produced by Guerbet coupling (composition shown in **Table 4.9**) is used as input to the etherification area. The products of the reaction are separated using a sequence of distillations (columns 1 to 4 in **Figure 4.13**), along with a heteroazeotropic separation system (columns 5 to 7 and decanter). The separation system following the etherification reactor ensures the recycling of unconverted alcohols (streams 10 and 19), and the distribution of olefins (streams 11, 23 and 32) and ethers (streams 7 and 8) such that olefins are oligomerized and ethers are used to produce a diesel blend. The oligomerization area (shown in red) increases the molecular weight of the smaller olefins, and thus, diesel yield. The reactor in this area is modeled following the approach described by Restrepo-Flórez et al, 2023[11]. Additionally, we use a final fractionation area (shown in blue) consisting of two distillation columns, where all streams used for fuel production are fractionated into three products according to their initial boiling point: diesel #1, diesel #2, and gasoline. Importantly, the Diesel #2 fraction is ~91% of the fuel obtained, which is higher than previous reported value of ~50%[11]. The diesel #1 fraction is 5%, and the gasoline fraction is 4%. This result is important, because it demonstrates that the fraction of recycled butanol can be used to control the ether distribution to favor the production of diesel #2.

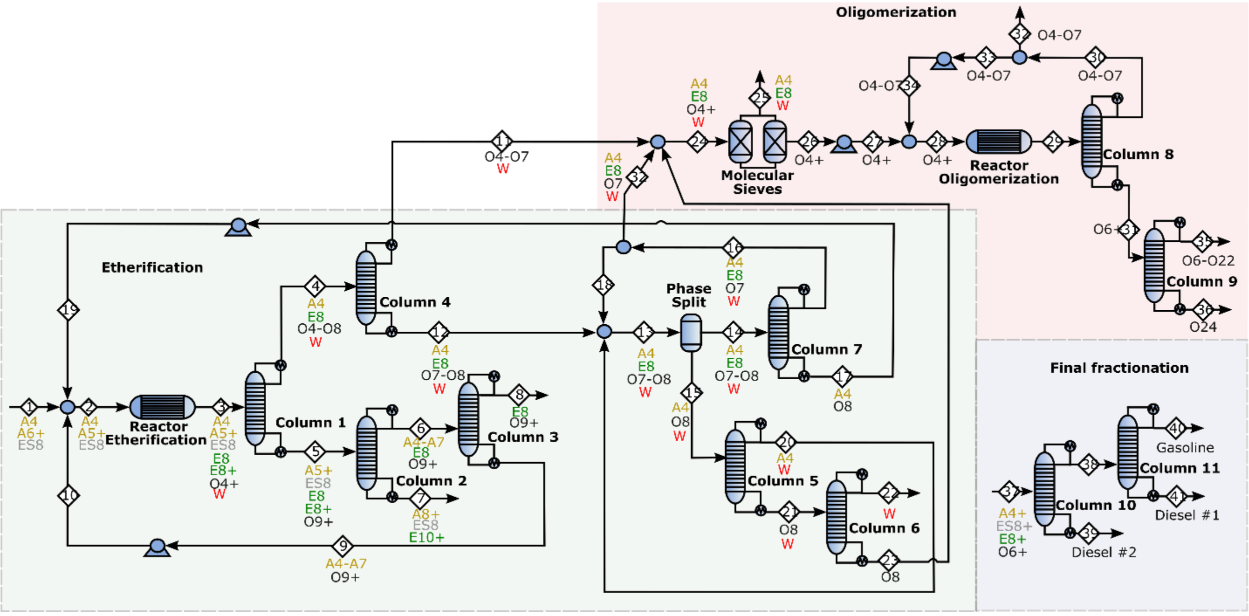

Figure 4.13. Layout of the etherification (green), oligomerization (red), and final production fractionation (blue) areas. Chemical species labeling: letter indicates species type, and number carbon length. A: alcohols, ES: esters, K: ketones, AL: aldehydes, OP: olefins/paraffins, H: hydrogen, and W: water.

4.5 Fuel characterization

The physicochemical properties of the fuels produced are estimated based on literature reported blending rules and in-house developed methods, as we have previously described[8, 11, 33]. The results obtained are shown in **Table 4.12**. The diesel #2 fraction produced (our primary product) is characterized by a very high cetane number (~94) and outstanding cold flow properties (cloud point of -28.9 ºC). While its density is slightly lower than that of a typical fossil diesel (795 kg/m^3 vs. 815-840 kg/m^3 for diesel #2) we note that this value is not regulated by an ASTM standard[25]. In the case of viscosity and flash point, we observe marginally lower values than those of the specification[25] and are the diesel fuel minimum values are within the uncertainty of the estimation method. The only property that is substantially below the ASTM standard requirement is the T90 (246.4 ºC vs. a minimum of 282 ºC for diesel #2[25]). The fact that this value is lower implies that to satisfy the ASTM standard, the fuel produced needs to be used in a blend. However, we note that a lower T90 can be beneficial from an operating perspective if the flash point requirement is satisfied, as it is in this case[34].Thus, there are no operational constraints to use the fuel produced as a drop-in diesel. If the diesel product in this work is used as a blend, an improvement in the cetane number of the base fuel may be obtained. For reference, the expected cetane number obtained for a 20% (vol/vol) blend between our diesel and a base diesel with a cetane number of 40 is ~50.8 (based on a linear blending rule by volume). The diesel #1 and gasoline fractions produced are a minority adding to less than 10% of the total product, their physicochemical characteristics are more suitable to be used in blends rather than as drop-in fuels. In the case of diesel #1, the main limitation is the flash point which is significantly lower than the requirement (22.2 °C vs 38 °C). In the case of gasoline, the octane number (estimated based on the calculated cetane[35]) is too low (~59 vs 89).

Table 4.12. Predicted properties of the fuels produced in this work. We present a comparison with typical values from fossil fuels based either the ASTM standards[25, 36] or the world fuel charter for gasoline and diesel[37]. Additionally, we show the results previously reported by our group[11].

Fuel	**Source**	**CN**	**ρ [Kg/m^3]***	**μ [mm^2/s]**	**FP [°C]**	**CP [°C]**	**T90 [°C]**
Diesel #2	Fossil	40[25]	815-840	1.9-4.1[25]	52[25]	-	282-338[25]
	Previous work	73.2	789.7	1.92	49.9	-37.3	241.9
	This work	94.4	794.7	1.71	51.4	-28.9	246.4
Diesel #1	Fossil	40[25]	815-840	1.3-2.4[25]	38[25]	-	<288[25]
	Previous work	69.6	815.3	0.7	20.7	-102.7	139.8
	This work	56.2	781.3	0.87	22.2	-108.1	134.3
Gasoline	Fossil	<10	715-770	<2*	-	-	<190[36]
	Previous work	11	827.9	0.64	-19.75	-98.25	87.9
	This work	33.1	707.4	0.50	-13.67	-99.4	110.2

4.6 Economics

To study the economics of the process, a detailed discounted cash flow analysis is performed. The main assumptions are listed in **Table 4.13**. Equipment costs are estimated using Aspen Process Economic Analyzer, as shown in **Table 4.14**. The installation factors are taken from the work of Humbird and coworkers[17]. Operating costs such as feedstocks, waste treatment, and utilities are calculated based on simulation results. The lignocellulosic ethanol price used in the base case ($2.85/Gal) corresponds to the value estimated by NREL[17]. For the catalyst cost estimation, we use either the recently developed tool CatCost[38] (Guerbet coupling and hydrogenolysis catalysts), or commercially available data for zeolites[39, 40] (etherification and oligomerization catalysts).

Utility consumption is reduced by more than 40% in heating and cooling duties by implementing heat integration based on pinch analysis[41]. The associated heat exchanger network (HEN) consists of 83 heat exchangers, and it is designed in Aspen Energy Analyzer®. Furthermore, energy rich purge streams are used to produce steam (~138 GJ/h assuming 80% efficiency with respect to the low heating value), partially offsetting the energy needs of the refinery.

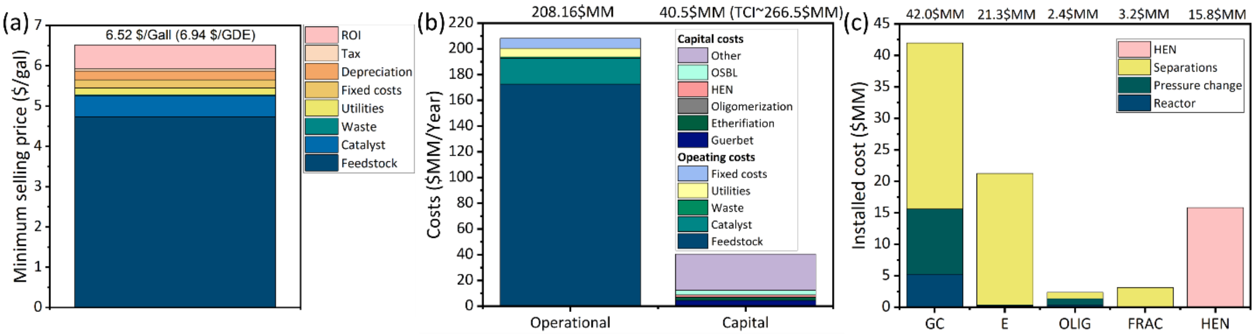

Figure 4.14. (a) minimum fuel selling price (MFSP) (b) annualized capital and operating costs (c) total installed cost per area. GC: Guerbet Coupling, E: Etherification, OLIG: Oligomerization, FRAC: final fractionation, HEN: Heat Exchanger Network.

In **Figure 4.14**, we show the minimum selling price (**Figure 4.14A**, annualized capital and operating costs (**Figure 4.14B**, and a breakdown of the installed costs per area (**Figure 4.14C**)). The minimum selling price is \$6.52/gal (\$6.94/GDE, where GDE stands for gallon of diesel equivalent). These results are obtained for an ethanol price of \$2.85/gal; if a cheaper feedstock is used (e.g., corn ethanol), then a significantly lower MFSP is obtained. For reference, the current price of corn ethanol is ~\$2.41/gal, and in the last 20 years it has reached a low price of ~\$1.5/gal[42]. If these prices are used, the MFSP is 5.78 \$/gal (6.15 \$/GDE) and 4.39 \$/gal(\$4.66/GDE), respectively. To put these results in perspective, the spot price of diesel in the last 5 years has been between \$2.03/gal-\$4.90/gal[43]. The main competing technologies available at a commercial scale are biodiesel produced by transesterification of vegetable oils and hydrotreated vegetable oils (HVO) produced by hydrogenating vegetable oils. Vegetable oils are a more expensive feedstock than ethanol with limited availability. Based on the average transesterification yield, methanol cost, and assuming product credits from glycerol in the amount of \$0.4/kg, the feedstock cost of biodiesel has been between \$2.0/gal-\$7.1/gal in the last 5 years[44]. For reference, the cost of feedstock represents ~81% of the total production cost[44]. Biodiesel also receives US federal subsidies of a \$1.00/gal blenders credit and a D4 RIN that ranged from \$1.46/gal-\$1.81/gal in 2022[45]. In contrast, the process that we propose leads to feedstock costs ranging from \$2.3/gal-\$4.6/gal based on corn ethanol price values. This highlights the advantages of using ethanol to produce diesel fuel as opposed to vegetable oils. At a low-to-medium Technology Readiness Level (TRL), several candidate technologies (See **Table 4.1**) have emerged for sustainable diesel fuel production. Among these technologies, gasification followed by Fischer-Tropsch synthesis received significant research attention[46-50]. In comparison with this technology, our system has similar economic potential, with two added advantages (1) it does not need to deal with tar contamination, an important bottleneck in biomass gasification systems[51], and (2) it offers a higher flexibility in tailoring fuel properties, as the recycle strategy developed in this work ensures that one can tune the ether distribution to achieve higher cetane numbers.

The total operational costs, shown in **Figure 4.14B**, are dominated by feedstock costs, ~92% of which are due to ethanol and the remaining 8% due to hydrogen. The total operational cost is ~208.2 $MM/year (~$5.7/gal) and the annualized capital cost is ~40.5 $MM. The total capital investment (TCI) is ~267$MM. The breakdown of capital costs per area in **Figure 4.14C** shows that the Guerbet coupling area is the most capital intensive with the cost of reactors and pressure changing equipment (mainly compressors required in the gas recycle streams) being the most significant. This result points toward the need to operate at higher conversion, while still maintaining high product selectivity. In addition, the operation of the hydrogenolysis reactor at a lower hydrogen to esters ratio would be beneficial because it would result in reduced compressor size.

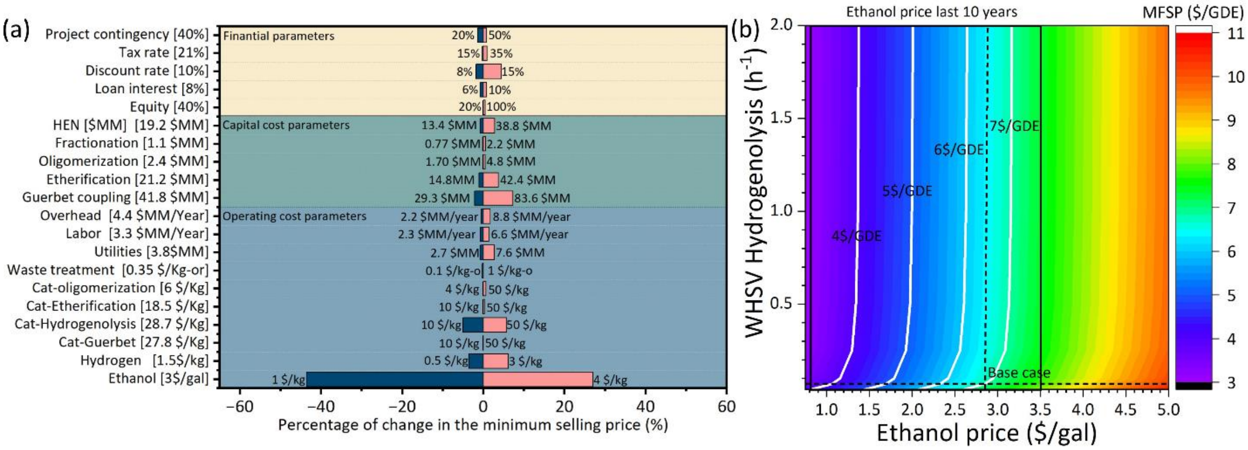

Figure 4.15. (a) Tornado plot showing the sensitivity of the MSFP to different parameters. The reference value is shown on the y-axis. Optimistic and pessimistic values for each parameter are used (shown at the sides of each bar) (b) Heat map showing the minimum selling price as a function of the ethanol price and the WHSV of the hydrogenolysis catalyst. The range for corn ethanol prices in the last 10 years is shown.

To further understand the impact of the different parameters and assumptions made in the estimation of the MFSP, we perform a sensitivity analysis as shown in **Figure 4.15A**. Reference values are shown on the y-axis legend. The parameters are varied within a range (shown at the sides of each bar) that represents reasonably optimistic and pessimistic scenarios with respect to the base case value. The corresponding percentage change in the MFSP is shown on the x-axis. Parameters are grouped into three categories: 1) operating costs, 2) capital costs, and 3) financial assumptions. Among the parameters in the first group, the costs of ethanol, hydrogenolysis catalyst, and hydrogen are the more influential in that order. Changes in the other parameters result in marginal changes in the MFSP. In terms of catalysis, the largest consumption is for the hydrogenolysis reaction – 613 ton/year, in comparison with 3.3 for Guerbet, 19 for etherification, and 32 for oligomerization. This is because the hydrogenolysis catalyst has a very low WHSV ($0.07h^{-1}$) and processes a large stream. Among the parameters in the second group, the total capital cost of the Guerbet area is the most influential. Reductions in its capital cost can be achieved, for example, by operating the Guerbet reactor at higher conversion. Finally, among the financial parameters the discount rate appears to be the most important one. In the base case scenario, we assume a value of 10%, consistent with other reference studies on biofuel production[17]. Based on **Figure 4.15A**, we conclude that the two most influential parameters are the price of ethanol and the cost of the hydrogenolysis catalyst. Accordingly, the impact of these two parameters is explored in more detail in **Figure 4.15B** where we use the WHSV as a proxy of catalyst cost (if the WHSV increases, the amount of catalyst decreases and the size of the hydrogenolysis reactor diminishes). The figure is based on the range in which the price of corn ethanol has oscillated in the last 10 years[42] and our reference case, based on lignocellulosic ethanol cost.

Table 4.13. Parameters and assumptions in the discounted cash flow analysis

General parameters	**Parameter value**	**Source**
Reference capacity	504 Ton/day	17
Reference year	2021	
Financial variables		17
Equity	40%	
Loan interest	8%	
Loan term (years)	10	
Operation period (years)	30	
Depreciation period (years)	7	
Construction period (years)	3	
Discount rate	10%	
Income tax	21%	
Working capital (% of FCI)	5%	
Direct costs		
OSBL (% of ISBL)	40%	17
Warehouse (% of ISBL)	4%	
Site development (% of ISBL)	9%	
Additional piping (% of ISBL)	4.5%	
Indirect costs		
Proratable expenses (% TDC)	10%	17
Field development (% TDC)	10%	
Office & construction fee (% TDC)	20%	
Contingency (% TDC)	40%	
Other cost (%TDC)	10%	
Materials		
Ethanol ($/kg)	0.999	17
H_2 ($/kg)	1.43	52
Catalyst Guerbet ($/Kg)	27.76	38
Catalyst Hydrogenolysis ($/Kg)	28.72	38
Catalyst Etherification ($/Kg)	18.5	40
Catalyst Oligomerization ($/Kg)	6	39
Utilities		
Refrigerant ($/kJ)	2.24×10^{-7}	11
Water ($/kJ)	2.24×10^{-7}	
Low pressure steam ($/kJ)	2.00×10^{-6}	
Medium pressure steam ($/kJ)	2.32×10^{-6}	
Hot oil ($/kJ)	3.69×10^{-6}	
Fired heat ($/kJ)	4.48×10^{-6}	
Electricity ($/kJ)	1.68×10^{-5}	
Waste management		
Waste treatment($/kg-organic)	0.35	53
Labor		
Shifts	5	17
Manager	1 ($193.000)	
Engineers	3($92.000)	
Maintenance supervision	3 ($75.000)	
Maintenance technicians	15 ($53.000)	
Shift supervisors	5 ($63.000)	
Shift operators	25($52.000)	

Table 4.14. Details of the process equipment cost and design parameters for the different areas. P: pressure of operation. T: temperature of operation. ΔP: pressure drop. N: number of plates.

	Equipment	**Cost**	**P [Bar]**	**T [°C]**	**Duty**	**ΔP [Bar]**	**N**	**Reflux**	**Feed stage**
Guerbet coupling area	Guerbet reactor	$1.41	25	325					
	Hydrogenolysis reactor	$3.85	25		0				
	Compressor 1	$5.15				1			
	Compressor 2	$1.41				3			
	Compressor 3	$1.52				5			
	Pump 1	$0.44				25			
	Pump 2	$0.54				25			
	Pump 3	$0.53				25			
	Pump 4	$0.39				22			
	Pump 5	$0.05				7			
	Pump 6	$0.35				17			
	Flash vessel 1	$0.56	24	25					
	Flash vessel 2	$0.18	1	35					
	Flash vessel 3	$0.08	3	35					
	Flash vessel 4	$0.08	8	35					
	Column 1-Guerbet	$4.63	1				20	1	10
	Column 2-Guerbet	$3.57	1				30	1	10
	Column 3-Guerbet	$4.25	1				60	1	10
	Column 4-Guerbet	$9.11	1				60	1.7	10
	Column 5-Guerbet	$1.71	1				31	1	10
Etherification area	Etherification reactor	$0.24	7		0				
	Pump 1	$0.13	6						
	Pump 2	$0.04	6						
	Flash vessel	$0.12	1	78					
	Column 1-Etherification	$3.39	5				35	2	10
	Column 2-Etherification	$1.08	1				20	2	10
	Column 3-Etherification	$4.79	1				60	6	15
	Column 4-Etherification	$7.93	3				40	4	9
	Column 5-Etherification	$0.61	1				20	2	10
	Column 6-Etherification	$1.84	1				20	2	10
	Column 7-Etherification	$1.10	1				20	2	10
Olig.	Oligomerization reactor	$0.41	40	230					
	Pump 1	$0.50				40			
	Pump 2	$0.49				38			
	Column 1-Oligomerization	$0.82	2				25	2	10
Sep.	Column 1-Final fractionation	$0.62	1				20	2	10
	Column 3-Final fractionation	$0.52	1				20	1.5	10
	Column 3-Final fractionation	$2.04	1				40	3	10

4.6 Life cycle analysis

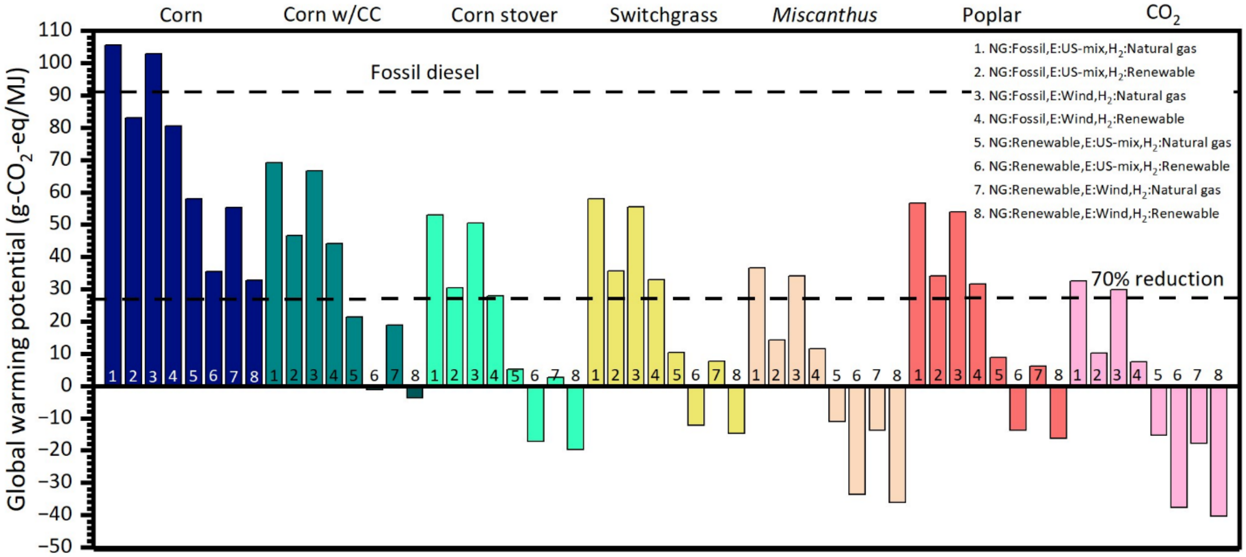

Figure 4.16. Well-to-wheels GHG emissions of the diesel fuel produced in this work. Seven different ethanol sources are evaluated. The numbers in the bars correspond to different scenarios (see legend for key).

A well-to-wheels LCA analysis of the proposed technology is performed using the GREET model[54] (**Figure 4.16**) and a functional unit of 1 MJ of fuel. Coproduction of gasoline is accounted for using a resource displacement approach based on the energy content. In terms of environmental impacts, we focus on characterizing the global warming potential of the proposed technology. The vehicle is modelled using the default parameters for a long-haul truck. We evaluate six different ethanol feedstocks (corn, corn stover, switchgrass, miscanthus, poplar, and CO_2). Additionally, we explore the case where ethanol is produced using corn in a biorefinery in which carbon capture is implemented (labeled "Corn w/CC”). Eight different scenarios are evaluated for each feedstock. These scenarios are defined considering the sources of natural gas (shale gas or food waste anaerobic digestion), electricity (current US mix or wind), and hydrogen (methane or water electrolysis using renewable electricity). Natural gas is used in the refinery to produce steam. The most conservative scenario (#1) assumes that natural gas and hydrogen are produced from nonrenewable resources while electricity is obtained from the grid. In this case, only ethanol from miscanthus or from CO_2 via gas fermentation and electrochemical reduction are close to the target of reducing GHG emissions more than 70% in comparison to fossil diesel. On the other hand, the most optimistic scenario (#8) assumes that natural gas, electricity, and hydrogen are produced from renewable sources. In this case, all feedstocks, except for corn, can attain carbon negative emissions. We note that in the optimistic scenario, we can significantly benefit from developments in renewable hydrogen production which is a priority area in the U.S. research agenda[55]. Importantly, corn ethanol has significant environmental benefits only if renewable natural gas is used (scenarios 5-8) or if it is coupled with a carbon capture strategy.

While the process that we have developed has been optimized to reduce cost and environmental impacts, potential future technological developments may lead to even lower environmental impacts. To explore the impact of these potential improvements on GHG emissions, we perform a parametric analysis shown in **Figure 4.17**. In this figure, we focus on two feedstocks, corn ethanol (coupled with carbon capture) and corn stover. We select these feedstocks considering their abundance in the U.S.[56]. In the parametric analysis, we systematically vary the biorefinery energy needs (which can be reduced for example by operating at higher conversions), and the hydrogen consumption in the system (which can be reduced for example by improving the gas separation operations). Two limiting cases are explored, a pessimistic case in which all settings correspond to scenario 1 on Figure **4.16**, and an optimistic case in which settings correspond to scenario 8. In the figure the relative energy and hydrogen consumption with respect to the base case design are systematically changed in the x-axis and y-axis respectively. Interestingly, in the optimistic case, the carbon footprint is reduced with increased energy consumption. This is explained by considering that the natural gas used in this case has negative emissions. One advantage of the fuels produced in this work is that they may lead to a moderate increase in energy efficiency (see engine performance section). In **Figure 4.18**, we explore how changes in vehicle energy efficiency lead to moderate improvements in the well-to-wheels GHG emissions.

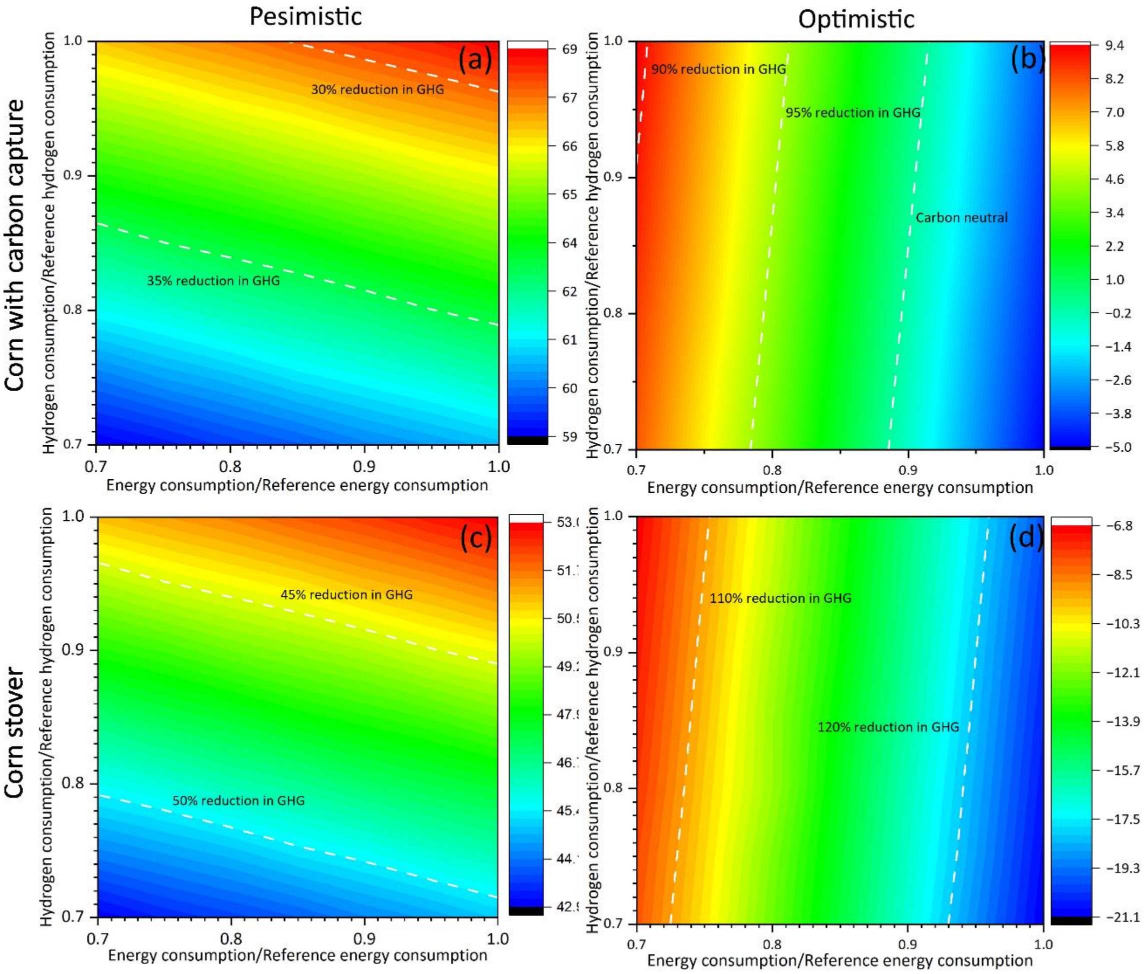

Figure 4.17. Sensitivity analysis showing the GHG emissions as a function of energy (x-axis) and hydrogen consumed (y-axis). Both axes are normalized with respect to the reference design. (a) Corn with carbon capture pessimistic scenario (b) Corn with carbon capture optimistic scenario (c) Corn stover pessimistic scenario (d) Corn stover optimistic scenario.

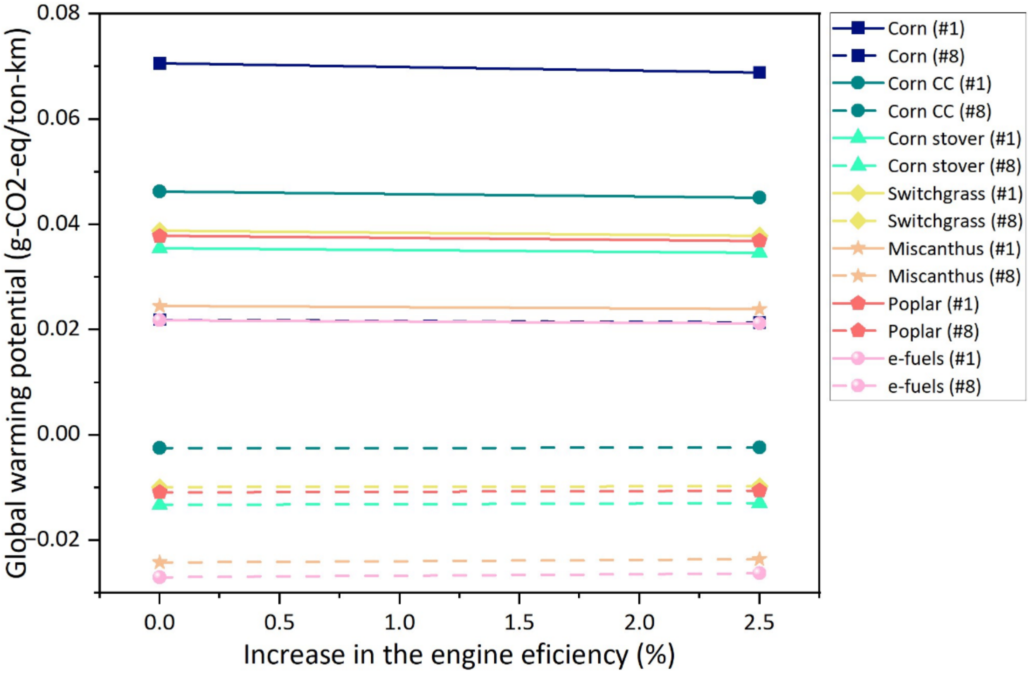

Figure 4.18. GHG emissions throughout the life cycle as a function of engine energy efficiency.

4.7 Engine performance

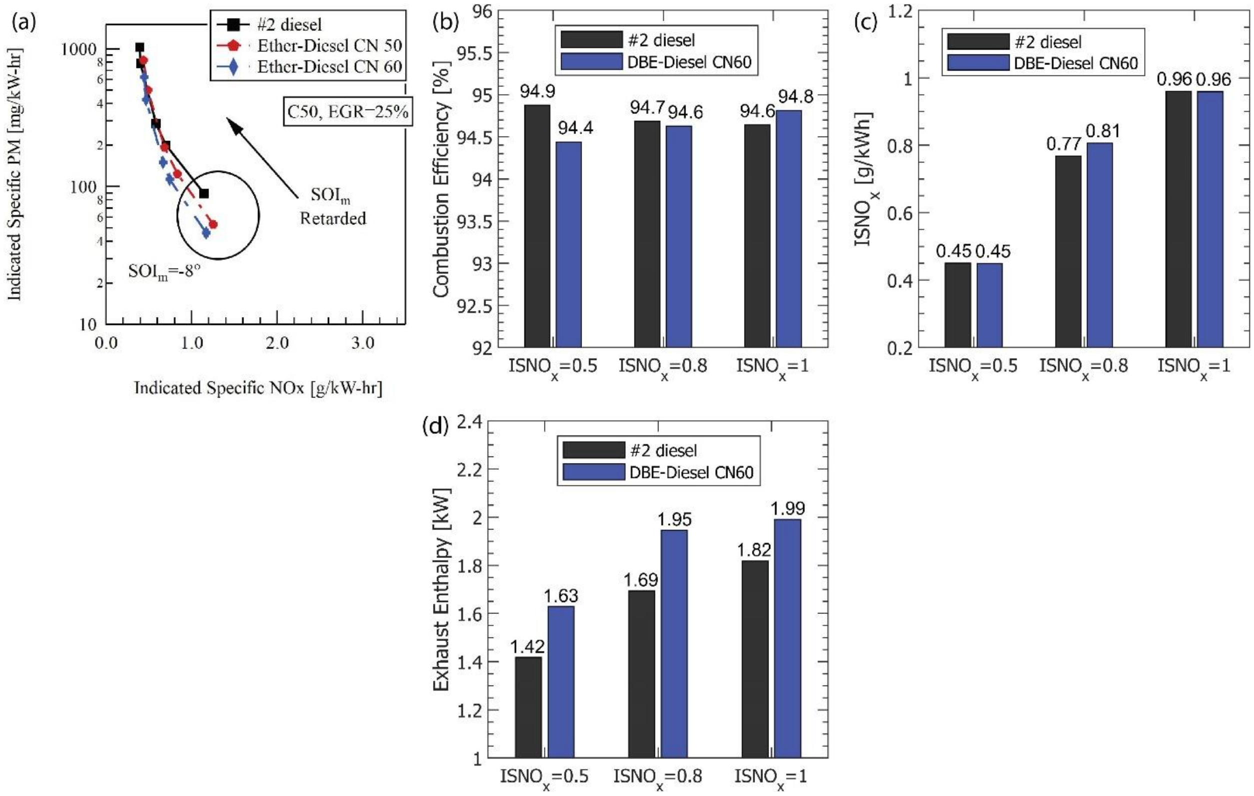

Figure 4.19. (a) Indicated specific particulate matter (soot) and NO_x for #2 diesel and ether-diesel cetane number 50 and 60 for C50 (10 bar gross indicated mean effective pressure and 2200 RPM). The data point corresponding to the most advanced injection timing is highlighted. (b) Combustion efficiency, (c) indicated specific NO_x emissions, and (d) exhaust enthalpy for #2 diesel and di-butyl ether-diesel blend as a function of targeted NO_x emissions. A combustion efficiency of 94.5% and three NO_x emissions of 0.5, 0.8 and 1 g/kWh was targeted to compare the fuels.

The performance of the mono-ether bioblendstock was evaluated, using a simple three component surrogate (composed of 65 vol. % dibutyl ether, 33 vol. % dihexyl ether, and 2 vol. % diisopentyl ether), in a single-cylinder compression-ignition direct-injection research engine[27, 57]. The surrogate was blended with a #2 diesel fuel (Haltermann Solutions, 2007 emissions certification fuel) at 20 vol. % and 37 vol. % to create two blends with derived cetane numbers of 50 and 60, respectively. Additional fuel property details for the surrogate-diesel blends can be found here[57]. Under different engine load and speed conditions, the blends with the surrogate bioblendstock were found to reduce engine-out soot emissions in comparison to the baseline #2 diesel fuel (Haltermann Solutions, 2007 emissions certification fuel). The decrease in engine-out soot emissions was observed to increase as the blend fraction of the surrogate ether bioblendstock increased. **Figure 4.17A** shows the soot-nitrogen oxides (NO_x) trade-off for the fuels for a C50 operating mode (10 bar gross indicated mean effective pressure and 2200 RPM engine load and speed, respectively), one of the four operating modes evaluated in this study. At this operating point, the cetane number 60 fuel blend had 48% lower soot emissions than #2 diesel at the most advanced injection timing evaluated, shifting the trade-off in a favorable direction despite a small penalty in NO_x emissions. This reduction in soot emissions for the bioblendstock surrogate was expected as the mono-ether fuel blends had a lower chemical sooting propensity to soot, as was quantified by yield sooting index (YSI)[58]. The cetane number 60 fuel, a blend with 37% (by volume) bioblendstock surrogate, had a YSI value of 165, significantly lower than the measured value for #2 diesel (246)[57]. The engine results at all four warmed up operating modes resulted in similar or slightly increased engine efficiency relative to the baseline #2 diesel fuel. The ether bioblendstock diesel blends also had a larger operating space where emissions constraints could be met. These results indicate overall equal or improved performance relative to the baseline #2 diesel fuel for warmed up operation.

The performance of the bioblendstock was also evaluated during operation designed to increase the exhaust enthalpy to bring the aftertreatment components to operational temperatures. The critical trade-off during this operation is the increase in fuel consumption and engine-out emissions of partial products of combustion[57, 59]. A large proportion of the total emissions of regulated pollutants during the federal certification test cycle occurs during this phase of engine operation[60]. A blend of di-butyl ether (Sigma Aldrich, RegentPlus, >99%), a mono-ether expected to be present in the bioblendstock, with #2 diesel with a derived cetane number (DCN)[61] of 60 was compared at matched engine-out emissions as #2 diesel (see **Figure 4.17B** and **C**). More details about the engine operating conditions and fuel composition can be found here[57]. This single component mono-ether surrogate was expected to replicate the combustion performance of the actual mono-ether bioblendstock at matched cetane number, as the effect of volatility level of the fuel was found to have limited sensitivity on engine operation at these conditions. Additionally, comparing fuels with different chemical composition (alkane vs diesel blended with oxygenated components) at matched reactivity was found to produce similar engine and emissions performance[1]. The higher reactivity fuel was observed to have ~13% higher exhaust enthalpy than #2 diesel at matched combustion efficiency and NO_x emissions[57], as shown in **Figure 4.17D**. This increase was driven by operating the higher reactivity fuel at a more retarded injection timing and lower exhaust gas recirculation (EGR) rate in comparison to the baseline fuel, leading to an increase in exhaust temperature and exhaust mass flow. Higher exhaust enthalpy at matched engine-out emissions for the mono-ether fuel blend was expected to reduce the overall fuel and emissions penalty associated with this operation, thereby, improving aftertreatment thermal management operation[57].

4.8 Conclusions

In this work, we have developed a new catalytic pathway for the production of diesel from ethanol and comprehensively studied its economic and GHG mitigation potential. Our results show that the proposed process is economically promising and leads to the production of fuels with 70% lower greenhouse gas emissions than their fossil counterparts, while in the most optimistic scenario carbon neutrality can be achieved. The process leads primarily to the production of diesel #2 (~92%), which can be used as a drop-in biofuel. Importantly, the properties of this fuel are outstanding, with a cetane number of ~94 and a cloud point ~ -28.9 °C. Importantly, we showed that a limitation of previous approaches can be overcome by a hydrogenolysis step which removes esters produced in the Guerbet reaction with significant impacts on the performance of etherification reactions. The strategy presented herein can play a key role in the energy transition by enabling the decarbonization of the heavy-duty transportation sector.

4.9 Acknowledgments

This material is based upon work supported by the U.S. Department of Energy's Office of Energy Efficiency and Renewable Energy (EERE) under the Co-Optima program award number E-EE0008480. The views expressed herein do not necessarily represent the views of the U.S. Department of Energy or the United States Government.

References

1. EIA, Annual energy outlook 2021, Washington, DC, vol. 2021.
2. EPA, Greenhouse Gases Equivalences Calculator - Calculations and References https://www.epa.gov/energy/greenhouse-gases-equivalencies-calculator-calculations-and-references, (accessed 19 September, 2022).
3. S. J. Davis, N. S. Lewis, M. Shaner, S. Aggarwal, D. Arent, I. L. Azevedo, S. M. Benson, T. Bradley, J. Brouwer and Y.-M. Chiang, Science, 2018, **360**, eaas9793.
4. US DOE, US Department of Transportation, US EPA and US Department of Housing, The U.S National BLueprint for Transportation Decarbonization, 2050.
5. D. J. Gaspar, C. J. Mueller, R. L. McCormick, J. Martin, S. Som, G. M. Magnotti, J. Burton, D. Vardon, V. Dagle and T. L. Alleman, Top 13 blendstocks derived from biomass for mixing-controlled compression-ignition (diesel) engines: bioblendstocks with potential for decreased emissions and improved operability, Pacific Northwest National Lab.(PNNL), Richland, WA (United States), 2021.
6. J.-M. Restrepo-Flórez and C. T. Maravelias, in Computer Aided Chemical Engineering, Elsevier, 2022, vol. 49, pp. 103-108.
7. J. M. Restrepo-Flórez and C. T. Maravelias, Energy & Environmental Science, 2021, **14**, 493-506.
8. J.-M. Restrepo-Flórez, J. Ryu, D. Witkowski, D. A. Rothamer and C. T. Maravelias, Energy & Environmental Science, 2022, **15**, 4376-4388.
9. N. M. Eagan, M. D. Kumbhalkar, J. S. Buchanan, J. A. Dumesic and G. W. Huber, Nature Reviews Chemistry, 2019, **3**, 223-249.
10. US Energy Information Administration, Monthly Energy Review - January 2024, 2024.
11. J.-M. Restrepo-Flórez, P. Cuello-Penaloza, E. Canales, D. Witkowski, D. A. Rothamer, G. W. Huber and C. T. Maravelias, Sustainable Energy & Fuels, 2023.
12. N. A. Huq, X. Huo, G. R. Hafenstine, S. M. Tifft, J. Stunkel, E. D. Christensen, G. M. Fioroni, L. Fouts, R. L. McCormick and P. A. Cherry, Proceedings of the National Academy of Sciences, 2019, **116**, 26421-26430.
13. J. E. Rorrer, A. T. Bell and F. D. Toste, ChemSusChem, 2019, **12**, 2835-2858.
14. M. Dahmen and W. Marquardt, Energy & Fuels, 2017, **31**, 4096-4121.
15. R. A. Dagle, A. D. Winkelman, K. K. Ramasamy, V. Lebarbier Dagle and R. S. Weber, Industrial & Engineering Chemistry Research, 2020, **59**, 4843-4853.
16. EIA, Monthly Energy Review - June 2021, Washington DC, 2021, vol. 159.
17. D. Humbird, R. Davis, L. Tao, C. Kinchin, D. Hsu, A. Aden, P. Schoen, J. Lukas, B. Olthof and M. Worley, Process design and economics for biochemical conversion of lignocellulosic biomass to ethanol: dilute-acid pretreatment and enzymatic hydrolysis of corn stover, National Renewable Energy Lab.(NREL), Golden, CO (United States), 2011.
18. D. R. Keshwani and J. J. Cheng, Bioresource technology, 2009, **100**, 1515-1523.
19. N. Sarkar, S. K. Ghosh, S. Bannerjee and K. Aikat, Renewable energy, 2012, **37**, 19-27.
20. X. Ou, X. Zhang, Q. Zhang and X. Zhang, Frontiers in Energy, 2013, **7**, 263-270.
21. P. A. Cuello-Penaloza, R. G. Dastidar, S.-C. Wang, Y. Du, M. P. Lanci, B. Wooler, C. E. Kliewer, I. Hermans, J. A. Dumesic and G. W. Huber, Applied Catalysis B: Environmental, 2022, **304**, 120984.
22. T. Tsuchida, J. Kubo, T. Yoshioka, S. Sakuma, T. Takeguchi and W. Ueda, Journal of Catalysis, 2008, **259**, 183-189.

23. N. M. Eagan, B. M. Moore, D. J. McClelland, A. M. Wittrig, E. Canales, M. P. Lanci and G. W. Huber, Green chemistry, 2019, **21**, 3300-3318.
24. O. V. Larina, K. V. Valihura, P. I. Kyriienko, N. V. Vlasenko, D. Y. Balakin, I. Khalakhan, T. Čendak, S. O. Soloviev and S. M. Orlyk, Applied Catalysis A: General, 2019, **588**, 117265.
25. ASTM D975-20c, Standard specification for diesel fuel, 2014.
26. P. A. Cuello-Penaloza, J. Chavarrio-Cañas, Y. Du, M. P. Lanci, D. A. Maedke, J. A. Dumesic and G. W. Huber, Applied Catalysis B: Environmental, 2022, **318**, 121821.
27. S. Subramanian and D. Rothamer, Exploration of Fuel Property Impacts on the Combustion of Late Post Injections Using Binary Blends and High-Reactivity Ether Bioblendstocks, Report 0148-7191, SAE Technical Paper, 2023.
28. I. Freitas, S. Damyanova, D. Oliveira, C. Marques and J. Bueno, Journal of Molecular Catalysis A: Chemical, 2014, **381**, 26-37.
29. N.-S. Kim, S.-Y. Hwang, E.-Y. Kim and K. N. Han, Japanese Journal of Applied Physics, 2010, **49**, 05EA04.
30. J. Schittkowski, K. Tölle, S. Anke, S. Stürmer and M. Muhler, Journal of catalysis, 2017, **352**, 120-129.
31. W. Zhang, Y. Yao, S. Xie, K. Gubsch, Y. Yang, X. Lan and H. Lin, Catalysis Today, 2021, **374**, 53-60.
32. T. K. Phung, International Journal of Hydrogen Energy, 2022, **47**, 42234-42249.
33. D. Witkowski, M. Groendyk and D. A. Rothamer, Combustion and Flame, 2023, **255**, 112883.
34. M. Groendyk and D. Rothamer, Fuel, 2017, **194**, 195-210.
35. J. Yanowitz, M. A. Ratcliff, R. L. McCormick, J. D. Taylor and M. J. Murphy, Compendium of experimental cetane numbers, National Renewable Energy Lab.(NREL), Golden, CO (United States), 2017.
36. ASTM D484-21c, DOI:10.1520/D4814-21C.
37. E. Huitema, D. Schwietert, J. Mandel and S. Nagatsuka, October, 2019.
38. F. G. Baddour, L. Snowden-Swan, J. D. Super and K. M. Van Allsburg, Organic Process Research & Development, 2018, **22**, 1599-1605.
39. HZSM5 Zeolite cost, https://www.alibaba.com/product-detail/Zeolite-Zsm5-Zsm-5-Price-Zeolite_62579342984.html?spm=a2700.galleryofferlist.topad_creative.d_title.2d7761c2HmAN7F%20Highlight, (accessed 1 May 2023).
40. HY Zeolite cost, HY zeolite cost, https://www.alibaba.com/product-detail/high-purity-hy-zeolite-catalyst-micro_1600062317816.html?spm=a2700.galleryofferlist.normal_offer.d_title.2f391e6b3Ao4kp, (accessed 1 May 2023).
41. B. Linnhoff and E. Hindmarsh, chemical engineering science, 1983, **38**, 745-763.
42. Trading economics, https://tradingeconomics.com/commodity/ethanol, (accessed 30 April 2023).
43. EIA, Diesel spot price, https://www.eia.gov/petroleum/gasdiesel/, (accessed 1 May 2023).
44. D. Hofstrand, Tracking biodiesel profitability, 2016.
45. US EPA, RIN Trades and Price Information, https://www.epa.gov/fuels-registration-reporting-and-compliance-help/rin-trades-and-price-information, (accessed 9 June 2023).

46. R. P. Anex, A. Aden, F. K. Kazi, J. Fortman, R. M. Swanson, M. M. Wright, J. A. Satrio, R. C. Brown, D. E. Daugaard and A. Platon, Fuel, 2010, **89**, S29-S35.
47. R. M. Swanson, A. Platon, J. A. Satrio and R. C. Brown, Fuel, 2010, **89**, S11-S19.
48. R. M. Swanson, A. Platon, J. A. Satrio and R. C. Brown, ACS National Meeting Book of Abstracts.
49. S. Safarian, R. Unnþórsson and C. Richter, Renewable and Sustainable Energy Reviews, 2019, **110**, 378-391.
50. M. Rafati, L. Wang, D. C. Dayton, K. Schimmel, V. Kabadi and A. Shahbazi, Energy conversion and management, 2017, **133**, 153-166.
51. D. C. de Oliveira, E. E. Lora, O. J. Venturini, D. M. Maya and M. Garcia-Pérez, Renewable and Sustainable Energy Reviews, 2023, **172**, 113047.
52. L. Tao, J. N. Markham, Z. Haq and M. J. Biddy, Green Chemistry, 2017, **19**, 1082-1101.
53. W. D. Seider, D. R. Lewin, J. Seader, S. Widagdo, R. Gani and K. M. Ng, Product and process design principles: synthesis, analysis, and evaluation, John Wiley & Sons, 2017.
54. M. Q. Wang, GREET 1.5-transportation fuel-cycle model-Vol. 1: methodology, development, use, and results, Argonne National Lab., IL (US), 1999.
55. A. Pareek, R. Dom, J. Gupta, J. Chandran, V. Adepu and P. H. Borse, Materials Science for Energy Technologies, 2020, **3**, 319-327.
56. M. H. Langholtz, B. J. Stokes and L. M. Eaton, 2016 billion-ton report: advancing domestic resources for a thriving bioeconomy, EERE Publication and Product Library, Washington, DC (United States), 2016.
57. S. Subramanian, Investigation of the Use of High-Cetane Mono-Ether Bioblendstocks to Improve Catalyst Heating and Warmed Up Operation of MCCI Engines, The University of Wisconsin-Madison, 2024.
58. C. S. McEnally and L. D. Pfefferle, Combustion and Flame, 2007, **148**, 210-222.
59. S. Busch, A. Wu and S. Cho, Catalyst-heating operation in a medium-duty diesel engine: operating strategy calibration, fuel reactivity, and fuel oxygen effects, Report 2641-9645, Sandia National Lab.(SNL-NM), Albuquerque, NM (United States), 2021.
60. C. Sharp, C. C. Webb, G. Neely, M. Carter, S. Yoon and C. Henry, SAE International Journal of Engines, 2017, **10**, 1697-1712.
61. P. Products and T. Methods, ASTM International, 2007, **C**, 1-12.

Chapter 5. Scale up studies for the dehydration of C_{4+} alcohols into drop-in diesel fuel

5.1 Introduction

The demand for diesel fuel is projected to increase in the next twenty years[1]. The electrification of heavy-duty vehicles has proven difficult due to the low energy density of batteries and the long time required for charging[2], necessitating alternative energy paths for the heavy-duty transportation sector. Previously, we have shown that an ethanol-to-diesel path using ethanol oligomerization and acid–catalyzed dehydration is an alternative process to produce economic and environmentally friendly diesel #2[3]. The last step in this process, the dehydration process, used a powder Y catalyst with inert beds to achieve high conversion of alcohols and high selectivity to C_{8+} ethers. C_{10+} ethers are the ideal candidates for drop-in diesel as they have properties comparable to conventional fossil diesel[4]. It has been shown that diesel-range ethers can be used in conventional diesel engines[5-7]. Fuels blended with diesel-range ethers with high cetane number have shown higher combustion stability and efficiency relative to lower cetane number fuels[5, 7]. Furthemore, the use of diesel-range ethers can lead to the reduction in engine-out soot and NO_x emissions compared to pure fossil #2 diesel[6, 7]. The ongoing efforts show that bioblendstocks rich with diesel-range ethers can possibly be used as either a) blends with fossil diesel or b) potentially as drop-in fuels depending on the ASTM specifications met.

The content of this chapter is largely adapted from the following reference:

Emmanuel Canales, Dustin Witkowski, David Rothamer, and George W. Huber. Scale up studies for the dehydration of C_{4+} alcohols into drop-in diesel fuel. In preparation.

EC conducted catalytic experiments and wrote chapter. DW determined fuel characterization properties and added written portion on fuel characterization. DW also contributed to editing.

In our previous alcohol dehydration studies, we used small bed sizes (1.8 g catalyst) with powder catalysts for dehydration using inert silica beads[3, 8, 9]. An industrial scale process, however, would require larger bed sizes (17,639 kg catalyst) for a 1,387 barrel per day plant[3, 8]. Additionally, in industrial fixed bed reactors, catalyst pellets rather than powder are used primarily to decrease the pressure drop in the reactor[10-12]. Pellets are made using the catalyst of interest, with the introduction of a binder to help maintain the particle strength and shape[10]. While binders do solve the physical issues arising from powder forms of catalyst, these binders may influence the original chemistry observed over powder forms. Depending on the binder used, issues such as coke deactivation[10, 11], lower catalytic activity[10, 12], mass transfer effects of molecules[10, 13], and changes in product selectivity can occur[10, 11]. Therefore, it is important to choose a binder that will work in tandem with the chemistry of interest.

In this study, we compare powder zeolite Y with a pellet version of the catalyst. We report the differences in reaction chemistry and determine if the pellet formulation plays a significant role in the change of dehydration chemistry over the zeolite Y catalyst in a continuous flow reactor. We then measure the fuel properties of the dehydration products produced in parr reactors to see if they can meet #2 diesel fuel specifications.

5.2 Experimental

5.2.1. Etherification feedstocks

Several combinations of reactor geometry and catalyst configuration (i.e powder or pellet) were studied in this work. For each, four feedstocks were used for dehydration experiments: 1) pure n-butanol 2) pure n-hexanol 3) An equimolar n-butanol/n-hexanol mixture and 4) a model feedstock made to represent oligomerization products from a real of ethanol/butanol (EtOH/ButOH) oligomerization reactor[8, 9]. The alcohols 1-butanol (Sigma Aldrich, ACS reagent

>99.4%), 1-hexanol (Sigma Aldrich, Reagent grade 98%) and 1-octanol (Alfa Aesar, 99%) were obtained to represent the linear alcohols. The alcohols 2-methyl-1-butanol (Thermo Scientific, 98%), 2-ethyl-1-butanol (Sigma Aldrich, 98%) and 2-ethyl-1-hexanol (Sigma Aldrich, >99.6%) were used to represent branched alcohols. 2-butanol (TCI chemicals, >99%), 2-heptanol (Acros Organics, 99+%), 2-octanol (TCI chemicals, >98%), and 2-nonanol (Sigma Aldrich, 99%) were obtained to represent secondary alcohols. **Table 5.1** represents the model feedstock representing the alcohol oligomerization products obtained from EtOH/ButOH oligomerization.

Table 5.1. Feedstock of EtOH/ButOH oligomerization products. 'L/B' represents the linear to branched alcohol ratio. 'L/S' represents the linear to secondary alcohol ratio. Reproduced from Ref 8 with permission from the Royal Society of Chemistry.

Alcohol	C#	Mol%
1-butanol	4	34.73
2-butanol	5	1.33
2-methyl-1-butanol	5	3.62
1-hexanol	6	40.35
2-ethyl-1-butanol	6	8.36
2-heptanol	7	3.42
2-ethyl-1-hexanol	8	3.60
1-octanol	8	4.26
2-octanol	8	0.11
2-nonanol	9	0.22
Alcohol ratios		
L/B		5
L/S		16

5.2.2. Continuous flow reactor configuration with Powder Y zeolite Catalyst

Both the powder and a pellet Y zeolite catalyst were studied in continuous flow reactors. The exact reactor dimensions, bed dilution ratios, gas flowrates, feed flowrates, and analytical techniques used to identify liquid and gas species can be found elsewhere[3, 8]. Bed dilutions for catalyst runs were used to minimize pressure drop across the reactor[8]. Due to the differences in particle sizes between the inert beads and catalyst particles, we assume a non-uniform bed when dilution is introduced. The temperature of the fixed-bed reactors was controlled using a built-in thermocouple within the furnace, connected to a temperature controller. Argon gas was flown at 10 mL/min and used to pressurize the reactor at 6.9 bar to favor ether selectivity. In our previous studies, we found that increasing the system pressure above the vapor pressure of the reaction feed shifted reactions from mono-molecular to bi-molecular dehydration[8]. The temperature profile across the reactor was measured to determine if a temperature gradient was present. Since no noticeable temperature gradient was present, we assume uniform heating across the catalyst bed. All reactions were conducted at 443.15K at 6.9 bar.

Table 5.2 shows the reactor configurations that were used with the powder catalyst. 'PC' denotes the experiments done in the 0.95-cm reactor. For PC runs, the catalyst bed length was 17.8-cm.'SP' denotes experiments done with powder Y for scale-up reactions. In PC-1, the mass ratio of catalyst to silica beads was 1:2, with a silica bead particle size of 600 - 180 microns. At this reactor size and bed configuration, collection, and chromatography analysis of the products downstream of the reactor were possible.

Table 5.2. Reactor dimensions and packing used for dehydration of alcohols with powder Y zeolite. Reaction conditions: 443.15 K, P = 6.9 bar , WHSV = 1.10 h^{-1}, Feedstock: EtOH/ButOH oligomerization products. Configuration A was obtained from ref 8, while configuration B and C represent the scale-up parameters used for powder Y in this section.

	Configuration A[8]	**Configuration B**	**Configuration C**
Dimensions			
Bed length (cm)	17.8	25.4	25.4
Reactor diameter (cm)	0.95	2.54	2.54
Catalyst packing			
Powder Y loading (g)	1.80	20	5
Silica bead loading (g)	3.60	40	80
Silica bead size (microns)	600 - 180	600 - 180	4,750 - 850
Run #	**PC - 1**	**SP - 1**	**SP - 2**
Feed flowrate (mL/min)	0.04	0.44	0.11

When 2.54 cm diameter stainless steel reactors were used, serious issues such as coke buildup and bed displacement did not allow for collection of samples. SP-1 in **Table 5.2** shows the reactor dimensions and packing for the 2.54 cm diameter reactor. Compared to PC-1, about 10x the amount of catalyst was used. The mass ratio of catalyst to silica beads and the size of the silica beads were the same as Configuration A. The buildup of the tar-like phase did not allow for any fluid to flow out, which did not make product collection possible. No pressure build up was observed, as the pump failed to further push the reactant stream out of the reactor. SP-2 in Table 2 shows a modified version of the 2.54-cm diameter stainless steel catalyst bed, in which larger silica bead particles (850 – 4,750 microns) and a lower mass ratio of catalyst to silica beads (1:16) was used compared to the previous configurations. In this case, the pump was able to flow reactant through the bed. However, after a day, bed displacement was observed. Upon removing the reactor, the catalyst was pushed out of the top of the reactor, leading to significant pressure build up in the continuous flow system. Increasing the dehydration reactor from lab to pilot scale for production

of drop-in diesel range ethers at larger volumes therefore requires different catalyst bed configurations with larger catalyst particle sizes to mitigate bed displacement.

5.2.3. Continuous flow reactor configuration with Pellet Y zeolite Catalyst

Etherification of alcohols was also performed with a pellet version of Zeolite Y obtained from Shell PLC in a stainless-steel packed fixed-bed reactor, as used in previous studies with powder Y catalyst[8]. The formulation consisted of zeolite Y (80 wt%) with alumina as the binder (20 wt%). Prior to loading the pellets into the reactor, 10 – 20 g batches of the pellets were calcined overnight at 873.15 K in a muffle furnace in static air, with a ramp of 4 K/min, and dried at 383.15 K until used. The reactor was 33-cm long with an outer diameter of 0.95-cm. For pellet Y catalyst, the catalyst bed length was 25.4-cm. TGA experiments were conducted in a TA instruments Q500 Thermogravimetric Analyzer as described in our previous studies[8]. Oxygen and nitrogen TGA were conducted at flowrate of 50 mL/min, with a balance gas of nitrogen at 50 mL/min. The ramp rate was set to 20 K/min up, with the final temperature set to 1073 K. **Table 5.3** provides the reactor dimensions and catalyst packing configuration used for Pellet Y catalyst beds. Due to the high concentration of catalyst in the pellet, it is reasonable to assume that the bed mainly consists of Zeolite Y. For the pellets, the weighted hour space velocity (WHSV) is defined as the feedstock mass flowrate divided by the mass of zeolite Y catalyst in the formulation.

Table 5.3. Reactor dimensions and packing used for dehydration of alcohols using Pellet Y. The powder zeolite Y mass represents the fraction of the catalyst in the formulation. [a]Signifies the average particle diameter of the pellet. [b]Signifies the average particle length of the pellet.

	Configuration D	**Configuration E**	**Configuration F**
Dimensions			
Bed length (cm)	25.4	25.4	25.4
Reactor diameter (cm)	0.95	0.95	0.95
Catalyst packing			
Pellet Y loading (g)	4.6	4.8	3.0
Pellet Y particle size (microns)	1,650[a], 4,700[b]	600 - 1,000	180 - 600
Powder Zeolite Y (g)	3.68	3.84	2.40
Silica bead loading (g)	0	0	6.00
Silica bead size (microns)	-	-	850 - 4,750

5.2.4. Parr reactor experiments and product quantification

Finally, etherification experiments were performed in 75ml and 450ml Parr reactors (Model 4562). The RPM for the 450 mL Parr reactor was estimated using tachometer. Batches (10-20 g) of HY zeolite powder (Zeolyst International, CBV-720) were calcined overnight at 873.15 K in a muffle furnace in static air, with a ramp of 4 K/min for the Parr reactor experiments. The powder catalyst was then dried at 383.15 K until used. The commercial catalyst has a Si/Al ratio of 30, with a surface area of 780 m^2/g. The temperature in Parr reactors was controlled using a thermocouple using a PID controller in a Parr Series Multiple Reactor System. Post-reaction, the products from parr reactors were either a) extracted with tetrahydrofuran (THF) and analyzed (denoted as ‘Y’) or B) centrifuged for 10 minutes at 3500 rpm to separate the powder catalyst before GC analysis (denoted as ‘N’ to signify no THF extraction). For GC analysis, THF was used as the analytical solvent to homogenize the organic and aqueous phases. After etherification, distillation experiments were conducted under a vacuum using a glass condenser without cooling water. The initial products were heated in a silicon oil bath. Two 500-mL flasks were used for collection of light and heavy products. Both products were cooled using an ice bath and then analyzed using gas chromatography.

5.3 Results and discussion

5.3.1 Continuous flow reactor tests of pure alcohols with pellet and powder zeolite Y

We have previously shown that high butyl ether selectivity (91.6%) can be obtained at high conversion (73.4%) over powder zeolite Y[8]. **Table 5.4** provides information on the pure alcohol runs. 'PC' denotes runs using powder Y catalyst, while 'FC' denotes runs using the pellet Y catalyst formulation. **Figure 5.1** shows the activity of the pellets at the conditions previously studied over powder Y (443.15 K, 6.9 bar)[8]. Table 4 compares the activity, selectivity and carbon balance for the powder and pellet zeolite catalyst. FC-2 has a lower conversion (73.4% vs. 68.8%), ether selectivity (91.6% vs 81.9%) and carbon balances (96.6% vs 91.4%) at constant WHSV when n-butanol was used as the feedstock compared to PC-2. These results indicate that the catalytic activity of zeolite Y is being affected by the pellet formulation. At constant WHSV, the pellets begin to favor coke formation, resulting in lower carbon balances and ether selectivity compared to powder Y catalyst. Over the pellets, decreasing the WHSV resulted in lower carbon balances and high conversion. These results indicate that increasing the contact time of the feedstock with the catalyst promotes coke formation. The ether selectivity also decreases with decreasing WHSV, indicating that at high conversions, the chemistry begins to shift from bi-molecular dehydration to coke formation.

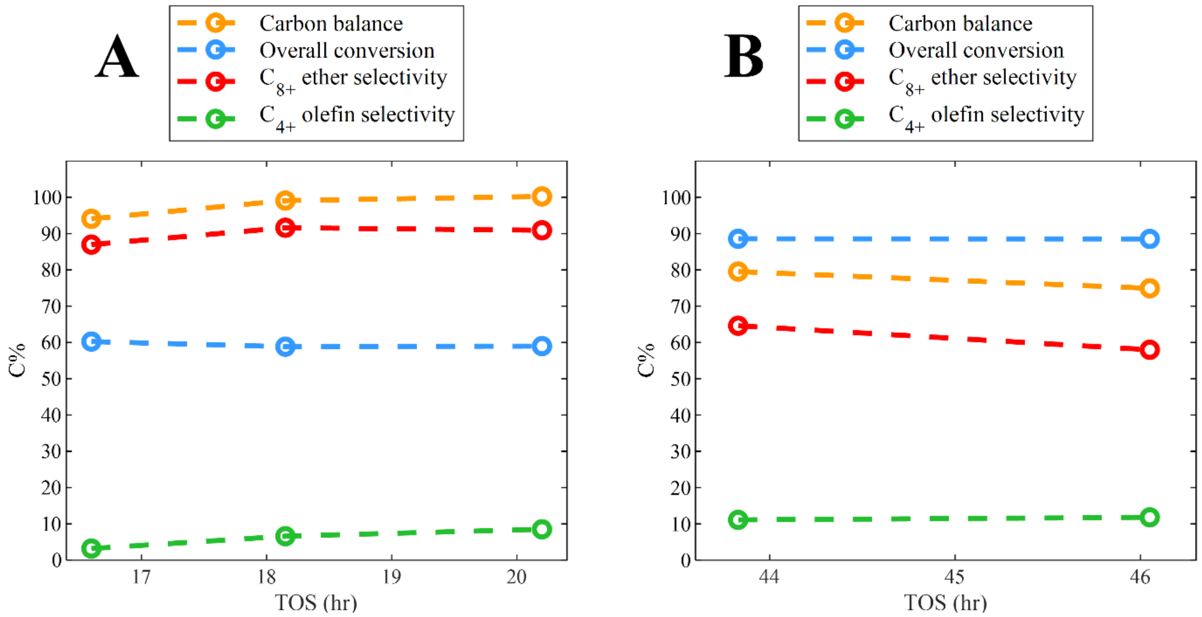

Figure 5.1. n-butanol dehydration over pellets for A) FC – 1 and B) FC – 2. For both runs Configuration D was used. n-butanol flowrate = 0.021 **(B)** – 0.051 **(A)** mL/min. Ar flowrate = 10 mL/min. Pellet Y loading = 4.63 g_{cat}, Temperature = 443.15 K, P = 6.9 bar.

Table 5.4. Catalytic activity comparison of powder and pellet zeolite Y using various alcohol feedstocks. Conversion, selectivity and carbon balances represent the average values of the reaction run. Powder Y catalyst runs were taken from ref 8. Reaction conditions: T = 443.15 K, P = 6.9 bar, Ar flowrate = 10 mL/min. Reactor diameter = 0.95 cm. n-butanol:n-hexanol represents an equimolar mixture of the pure alcohols. The powder zeolite Y mass represents the fraction of the zeolite Y in the formulation. *Signifies the values were calculated by linear correlation of the WHSV experiments.

Catalyst	**Powder Y catalyst**[8]		**Pellet Y catalyst**			
Feed	**n-butanol**	**n-hexanol**	**n-butanol**			**n-butanol: n-hexanol**
WHSV powder Y (h^{-1})	**0.54**	**0.54**	**0.67**	**0.54***[*]	**0.26**	**0.59**
Run #	**PC – 2**	**PC – 3**	**FC – 1**	**FC - 2**	**FC – 3**	**FC – 4**
Conversion (C%)	73.4	84.7	59.4	68.8	88.6	87.3
C_{8+} ether selectivity (C%)	91.6	82.7	89.9	81.9	61.8	43.5
Carbon balance (C%)	96.6	91.2	97.8	91.4	77.6	56.7
Pellet Y loading (g)	-	-	4.63	-	4.63	4.62
Powder Zeolite Y mass (g)	1.80	1.80	3.70	-	3.70	3.70
Inert bead mass (g)	3.60	3.60	-	-	-	-
Inert bead size (microns)	180-600		-	-	-	-
Dimensions and packing	**Configuration A**		**Configuration D**			

The equimolar mixture was fed over the pellet catalyst (FC-4) to note any differences in activity when larger alcohols are introduced as shown in **Figure 5.2** and **Table 5.4**. In our previous studies using powder Y catalyst, it was shown that increasing the alcohol chain length led to lower carbon balances and ether selectivity at constant WHSV[8]. For PC-2 and PC-3, the conversion, carbon balances and ether selectivity are in the ranges of 73 – 85%, 91.2 – 96.6%, and 83 – 92%, respectively. If the pellet formulation has no effect on reaction chemistry (i.e., is inert), the ether and carbon balances should fall within these ranges for an equimolar feed. The overall conversion of the feed was 87%, within the range of the PC-2 and PC-3. However, the carbon balance and ether selectivity were 57% and 43.5%, respectively. These values are well below the ranges reported for powder Y catalyst at similar reaction conditions (**Table 5.4**). While larger alcohol feeds do decrease carbon balances and ether selectivities, the effect is much more prevalent with the catalyst formulation. The carbon balance from PC-2 and PC-3 decreased by 5.4%, while the carbon balance from FC-2 to FC-4 decreased by 34.7%. These results indicate that other factors may be influencing coke formation that are primarily due to the catalyst formulation.

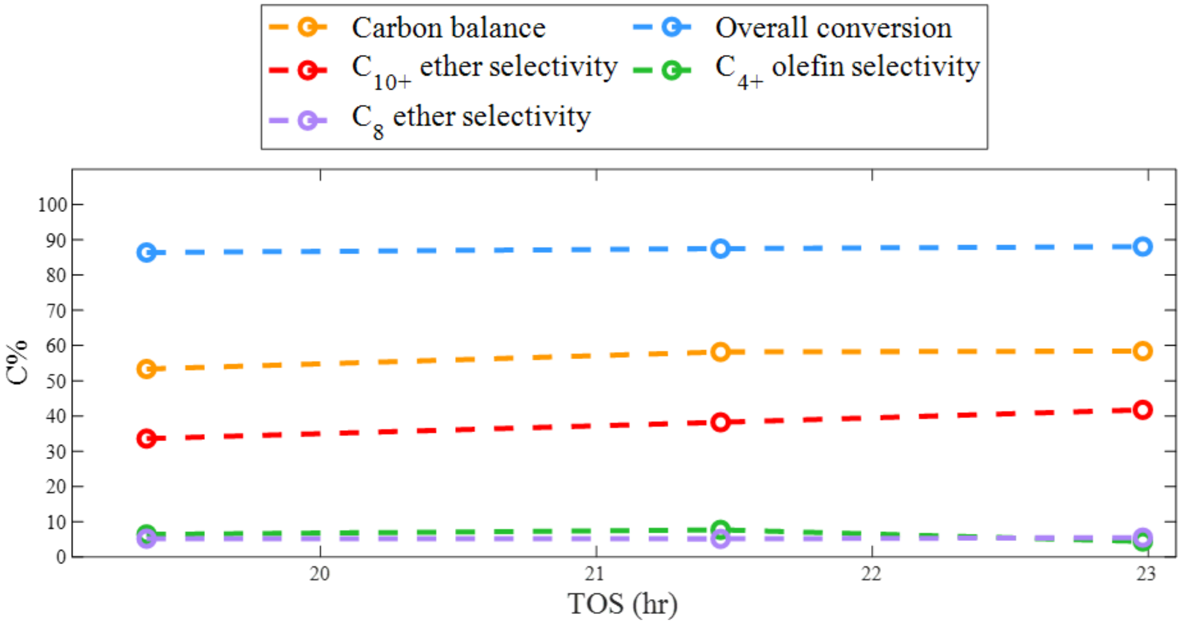

Figure 5.2. Dehydration of equimolar n-hexanol and n-butanol mixture over pellets for run FC – 4. Reactant flowrate = 0.045 mL/min Ar flowrate = 10 mL/min. Pellet Y loading = 4.62 g_{cat}, Temperature = 443.15 K,

Table 5.5. Catalytic activity comparison of powder and pellet zeolite Y using EtOH/ButOH oligomerization products. EtOH/ButOH oligomerization products represent alcohol oligomerization of an ethanol/butanol cofeed using a real oligomerization reactor from ref 8, 9. Conversion, selectivity and carbon balances represent the average values of the reaction run. The powder zeolite Y mass represents the fraction of the catalyst in the formulation. Reaction conditions: 443.15 K, P = 6.9 bar, Ar flowrate = 10 mL/min.

Catalyst	**Powder Y Zeolite**[8]	**Pellet Y Zeolite**	
WHSV powder Y (h^{-1})	**1.1**	**1.0**	**2.0**
Run #	**PC - 1**	**FC - 5**	**FC - 6**
Conversion (C%)	71.1	57.4	30.2
Ether selectivity (C%)	61.4	45.4	55.4
Carbon balance (C%)	86.5	79.7	93.9
Pellet Y loading(g)	-	4.63	4.62
Powder Zeolite Y mass (g)	1.80	3.70	3.70
Inert bead mass (g)	3.60	-	-
Inert bead size (microns)	180-600	-	-
Dimensions and packing	**Configuration A**	**Configuration D**	

EtOH/ButOH oligomerization products were also studied, as these products include high fractions of C_{6+} linear, branched and secondary alcohols (See **Table 5.1**). **Figure 5.3** shows the TOS data of dehydrated EtOH/ButOH oligomerization products. **Table 5.5** shows the comparison of dehydrated EtOH/ButOH oligomerization products over powder and pellet Y. Compared to PC-1, the conversion, ether selectivity and carbon balances all decrease with the catalyst formulation, as shown for FC-5 at constant WHSV. These results agree with those found using n-butanol. When the space velocity increases from FC-5 to FC-6, there is an increase in the carbon balances and ether selectivity. This indicates that decreasing the catalyst contact time mitigates coke formation. However, the alcohol conversion further decreases. Therefore, with the current pellet formulation, high conversion regimes at selectivities above 60% are unlikely to be obtained.

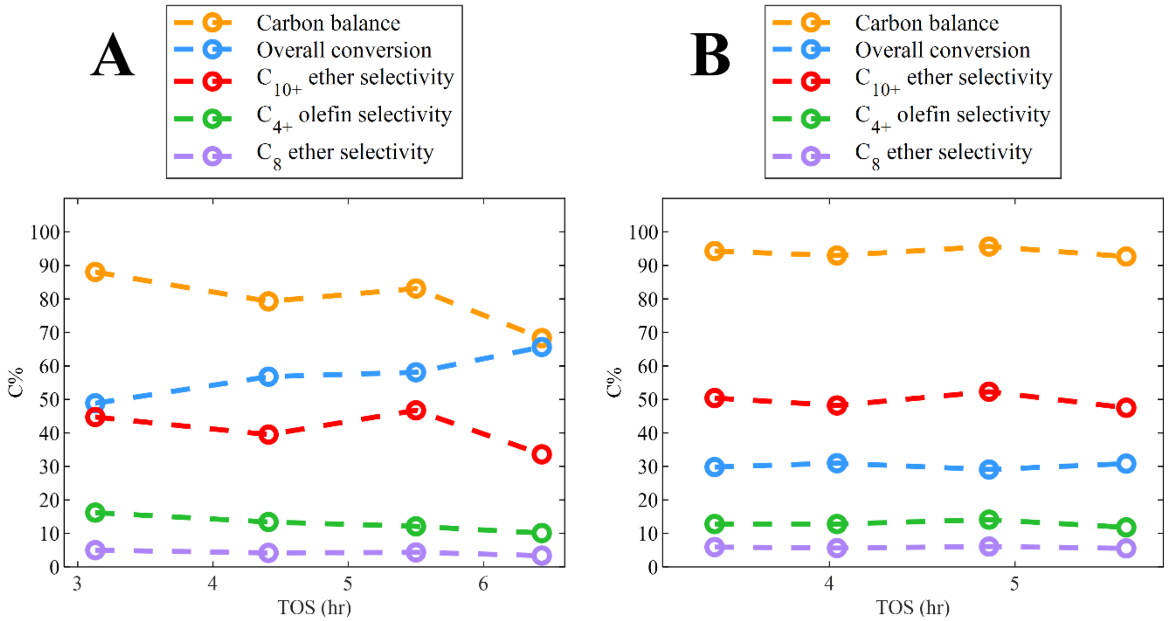

Figure 5.3. EtOH/ButOH oligomerization products dehydration over pellets in their original form at **A)** WHSV = 1.0 h^{-1} and **B)** WHSV = 2.0 h^{-1}. Reactant flowrate: 0.075 **(A)** – 0.150 **(B)** mL/min. Ar flowrate = 10 mL/min. Pellet Y loading = 4.63 g_{cat}, Temperature = 443.15 K, P = 6.9 bar.

5.3.2 Continuous flow reactor testing with crushed pellets

Often the catalytic activity of pellets can be increased by grinding pellets to smaller particle sizes of pellets due to increases in transport[14].The pellets were crushed to a size of 180 - 600 microns and tested with a silica bead dilution using a particle size of 850 – 4,750 microns at a dilution ratio of 1:2 g_{pellet}:g_{beads}. Configuration F in **Table 5.3** was chosen to minimize pressure buildup across the reaction bed. **Figure 5.4** shows the TOS data using a pure n-butanol run over the diluted bed (FC-7). **Table 5.6** compares the activity of the pellet and powder Y catalyst at different particle sizes. The crushed pellets had similar activity as the powder Y at WHSV = 0.54 h^{-1}. However, the ether selectivity and carbon balances were lower for the pellet Y than the powder Y. This again indicates that the pellet formulation is influencing the catalytic chemistry in a detrimental way.

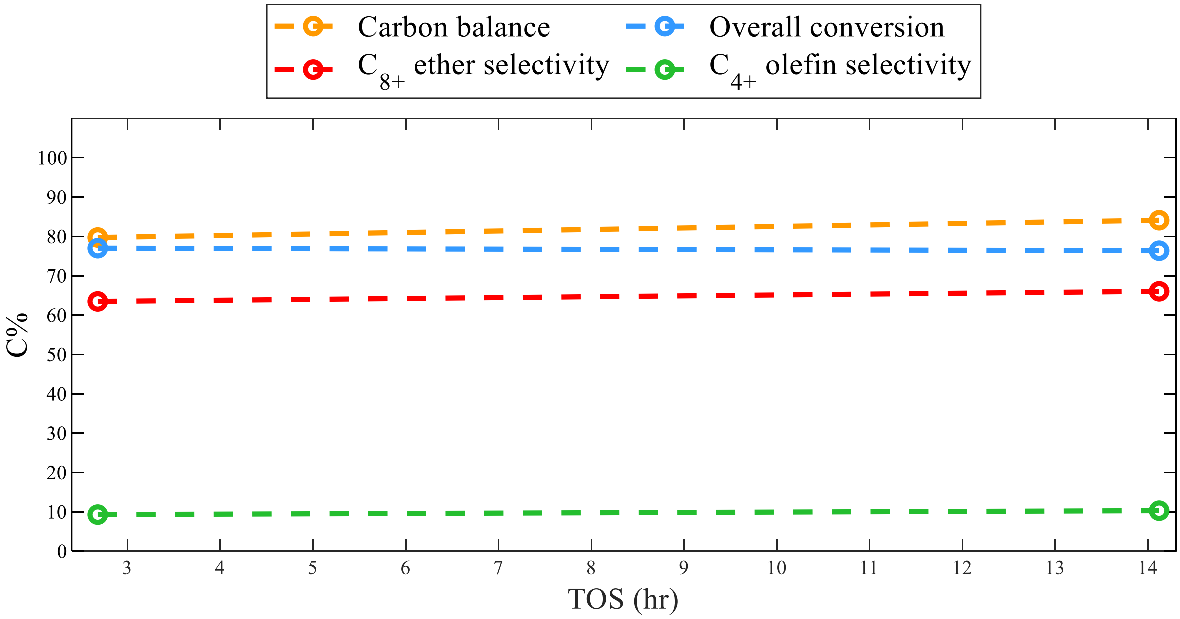

Figure 5.4. pure n-butanol dehydration over pellets at a particle size of 600 - 180 microns at a WHSV = 0.54 h^{-1}. The silica bead size was 4750 - 850 microns. Feedstock flowrate: 0.027 mL/min. Pellet Y loading: 3.00 g_{cat}, Temperature = 443.15 K, P = 6.9 bar. Dilution ratio: 1:2 g_{pellet}:g_{silica}.

Table 5.6. Catalytic activity comparison of powder and pellet zeolite Y using a pure n-butanol feed with different particle sizes. Powder Y catalyst run was taken from ref 8. Conversion, selectivity and carbon balances represent the average values of the reaction run. Reaction conditions: T = 443.15 K, P = 6.9 bar, Ar flowrate = 10 mL/min, Reactor diameter = 0.95-cm. *Signifies the values were calculated by linear correlation of the WHSV experiments. [a]Signifies the average particle diameter of the pellet. [b]Signifies the average particle length of the pellet.

Catalyst	**Powder Y Zeolite**[8]	**Pellet Y Zeolite**	
Particle size (microns)	**75**	**1650[a], 4700[b]**	**180 - 600**
WHSV Powder Y (h^{-1})	**0.54**	**0.54***	**0.54**
Run #	**PC - 2**	**FC - 2**	**FC - 7**
Conversion (C%)	73.4	68.8	76.7
Ether selectivity (C%)	91.6	81.9	64.8
Carbon balance (C%)	96.6	91.4	81.9
Pellet Y loading (g)	-	-	3.00
Powder Zeolite Y mass (g)	1.80	-	2.41
Silica bead mass (g)	3.60	-	6.00
Silica bead size (microns)	180 - 600	-	850 - 4,750
Dimensions and packing	**Configuration A**	**Configuration D**	**Configuration F**

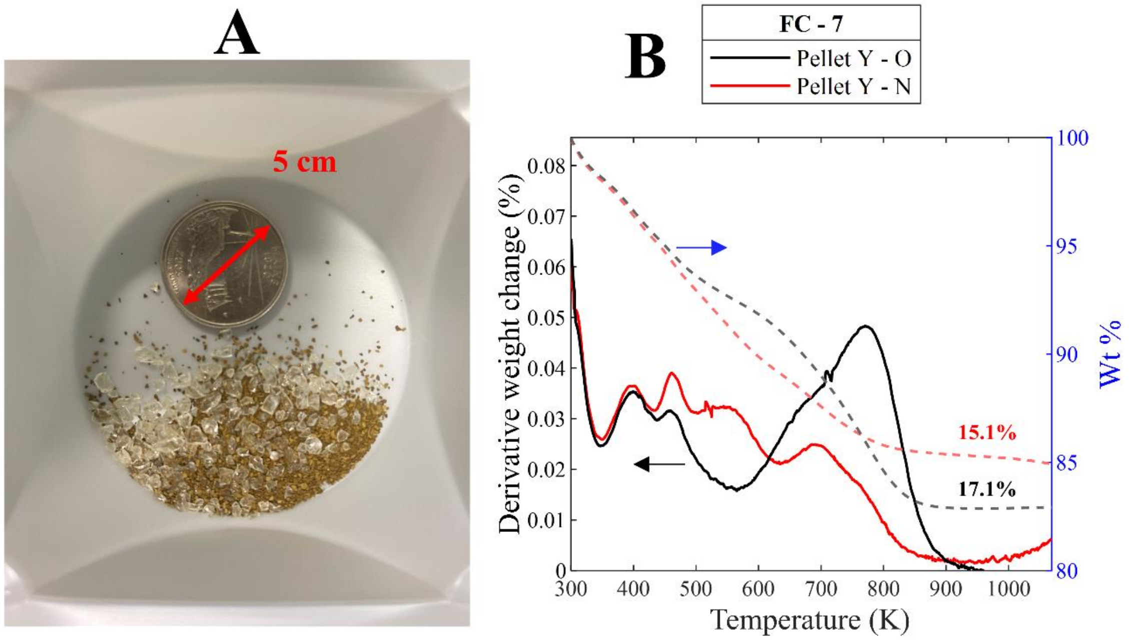

Figure 5.5. A) Spent catalyst bed for FC-7 and B) the corresponding TGA data. Red solid lines signify TGA done in a N_2 environment, while black sold lines represent TGA done in an O_2 environment. Dashed lines represent the weight percent change in O_2 and N_2 environments. Values represent the final weight percent loss from the experiments.

Figure 5.5 shows the spent catalyst bed (FC-7) as well as the TGA analysis of the spent catalyst. The spent catalyst bed and TGA data for FC-7 will be compared to other spent catalyst beds in the following section. The carbon balances for FC-7 are lower than PC-2 and the runs with the pellets before grinding (FC-1 - FC-3). The conversion is also higher for FC-7 than the pellets. Based on the TGA data, a higher fraction of coke products is in the temperature range of 600 – 900K, indicating the formation of hard coke products. A potential explanation is that the crushed pellets mitigate mass transfer effects at the expense of causing other undesired side reactions to occur. These side reactions include alcohol adsorption and olefin oligomerization. The formulation uses a mixture of zeolite Y (80 wt%) and alumina (20 wt%). It has been shown in the literature that compared to other materials (e.g., Kaolin clay), the use of alumina increases coke deactivation over zeolites[11]. Another mechanism that can occur is the cracking of ethers to low molecular weight products, a phenomenon seen in FCC catalysts that use alumina[15], which may cause a decrease in ether selectivity with the pellets (91.6 to 64.8%). Based on these findings, we cannot assume that the binder is inert in the pellet formulation.

5.3.3 Effectiveness factor of pellet formulation

Based on the differences in catalytic activity of the powder and pellet Y catalysts, The effectiveness factor for PC-1, FC-2 and FC-7 was calculated to assess the mass transfer effects occurring with using the pellet formulation. n-butanol was used as the reaction feed. As there is variation between the fluid flowrates and concentrations, the observed effectiveness factor is calculated by **equation 1**:

$$\eta_{obs}=\frac{R_{obs,pellet}}{R_{obs,Powder\ Y}}=\frac{k_{obs,pellet}Ca^2}{k_{obs,powder\ Y}Ca^2}=\frac{k_{obs,pellet}}{k_{obs,Powder\ Y}} \quad (1)$$

Assuming similar temperature, pressure and rate of catalyst deactivation. For powder Zeolite Y, $\eta = 1$. Using the rate constant obtained from powder Y catalyst, the calculated Thiele modulus and effectiveness factors were also determined.

An irreversible, second order reaction is considered within a plug flow reactor filled with known catalyst volume. The rate equation is integrated to obtain the design equation. The volume change in the reactor is constant due to stoichiometric balances of bi-molecular dehydration. τ is calculated with respect to the total volumetric flowrate of the incoming vapor stream. The density of the catalysts was estimated using a graduated cylinder. The calculated Thiele modulus and effectiveness factor are determined based on **equations 2** and **3**:

$$\phi_{2,calculated}=L\sqrt{\frac{3(k_{obs,powder\ Y})C_a}{2D_e}} \quad (2)$$

$$\eta_{calculated} = \frac{\tanh(\phi_{2,calculated})}{\phi_{2,calculated}} \qquad (3)$$

Where L is the characteristic length of the catalyst. For cylinders and spheres, L = R/2 and L = R/3, respectively. It is assumed that the crushed pellets and Powder Y are spherical. R is the particle radius of the catalyst and D_e is the effective diffusivity of n-butanol. D_e was calculated by equation 4:

$$D_e = \frac{D_{AB}\phi_p\sigma}{\bar{\tau}} \qquad (4)$$

Where ϕ_p is the catalyst porosity, σ is the constriction factor, and $\bar{\tau}$ is the tortuosity factor. For the porosity, $\phi_p = 0.24 - 0.47$ were void fractions determined by Bey and Eigenberger[16] for cylindrical and spherical pellets. $\phi_p = 0.24$ for the extreme case of low void fraction over catalyst beds. Typical values of the constriction and tortuosity factor are 0.8 and 3, respectively[17]. In this case, we assume $\bar{\tau} = 10$ in the extreme case of high obstruction within the catalyst. The reaction is assumed to occur in the vapor phase. The reaction phase was determined using the NRTL model and flash tank in ASPEN corresponding to the initial volumetric flowrates of n-butanol and argon at reaction temperature and pressure. D_{AB} refers to n-butanol diffusing into argon in the gas phase. The diffusion coefficient was calculated using the correlations of Fuller[18]. At reaction temperature and pressure, the estimated value was $D_{AB} = 0.0239$ cm^2/s.

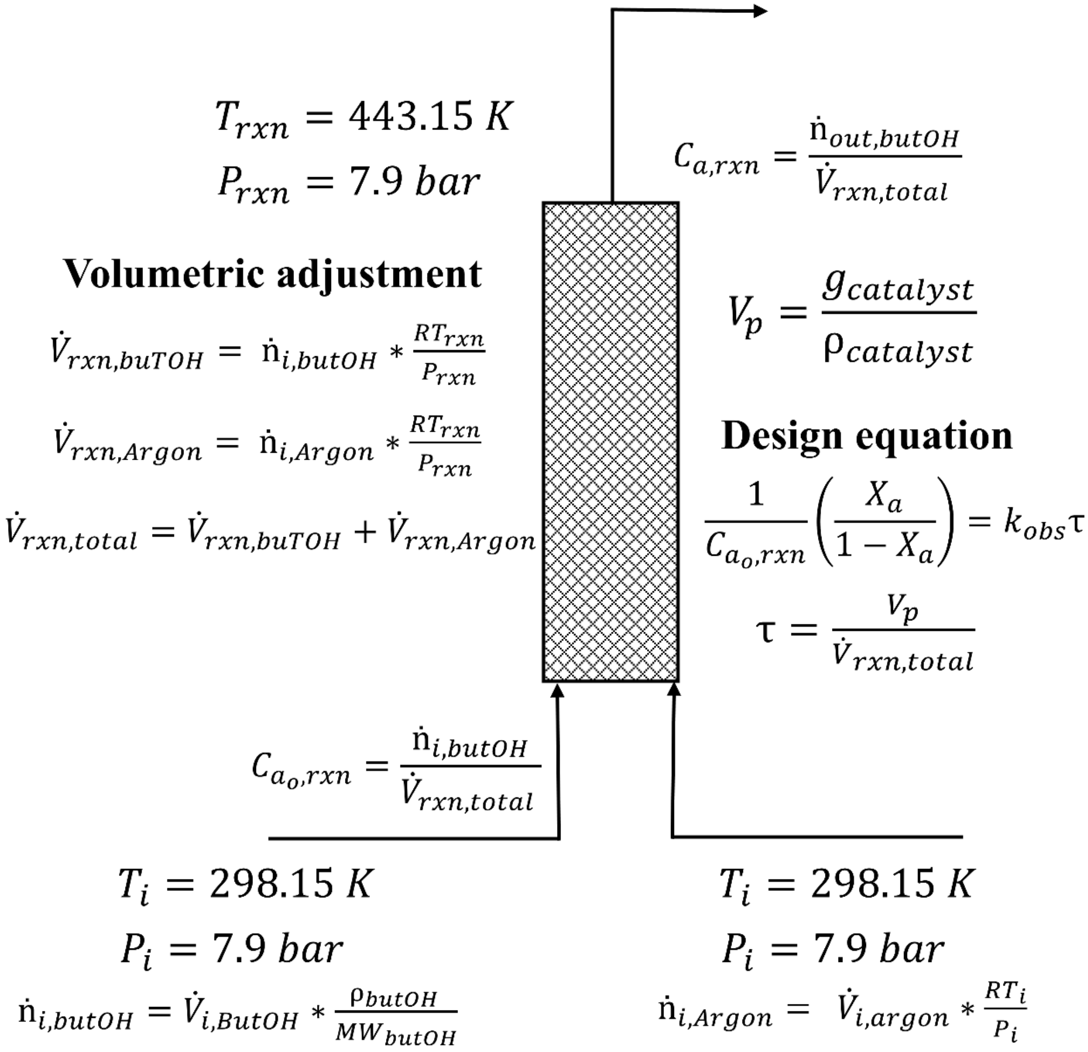

Figure 5.6. Plug flow reactor design and equations for the dehydration of n-butanol at reaction conditions. Pressure is with respect to the absolute pressure of the system.

Table 5.7. Computed values for the second order, irreversible reaction in a plug flow reactor. Particle diameters for crushed pellets and powder Y were determined using ASTM standard sieves. The density of catalysts was estimated using a graduated cylinder.

		Computed values at reaction conditions			
Run	Catalyst	$k_{obs}\left(\frac{(cm^3 fluid)^2}{(cm^3 solid)*mmol*s}\right)$	$\eta_{observed}$	$\eta_{calculated}$	$\phi_{calculated}$
PC – 1	Powder Y	9.68	1.00	1.00	0.013
FC – 7	Crushed pellets	8.10	0.839	0.996	0.116
FC – 2	Cylindrical pellet	1.27	0.131	0.818	0.836
		Particle diameter (cm)	Conversion (C%)	Ether selectivity (C%)	Carbon balance (C%)
PC – 1	Powder Y	0.0075	73.4	91.6	96.6
FC – 2	Crushed pellets	0.06	76.7	64.8	81.9
FC – 7	Cylindrical pellet	0.165	59.4	89.8	97.8
		$g_{catalyst}$	$\rho_{catalyst}\left(\frac{g}{cm^3}\right)$	$\dot{V}_{i,butOH}\left(\frac{cm^3}{s}\right)$	$\dot{V}_{i,Argon}\left(\frac{cm^3}{s}\right)$
PC – 1	Powder Y	1.80	0.328	$3.3*10^{-4}$	0.167
FC – 2	Crushed pellets	3.01	0.498	$4.5*10^{-4}$	0.167
FC – 7	Cylindrical pellet	4.63	0.440	$8.5*10^{-4}$	0.167

The rate constants calculated are with respect to the amount of n-butanol consumed for dehydration reactions. **Figure 5.6** shows the calculations conducted to determine the outlet concentration C_a and the rate constant k. **Table 5.7** compares the observed rate constants, effectiveness factor and Thiele modulus calculated for each run. The calculated effectiveness factors are higher than the observed values. Cylindrical pellets had the lowest observed effectiveness factor ($\eta = 0.131$). The low effectiveness factor may indicate potential mass transfer limitations as the carbon balances for PC-1 and FC-2 are over 95%. The crushed pellets had a higher effectiveness factor ($\eta = 0.839$) compared to the cylindrical pellets. However, it is worth noting that the carbon balances are significantly lower compared to the cylindrical pellet and powder Y catalyst (**Table 5.7**). While the crushed pellets may reduce internal mass transfer effects, it is unclear if this lower rate constant is due to catalyst deactivation or entirely to internal mass transfer. More research is needed, likely requiring testing of pellets of different known formulations, to understand the roles of the pellets on dehydration and mass transfer. We conclude that the pellet formulation plays a significant role in changing the acid catalyzed dehydration chemistry of alcohols.

5.3.4 Spent catalyst analysis

Figure 5.7 shows images of the spent beds after reaction. Typically, after 20 hrs time on stream (TOS), a tar phase is formed, consisting of absorbed alcohols and coke products that were detected using thermogravimetric analysis (TGA)[8]. This tar phase leads to particle agglomeration, contributing to pressure build up. PC-1 used the EtOH/ButOH oligomerization feed with powder Y in 0.95-cm diameter reactors, using Configuration A in **Table 5.2**. With this catalyst bed, we were able to obtain product flow, as there was no catalyst agglomeration. SP-1 refers to the powder Y catalyst in 2.54-cm diameter reactors using Configuration B in **Table 5.2**. When comparing the spent catalysts of PC-1 and SP-1, the presence of catalyst agglomeration after reaction is evident. The agglomeration arises from the formation of tar products from dehydration reactions. Particle agglomeration in Configuration B did not allow for product collection. Therefore, it appears that increasing the reactor diameter can amplify the effects of particle agglomeration in the catalyst bed (See **Figure 5.7** for PC-1 and SP-1).

FC-1 to FC-6 represent the pellet Y catalyst after dehydration of alcohols of varying feedstocks using configuration D in **Table 5.3**. FC-1 - FC-3 used pure n-butanol as the feed. FC-4 used an equimolar mixture of n-butanol and n-hexanol. Larger alcohols influence coke buildup over the catalyst bed, as shown in **Figure 5.7**. The addition of n-hexanol resulted in lower carbon balances (see **Table 5.4**). These results agree with our previous studies, in which larger alcohols have lower carbon balances and higher coke selectivities at constant WHSV[8]. As shown in **Figure 5.7**, unlike the powder catalyst, there is no evidence of tar phase products with the pellets. Rather, the main issue with pellets may be that the alcohols are absorbing strongly onto the interior of the formulation, resulting in significant drops in carbon balances via coking mechanisms (See **Table 5.4**). This explanation is more evident when the catalyst bed of FC-1 - FC-3 (**Figure 5.7**) is compared with the catalyst bed of FC-7 (**Figure 5.5**). Using n-butanol as the feedstock, the carbon balances were significantly lower when the pellets were crushed to smaller particle sizes (**Table 5.6**). An improvement in transport (i.e increase in effectiveness factor) may have resulted in further favoring coke products.

FC-5 and FC-6 are the spent catalyst Pellet Y bed at WHSV = 1.0 and 2.0 h^{-1}, respectively with EtOH/ButOH oligomerization feeds. A noticeable coke formation on the pellets can be observed. This suggests that mass transfer may be influencing the dehydration reaction chemistry over the pellets, as shown with the observed effectiveness factors. FC-5 shows that the pellets are slightly darker at lower WHSV, which results in lower carbon balances (See **Table 5.5** and **Figure 5.3**). In all cases, lower space velocities and larger alcohols led to lower carbon balances. Depending on the feedstock used, the color of the spent catalyst changes due to differences in coke products produced.

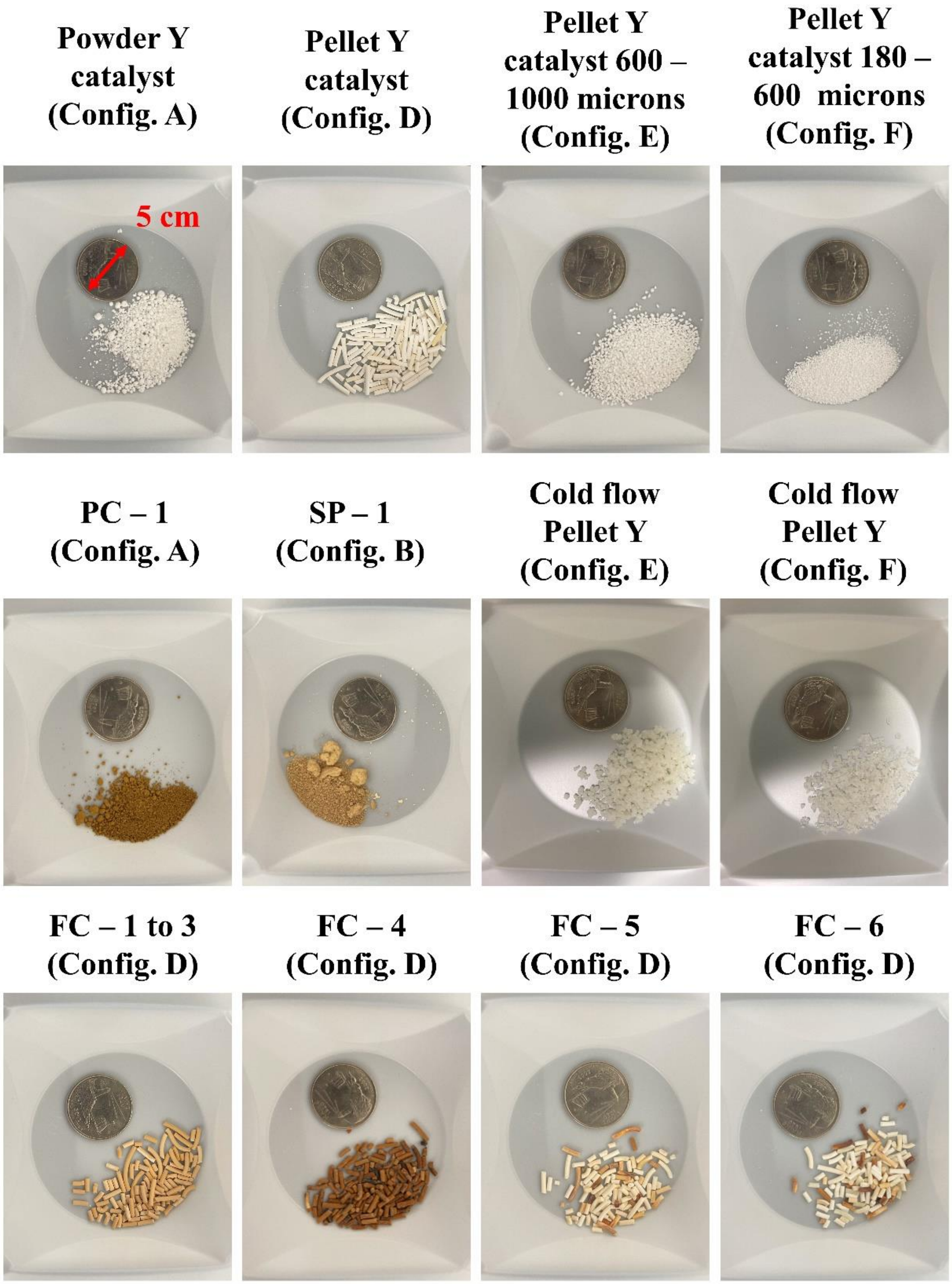

Figure 5.7. Fresh and spent catalyst beds from alcohol dehydration and cold flow experiments. Top: Fresh powder and pellet Y catalyst at varying particle sizes. Middle: Spent catalyst beds from scale up studies and cold flow experiments. Bottom: Spent catalyst beds from alcohol dehydration experiments. A quarter is used as a reference for the size of the catalyst particles, with a diameter of 5 cm.

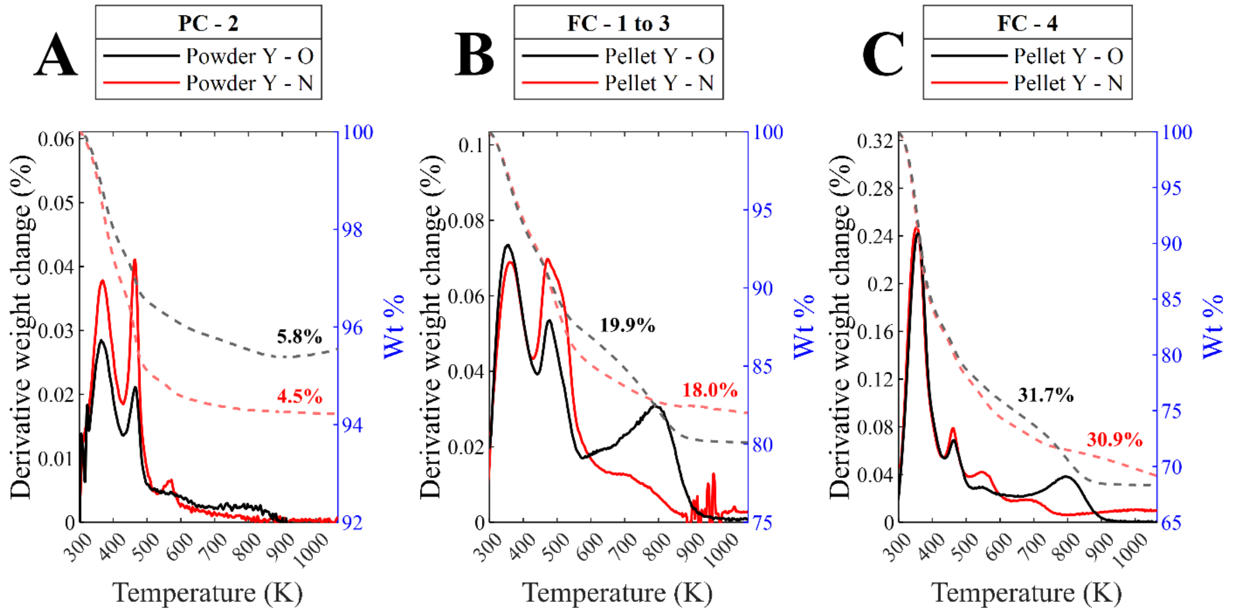

Figure 5.8. Thermal analysis of spent powder and pellet catalysts after dehydration of A) PC - 2 B) FC-1 - FC-3 and C) FC-4. Red solid lines signify TGA done in a N_2 environment, while black sold lines represent TGA done in an O_2 environment. Dashed lines represent the weight percent change in O_2 and N_2 environments. Values represent the final weight percent loss from the experiments.

TGA experiments were conducted for all spent catalysts shown in **Figure 5.7**. Three different regions can be observed; the volatile, soft coke, and hard coke regions from 323-473 K, 473-673 K, and 673-873 K, respectively[19]. **Figure 5.8** shows the TGA experiments for the Powder and Pellet Y spent catalyst beds using n-butanol, as well as the equimolar alcohol mixture. **Figure 5.8B** has a similar TGA profile to the powder Y bed (**Figure 5.8A**) from previous TGA studies[8]. The overall amount of carbon on the pellets is higher than the powder. When comparing **Figure 5.8B** and **C**, we see a larger amount of carbon deposition with the introduction of larger alcohols. This agrees with the carbon balances observed in these runs, which decrease with the introduction of n-hexanol (See **Table 5.4**). For the equimolar mixture, most of the products lie within the volatile and soft coke region.

The area under the TGA curve was split into two regions to classify the coke products observed over the spent catalyst beds in **Figure 5.7**. Region 1 is defined as the lumped volatile and soft coke products. Region 2 is defined as the hard coke products. The integrated areas represent the approximate weight percent contributions of the lumped volatile and soft coke regions (323 – 673K) and the hard coke region (673 – 873K). The TRAPZ method was used in MATLAB to estimate these values. **Table 5.8** shows the calculated weight percents. Comparing PC-2 and FC-1 – FC-3, there is a higher concentration of coke products in both Region 1 and 2 when using the pellet formulation. For PC-7, where smaller pellet particles were used for the dehydration of n-butanol, there is an increase in the coke concentration in Region 2. Compared to the other beds that used n-butanol (PC-2, FC-1 - FC-3) a higher concentration of hard coke is observed. When n-hexanol was introduced over the pellet (FC – 4), there was a 11.0 wt% increase in Region 1, and a negligible increase in Region 2 compared to FC-1 - FC-3.

Table 5.8. Weight loss contributions for the products observed in the TGA in an O_2 environment in Figure 3. Volatile and soft coke region: 323 – 673 K, Hard coke region: 673 – 873 K.

Run #	Total weight loss (wt%)	Region 1 (wt%)	Region 2 (wt%)
PC-2	4.5	4.1	0.4
FC-1 - FC-3	19.9	14.5	5.4
PC-7	17.0	10.0	7.0
FC-4	31.7	25.6	6.1

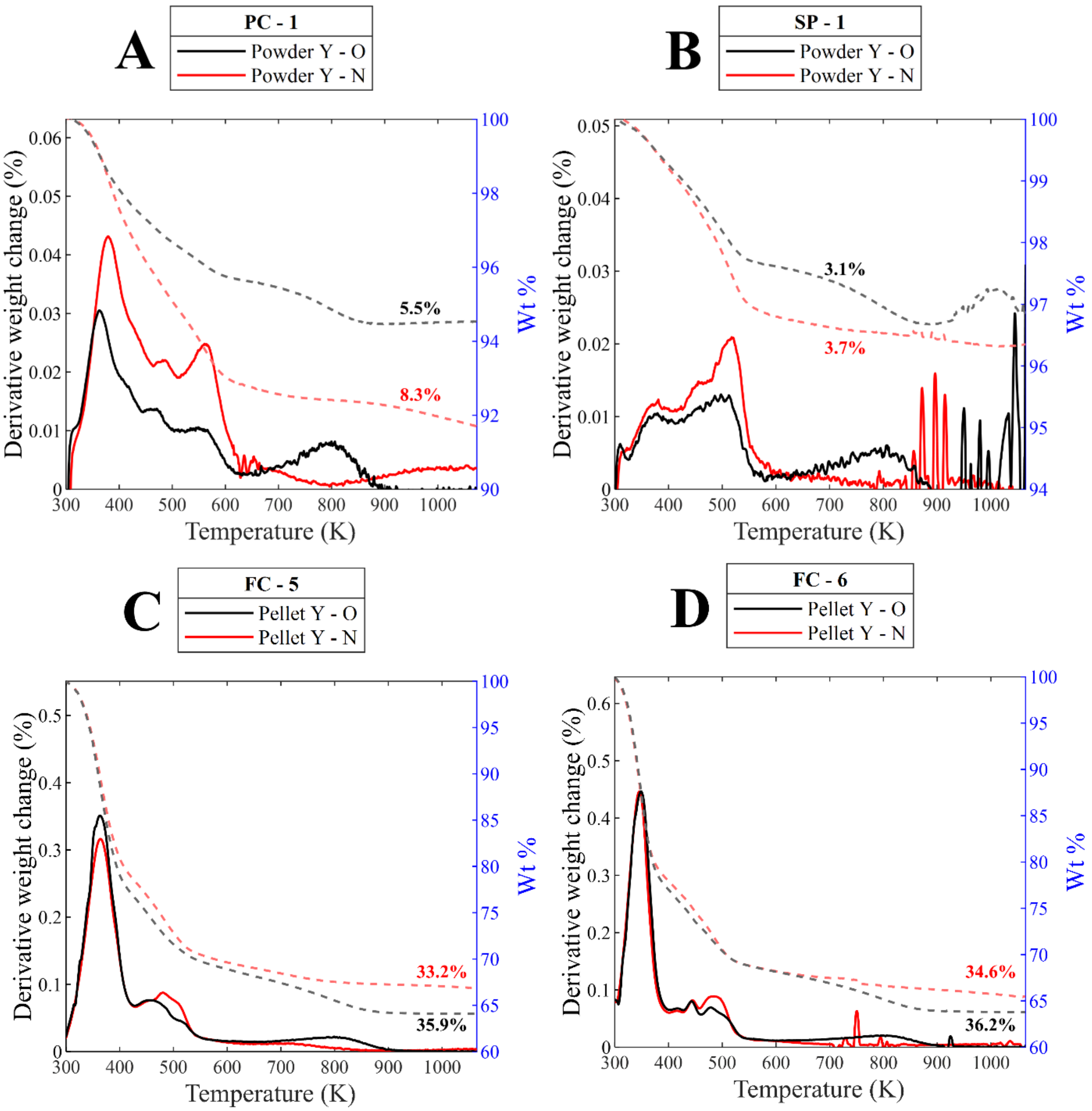

Figure 5.9. Thermal analysis of spent powder catalysts after etherification with EtOH/ButOH oligomerization feeds for A) PC-1, B) SP-1, C) FC-5 and D) FC-6. Red solid lines signify TGA done in a N_2 environment, while black sold lines represent TGA done in an O_2 environment. Dashed lines represent the weight percent change in O_2 and N_2 environments. Values represent the final weight percent loss from the experiments.

Figure 5.9 shows the TGA experiments of the dehydrated EtOH/ButOH oligomerization spent powder and pellet Y catalysts. PC-1 in 0.95-cm and SP-1 in 2.54-cm diameter reactors exhibit similar TGA profiles, in which the coke products mainly lie in the volatile and soft coke region. (See **Figure 5.9A** and **B**). **Figure 5.9C** and **D** represent the EtOH/ButOH oligomerization spent Pellet Y catalyst beds. FC-5 and FC-6 have more coke on catalyst than FC-1 to FC-4. The differences between these beds are that the EtOH/ButOH oligomerization feed has branched, and secondary alcohols present in the reaction mixture. Comparing the TGA profiles, FC-5 had a lower coke yield compared to FC-6. FC-5 also had lower carbon balances than FC-6, as shown in **Table 5.5** (79% vs. 93%, respectively). The average liquid mass balance for FC-5 was 91%, while FC-6 had a mass balance of 101%. One possible explanation for the lower carbon and mass balances is that at lower WHSV, heavy oligomers could be forming and solubilizing in the reaction feed. This theory would agree with the trends observed in powder Y catalyst, in which feedstocks with heavier alcohols led to the formation of heavy, soluble oligomers[8]. These heavy oligomers have also been observed in other systems, where acid-catalyzed dehydration of biomass led to the formation of heavy oligomers[20, 21]. In all cases, the use of pellets led to higher carbon uptake compared to powder Y catalyst beds previously studied[8].

5.3.5 Cold flow experiments over pellets at varying particle sizes

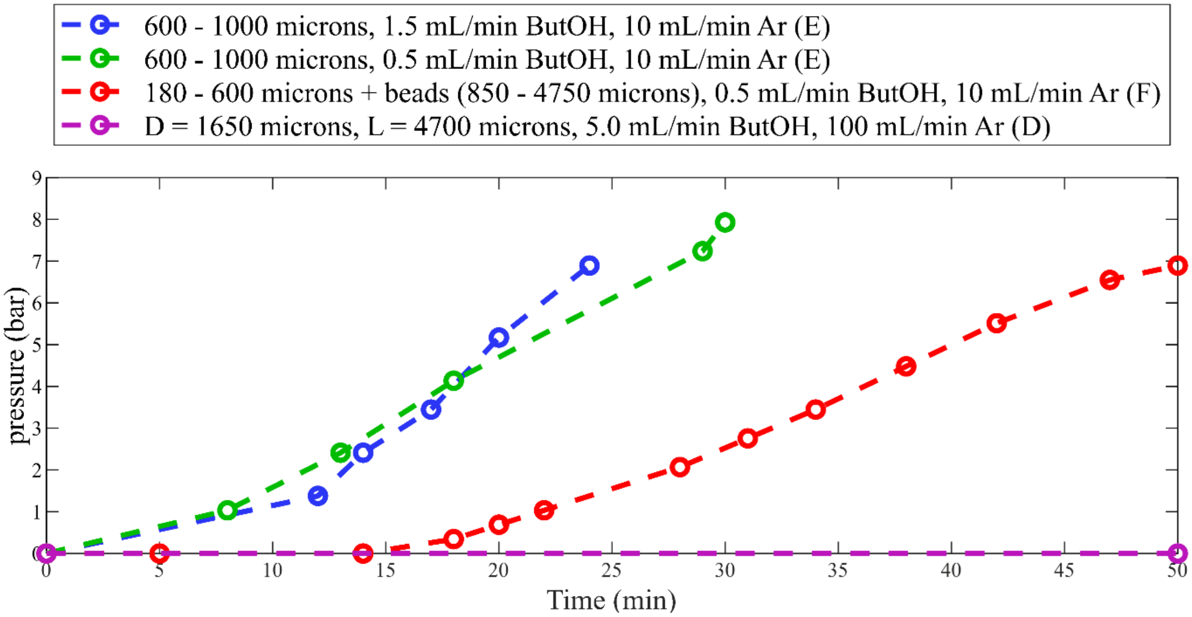

Figure 5.10. Cold flow experiments using zeolite Y pellet at different liquid flowrates and particle sizes. Liquid stream: n-butanol. Letters at the end correspond to the reactor configuration used for the run.

N-butanol at room temperature was passed over different particle sizes of the pellets to understand the differences in pressure buildup in the reactor. **Figure 5.10** shows four cold flow experiments conducted with n-butanol at atmospheric pressure and room temperature. The pressure buildup was recorded and timed to see how long each run would take to build up to approximately 6.9 bar. The pellets (Configuration D) show no pressure increase using high liquid (5 mL/min) and gas flowrates (100 mL/min) at the same time.

The pressure drop increased for all crushed pellets (Configurations E and F) as shown in **Figure 5.10**. In 24 minutes, the pressure drop over the bed increased from 0 to 6.9 bar at a n-butanol and argon flowrate of 1.5 mL/min and 10 mL/min, respectively for the 600 - 1,000 micron crushed pellets (Configuration E). The catalyst bed was drained, and the butanol flowrate was decreased to 0.5 ml/min. Again, the pressure drop increased from 0 to 6.9 bar in approximately 30 minutes. A lower amount of crushed powder (600 - 1,000 microns) was then mixed with silica beads (Configuration F) and the experiment was retested. The pressure drop for this new configuration also increased. These results show that the n-butanol absorbs on the zeolite Y catalyst and creates a pressure buildup during the reaction even at room temperature.

The Ergun equation[22] was used to compare our experimental results with the expected pressure drop across the catalyst bed. The Ergun equation is given by **equation 5**. Here, L is the length of the catalyst bed, μ is the dynamic viscosity of the fluid, u is the superficial velocity of the fluid, D_p is the spherical particle diameter of the catalyst, and ε is the void fraction. Typically, the void fraction is the most difficult parameter to estimate[22]. For simplicity, since there is gas and liquid phases flowing through the reactor, the total pressure drop across the catalyst bed is given by **equation 6**. The total pressure drop is given as the addition of the friction losses produced from the gas and liquid fluids flown through the catalyst bed.

$$\frac{\Delta P_{ergun}}{L}=150\frac{(1-\varepsilon)^2}{\varepsilon^3}*\frac{\mu u}{D_p^2}+1.75\frac{1-\varepsilon}{\varepsilon^3}*\frac{\rho u^2}{D_p} \quad (5)$$

$$\frac{\Delta P_{total}}{L}=\frac{\Delta P_{Ergun,gas}}{L}+\frac{\Delta P_{Ergun,liquid}}{L} \quad (6)$$

Table 5.9. Parameters used for the Ergun equation. [a]Signifies that the particle size considered were based on the lowest particle size from the micron range for the pellet Y catalyst. [b]Signifies the average particle diameter of the pellet. [c]Signifies the average particle length of the pellet. Dynamic viscosities and densities for argon and n-butanol were taken from ref 23-25. Void fraction values were taken from ref 16.

	Configuration D	**Configuration E**	**Configuration F**
Reactor Dimensions			
Bed length (m)	0.254	0.254	0.254
Reactor diameter (m)	$9.53E^{-3}$	$9.53E^{-3}$	$9.53E^{-3}$
Wall thickness (m)	$8.89E^{-2}$	$8.89E^{-2}$	$8.89E^{-2}$
Adjusted reactor diameter (m)	$8.64E^{-3}$	$8.64E^{-3}$	$8.64E^{-3}$
Cross sectional area (m^2)	$5.86E^{-5}$	$5.86E^{-5}$	$5.86E^{-5}$
Fluid properties			
$\mu_{\text{Argon}} \left(\frac{\text{N*s}}{\text{m}^2}\right)$[25]	$2.23E^{-5}$	$2.23E^{-5}$	$2.23E^{-5}$
$\mu_{\text{n-butanol}} \left(\frac{\text{N*s}}{\text{m}^2}\right)$[23]	$2.54E^{-3}$	$2.54E^{-3}$	$2.54E^{-3}$
$\rho_{\text{argon}} \left(\frac{\text{kg}}{\text{m}^3}\right)$[24]	1.61	1.61	1.61
$\rho_{\text{n-butanol}} \left(\frac{\text{kg}}{\text{m}^3}\right)$[23]	810	810	810
Catalyst properties			
Particle diameter (microns)	1650[b], 4700[c]	600	180
Particle diameter D_p (m)	[b]$1.65E^{-3}$	[a]$6.00E^{-4}$	[a]$1.80E^{-4}$
Void fraction (min) (ε)[16]	0.275	0.240	0.240
Void fraction (max) (ε)[16]	0.440	0.470	0.470
Fluid flowrates			
n-butanol flow (mL/min)	5	1.5, 0.5	0.5
Argon flow (mL/min)	100	10	10
Calculated pressure drop			
$\Delta P_{\varepsilon,\text{ min}}$ (bar)	0.02	0.05, 0.02	0.04
$\Delta P_{\varepsilon,\text{ max}}$ (bar)	0.00	0.00, 0.00	0.01

Table 5.9 shows the parameters used for the Ergun equation for configurations D, E and F. The void fractions were obtained from the work of Bey and Eigenberger[16], who identified void fractions for materials of varying structure. Void fractions for cylinders were used for configuration D. Void fractions for spheres were used for configurations E and F. ε_{min} represents the lowest void

fraction that was observed, while ε_{max} represents the void fraction of the entire cross section of the bed. As shown by our calculations in **Table 5.9**, configurations D, E, and F of the reactor should have minimal pressure drop (~0 bar). These results further indicate that the pressure drop is due to buildup of a species that is coking the surface of the catalyst at room temperature. SI – Section 2 shows the TGA profiles of the cold flow runs. Particle agglomeration is present even at room temperature due to feedstock absorption (See **Figure 5.7**, **Figure 5.11** and **Figure 5.12**), which can lead to increased pressure drop over the reactor bed. This effect is seen in both configuration E and F (**Figure 5.12**).

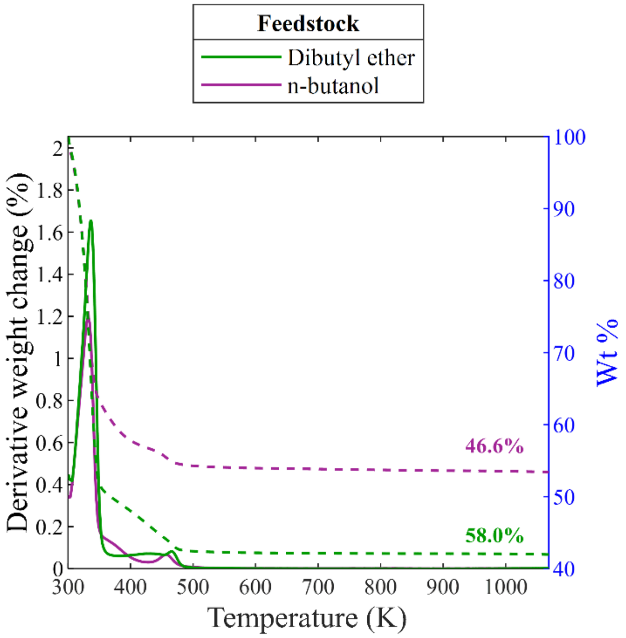

Figure 5.11. Cold-flow TGA data of powder Y catalyst mixed with single feed Dibutyl ether and n-butanol at ~ 1:1.2 g_{cat}:g_{feed} ratio. Ramp rate: 20 K/min under a N_2 environment.

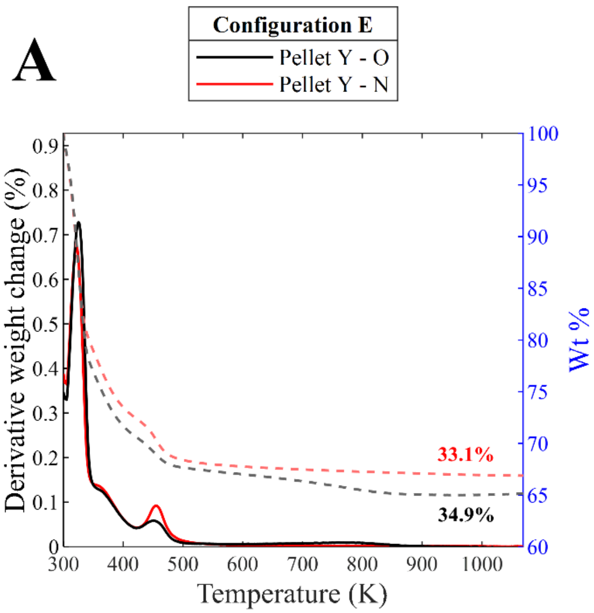

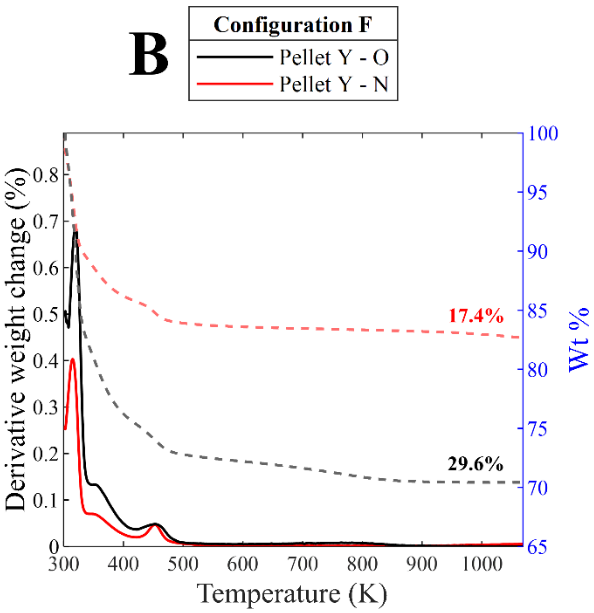

Figure 5.12. Thermal analysis of cold flow experiments for A) Configuration E and B) Configuration F using n-butanol as the feed. Red solid lines signify TGA done in a N_2 environment, while black sold lines represent TGA done in an O_2 environment. Dashed lines represent the weight percent change in O_2 and N_2 environments. Values represent the final weight percent loss from the experiments. Ramp rate: 20 K/min.

5.3.6 75 mL batch dehydration reactions

Dehydration experiments were done in a batch reactor to produce enough product for fuel characterization. **Table 5.10** summarizes the results for dehydration of EtOH/ButOH oligomerization products in a 75 ml Parr reactor. All experiments in **Table 5.10** were performed with the powder catalyst. Increasing the reaction time led to higher conversion and ether selectivity, as shown from Runs 75 - 3 to 75 - 4. The ether selectivity was not a strong function of the residence time. Increasing the temperature from 443.15 to 473.15 K (Runs 75 - 3, 75 - 5 and 75 - 6) increased the conversion and olefin selectivity. The decrease in ether yield agrees with our thermodynamic trends, as high temperatures favor mono-dehydration over bi-molecular dehydration[8]. Therefore, to favor bi-molecular dehydration, temperatures lower than 463.15 K must be used. The amount of catalyst was further increased to 14 g, and two different temperatures up to 458.15 K were analyzed. The highest C_{10+} ether yields were obtained at high conversion with 14 g of catalyst at 458.15 K.

Table 5.10. Dehydration of EtOH/ButOH oligomerization products over powder zeolite Y in 75 mL Parr reactors. Stir peed: 750 rpm, pressurized with 6.9 bar of Ar. Carbon balances are defined only by the liquid mass balance.

	75 mL Parr reactors							
Run #	**75 - 1**	**75 - 2**	**75 - 3**	**75 - 4**	**75 - 5**	**75 - 6**	**75 - 7**	**75 - 8**
Time (hr)	26.5	48	28	42	22	24	23	22
Feed volume (mL)	30	30	30	30	30	30	30	30
Catalyst loading (g)	5	5	10	10	10	10	14	14
Residence time	0.19	0.10	0.09	0.06	0.11	0.10	0.08	0.08
Temperature (K)	443.15	443.15	443.15	443.15	458.15	473.15	451.15	458.15
THF extraction	Y	N	Y	Y	Y	Y	Y	Y
C%								
Conversion	31.5	66.3	47.4	65.0	62.1	93.6	65.4	88.9
C_{10+} ether yield	15.4	22.7	21.2	34.4	30.3	29.8	32.7	44.3
C_{10+} ether selectivity	49.0	34.2	44.8	52.8	48.8	31.8	50.0	49.9
Butyl ether selectivity	5.9	4.1	5.3	6.7	6.2	4.8	6.1	6.8
C_{4+} olefin selectivity	6.2	2.6	3.8	3.7	4.3	12.9	3.0	9.8
Carbon balance	87.7	60.9	78.2	76.1	74.8	52.7	73.2	70.2

The activation energy of dehydration reactions was calculated based on the total concentration of alcohol introduced into the batch reactor. A second order, irreversible reaction is assumed, where V = 75 mL at reaction conditions. The volume corresponds to the constant volume of the parr reactor used for the experiments. The rate constant is calculated by **equation 6**:

$$\frac{\frac{1}{C_{a_o}}\left(\frac{X_a}{1-X_a}\right)}{g_{cat}} = kt \qquad (6)$$

Table 5.11. Calculated rate constants as a function of temperature in 75 mL Parr reactors for a second order, irreversible reaction. $C_{a,o}$ is based on the initial concentration of all alcohols added in the reactant feed.

Run	$C_{a_o}\left(\frac{mmol}{cm^3}\right)$	T (K)	Time (hr)	$g_{catalyst}$	Fraction conversion (X_a)	$k\left(\frac{(cm^3\ alcohol)^2}{mmol*g_{catalyst}*s}\right)$
75 – 3	3.465	443.15	28.0	10	0.477	$2.61*10^{-7}$
75 – 5	3.464	458.15	22.1	10	0.621	$5.95*10^{-7}$
75 – 6	3.464	473.15	24.3	10	0.934	$4.70*10^{-6}$

Table 5.11 shows the calculated rate constants for runs 75 - 3, 75 - 5 and 75 - 6, over a temperature range of 443.15 – 473.15 K. Based on the calculated rate constants, the estimated activation energy for n-butanol dehydration was calculated to be 167.1 ± 44.9 kJ/mol. With a second order reaction, the range agrees with the activation energies observed for bi-molecular and mono-molecular dehydration[14, 26-28]. For zeolite catalysts, the range can fall between 110 – 160 kJ/mol[14, 27, 28].

The products were in two phases, an organic phase and an aqueous phase. In some of the reactions THF was used as a solvent to solubilize the final products after reaction. However, the THF volume was 2 times the final product volume. Therefore, from a scale-up perspective, it would not be feasible to use THF as distillation steps would be needed to remove the solvent from the products. It was desired to produce larger amounts of products without using THF as a solvent, so that we could produce a larger amount of product that could be characterized in fuel tests. As a result, run 75 - 2 did not use THF and underwent centrifuge separation, leading to a lower carbon balance.

Table 5.12. Dehydration of EtOH/ButOH oligomerization products over power zeolite Y in 75 mL Parr reactors using 1.5g of catalyst. Stirspeed: 750 rpm, pressurized at 6.9 bar Ar. Carbon balances are defined only by the liquid mass balance.

	75 mL Parr reactors				
Run #	**75 - 9**	**75 - 10**	**75 - 11**	**75 - 12**	**75 - 13**
Time (hr)	23	24	48	96	45
Feed volume (mL)	30	30	30	30	30
Catalyst loading (g)	1.5	1.5	1.5	1.5	1.5
Residence time ($\frac{g_{reactant}}{g_{cat}*t\ (hr)}$)	0.71	0.68	0.34	0.17	0.36
Temperature (^{o}C)	443.15	443.15	443.15	443.15	458.15
THF extraction	Y	N	N	N	N
C%					
Conversion	9.2	25.7	30.8	46.6	50.9
C_{10+} ether yield	4.0	2.4	4.7	13.8	17.1
C_{10+} ether selectivity	43.7	9.5	15.1	29.7	33.5
Butyl ether selectivity	5.6	1.4	2.2	3.3	3.8
C_{4+} olefin selectivity	12.4	2.9	3.9	3.4	3.5
Carbon balance	96.5	77.8	75.7	70.4	69.9

Table 5.13. Collection of remaining products that underwent centrifuge in 75 mL Parr reactors with no THF extraction. Rpm = 3500 for 10 minutes. The mass from products is determined by subtracting the catalyst mass initially loaded into the reactor from the product mass after centrifuge. The mass absorbed is defined as the leftover product mass (accounted for catalyst loading) divided by the initial mass of the reaction.

Run #	**75 - 10**	**75 - 11**	**75 - 12**	**75 - 13**
Time (hr)	24	48	96	45
Catalyst loading (g)	1.5	1.5	1.5	1.5
Reaction feed mass (g)	24.5	24.5	24.5	24.5
Mass after centrifuge (g)	3.2	3.3	3.0	3.3
Product mass (g)	1.7	1.8	1.5	1.8
Mass absorbed (wt%)	6.9	7.3	6.1	7.3

Table 5.12 summarizes the results of parr reactors undergoing centrifuge without the presence of THF using 1.5 g of catalyst. The C_{10+} ether yields were lower compared to the runs using THF extraction. Comparing Run 75 - 9 and 75 - 10, the carbon balance decreases because

not all the liquid products could be separated from the catalyst, as shown in **Table 5.13**. Increasing the reaction time did not have any notable change on the conversion or ether yields. Increasing the temperature to 458.15 K led to a slight increase in the conversion and overall ether yield.

Table 5.14. Comparison of data from continuous flow reactor and batch reactor for dehydration of EtOH/ButOH oligomerization products using pure powder Zeolite Y. [a]Signifies the unknown GC area only detected in the liquid phase.

	PC - 1	**75 - 4**	**75 – 8**	**75 - 13**
Feed flowrate (mL/min)	0.04	NA	NA	NA
Catalyst loading (g)	1.8	10	14	1.5
WHSV (h^{-1}) or $t*g_{cat}/g_{alcohol}$	1.1	17.1	12.7	2.8
Temperature (K)	443.15	443.15	458.15	458.15
THF extraction	-	Y	Y	N
C%				
Conversion	71.1	65.0	88.9	50.9
C_{10+} ether yield	39.7	34.4	44.3	17.1
C_{10+} ether selectivity	56.1	52.9	49.9	33.5
Butyl ether selectivity	5.3	6.7	6.8	3.8
C_{4+} olefin selectivity	14.8	3.7	9.8	3.5
Carbon balance	86.5	76.2	70.2	69.9
Unknown liquid GC area (%)	4.4	10.2	11.8	8.9

Table 5.14 compares data obtained in a continuous flow reactor with the batch reactor data for the dehydration of EtOH/ButOH oligomerization products obtained from oligomerization of ethanol/butanol[8, 9]. The WHSV was used for the continuous flow reactor and the residence time was used for the batch reactor. At 443.15 K, the conversion in the batch reactor is lower than in the continuous flow reactor even though the WHSV is 16 times lower than the contact time in the batch reactor. In the continuous flow reactor, an inert argon gas stream was passed through the reactor bed which likely served to transport the product away from the catalyst surface. The unknown area detected is also higher in the batch reactor compared with the continuous flow reactor. From our TGA results, we know that products build up on the catalyst surface causing a

tar phase to form. It is likely that in the batch reactor more of this phase is forming. The ether selectivities are lower in the batch reactor compared to the continuous flow reactor. Based on these findings at the 75 mL scale, the conditions from Run 75 - 13 were used for studies at the 450 mL scale.

5.3.7 Scale up parameters

Figure 5.13 depicts the issues of using 5 – 10g of catalyst for the parr reactions. The top image represents the reaction products of run 75 - 6 in **Table 5.10** using 10g of catalyst. At high conversion, and using THF as the extraction solvent, there is a clear separation between the dehydration products, catalyst and THF. The use of THF and assumption of using the total feedstock volume for product quantification led to an overestimation of the final C_{10+} yields. This would explain the differences between the centrifuged and THF extracted analyzed products. As shown in **Figure 5.13**, the parameters for run 75 - 2 in **Table 5.10** used in 450 mL reactors resulted in undesired products. Heavy tar products were produced at the bottom of the reactor, and particle agglomeration created a catalyst ring at the top of the Parr reactor. **Figure 5.13** shows the solid ring before, during and post heat treatment on a hotplate. The solid phase shows how the catalyst particles agglomerated, with an oil phase at the bottom of the crucible. The agglomerated catalyst particles mix with the oil phase when heated. Both the oil and solid phases mixed homogenously together during the heat treatment. The heating treatment may explain the particle agglomeration observed in the continuous flow reactors. After cooling, the homogenous mixture solidifies. Based on these results, the ideal conditions were chosen based on the parameters of run 75 - 13 (**Table 5.12**) to minimize particle agglomeration, oil products, and heavy tar products as shown in **Figure 5.13**.

10 g powder Y, 30 mL feed at 443.15 K

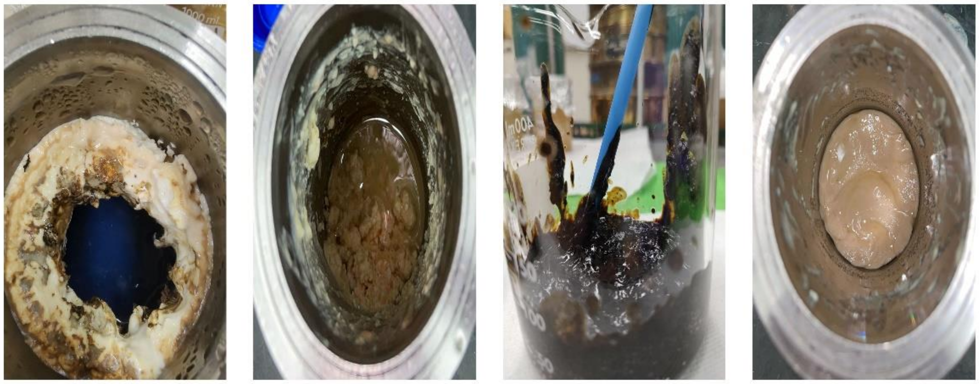

50 g powder Y, 300 mL feed at 443.15 K

15 g powder Y, 300 mL feed at 458.15 K

50 g powder Y, 300 mL feed at 443.15 K

15 g powder Y, 300 mL feed at 458.15 K

Catalyst Ring – 50 g Powder Y, 300 mL feed at 443.15 K

Figure 5.13. Scale up issues observed at high catalyst loadings. Top: THF and product separation of products obtained in 75 mL Parr reactors. Middle: Changes in product composition by decreasing catalyst loading (50 to 15g of catalyst). Bottom: Particle and product behavior at high catalyst loadings (50g) on a hotplate.

5.3.6 450 mL batch dehydration reactions

Table 5.15. Dehydration of EtOH/ButOH oligomerization products over power zeolite Y in 450 mL Parr reactors using 15g of catalyst and 300 mL of feed. Temperature: 458.15 K. Carbon balances are defined only by the liquid mass balance.

	450 mL parr reactors							
Run #	**450 - 1**	**450 - 2**	**450 - 3**	**450 – 4**	**450 - 5**	**450 - 6**	**450 - 7**	**450 – 8**
Time (hr)	47.2	45.0	39.3	34.2	34.2	29.2	29.2	29.2
Motor speed (RPM)	370	370	370	370	370	370	200	80
Pressure (bar)	6.9	6.9	6.9	6.9	20.7	20.7	20.7	20.7
Residence time	0.35	0.36	0.42	0.48	0.48	0.56	0.56	0.56
C%								
Conversion	85.5	86.6	85.6	83.6	89.0	81.1	84.2	89.5
C_{10+} ether yield	39.2	42.4	44.0	43.8	44.4	42.6	43.3	32.5
Carbon balance	67.5	70.3	73.3	75.1	72.9	76.5	75.9	59.9
Volume (mL)								
C_{10+} ethers	115.0	127.2	129.4	129.0	130.1	119.4	122.3	93.2
Butyl ether	17.4	18.8	19.5	19.3	19.9	19.2	19.7	14.6
C_{4+} olefins	22.6	23.3	24.3	24.2	31.3	24.5	29.7	34.8
Leftover alcohols	43.3	40.2	43.1	48.9	33.0	56.6	47.3	31.6
Unknown products	53.5	49.2	47.5	40.8	51.7	44.6	54.6	98.8
Unknown liquid GC area (%)	9.7	9.9	10.1	10.2	10.6	9.9	10.1	14.6

The batch experiments were scaled up to a 450 ml Parr reactor to produce larger amounts of liquid product as shown in **Table 5.15**. These conditions were based on run 75 - 13 from **Table 5.12**. The C_{10+} ether yield in the 450 mL batch reactors was more than two times higher than in the 75 mL batch reactors (see run 75 - 13, **Table 5.12** and run 450 - 1, **Table 5.15**).

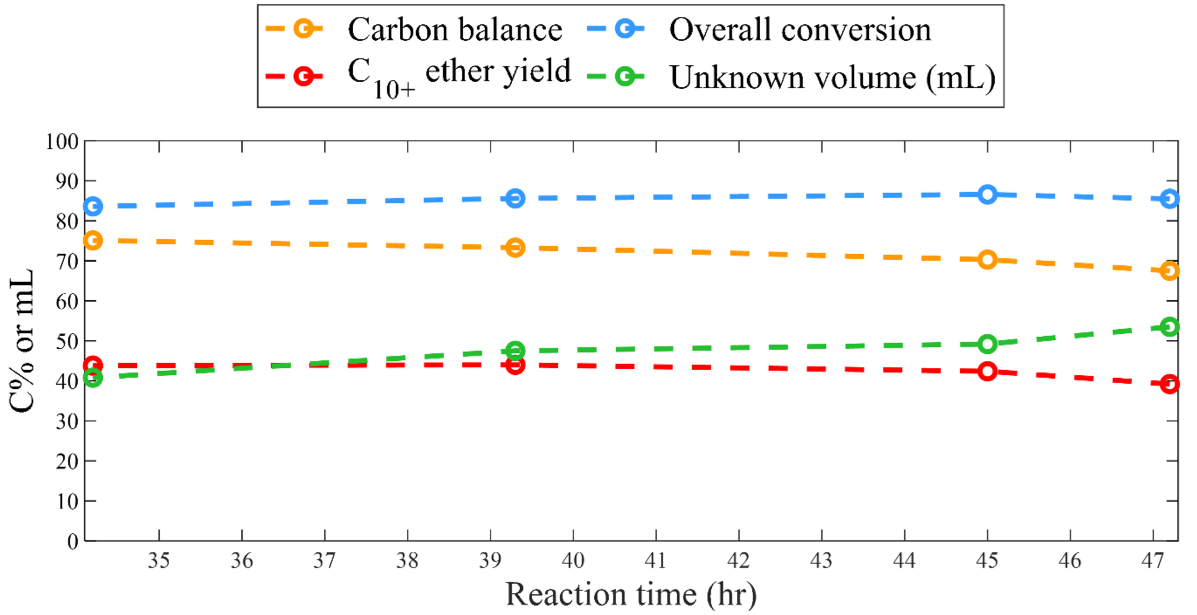

Figure 5.14. 450 mL Parr reactors at constant conversion using EtOH/ButOH oligomerization products as a function of reaction time. Reaction conditions: T = 458.15 K, P = 6.9 bar, motor speed = 370.

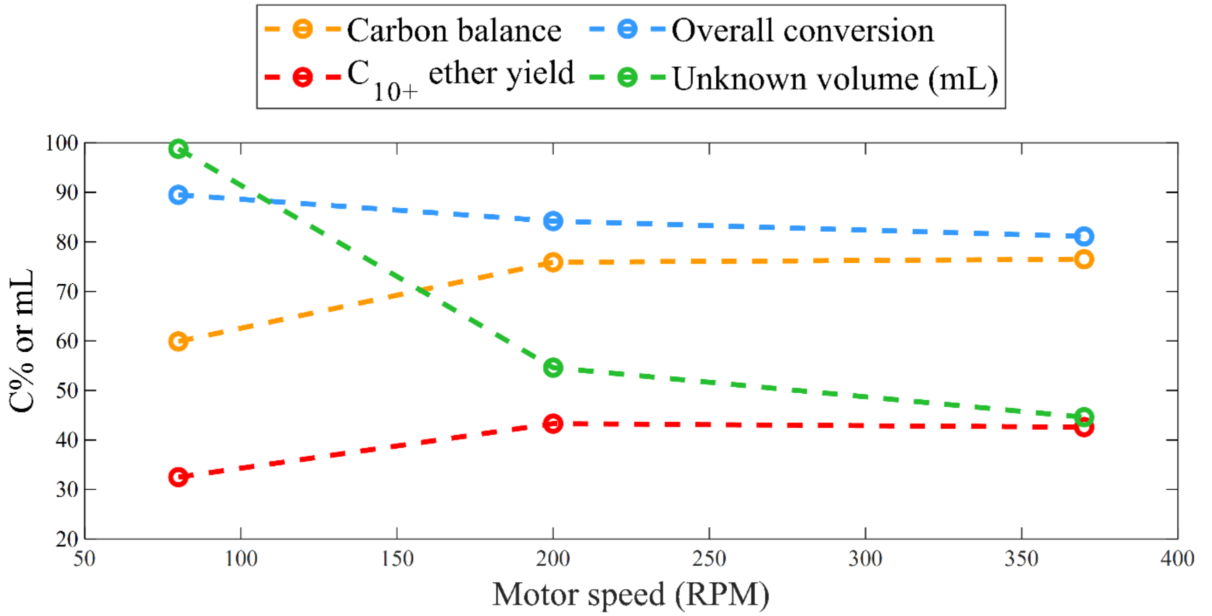

Figure 5.15. 450 mL Parr reactors at varying motor speeds using EtOH/ButOH oligomerization products. Reaction conditions: Time = 29.2 hr, T = 458.15 K, P = 20.7 bar.

As shown in **Table 5.15**, decreasing the reaction time did not affect the conversion. However, the C_{10+} ether yield and carbon balances increased with decreasing reaction time, as shown in **Figure 5.14**. There was only a slight increase in the conversion and no increase in the ether yield when the pressure was increased. As the motor speed decreases, the ether selectivity and carbon balances decrease, as shown in **Figure 5.15**. **Table 5.16** summarizes the final volumes obtained and collected from all reaction runs. Based on the GC analysis, approximately 10.6% of the unknowns can be detected in the GC. Based on the total unknown volume obtained (440.7 mL, **Table 5.16**), approximately 46.7 mL (2.2 vol%) is detected in the GC while 394.0 mL (18.6 vol%) cannot be detected.

Table 5.16. Volume distribution of the final products obtained from 450 mL Parr reactor experiments. Centrifuge rpm = 3500 for 10 minutes.

Compounds	**Volume (mL)**	**Vol %**
Unknowns	440.7	20.9
C_{10+} ethers	965.6	45.7
Butyl ether	148.4	7.0
Unreacted alcohols	344.0	16.3
C_{4+} olefins	214.7	10.2
Total volume	2113.4	

5.3.7 Distillation of final products

Table 5.17. Mass composition of the starting feed, light and heavy cuts obtained from vaccum distillation using run 450 - 1.

Ether	**C#**	**Feed**	**Light**	**Heavy**
di-n-butyl ether	8	7.0%	18.6%	0.9%
butyl ethylbutane ether	10	0.5%	0.5%	0.5%
C10 ether	10	21.6%	15.6%	28.2%
butyl ethylhexane ether	10	0.7%	0.2%	1.2%
hexyl ethylbutane ether	12	2.3%	0.5%	3.7%
C12 ether	12	18.2%	2.7%	30.2%
C14 ether	14	2.7%	0.1%	4.7%
hexyl ethylhexane ether	14	0.7%	0.0%	1.2%
C16 ether	16	0.2%	0.0%	0.4%
Olefins				
C4 olefins	4	0.5%	0.0%	0.0%
C5 olefins	5	0.4%	0.0%	0.0%
C6 olefins	6	3.1%	0.1%	0.0%
C7 olefins	7	2.5%	1.6%	0.0%
C8 olefins	8	1.8%	3.6%	0.0%
Unreacted Alcohols				
1-butanol	4	5.2%	14.0%	0.0%
2-methyl-1-butanol	5	0.5%	1.4%	0.0%
1-hexanol	6	10.2%	22.1%	5.1%
2-ethyl-1-butanol	6	0.5%	1.5%	0.2%
2-heptanol	7	0.1%	0.2%	0.1%
1-octanol	8	1.6%	0.7%	2.7%
2-octanol	8	0.0%	0.0%	0.0%
2-ethyl-1-hexanol	8	0.4%	0.2%	0.5%
Unknown products (wt%)	-	19.2%	16.1%	20.4%
C_{10+} ethers (wt%)	-	46.8%	19.7%	70.1%
C_{4+} olefins (wt%)	-	8.4%	5.3%	0.0%
Unreacted alcohols (wt%)	-	18.6%	40.3%	8.6%
Butyl ether (wt%)	-	7.0%	18.6%	0.9%
Total weight (g)		192.5	63.8	107.4

Table 5.18. Mass composition of the starting feed, light and heavy cuts obtained from vaccum distillation using run 450 - 2.

Ether	**C#**	**Feed**	**Light**	**Heavy**
di-n-butyl ether	8	7.2%	18.9%	4.9%
butyl ethylbutane ether	10	0.4%	0.3%	0.5%
C10 ether	10	22.3%	8.3%	27.5%
butyl ethylhexane ether	10	0.7%	0.1%	1.0%
hexyl ethylbutane ether	12	2.3%	0.2%	3.1%
C12 ether	12	19.0%	1.3%	24.9%
C14 ether	14	2.8%	0.0%	3.7%
hexyl ethylhexane ether	14	0.8%	0.0%	0.9%
C16 ether	16	0.2%	0.0%	0.2%
Olefins				
C4 olefins	4	0.5%	0.0%	0.0%
C5 olefins	5	0.4%	0.0%	0.0%
C6 olefins	6	2.9%	0.7%	0.0%
C7 olefins	7	2.4%	5.3%	0.0%
C8 olefins	8	1.7%	7.1%	0.3%
Unreacted Alcohols				
1-butanol	4	4.4%	24.0%	0.3%
2-methyl-1-butanol	5	0.4%	1.7%	0.2%
1-hexanol	6	9.1%	11.0%	9.6%
2-ethyl-1-butanol	6	0.4%	0.7%	0.4%
2-heptanol	7	0.1%	0.1%	0.1%
1-octanol	8	1.4%	0.3%	2.1%
2-octanol	8	0.0%	0.0%	0.0%
2-ethyl-1-hexanol	8	0.3%	0.1%	0.4%
Unknown products (wt%)	-	20.1%	19.8%	19.7%
C10+ ethers (wt%)	-	48.6%	10.3%	61.9%
C4+ olefins (wt%)	-	7.9%	13.0%	0.3%
Unreacted alcohols (wt%)	-	16.2%	37.9%	13.1%
Butyl ether (wt%)	-	7.2%	18.9%	4.9%
Total weight (g)		198.6	32.8	134.3

The products from the batch reactor experiments were then distillated into a heavier cut that had the larger ethers. This product was then analyzed. **Tables 5.17** and **5.18** show the mass compositions of the starting feedstock, light and heavy cuts obtained for run 450 - 1 and 450 - 2, respectively. For run 450 - 1, the distillation was conducted for 1 hr and 40 minutes, between the temperature range of 413.15 – 423.15 K. From this distillation experiment, we were able to collect 134 mL of heavy products, maintaing the butyl ether content below 1.0 wt%. Furthermore, no light olefins and minimal alcohols were detected in the heavy phase. The light cut mainly had light alcohols and dibutyl ether. The unknown content was around 26.8 wt% in the heavy cut, signifying that there are undetected heavy molecules that are produced in the dehydration of EtOH/ButOH oligomerization products at high conversion regimes in parr reactors.

For run 450 - 2, the distillation was conducted for 1 hr and 10 minutes, between the temperature range of 403.15 – 413.15 K. As shown, this distillation step had more butyl ether content (4.9 wt% vs. 0.9 wt%) and more alcohols (13.1 wt% vs. 8.6 wt%) in the heavy phase compared to the vaccum distillation of run 450 - 1. The C_{10+} ether content was also lower (61.9 vs. 70.1 wt%). Therefore, we chose the final distillation parameters used for run 450 - 1. The specifications obtained will be used as a reference for the final blend produced from all distillation experiments. The increase in distillation time seems to have a greater impact in removing lighter compounds for the initial mixture. Increasing the distllation temperature could possibly remove more C_{10+} ethers from the mixture, lowering our final C_{10+} ether process yields obtained from distillation. **Figure 5.16** represents the final heavy cuts produced from vaccum distillation.

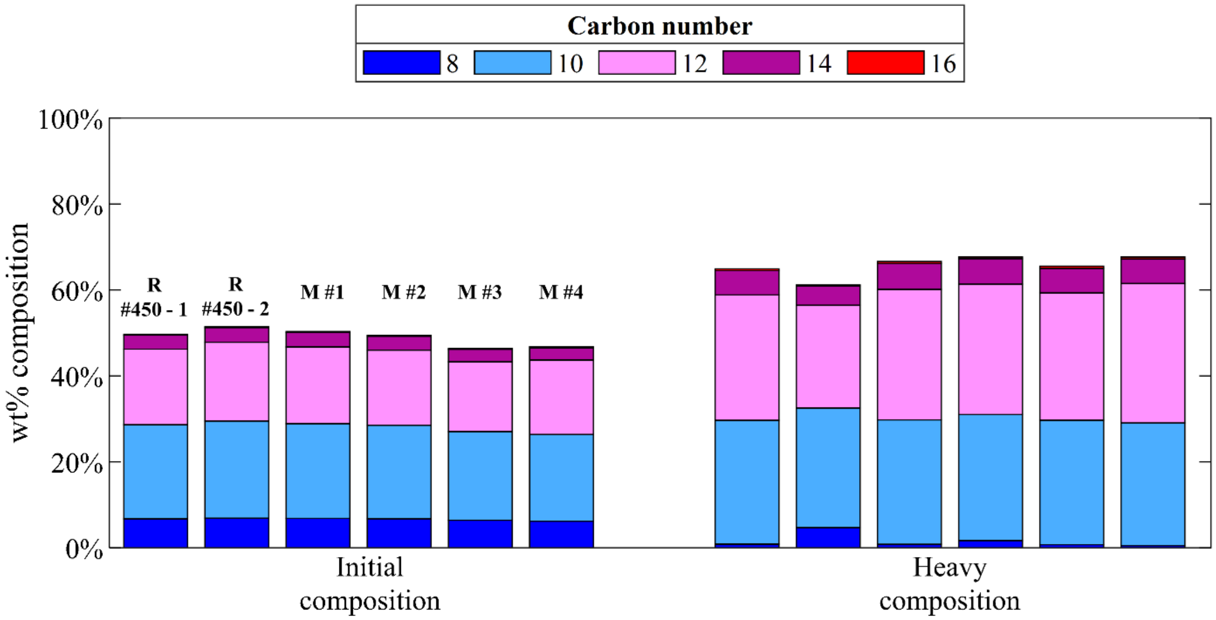

Figure 5.16. Initial and final ether weight compositions of feed and products from vacuum distillation. 'M' represents mixtures of various parr reactor experiments. The remaining weight composition can be attributed to unreacted alcohols, olefins, and unknown products in the blends.

A detailed breakdown of the mass composition of the final heavy and light products can be found in **Table 5.21**. The GC chromatograms for the products can be found in **Figure 5.17**. In all cases, a significant amount of butyl ether was removed and detected in the light products. The final heavy product volume obtained was approximately 1.025 liters, with a calculated density of 0.802 g/ mL. **Table 5.19** shows the final weight percent yield of the products obtained from vaccum distillation. The final heavy cut process yield was 50.7 wt%. **Table 5.20** compares the final specifications of the heavy mixtures obtained compared to the requested specifications obtained from the distillation of run 450 - 1, which are in agreement. Comparing **Table 5.17** with **Table 5.21**, the product distributions of run 450 - 1 and the final liter produced are also in agreement. Our final product was sent for fuel characterization, and will be labeled as blend 2 (B2) in the following section.

Table 5.19. Final yields obtained from vacuum distillation and product distillation.

Run #	Initial mass (g)	Heavy cut mass (g)	Light cut mass (g)
450 – 1	192.5	107.4	63.8
450 – 2	198.6	134.3	32.8
M#1	387.7	205.5	154.8
M#2	352.3	136.9	188.9
M#3	348.8	173.7	146.2
M#4	142.2	73.8	55.4
Total (g)	1,622.1	831.6	641.9
Distillate yield (wt%)	-	51.3	39.6
Collected mass (g)	-	822.9	633.6
Yield cut (wt%)	-	50.7	39.1
Process yield (wt%)	89.8	**Mass loss (wt%)**	10.2

Table 5.20. Final compositions of heavy products distilled, compared to the composition of run **450 - 1**.

	Mass composition (wt%)		**Volume composition (vol%)**	
Compound	**B2**	**Run # 450 - 1**	**B2**	**#450 - 1**
C_{10+} ethers	63.7	70.1	65.1	71.4
Unreacted alcohols	7.3	8.6	7.3	8.4
C_{4+} olefins	0	0.0	0.1	0
Unknowns	27.4	20.4	26.1	19.1
Butyl ether	1.5	0.9	1.5	0.9

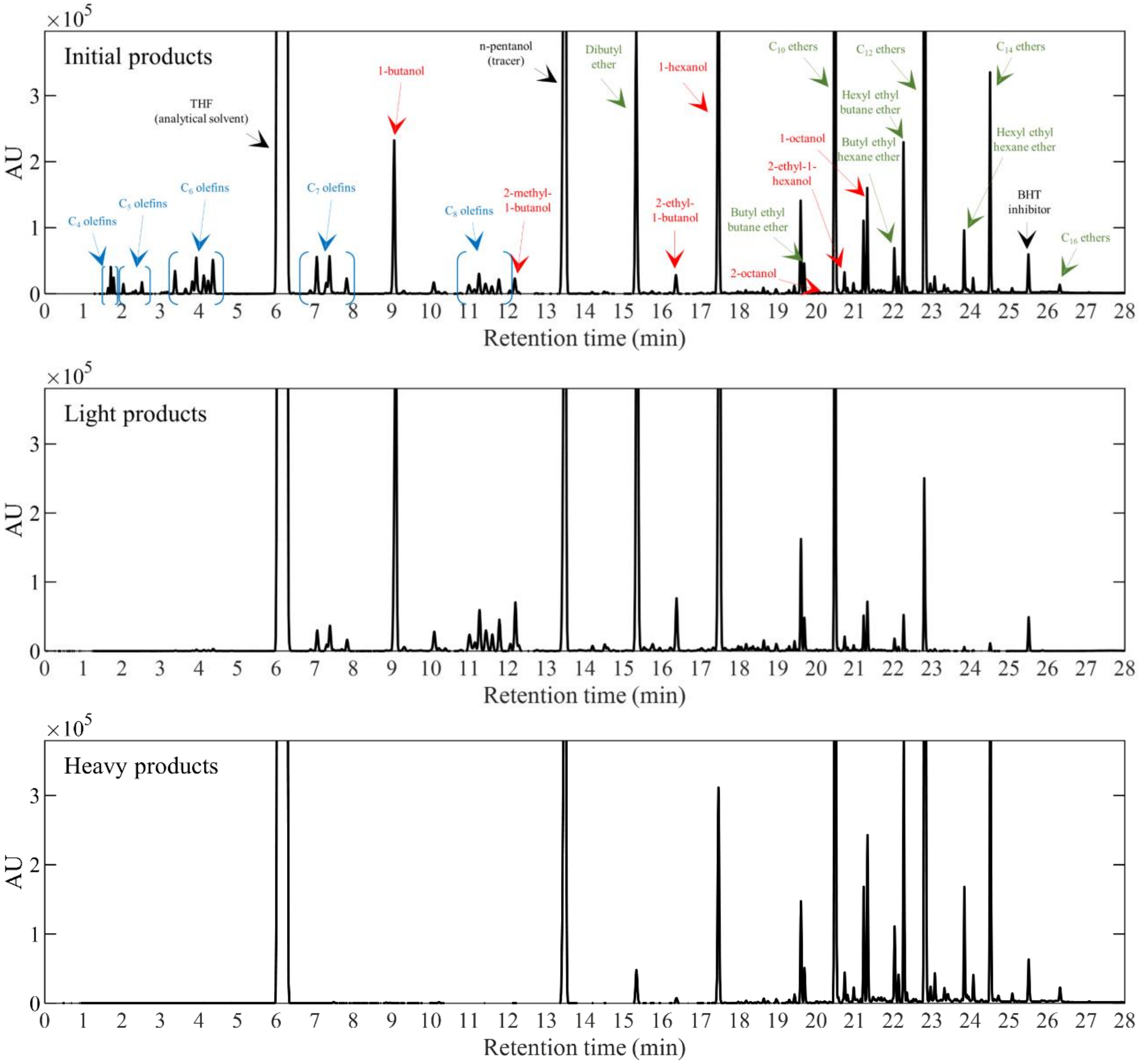

Figure 5.17. GC-chromatogram of the major components in run 450 – 1. Top: GC-chromatogram of the initial products. Middle: GC-chromatogram of the light products obtained. Bottom: GC – chromatogram of the heavy products obtained. Blue represents olefin products, red represents unreacted alcohols, and green represents ether products.

Table 5.21. Mass composition of heavy and light products from distillation experiments.

Ether	C#	Heavy products	Light products
di-n-butyl ether	8	1.5%	14.2%
butyl ethylbutane ether	10	0.5%	0.5%
C10 ether	10	25.7%	14.7%
butyl ethylhexane ether	10	1.1%	0.3%
hexyl ethylbutane ether	12	3.1%	0.3%
C12 ether	12	27.6%	5.0%
C14 ether	14	4.4%	0.5%
hexyl ethylhexane ether	14	1.0%	0.2%
C16 ether	16	0.3%	0.0%
Olefins			
C4 olefins	4	0.0%	0.0%
C5 olefins	5	0.0%	0.0%
C6 olefins	6	0.0%	2.3%
C7 olefins	7	0.0%	3.8%
C8 olefins	8	0.0%	4.0%
Unreacted Alcohols			
1-butanol	4	0.0%	11.0%
2-methyl-1-butanol	5	0.0%	0.8%
1-hexanol	6	1.9%	16.1%
2-ethyl-1-butanol	6	2.6%	0.9%
2-heptanol	7	0.1%	0.1%
1-octanol	8	1.3%	0.7%
2-octanol	8	1.1%	0.0%
2-ethyl-1-hexanol	8	0.3%	0.2%
Unknown products (wt%)	-	27.4%	24.4%
C10+ ethers (wt%)	-	63.7%	21.5%
C4+ olefins (wt%)	-	0.0%	10.1%
Unreacted alcohols (wt%)	-	7.3%	29.8%
Butyl ether (wt%)	-	1.5%	14.2%
Total weight (g)		822.9	633.6
Total volume (mL)		1025.6	817.8

5.3.8 Fuel characterization of the one-liter blendstock

Table 5.22. Measured fuel properties of blend 1, 2, 3, 4, and 5.

Fuel	**Flash point (K)**	**ICN**	**Viscosity (mm^2/s)**	**Density (kg/m^3)**	**Cloud point (K)**
#2 diesel (**B1**)	344.85	43.9	2.64	857.9	250.35
Bioblendstock (**B2**)	337.65	> 95.0	1.40	793.8	202.15
57% B1 + 43% B2 (**B3**)	339.65	59.8	1.92	831.3	247.85
Surrogate (**B4**)	323.95	> 95.0	1.32	794.4	216.15
57% B1 + 43% B4 (**B5**)	335.95	63.0	1.87	830.8	246.65

B2 was sent to the National Renewable Energy Laboratory (NREL) to determine the fuel properties. Three sample compositions were studied to assesss the differences between mixtures of fossil diesel and the biodiesel blendstock produced from dehydration reactions. B1, a pure fossil #2 diesel, was used as a reference for property characterization. B2 is pure bioblendstock that we produced from the dehydration reactions, and B3 is a mixture of 57% fossil #2 diesel (B1) and 43% B2 by volume. The flashpoint (ASTM D6450[29]), density (ASTM D445[30]), cloud point (ASTM D5773[31]), viscosity (ASTM D7042[32]), and the indicated cetane number (ASTM D8183[33]) were measured for each blend. The results for all blends are shown in **Table 5.22**. B2 exhibits an excellent cetane number and cloud point relative to B1. The higher cetane number indicates that the produced fuel has superior autoignition characteristics (i.e., shorter ignition delay) relative to typical #2 diesel fuel, whereas it's low cloud point allows the fuel to remain pure liquid, with no risk of crystal formation, even at very low temperatures. B2 does not meet the full ASTM D975 property specifications due to its low viscosity[34]. It is worth mentioning that the viscosity requirement is primarily a hardware constraint, and less relevant to the actual in-cylinder combustion performance of the fuel. However, B2 does meet the viscosity requirements for a diesel #1, and further, it represents a very attractive blending component for fossil #2 diesel. This is shown in **Table 5.22** by B3 which consists of a high fraction of the pure bioblendstock (43% by volume). B3 meets all ASTM D975 standards including viscosity, and still retains an indicated cetane number 16 points higher and a cloud point 2.5 ^{o}C lower than the fossil #2 diesel. As stated previously, the blendstock consists of a decent fraction of unknowns (20.9 vol%). The EPA has established benchmarks for the characterization of unknown compounds for evaporative and combustion emission studies[35]. Ethers with 6 or fewer carbons must be characterized, while for all other species, molecules with 12 or fewer carbons must be characterized. In our previous studies, we characterized ethers and hydrocarbons in the C_2 – C_{20} range[8]. In this study, we have characterized ethers and hydrocarbons in the C_4 – C_{16} range. It is is likely that the undetected species are molecules in the C_{12+} range, as high boilers (>240 ^{o}C) cannot be detected using low temperature GC methods.

Table 5.23. Bioblendstock surrogate palette and composition.

Component	Surrogate mole fraction
Butyl ether	0.08
Hexyl ether	0.612
Octyl ether	0.033
Isoamyl ether	0.198
Hexanol	0.04
Octanol	0.016
Octene	0.022

As most of the final product was used for the ASTM specification testing, A bioblendstock surrogate, defined as B4, was also made to model the final product produced from the dehydration experiments. **Table 5.23** shows the mole fraction of each component chosen to model B2. To verify its similarity to B2, B4 and a mixture of 57% B1 and 43% B4 were also sent for testing at NREL. The comparison between the two fuels are provided in **Table 5.22**. It can be seen that B4 has similar properties to the bioblendstock produced from dehydration experiments (B2), with the exception of its' lower flash point and higher cloud point. Good agreement between all measured properties was obtained when comparing B5 to B3 **Table 5.22**. This similarity of the fuel properties is somewhat surprising, considering approximately 20.9 vol% of B2 is composed of unknown components (see **Table 5.16**). Based on these results, the surrogate blend appears to be a reasonable representation of the real fuel produced from dehydration reactions and these unkonwn components from the GC are good blendstocks for diesel fuel.

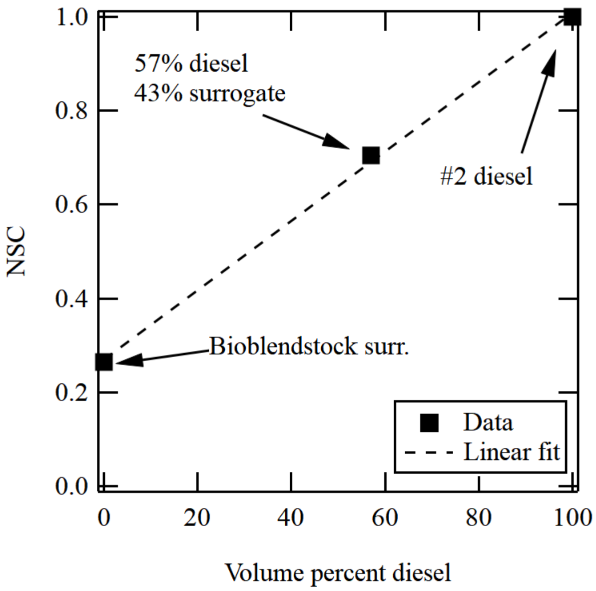

Figure 5.18. Measured normalized soot concentration of each fuel sample test, plotted vs. volume percent of #2 diesel present in the sample.

B1, B4, and B5 were also sent for testing to the Pfefferle Lab at Yale University to perform normalized soot concentration (NSC) measurements[36], used to compare the sooting propensity of the fuels. The NSC measurements were conducted using a photmultiplier tube to measure the maximum line-of-sight spectral radiance along the centerline of a methane/nitrogen diffusion flame seeded with 1000 ppm of the test sample. The results were then normalized to the results obtained from pure fossil #2 diesel to quantify the relative sooting propensity of each fuel. **Figure 5.18** presents the results obtained from the NSC measurements. The NSC measurements are plotted with respect to the volume percent of fossil #2 diesel blended into each sample. For pure bioblendstock surrogate, significantly less soot (less than 30%) is produced compared to fossil diesel #2. This is likely due to the composition, in which only oxygenate compounds are present[37]. As the fraction of fossil diesel #2 increases, the NSC increases linearly. The results confirm the high likelihood of lower sooting propensity for the bioblendstock produced from the dehydration reactions compared to fossil #2 diesel.

5.4 Conclusions

The following conclusions have been drawn based on the work reported here:

1. The powder zeolite Y had a higher carbon balance, activity and ether selectivity than the pellet zeolite Y in a continuous flow reactor using for dehydration of pure n-butanol and a EtOH/ButOH oligomerization feed. This indicates that the binder in the zeolite causes undesired reactions. During the reaction the products adsorb on the catalyst surface and cause the powder catalyst to agglomerate. This agglomeration increases the pressure drop in the reactor.
2. Even at room temperature the pressure drop in the continuous flow reactor increased to above 6.9 bar when using pellet Y catalyst with a n-butanol feed. The pressure drop under these

conditions was estimated by the Ergun equation to be 0 bar. The feedstock absorbs strongly onto the interior of the pellets, resulting in higher carbon uptake compared to powder Y catalyst. Large alcohols, as well as branched and secondary alcohols, increase the carbon uptake on pellet Y catalyst. This resulted in lower carbon balances compared to Powder Y catalyst. High WHSV led to a coke concentration gradients across the Pellet Y catalyst bed, signifying that mass transfer effects are present during dehydration reactions. Using smaller particle sizes of pellet Y, mass transfer effects may be reduced, at the expense of higher coke formation. More rigorous studies of the pellet formulation will be needed to mitigate the formation of coke for the dehydration reactor and scale up this process.

3. Based on fuel property testing of 1 L of fuel produced in Parr batch reactors and distilled to eliminate high volatility components, the bioblendstock from alcohol dehydration can meet the ASTM standards for density, cetane number, cloud point and flash point. High volume fractions of the blendstock produced from dehydration reactions can be blended with fossil #2 diesel to satisfy the ASTM standard for viscosity. The surrogate blendstock had a higher amount of soot reduction for the bioblendstock than for fossil #2 diesel. This chapter shows that fuels produced by dehydration of ethanol oligomerization products can be used as a high quality blendstock for #2 diesel fuel.

5.5 Acknowledgements

We would like to thank the National Renewable Energy Laboratory (NREL) for testing and providing the fuel property characterization of our blendstock produced. We would like to thank the Pfefferle Lab at Yale University for providing the soot concentration measurements.

This work was supported and financed by the U.S. Department of Energy – Vehicle Technology Office (DOE-VTO), based upon work supported by the U.S. Department of Energy's Office of

Energy Efficiency and Renewable Energy (EERE) under the Bioenergy Technologies Office, Cooptimization of Fuels and Engines (Co-optima) initiative award number DE-EE0008480. The views expressed in this manuscript do not necessarily represent the views of the U.S. Department of Energy or the United States Government.

References

1. 2018 Outlook for Energy: A View to 2040, ExxonMobil, Irving, 2018.
2. D. Smith, R. Graves, B. Ozpineci, P. Jones, J. Lustbader, K. Kelly, K. Walkowicz, A. Birky, G. Payne and C. Sigler, An Assessment of Technology and Knowledge Gaps (US DOE report ORNL/SPR-2020/7), 2019, 1-85.
3. J.-M. Restrepo-Flórez, P. Cuello-Penaloza, E. Canales, D. Witkowski, D. A. Rothamer, G. W. Huber and C. T. Maravelias, Sustainable Energy & Fuels, 2023, **7**, 693-707.
4. N. M. Eagan, B. M. Moore, D. J. McClelland, A. M. Wittrig, E. Canales, M. P. Lanci and G. W. Huber, Green Chemistry, 2019, **21**, 3300-3318.
5. S. Subramanian and D. Rothamer, Exploration of Fuel Property Impacts on the Combustion of Late Post Injections Using Binary Blends and High-Reactivity Ether Bioblendstocks, Report 0148-7191, SAE Technical Paper, 2023.
6. S. Subramanian, Investigation of the Use of High-Cetane Mono-Ether Bioblendstocks to Improve Catalyst Heating and Warmed Up Operation of MCCI Engines, The University of Wisconsin-Madison, 2024.
7. S. Subramanian and D. Rothamer, Fuel, 2024, **373**, 132139.
8. E. Canales, S. C. Hower, D. P. Li, A. Tambe, D. Rothamer and G. W. Huber, Sustainable Energy & Fuels, 2024, **8**, 3036-3047.
9. J.-M. Restrepo-Flórez, J. E. Chavarrio, E. Canales, P. Cuello-Peñaloza, D. Witkowski, S. Subramanian, D. A. Rothamer, G. W. Huber and C. T. Maravelias, Under review.
10. R. V. Jasra, B. Tyagi, Y. M. Badheka, V. N. Choudary and T. S. Bhat, Industrial & engineering chemistry research, 2003, **42**, 3263-3272.
11. V. R. Choudhary, P. Devadas, A. K. Kinage and M. Guisnet, Applied Catalysis A: General, 1997, **162**, 223-233.
12. J. Fougerit, N. Gnep, M. Guisnet, P. Amigues, J. Duplan and F. Hugues, in Studies in surface science and catalysis, Elsevier, 1994, vol. 84, pp. 1723-1730.
13. F. Dorado, R. Romero and P. Cañizares, Industrial & engineering chemistry research, 2001, **40**, 3428-3434.
14. I. Hoek, T. Nijhuis, A. Stankiewicz and J. Moulijn, Applied Catalysis A: General, 2004, **266**, 109-116.
15. G. M. Woltermann, J. S. Magee and S. D. Griffith, in Studies in Surface Science and Catalysis, Elsevier, 1993, vol. 76, pp. 105-144.
16. O. Bey and G. Eigenberger, Chemical Engineering Science, 1997, **52**, 1365-1376.
17. H. S. Folger, Elements of Chemical Reaction Engineering, Fifth Edition, 2016.
18. E. N. Fuller, P. D. Schettler and J. C. Giddings, Industrial & Engineering Chemistry, 1966, **58**, 18-27.
19. R. Ahmed, C. Sinnathamb and D. Subbarao, Journal of Applied Sciences, 2011, **11**, 1225-1230.
20. I. Van Zandvoort, Y. Wang, C. B. Rasrendra, E. R. van Eck, P. C. Bruijnincx, H. J. Heeres and B. M. Weckhuysen, ChemSusChem, 2013, **6**, 1745-1758.
21. I. Van Zandvoort, E. J. Koers, M. Weingarth, P. C. Bruijnincx, M. Baldus and B. M. Weckhuysen, Green Chemistry, 2015, **17**, 4383-4392.
22. S. Ergun, Chemical engineering progress, 1952, **48**, 89.
23. National Center for Biotechnology Information, 1-butanol, https://pubchem.ncbi.nlm.nih.gov/compound/1-Butanol, (accessed April 2, 2024).

24. The Engineering Toolbox, Argon - Density and Specific Weight, https://www.engineeringtoolbox.com/argon-density-specific-weight-temperature-pressure-d_2089.html, (accessed April 2, 2024).
25. The Engineering Toolbox, Gases - Dynamic Viscosities, https://www.engineeringtoolbox.com/gases-absolute-dynamic-viscosity-d_1888.html, (accessed April 2, 2024).
26. J. Rorrer, S. Pindi, F. D. Toste and A. T. Bell, ChemSusChem, 2018, **11**, 3104-3111.
27. F. Collignon, M. Mariani, S. Moreno, M. Remy and G. Poncelet, Journal of Catalysis, 1997, **166**, 53-66.
28. W. Song, Y. Liu, E. Barath, L. L. Wang, C. Zhao, D. Mei and J. A. Lercher, ACS Catalysis, 2016, **6**, 878-889.
29. ASTM D6450-16a, Standard Test Method for Flash Point by Continuously Closed Cup (CCCFP) Tester, 2021.
30. ASTM D445-24, Standard Test Method for Kinematic Viscosity of Transparent and Opaque Liquids (and Calculation of Dynamic Viscosity), 2024.
31. ASTM D5773-21, Standard Test Method for Cloud Point of Petroleum Products and Liquid Fuels (Constant Cooling Rate Method), 2021.
32. ASTM D7042-21a, Standard Test Method for Dynamic Viscosity and Density of Liquids by Stabinger Viscometer (and the Calculation of Kinematic Viscosity), 2021.
33. ASTM D8183-18, Standard Test Method for Determination of Indicated Cetane Number (ICN) of Diesel Fuel Oils using a Constant Volume Combustion Chamber—Reference Fuels Calibration Method., 2018.
34. ASTM D975-21, Standard Specification for Diesel Fuel, 2021.
35. EPA Registration of fuels and fuel additives 40 CFR Part 79, 514-611.
36. V. L. Dagle, M. Affandy, J. S. Lopez, L. Cosimbescu, D. J. Gaspar, S. S. Goldsborough, T. Rockstroh, S. Cheng, T. Han and C. P. Kolodziej, Fuel, 2022, **310**, 122314.
37. J. Abboud, J. Schobing, G. Legros, J. Bonnety, V. Tschamber, A. Brillard, G. Leyssens, V. Lauga, E. E. Iojoiu and P. Da Costa, Fuel, 2017, **193**, 241-253.

Chapter 6. Conclusions

6.1 Conclusions

The dehydration of C_{4+} alcohol streams were studied in a continuous flow system using powder zeolite Y. Crucial process design and decisions were derived from the results obtained using feedstocks obtained from a real ethanol oligomerization reactor. The dehydration results indicated that feedstocks with high concentrations of C_{6+} alcohols can mainly produce diesel #2. Based on the initial technoeconomic analysis, the second technoeconomic analysis implemented a ester hydrogenolysis and n-butanol recycling unit, further improving the final diesel fuel yield obtained from the ethanol to diesel process. Due to the ongoing issues with pelletized zeolite Y, batch reactors were the alternative route to produce drop-in diesel at the liter scale.

The reaction chemistry of C_{4+} alcohols were studied to uncover how alcohol structure and length play a role in competitive mono-molecular and bi-molecular dehydration reactions. Pressurizing the system above the vapor pressure of the incoming reactant streams heavily favored bi-molecular dehydration. Increasing the size of the alcohol led to lower ether selectivities and carbon balances. As the carbon number of the reactant feed obtained from ethanol oligomerization increased, the overall ether selectivity decreases. At the same time, the ether distribution begins to shift from the C_8 to C_{10+} range. The increase in secondary alcohol concentration led to lower yields of ethers, as these molecules prefer mono-molecular dehydration. The ethanol:butanol oligomerization products further increased the carbon number of the incoming reactant stream. Using these alcohols, the C_{10+} ether yield further increased compared to the previous feedstocks studied.

Esters play a significant role in the dehydration reactor. At low concentrations, low carbon balances and ether selectivity were observed, necessitating the removal of these molecules prior to entering the dehydration reactor. High purity alcohol streams are necessary for the dehydration reactor, ideally above 99.90 wt%. Based on these findings, the final model feedstocks were developed, assuming the esters undergo 100% ester hydrogenolysis to produce their respective alcohols.

The first technoeconomic analysis did not implement an ester hydrogenolysis or n-butanol recycling unit. The model feedstock at 67% ethanol conversion was chosen as it favored the formation of C_{10+} ethers in the dehydration reactor, due to the high concentration of C_{6+} alcohols that could undergo bi-molecular dehydration. High conversion ethanol oligomerization reactors significantly reduced plant costs. The final diesel #2 yield was 34.5 wt%, on a dry ethanol basis. The ether blend produced had a positive engine impact, leading to higher combustion efficiencies and lower NO_X emissions compared to its fossil counterpart. The flashpoint was slightly below ASTM standards, and the cetane number of the ether-rich blend was 73. The chemical process can be implemented with existing carbon-reduction technology, showing a maximum of 132.7% reduction in greenhouse gas emissions.

The second technoeconomic analysis improved the initial work, by implementing the ester hydrogenolysis and n-butanol recycling units. The final diesel #2 yield was 57.9 wt%, on a dry ethanol basis. The implementation of the n-butanol recycling unit showed the process can be tuned to produce heavier fuels. The cetane number of the diesel #2 blend produced was 90, showing an improvement in specification from our previous results. The technology was shown to be price-competitive with current bio-diesel technologies when ethanol was used as a starting feedstock.

Lastly, scale up studies were conducted to uncover the issues of developing the ethanol to diesel process from the lab to pilot scale. Using a pellet formulation of Zeolite Y, the catalytic activity was significantly different from the powder form of Y. Lower carbon balances and ether selectivities were observed, and crushing the pellets to smaller particle sizes did not fully recover the activity of zeolite Y. A more rigorous pellet formulation program will need to be developed to improve the activity of the formulation for diesel fuel production at larger scales.

Batch reactors were used to produce one liter of bio-ether blendstock for engine testing. 45 mL parr reactors showed significant differences in ether yields compared to 450 mL parr reactors. High conversion regimes showed that ethers may be decomposing to form other unknown heavy products. The reaction time was successfully decreased from two days to approximately one day. Increasing the pressure showed no increase in the C_{10+} ether yield. Centrifuge and vacuum distillation were successful in fully separating the catalyst and light products from the final heavy blend. A high concentration of C_{10+} ethers in the final blend was obtained, with the second highest concentration being unknown products.

6.2 Future directions

6.2.1 Metal doping of zeolites

Catalyst synthesis will be crucial in understanding the adsorption effects pertaining to alcohols. Furthermore, mitigating coke production would further improve the carbon yields obtained for diesel production. In literature, zeolites have undergone many modifications, mainly the addition of metal dopants. It has been observed that gas phase 1-hexanol dehydration to hexenes at 300ºC is enhanced at higher nickel (Ni) loadings on Zeolite NaY[1]. Conversion increased with a Ni loading up to 4.7 wt% and led to an increase in acid site concentration, the latter hypothesized to be more important than acid site strength for dehydration of alcohols. It has also been observed that alkali metals increases the energetic stability of the zeolite Chabazite, and that larger ions (K > Na > Li > Ca) prevent the zeolite framework from collapsing[2]. Zeolites have also been doped with Barium (Ba) and Silver (Ag) for the dehydration of methanol to light alkenes, exhibiting greater carbon yields towards C_2-C_4 olefins[3]. Doping of rare-earth metals has also been studied for fluid catalyzed cracking (FCC) catalysts, in which USY Zeolite is exchanged with rare-earth metals such as Ytrrium (Y) and Lanthanum (La)[4]. Y-USY Zeolite exhibited greater surface area retention after deactivation. Furthermore, there was an improvement in turnover frequency per framework Al site and higher selectivity towards C_{4+} gasoline molecules relative to La catalysts. Published work has currently been on improving dehydration of alcohols at temperatures >300°C for alkene formation. However, unimolecular dehydration and bimolecular dehydration compete due to temperature. Since unimolecular dehydration is endothermic and etherification exothermic, lowering the temperature would favor alcohol dehydration to ethers[5].

6.2.2 Pellet formulation

As shown in chapter 5, pellet formulation will be crucial for scaling up the production of drop-in diesel at the liter scale. The pellet must complement the reaction chemistry of interest to not significantly change the yields seen over powder catalysts. The introduction of binders can decrease catalytic activity and also affect the reaction chemistry over the catalyst of interest[6, 7]. These effects can be attributed to affecting the zeolite crystallinity, shape selectivity of products, and coke deactivation mechanisms. Lower activity is likely to be observed for zeolite pellets, as some formulations can lower the acid site density of the parent catalyst, even with the introduction of metal dopants on the catalyst[8, 9]. The binder material can also play a crucial role in changing the crystallinity of the zeolite catalyst. Therefore, testing the concentration of different materials would be crucial to understand what formulation mechanisms have the greatest effect on dehydration chemistry. Researchers are also currently developing synthesis methods that improve the overall catalytic activity of the zeolite in shaped pellets. One interesting method involves growing the zeolite powder into crystals, while simultaneously removing the added binder to produce a binderless pellet[10-12]. These pellets exhibited superior activity and longer time on stream reactions compared to their powder zeolite ZSM-5 counterpart[10]. Furthermore, the mechanical strength of these pellets shows that they can be used in continuous flow systems without affecting the flow pattern. While these techniques are novel and would require more investigation in a practical reaction system, they nonetheless show promise in tackling the ongoing issues with binder/zeolite mixtures affecting catalytic activity.

6.2.3 Outlook

At the current moment that this dissertation is written, there are no known commercial processes that have the capability of producing diesel range ethers suitable to be used for drop-in fuels. The success of our current project is attributed to understanding the fundamental chemistry (Chapter 2) and catalysis research pertaining to the effects alcohol structure and size, as well as the implementation of the technoeconomic and lifecycle analysis of our process (Chapters 3 and 4). The initial analysis was promising and was further improved with the implementation of crucial process design decisions such as the ester hydrogenolysis and n-butanol recycling units. Understanding the underlying issues with scaling up from bench to pilot scale was also crucial for the next steps of the ethanol to diesel process (Chapter 5).

Firstly, catalyst design can hopefully solve the issues of alcohol absorption and coking. These two mechanisms are the main contributors that negatively affect the ethanol to diesel process. Mitigating these two effects can lead to higher carbon balances, ether yields, and profitability, as fuel yield is an important economic factor[13]. The current process shows catalyst stability for up to 50 hours time on stream. While this is promising, the use of larger alcohol feeds will ultimately decrease the time on stream of the reaction. It is therefore safe to assume that the current bottleneck of the process is the development of the dehydration unit to produce drop-in diesel at reasonable yields. Furthermore, ideal feedstocks for the dehydration step would be linear alcohol feeds. This may not be realistic, as the ethanol oligomerization reactor produces a wide distribution of alcohols with varying sizes and structure. While secondary alcohols will mainly produce olefins, tuning the catalyst to further promote bi-molecular dehydration of branched alcohols can further improve the final ether yields obtained. Another challenge is possibly addressing the negative effects of esters on dehydration chemistry, though this may be more challenging. Perhaps growing the esters and ethers in the same unit would lead to lower capital costs in the ethanol to diesel process, as the ester hydrogenolysis unit uses a significant amount of hydrogen. Furthermore, large chain esters are already used in commercially produced biodiesel. This can lead to a more valuable product, as another class of oxygenate molecules can be used to produce drop-in diesel.

Secondly, it will be crucial to develop a pellet formulation program to make this process a reality. As we showed in chapter 5, one cannot assume that the binder is inert, as it is likely contributing to the low carbon balances and ether yields observed. Understanding pellet geometry can help improve the flow pattern of the liquid phase in the reactor, addressing any mass transfer effects that can be present. Understanding the effects of binder concentration can shed light on formulation limits to not negatively affect the reaction chemistry seen at the bench scale. Using different binder materials and comparing them at different concentrations will be useful to produce pellets that can achieve the same catalyst activity compared to their powder counterparts[6, 7]. In other words, the ideal pellet would be one that mitigates coke and alcohol absorption mechanisms. This would alleviate the sticky phase that has the potential to be formed, leading to no pressure buildup, or clogging in the reactor, a common issue found when scaling up processes[14]. These tests should be done in the 3/8-inch reactor before going to a one-inch reactor to establish proof of concept. Ultimately, addressing these challenges will allow us to produce diesel-range ethers at commercially relevant quantities in a continuous flow system. At the current moment that this dissertation is written, parr reactors are the only alternative to producing drop-in diesel-range ethers at the liter scale.

Lastly, it is thus my suggestion that catalyst design must be the next and most important challenge that needs to be addressed. The reaction chemistry has now been understood[15], and researchers should focus their efforts on catalyst and pellet synthesis. Combining their findings with researchers with expertise in economic and lifecycle analysis of biorefineries, there is significant potential in this technology to become reality. Time will tell as to whether this is possible, but the likelihood of the ethanol to diesel process being transitioned to the pilot scale is only a pellet away.

References

1. C. Park and M. A. Keane, Journal of Molecular Catalysis A: Chemical, 2001, **166**, 303-322.
2. G. Cruciani, Journal of Physics and Chemistry of Solids, 2006, **67**, 1973-1994.
3. A. M. Al-Jarallah, U. A. El-Nafaty and M. M. Abdillahi, Applied Catalysis A: General, 1997, **154**, 117-127.
4. Y. Shu, A. Travert, R. Schiller, M. Ziebarth, R. Wormsbecher and W.-C. Cheng, Topics in Catalysis, 2015, **58**, 334-342.
5. T. K. Phung, L. P. Hernández, A. Lagazzo and G. Busca, Applied Catalysis A: General, 2015, **493**, 77-89.
6. J. Fougerit, N. Gnep, M. Guisnet, P. Amigues, J. Duplan and F. Hugues, in Studies in surface science and catalysis, Elsevier, 1994, vol. 84, pp. 1723-1730.
7. V. R. Choudhary, P. Devadas, A. K. Kinage and M. Guisnet, Applied Catalysis A: General, 1997, **162**, 223-233.
8. F. Dorado, R. Romero and P. Cañizares, Industrial & engineering chemistry research, 2001, **40**, 3428-3434.
9. F. Dorado, R. Romero and P. Cañizares, Applied Catalysis A: General, 2002, **236**, 235-243.
10. J. Zhou, J. Teng, L. Ren, Y. Wang, Z. Liu, W. Liu, W. Yang and Z. Xie, Journal of Catalysis, 2016, **340**, 166-176.
11. B. Yan, S. Yu, C. Zeng, L. Yu, C. Wang and L. Zhang, Microporous and Mesoporous Materials, 2019, **278**, 267-274.
12. J. Liu, S. Li, Z. Zhang, N. Fusi, C. Liu, G. Xiong, G. Vilé and N. He, ACS Applied Nano Materials, 2021, **4**, 11997-12005.
13. J.-M. Restrepo-Flórez, P. Cuello-Penaloza, E. Canales, D. Witkowski, D. A. Rothamer, G. W. Huber and C. T. Maravelias, Sustainable Energy & Fuels, 2023, **7**, 693-707.
14. R. V. Jasra, B. Tyagi, Y. M. Badheka, V. N. Choudary and T. S. Bhat, Industrial & engineering chemistry research, 2003, **42**, 3263-3272.
15. E. Canales, S. C. Hower, D. P. Li, A. Tambe, D. Rothamer and G. W. Huber, Sustainable Energy & Fuels, 2024, **8**, 3036-3047.